Measurements and Models Related to Solar Optics in Windows with Shading Devices

by

Nathan Amon Kotey

A thesis

presented to the University of Waterloo

in fulfillment of the

thesis requirement for the degree of

Doctor of Philosophy

in

Mechanical Engineering

Waterloo, Ontario, Canada, 2009

Author's Declaration

I hereby declare that I am the sole author of this thesis. This is a true copy of the thesis, including any required final revisions, as accepted by my examiners.

I understand that my thesis may be made electronically available to the public.

Abstract

Shading devices have the potential to reduce peak cooling load and annual energy consumption because they can be used to control solar gain. Thus, the need to model shading devices in a glazing system analysis is important.

This thesis deals with various measurement techniques and model development related to solar optics in windows with shading devices. It also considers longwave radiative properties of shading devices via model development and experimentation. The different shading devices examined were roller blinds, insect screens, pleated drapes and venetian blinds.

The energy performance of windows with shading devices was modeled using a two step procedure. Solar radiation was considered in the first step by developing a multi-layer solar optical model for glazing/shading systems. This newly developed model is an extension of an existing model for systems of specular glazing layers and includes the effect of layers that create scattered, specifically diffuse, radiation in reflection and/or transmission. Spatially-averaged (effective) optical properties were used to characterise shading layers, including their beam-diffuse split. The multi-layer solar optical model estimates the system solar transmission and absorbed solar components. The absorbed solar components appear as energy source terms in the second step – the heat transfer analysis. The heat transfer analysis involves the formulation of energy balance equations and requires both effective longwave properties and convective heat transfer coefficients as input. The simultaneous solution of the energy balance equations yields the temperature as well as the convective and radiative fluxes.

The effective solar optical properties of flat materials like drapery fabrics, roller blinds and insect screens were obtained by developing a new measurement technique. Special sample holders were designed and fabricated to facilitate measurements using an integrating sphere installed in a commercially available spectrophotometer. Semi-empirical models were then developed to quantify the variation of solar optical properties with respect to incidence angle. In turn, effective layer properties of venetian blinds and pleated drapes were modeled using a more fundamental net radiation scheme.

The effective longwave properties of flat materials were obtained by taking measurements with an infrared reflectometer using two backing surfaces. The results enabled simple models to be developed relating emittance and longwave transmittance to openness, emittance and longwave transmittance of the structure. In turn, effective longwave properties of venetian blinds and pleated drapes were modeled using a net radiation scheme. Convective heat transfer correlations were readily available.

Finally, the newly developed models were validated by measuring the solar gain through various shading devices attached to a double glazed window using the National Solar Test Facility (NSTF) solar simulator and solar calorimeter. Solar gain results were also obtained from simulation software that incorporated the models. There was good agreement between the measured and the simulated results thus strengthening confidence in the newly developed models.

Acknowledgements

My first and foremost thanks go to God Almighty for bringing me this far in life.

My sincere thanks and appreciation goes to Prof. J. L. Wright, my research supervisor who not only chose this topic for study but also nurtured its successful realization through the very useful criticisms and materials provided during the research. Prof. J. L. Wright has been exceptionally helpful. Words cannot express the value of what you have done for me and once again, thank you very much. I look forward to future opportunities to interact on projects and papers.

For your invaluable assistance, personal involvement and encouragement, Prof. M.R. Collins, I wish to extend my profound gratitude. You did not only help me in my research work but also assisted me throughout my studies on this campus.

For your immense love, patience and understanding, Sally Amon-Kotey, my beloved wife, words cannot express how much you have been so supportive while I pursue my studies. Carol-Jane Naa Dei Amon-Kotey, my sweet little daughter, although you did not understand what was going on while I deserted you during the week, I really appreciate your ever willingness to hug me with love and cheerfulness each time I showed up at the end of the week.

I would also like to express my indebtedness to Professor David Naylor for his willingness to be my external examiner. Special thanks to my internal examiners, Professors Gordon Stubley, Metin Renksizbulut and John Straube for your encouragement and support. To Dr. Alfred Brunger and Mr. Larry West, I say a big thank you for taking time from your busy schedule to make my experiments a realization. Special thanks to Corey Lindner of Golden Windows Ltd for supplying the IGU. My appreciation also goes to the staff in the engineering machine shop

especially to John Boldt, John Potzold, Fred Bakker, Rob Kaptein, Jorge Cruz and Juan Ulla for helping me with the fabrication of sample holders, window frame and special adapters that I used in my experiments. Special thanks to Steve Hitchman and Martha Morales for fixing all my computer related problems while I was on campus. My sincere thanks also go to the department secretaries and Lisa Tomalty-Crans for their administrative support.

Special thanks also go to Chris and Blythe Hadlock, Vivek Kansal, Martin Kegel, Veronique Delisle, Victor Halder, Shohel Mahmud, Ned Haung, Tao Jiang, Syeda Tasnim, Darryl Yahoda, Bart Lomanowski, Omid Nemati, Andrew Marston, Sebastein Brideau, Hani Abulkhair for their support during the course of my study. Finally, to all those kind people including my mother, brother and sisters, course mates and friends who helped in the successful realization of this project, I extend my humble appreciation for a good work done.

Financial support from the Natural Sciences and Engineering Research Council of Canada (NSERC), Alexander Graham Bell Graduate Scholarship, University of Waterloo President's Scholarship, Faculty of Engineering Graduate Scholarships and Department of Mechanical and Mechatronics Engineering Scholarships and American Society of Heating, Refrigerating, and Air-Conditioning Engineers Inc. (AHSRAE) Research Award are acknowledged and sincerely appreciated.

Dedication

This thesis is dedicated to my late father, Mr. Richard Kotey

Table of Contents

List of Figures

List of Tables

Nomenclature

Symbols

A	area (m^2), absorbed portion of solar radiation (dimensionless)
A_C	surface area of a portion of integrating sphere (m^2)
A_O	openness factor (dimensionless)
A_S	surface area of integrating sphere (m^2)
b	exponent used in semi-empirical solar property models for flat shading materials
B	beam flux (W/m^2), systematic (bias) uncertainty
$B_{X_{ij}}$	covariance estimator for systematic uncertainties in X_i and X_j
c	slat crown (m)
C	diffuse source term due to incident beam radiation on shading layer (W/m^2)
C_p	specific heat at constant pressure (J/kgK)
dA	elemental area (m^2)
D	diffuse flux (W/m^2), distance (m), wire diameter (m)
diff	difference between two sets of solar optical measurements (dimensionless)
F	view factor, exchange factor (dimensionless)
Fr	folding ratio (dimensionless)
F_λ	0% baseline reading (μm)
g	acceleration due to gravity (m/s^2)
G	irradiance (W/m^2)
h	heat transfer coefficient (W/m^2K), height of window (m),
I	incident flux (W/m^2)

IAC	Interior Attenuation Coefficient (dimensionless)
J	radiosity (W/m^2)
k	thermal conductivity (W/mK)
K	solar heat transfer factor (dimensionless)
L	spacing between glazing/shading layers (width of the gap) (m), length of drapery (m), number of identical sources of error
$\dot{m}$	mass flow rate (kg/s)
M	molecular mass (kg/kmol)
N	inward flowing fraction (dimensionless), number of different readings
P	Random (precision) uncertainty
$P_{X_{ij}}$	covariance estimator for random uncertainties in X_i and X_j
R	thermal resistance (m^2K/W), radius of integrating sphere (m), result
S	absorbed solar flux (W/m^2), distance between elemental areas (m), standard deviation, centre-to-centre spacing of wires (m)
S_λ	unadjusted spectrophotometer reading (μm)
SC	shading coefficient (dimensionless)
SHGC	Solar Heat Gain Coefficient (dimensionless)
SHGF	Solar Heat Gain Factor (dimensionless)
s	slat spacing (m)
t	layer thickness (m), reading from t-distribution
T	temperature (K)
q	heat flux (W/m^2)
Q	heat transfer rate (W)

U	overall uncertainty
U-factor	Overall coefficient of heat transfer (W/ m^2K)
w	slat width (m), pleat width (m), width of window (m)
X_1, X_2, etc.	measured variables
Z	source term for beam or diffuse radiation (W/m^2)
Z_λ	100% baseline reading (μm)

Greek Letters

α	absorptance (dimensionless)
β	solar altitude angle
ΔT	temperature difference (K)
γ	wall-solar azimuth angle
ε	emissivity, emittance (dimensionless)
θ	incidence angle
λ	wavelength (μm)
μ	dynamic viscosity (kg/ms)
ρ	reflectance (dimensionless), density (kg/m^3)
σ	Stefan-Boltzmann constant (W/m^2K^4)
τ	transmittance (dimensionless)
ϕ	slat angle
Ω	profile angle

Roman Numerals

I	open weave

II	semi-open weave
III	closed weave

Subscripts

1, 2, etc.	related to first reflection, second reflection, etc., related to location 1, location 2, etc.
∞	related to infinite summation of radiosities
a	related to air temperature
abs	related to absorber plate
al	related to air leakage
b	related to back surface
B1, B2	related to backing surfaces 1 and 2
bb	related to beam-beam property
beam	related to beam flux
bd	related to beam-diffuse property
bt	related to beam-total property
c	related to convective surface coefficient
cfs	related to complex fenestration system
cg	related to centre glass area
conv	related to convective heat flux
cutoff	related to cutoff angle
d	related to downward-facing surface
dd	related to diffuse-diffuse property
diff	related to diffuse flux
eg	related to edge glass area
g	related to total glass area

gap	related to spacing between glazing/shading layers
gas	related to thermophysical property of gas
gl	related to glazing layer
f	related to front surface
fan	related to air circulation fan
fr	related to frame
H	related to horizontal
ht	related to heat loss due to temperature difference
i	related to the i^{th} layer or the i^{th} gap, index used in counting
in	related to indoor-side, related to inlet port
inc	related to incident radiation
inp	related to input power
m	related to mean temperature
M1, M2	related to system reflectance with backing surfaces 1 and 2 in place
mw	related to mask wall
net	related to net heat transfer
out	related to outdoor-side
PARL	related to parallel surface
PERP	related to perpendicular surface
pump	related to recirculation pump
rad	related to radiative heat flux
r	related to radiative surface coefficient
R	related to results

sol	related to incident solar radiation
solar	related to heat transfer due to solar radiation
sys	related to glazing/shading system
tot	related to total quantity, related to total surface coefficient
trans	related to transmitted solar irradiance
u	related to upward-facing surface
V	related to vertical

Superscripts

+	related to outgoing flux
-	related to incoming flux
lw	related to longwave
m	related to drapery fabric (material) property
norm	related to normalised property
ref	related to reference radiosity
s	related to slat material
str	related to “structural” property of roller blind
w	related to wire material, related to window area
y	related to yarn property

Abbreviations

AM	Air Mass
ANSI	American National Standards Institute
ASHRAE	American Society of Heating, Refrigerating and Air Conditioning Engineers
ASTM	American Society for Testing and Materials

BAI	Broad Area Illumination
CDG	Conventional Double Glazed
CSA	Canadian Standards Association
CTS	Calibration Test Standard
D	Dark Colour
EEL	Enermodal Engineering Limited
ESP-r	Environmental Systems Performance-research
FTIR	Fourier Transform Infrared Spectroscopy
HB	Heat Balance
IGU	Insulated Glazing Unit
IS	Integrating Sphere
ISO	International Organization for Standardization
L	Light Colour
LBNL	Lawrence Berkeley National Laboratory
M	Medium Colour
NIR	Near infrared
NSTF	National Solar Test Facility
PbS	Lead Sulphide
PMT	Photomultiplier Tube
PTFE	polytetrafluoroethylene
RSS	Root-Sum-Square
RTS	Radiant Time Series
SOC	Surface Optics Corporation

SS	Stainless Steel
UV	Ultraviolet
UW	University of Waterloo
VIS	Visible
WIS	Window Information System

CHAPTER 1

INTRODUCTION

1.1 Background

Building energy consumption constitutes more than 40% of the total energy consumption in the US and Canada. It has also been estimated that about 25% of this consumption is attributed to windows. Due to rising cost of conventional energy sources like coal, petroleum and natural gas, there is an increased interest in conversion from conventional energy to renewable energy. Furthermore, renewable energy is generally known to be clean and environmentally friendly. The first approach to the conversion from conventional energy to renewable energy is conservation. Thus, improving the thermal performance of windows is a great potential for energy conservation.

Windows are openings in the wall of a building that generally allow the passage of solar radiation, thermal energy and air. Solar radiation entering the building through a window provides both daylight and heat gain to the indoor space. Thus, building energy requirements are directly influenced by the presence of windows. A typical window consists of glazing and framing components. The glazing may be a single layer or multiple layers. In a multi-layer glazing unit, the glazing layers are usually separated at the perimeter by a spacer and sealant. Such a unit is called an insulated glazing unit (IGU) with the cavity between the glazing layers usually filled with air or argon. The most common glazing material is glass although

plastics and other transparent materials are also used. The glazing unit is held in a sash which forms part of the framing system. The framing components are usually made of wood, metal, and/or polymers. Current technologies in energy efficient window design use low-emissivity (low-e) coating on the glazing, additional glazing layers, spectrally selective glass and substitute fill gas, usually argon, in the glazing cavity. To further control solar gain in addition to providing privacy, reducing glare and improving aesthetics, shading devices like venetian blinds, roller blinds and drapes are often attached to windows. If properly designed and controlled a shading device can be used to admit solar energy when and where heating is required, and reject it otherwise. Insect screens are frequently attached to windows as well. In the current context, an insect screen will be classified as a shading device because it can have a significant influence on solar gain (Brunger et al. 1999).

The performance of a window can be determined by energy analysis of the glazing and framing components. However, glazing system analysis continues to be the most important aspect of window research since it is the glazing through which the majority of the solar gain arises. In glazing system analysis, the glazing area is usually divided into one-dimensional centre glass region and two-dimensional edge glass section at the glass-frame interface. Window frame energy analysis is two-dimensional. Both edge glass and frame energy analyses have been given considerable attention (e.g., Wright et al. 1994, Wright and McGowan 1999). Nevertheless, it is the centre glass region that is associated with the majority of the energy transfer (Wright 1998).

Energy analysis of a glazing system takes advantage of the fact that there is no appreciable overlap in wavelengths between the shortwave (solar) and the longwave radiation. This leads to a two-step analysis. First, solar radiation models are used to determine the fraction of incident solar radiation directly transmitted through the glazing system and the fraction that is absorbed in each layer. The absorbed solar radiation in each layer then serves as a source term in the second step – the heat transfer analysis. The temperatures and the heat fluxes at each layer can be determined by this two-step analysis (e.g., Hollands et al. 2001, Finlayson et al. 1993).

When solar radiation is incident on glazing layers, a portion of it is directly transmitted to the indoor space while another portion is absorbed by the glazing layers, some of which is redirected to the indoor space by heat transfer. For any glazing system, the solar gain is characterised by the Solar Heat Gain Coefficient (SHGC) which is defined as the ratio of the total solar gain to the solar irradiance (e.g., ASHRAE 2005). Moreover, the temperature difference between the indoor space and the outdoor surrounding results in heat transfer through the glazing system via conduction, convection and longwave radiation. The heat transfer through the glazing system is characterised by the overall coefficient of heat transfer (U-factor). Considerable effort has been made in the past to rate windows in terms of SHGC and U-factor (e.g., CSA 1998). The SHGC and the U-factor used in energy rating methods are obtained by either measurement or computer simulation. Measurement of SHGC and U-factor can be obtained using a solar simulator and a solar calorimeter test facility (e.g., Harrison and Dubrous 1990). Measurements are usually taken with the irradiance from the solar simulator at normal incidence to the window. Various performance rating tools are also

available to calculate the SHGC and the U-factor of windows (e.g., VISION4 (UW 1996), FRAMEplus (EEL 1995), WIS (van Dijk et al. 2002), WINDOW 4.0 (Finlayson et al. 1993)). In all of these performance rating tools, the performance indices are calculated using the optical properties of the glazing layers at normal incidence.

The SHGC and the U-factor are the two performance rating indices that characterise the thermal performance of a glazing system. However, due to the hourly variation of solar radiation and intermittent cloud cover, solar gain represents the most variable heat gain imposed on the indoor space through a window. It is also likely to represent the largest heat gain of the indoor space. These two observations highlight the importance of determining the SHGC.

Solar gain through a window constitutes a significant portion of the cooling load and annual energy consumption of many buildings. The solar gain through a window becomes a cooling load only when the energy is transferred to the air by convection. The directly transmitted solar radiation is absorbed by the surfaces within the indoor space. When these surfaces become warmer than the surrounding air, heat is transferred to the air. Furthermore, the convective portion of the absorbed solar radiation in the glazing system gets transferred to the air in the indoor space almost instantly while the radiant portion (longwave radiation) gets absorbed by the surfaces in the indoor space and subsequently transferred to the air. There is therefore a time lag between the heat gain and its associated cooling load due to the delayed conversion of the radiant portion of the heat gain. The thermal storage capacity of the surfaces within the indoor space is critically important in differentiating between the

instantaneous heat gain and the cooling load. The reduction of the peak cooling load because of this time lag can be quite important in sizing the cooling equipment.

Recently, two cooling load calculation methods have been developed to account for the time delay effect. These methods (Heat Balance (HB) and Radiant Time Series (RTS)) are currently being used in building load and annual energy calculation tools (e.g., Pedersen et al. 1998, EnergyPlus 2005). Building load and annual energy calculations generally involve hour-by-hour computer calculations. The calculations are iterative in nature because of the nonlinear equations in the heat transfer models. They also require solar optical properties of glazing layers at various angles of incidence. Furthermore, the analysis involves the determination of the radiative/convective split to resolve the time lag between the instantaneous heat gain of a given space and its cooling load. The analysis is therefore computationally intensive and thus, simplicity and speed are assets. Spectral calculations in the solar optical models are therefore unrealistic and total optical properties are expected to give the desired accuracy.

1.2 Motivation

Over the past several decades, window energy analysis has been focused on glazing systems without examining the effects of shading devices (e.g., Pettit 1979, Pfrommer et al. 1995, Roos 1997, Rubin et al. 1998). However, shading devices are common. Shading devices like venetian blinds, roller blinds and drapes are frequently used to control solar gain through windows and their potential for reduction of building load and annual energy consumption is recognized to be large (e.g., Grasso and Buchanan 1982). As many windows have some

form of shading device attached, there is a clear need to include the effect of shading devices in the energy analysis (e.g., Wright et al. 2004). The effect of shading devices on window energy performance has therefore become an important topic in recent years (e.g., Rosenfeld et al. 2000, Breitenbach et al. 2001, Collins et al. 2004a and b, Yahoda and Wright 2004a and b, Yahoda and Wright 2005).

Several studies have shown that roller blinds, for example, can significantly reduce energy costs associated with windows. Using experimental techniques, Grasso and Buchanan (1979, 1982) reported a 60% reduction in energy costs when a light coloured opaque roller blind was used during the cooling season. A light coloured translucent roller blind yielded an annual cost reduction of 50%. During the heating season, they found that roller blinds had the potential of reducing energy cost since they reduce heat transfer through the window. For climates with net seasonal energy loss, an average of 34% reduction in energy cost was realised when conventional roller blinds were attached to a window. They also noted that the percentage reduction in the energy cost during the heating season was insensitive to the type and colour of the roller blind used, but was sensitive to the proximity of the roller blind to the window. The roller blinds tended to be more effective in reducing heat transfer when installed closer to the window. The energy saving potential of roller blinds has also been examined by means of calorimetric measurements (e.g., Ozisik and Schutrum 1959, Grasso and Buchanan 1982, Harrison and van Wonderen 1998). Such measurements are time consuming and expensive.

To provide validation data for numerical modeling of complex fenestration systems (windows with shading devices), Collins and Harrison (2004) used an outdoor solar calorimeter facility to measure the SHGC and the U-factor of a window with an indoor-side louvered blind. They obtained a limited amount of data in their investigation which took over 33 test days in late spring, summer and early fall. They further pointed out that approximately 700 test days or 20 years of testing would be required to provide sufficient experimental data for use in building energy analysis software. They therefore recommended indoor solar calorimetry which would reduce testing time although it would still require an appreciable time commitment.

In order to obtain the SHGC and the U-factor of a window with an insect screen attachment, Brunger et al. (1999) carried out measurements using an indoor solar simulator and solar calorimeter facility. Their test results showed that when the insect screen was placed on the outdoor side of a double-glazed window, SHGC was reduced by 46% while U-factor was reduced by 7%. On the other hand, SHGC was reduced by 15% while U-factor was reduced by 14% when the insect screen was placed on the indoor side of the window. In light of the aforementioned observations, there is clearly a need to model the effect of insect screens on window energy performance as Brunger et al. (1999) stated their intention to do so in future research.

VISION4 (UW 1996) and FRAMEplus (EEL 1995), recently used in Canada as standard computer programs for window performance rating and design, have proved to be successful. These computer programs can handle up to six glazing layers, coatings on any glazing,

different kinds of substitute fill gases and even diathermanous layers (layers that can transmit longwave radiation). The only drawback of these computer programs is that they cannot handle windows with shading devices.

WIS (van Dijk et al. 2002), a window analysis software package, does incorporate shading devices. In the data base (Rosenfeld 2004), WIS requires solar optical properties of shading devices from manufacturers without documenting any standard measurement or calculation procedure that could be used to obtain these optical properties. Furthermore, WIS requires flow resistance data that is not readily available. It is therefore difficult to fully assess the capability of WIS in analyzing complex fenestration systems.

Klems (1994a and 1994b) developed a new method to predict the solar gain of complex fenestration systems. The method involves measuring the bi-directional optical properties of a shading layer using a scanning radiometer to compile a detailed optical property map for the layer. The properties of the overall complex fenestration system are then built up using matrix layer calculation and the measured layer properties. Although accurate, this method is very complex and computationally intensive. In addition, there is currently no practical method by which the bi-directional property matrices can be produced en-masse for input to the matrix routine. It is therefore impractical to be used in any building load and annual energy simulation tool. Klems (1994b) further points out that the use of a bi-directional grid to characterise a non-specular layer with azimuthal dependence requires handling huge matrices with special-purpose computer programs.

Hunn et al. (1991) designed an apparatus to measure the bi-directional transmittance and reflectance distribution of fabrics. The measurements revealed the effect of textile properties (openness of weave, fibre cross section and fabric structure) on the distribution of sunlight. Such information is particularly useful in the context of daylighting simulation. Bi-directional solar optical properties can be incorporated into matrix layer calculation methods (e.g., Klems 1994a and 1994b) to predict the solar gain of glazing/shading systems. However, this experimental method and the associated glazing/shading system layer system analysis are not well suited to building energy simulation because of their complexity and because of the significant amount of CPU time required.

ASHRAE (2005) contains extensive models that could be used to estimate the SHGC of complex fenestration systems while accounting for angular and spectral variations in the incident solar radiation as well as any coating, fill gas and environmental conditions. The models in ASHRAE (2005) were developed for building load and annual energy analysis. More specifically, the SHGC is separated into the directly transmitted solar radiation and the inward-flowing fraction of the absorbed solar radiation. However, the inward-flowing fraction which includes both convective and radiative portions is treated as one quantity in the cooling load without providing the radiative/convective split necessary for the estimation of time lag to the radiant portion of the cooling load. The models also require both normal and off-normal solar optical properties of glazing/shading layers. Even though off-normal solar optical properties can easily be obtained for glazing layers, the off-normal solar optical properties are not readily available for shading layers. Furthermore, the models require calorimetric measurement of the inward-flowing fraction for the complex fenestration

system. These models are therefore unsuitable for use in building load and annual energy analysis software.

Other simplified models in ASHRAE (2005) applicable to windows with outdoor-side, indoor-side and between-the-pane shading layers use an angle-dependent SHGC of a glazing system in combination with a constant attenuation coefficient of a shading layer to estimate the solar gain of a complex fenestration system. Having obtained the solar gain, ASHRAE (2005) then assigns a hypothetical radiative/convective split to the solar gain in order to calculate the cooling load using Radiant Time Series. Obviously, the attenuation coefficient will be a weak function of the incidence angle for shading devices like insect screens and a strong function of the profile angle for shading devices like venetian blinds. In other words, angular variations in the attenuation coefficient must be accounted for when using this method in an hour-by-hour cooling load calculation. Furthermore, the radiative/convective split will be a function of the type of shading layer and its location in the complex fenestration system. Therefore, cooling loads calculated using these simplified methods can be expected to be inaccurate.

EnergyPlus (2005), a building annual energy analysis software, uses models that calculate the cooling loads of windows with indoor-side and outdoor-side shading devices. The models are not applicable to windows with more than one shading device.

As described above, the results from performance rating tools do not embody the complete set of information required for building load and annual energy analysis. More specifically, the methods used in performance rating tools are not applicable to building load and annual

energy analysis since they do not provide the radiative/convective split. Although normal incidence solar optical properties of glazing/shading layers are sufficient for performance rating calculations, off-normal solar optical properties of glazing/shading layers are required for building load and annual energy analysis.

In summary, solar optics and heat transfer analyses continue to be important topics in window research. However, more attention has been given to heat transfer analysis in recent years (e.g., Rheault and Bilgen 1989, Wright 1990, Wright et al. 1994, Wright 1996, Garnet 1999, Collins and Harrison 1999, Collins et al. 2002, Collins et al. 2004a and 2004b). Solar optics in windows with shading devices on the other hand lags behind current research. Current emphasis will therefore be placed on solar optics in windows with shading devices by extending the glazing system analysis to include shading devices. Moreover, computational procedures for solar optics in windows with shading devices are especially useful in the design stages when one wishes to compare the performance of various glazing/shading system configurations.

1.3 Purpose and Objectives

The main purpose of this research is to provide simple but accurate models and measurement techniques for estimating the solar gain through windows with shading devices. It is worth emphasizing that the methods sought in this research are intended for use in the context of building energy simulation. This type of computationally intensive, iterative simulation places a strong requirement for speed on any of its sub-models. Simplicity is also an important asset because of its inherent connection with speed and because of the desire to

offer models that can be widely and reliably implemented. The methods will also be invaluable in window performance rating.

The objectives of the proposed research are:

- To develop a generalized multi-layer solar optical model for windows with shading devices
- To develop quick and accurate methods for measuring solar optical and longwave radiative properties of flat shading materials
- To develop simplified solar optical and longwave properties models for flat shading materials using measurement data
- To develop simplified models to calculate the effective solar optical and longwave radiative properties of shading devices like venetian blinds and pleated drapes

1.4 Scope of Work

The scope of the present research is limited to the determination of normal and off-normal solar optical properties as well as longwave radiative properties of the following shading devices:

- Roller Blinds
- Insect Screens
- Pleated Drapes
- Venetian Blinds

There are significant differences between these categories and any one of these categories represents a very large variety of products. In order to retain generality and practicality while striking a balance between complexity and computational speed a simplified approach was taken regarding the way in which radiation interacts with a shading layer. Two points are worth mentioning:

- Shading layers are characterised by making the assumption that each layer, whether homogeneous or not, can be represented by an equivalent homogenous layer that is assigned spatially-averaged "effective" optical properties. This approach has been used in a number of studies (e.g., Parmelee and Aubele 1952, Parmelee et al. 1953, Farber et al. 1963, Rheault and Bilgen 1989, Pfrommer et al. 1996, Rosenfeld et al. 2000, Yahoda and Wright 2004, 2005) and has been shown to provide accurate characterization of venetian blinds (e.g., Huang et al. 2006, Wright et al. 2008, Kotey et al. 2008).

- Some portion of the incident solar radiation passes undisturbed through openings in a shading layer and the remaining portion is intercepted by the structure of the layer. The structure may consist of yarn, slats, or some other material. The portion of the intercepted radiation that is not absorbed will be scattered and will leave the layer as an apparent reflection or transmission. These scattered components are assumed to be uniformly diffuse. In addition, a shading layer will generally transmit longwave radiation, by virtue of its openness, and effective longwave properties are assigned accordingly.

Using effective optical properties and a beam/diffuse split of solar radiation at each layer, the framework used to represent multi-layer systems provides virtually unlimited freedom to consider different types of shading layers. This framework also delivers the computational speed needed in the context of building energy simulation.

A list of properties needed to completely carry out solar optical and heat transfer analyses of windows with shading devices is given in Table 1.1. It includes solar optical, longwave radiative, geometric and thermophysical properties of glazing/shading layers as well as thermophysical and geometric properties of the fill gas in between the layers. Geometric properties of glazing/shading layers can readily be measured. In addition, thermophysical properties of the fill gas are well documented. Normal incidence beam-beam solar optical properties and longwave properties of coated, uncoated and tinted glazing layers are well documented (e.g., LBNL 2008, Pettit 1979, Roos 1997, Pfrommer et al. 1995, Furler 1991). Off-normal solar optical properties of glazings can be estimated by assuming that the ratio between direct-normal and off-normal property (e.g. transmittance) is the same for the glazing in question and a reference piece of uncoated glazing with moderate tint. Details are provided in (Wright et al. 2009). In addition, several models have been devised to characterise the off-normal solar optical properties coated glass (e.g., Pfrommer et al. 1995, Roos 1997, Rubin et al. 1998, Rubin et. al. 1999).

For flat shading materials such as roller blinds, insect screens, drapery fabrics and venetian blind slats, normal incidence solar properties were measured using an integrating sphere installed in a commercially available spectrophotometer. In addition, special sample holders

were designed and fabricated to facilitate off-normal solar optical measurements of roller blinds, insect screens and drapery fabrics. For each category of flat material (roller blinds, insect screens and drapery fabrics), semi-empirical models were developed to quantify the variation of solar optical properties with respect to incidence angle. Given solar optical properties obtained at normal incidence, these models can be used to characterise the off-normal beam-beam, beam-diffuse and diffuse-diffuse properties of the material. On the other hand, the longwave properties of flat materials were measured using an infrared reflectometer. For venetian blind slats, only the emittance of the slat surface was measured. Since roller blinds, insect screens and drapery fabrics generally have some form of openness, two backing surfaces were used in order to obtain both emittance and longwave transmittance. In turn, effective layer properties of pleated drapes and venetian blinds were modeled using a more fundamental net radiation scheme with fabric models and slat properties as respective input.

Different attributes of each shading device were investigated; colour, openness factor (ratio of the open area between the fibres to the total area of the fabric) and texture of materials used for drapes and roller blinds (e.g., Grasso et al. 1997), openness factor and various types of wire material used for insect screens, the effects of pleating on drapes, and the effects of varying slat angles on the optical properties of venetian blinds.

Finally, solar transmittance and solar gain results obtained from measurements using the National Solar Test Facility (NSTF) solar simulator and solar calorimeter were compared with results obtained from simulation software that incorporated the newly developed

models. Each category of shading device attached to a conventional double glazed (CDG) window was considered in this comparison study.

1.5 Outline of Thesis

The thesis consists of eleven chapters and two appendices. The Multi-layer framework and system analysis is presented in Chapter 2 with emphasis placed on the development of the multi-layer solar optical model. The development of a novel measurement technique using special sample holders in an integrating sphere is outlined in Chapter 3. The measurement technique is subsequently used to obtain off-normal solar properties of drapery fabrics, roller blinds and insect screens and the results are presented in Chapters 4, 5 and 6, respectively. Also presented in Chapters 4, 5 and 6 is the development of semi-empirical models using the measurement results. The methods used to establish the longwave properties of drapery fabrics, roller blinds and insect screens are given in Chapter 7. The development of effective property models for pleated drapes and venetian blinds are discussed in Chapters 8 and 9, respectively. A comparison study between measured and simulated solar gain through a window with various shading devices is presented in Chapter 10. Finally, summary, conclusions and recommendations for future work are presented in Chapter 11. Appendix A gives a brief review of integration sphere theory while Appendix B outlines an uncertainty analysis pertaining to all measurements taken in this research.

Note that Chapters 1 through 10 are written as stand-alone items although the topics in these chapters are somewhat inter-related.

Table 1.1: Summary of Properties Required for Solar-Thermal Analysis of Windows with Shading Devices

Glazing/Shading Layer Properties		
Normal and Off-Normal Solar Optical Properties	Beam-beam reflectance, front side	$\rho_{f,bb}$
	Beam-beam reflectance, back side	$\rho_{b,bb}$
	Beam-beam transmittance, front side	$\tau_{f,bb}$
	Beam-beam transmittance, back side	$\tau_{b,bb}$
	Beam-diffuse reflectance, front side	$\rho_{f,bd}$
	Beam-diffuse reflectance, back side	$\rho_{b,bd}$
	Beam-diffuse transmittance, front side	$\tau_{f,bd}$
	Beam-diffuse transmittance, back side	$\tau_{b,bd}$
Diffuse Solar Optical Properties	Diffuse-diffuse reflectance, front side	$\rho_{f,dd}$
	Diffuse-diffuse reflectance, back side	$\rho_{b,dd}$
	Diffuse-diffuse transmittance	τ_{dd}
Longwave Radiative Properties	Emissivity, front side	ε_f
	Emissivity, back side	ε_b
	Transmittance	τ^{lw}
Geometric Property	Thickness	t
Thermophysical Property	Thermal conductivity	k
Fill Gas Properties		
Thermophysical Properties	Thermal Conductivity	k_{gas}
	Specific Heat Capacity	C_{pgas}
	Density	ρ_{gas}
	Viscosity	μ_{gas}
	Molecular mass	M_{gas}
Geometric Property	Spacing between shading/glazing layer	L

CHAPTER 2

MULTI-LAYER FRAMEWORK AND SYSTEM ANALYSIS

2.1 Introduction

This chapter gives an overview of the energy analysis of multi-layer systems consisting of specular glazing and nonspecular shading layers. The analysis can be divided into two major steps, namely, the solar optical and the heat transfer analyses. Particular emphasis is placed on the solar optical analysis by extending existing solar optical models for systems of specular glazing layers to include the effect of nonspecular layers that create scattered, specifically diffuse, radiation in reflection and/or transmission. Solution techniques can be formulated on the basis of matrix reduction. However, an alternate technique has been developed with the goal of computational simplicity and speed. The development of the theory related to the heat transfer analysis (Wright 2008) is beyond the scope of the current research. As such, only a brief review of the heat transfer analysis is presented in this chapter.

2.2 Structure of the Multi-Layer System Analysis

In the multi-layer analysis each glazing/shading layer system is treated as a series of parallel layers separated by gaps as shown in Figure 2.1. The index i is used to indicate location

within the system consisting of layers ranging from i = 1 at the indoor space to i = n at the outdoor space. Within the glazing/shading system itself i ranges from i = 2 to i = n-1. The gaps are also numbered. The i^{th} gap is located between layer i and layer i+1. This multi-layer structure has been used in several computer programs (e.g., Finlayson et al 1993, Wright 1995, van Dijk and Goulding 1996) and the underlying theory has been documented (e.g., Wright 1980, Hollands and Wright 1983, Rubin 1982, Hollands et al 2001).

Solar-thermal separation is used to set up a two-step analysis. First, the flux of absorbed solar radiation at each layer, S_i , caused by the incident flux, I_{sol} , is determined. Second, an energy balance is applied at each layer accounting for both convective and radiative heat transfer, and the known set of S_i values, in order to obtain the set of layer temperatures, T_i , and the corresponding set of heat flux values, q_i . This one-dimensional (1-D) centre glass analysis is customarily used and applied to the view area of the window since solar gain of the window frame can safely be ignored in almost all cases (Wright and McGowan 1999).

2.3 Solar Optical Analysis

Methods exist for modeling the interaction of incident solar radiation with a glazing system composed of any number of parallel, planar, specular glazing layers. Techniques include ray tracing, net radiation analysis, matrix reduction and iterative numerical processing. The most noteworthy method is a recursion algorithm devised by Edwards (1977). Edwards' method stands out for many reasons; it is simple, compact and easily programmed (It can even be

applied as a hand calculation.), it is computationally fast and efficient, it can be applied to any number of layers, diffuse and/or off-normal beam insolation can be handled and it does not require the use of matrices or matrix manipulations.

The presence of a shading layer entails added complexity. A portion of the solar radiation that encounters the shading layer will be scattered in some fashion. A full set of bi-directional solar optical properties is required for each layer in the system (Klems and Warner 1995), along with computationally intensive matrix manipulations (Klems 1994a, 1994b), if a high level of detail is required regarding the directional nature of the solar radiation within or leaving the system. This may be the case if daylighting is a high priority.

In the present analysis a more practical approach is taken. It is assumed that only specular and/or isotropically diffuse components of solar radiation result from the interaction of insolation with any item in a glazing/shading layer array. An expanded set of solar optical properties is assigned to each layer accordingly.

2.3.1 Solar Optical Properties

2.3.1.1 Properties of Individual Layers

Consider the interaction of solar radiation with a single layer. The quantities of interest are shown in Figure 2.2.

A portion of the beam radiation incident at a given layer will leave the layer without being scattered. The solar optical properties associated with this unscattered beam radiation are

called beam-beam properties and are given the subscript “bb”. More specifically, these properties pertain to beam radiation that is transmitted without change in direction or reflected in a direction consistent with specular reflection from the plane of the layer. The properties needed are front and back reflectances, $\rho_{f,bb}$ and $\rho_{b,bb}$, and front and back transmittances, $\tau_{f,bb}$ and $\tau_{b,bb}$. In the analysis of specular glazing layers it is recognized that $\tau_{f,bb} = \tau_{b,bb}$. However, this may not be true for shading layers. Figure 2.3 shows an example, a venetian blind and glazing combination, where it is clear that $\tau_{f,bb} \neq \tau_{b,bb}$ for the venetian blind.

The solar optical properties associated with diffuse radiation incident on the front or backside of the layer are $\rho_{f,dd}$, $\rho_{b,dd}$ and τ_{dd}. Diffuse insolation is assumed to produce only diffuse radiation in reflection or transmission at each layer and the diffuse-diffuse properties are given the subscript "dd". It can be shown that the diffuse-diffuse transmittance must be the same regardless of whether the incident radiation arrives at the front side or the back side of the layer. Therefore, no f or b subscript is attached to τ_{dd}.

Beam-beam properties and diffuse-diffuse properties can readily be assigned to specular glazing layers and used to track beam and diffuse insolation, respectively. This is routinely done using Edwards (1977) method for example. Added complexity results from the presence of a nonspecular layer because beam radiation can be converted to diffuse radiation. Four additional optical properties are needed: $\rho_{f,bd}$, $\rho_{b,bd}$, $\tau_{f,bd}$ and $\tau_{b,bd}$. The "bd"

subscript denotes the beam-diffuse conversion. Again the front and back transmittance values are not necessarily equal. The solar properties of shading layers can be estimated using procedures outlined in Chapters 3, 4, 5, 6, 8 and 9.

2.3.1.2 Properties of the Environment

In order to fully specify the problem and establish the problem domain it is useful to assign solar optical properties to the layers that represent the indoor and outdoor environment.

Regarding the outdoor side, it is assumed that none of the radiation leaving the outdoor surface returns. Thus, all reflectance values of the outdoor environment are set to zero. This is quite realistic. No such limitation applies to the reflectance of the indoor side. It is necessary to set transmittance values to zero for the layers that represent the indoor environment and the outdoor environment.

2.3.2 Model and Solution Technique

2.3.2.1 Solar Flux Components

Figure 2.4 shows two sets of solar flux quantities, B and D. The variables B_i^+ and B_i^- are assigned to the indoor-to-outdoor and outdoor-to-indoor fluxes of beam radiation, respectively, in the i^{th} gap. The superscript notation, and the numbering scheme is consistent with Edwards (1977), allowing for convenient cross-reference.

The beam fluxes are interrelated. Equations 2.1 and 2.2 can be obtained by inspection of Figure 2.4.

$$B_i^+ = \rho_{f,bb,i} B_i^- + \tau_{b,bb,i} B_{i-1}^+ \tag{2.1}$$

$$B_i^- = \rho_{b,bb,i+1} B_i^+ + \tau_{f,bb,i+1} B_{i+1}^- \tag{2.2}$$

The i (or i+1 or i-1) subscript has been added to the optical properties to indicate the appropriate glazing/shading layer. It is also worth noting that B_{n-1}^- must simply be set equal to the incident flux of beam solar radiation, I_{beam}. B_{n-1}^- is not influenced by B_n^- or B_{n-1}^+, and this is consistent with the optical properties assigned to the surface that represents the outdoor environment: $\rho_{b,bb,n} = 0$ and $\tau_{f,bb,n} = 0$.

Similarly, D_i^+ and D_i^- are fluxes of diffuse radiation. Note that the incident diffuse flux, I_{diff} and D_{n-1}^- are equal. Expressions similar to Equations 2.1 and 2.2 can be written for D_i^+ and D_i^- by noting that each diffuse flux arises from both beam and diffuse incident fluxes. These are:

$$D_i^+ = \rho_{f,dd,i} D_i^- + \tau_{dd,i} D_{i-1}^+ + \rho_{f,bd,i} B_i^- + \tau_{b,bd,i} B_{i-1}^+ \tag{2.3}$$

$$D_i^- = \rho_{b,dd,i+1} D_i^+ + \tau_{dd,i+1} D_{i+1}^- + \rho_{b,bd,i+1} B_i^+ + \tau_{f,bd,i+1} B_{i+1}^- \tag{2.4}$$

Once all of the B_i^+, B_i^-, D_i^+ and D_i^- values have been determined, it is easy to calculate S_i, the flux of solar radiation absorbed at the i^{th} layer:

$$S_i = B_i^- + B_{i-1}^+ - B_i^+ - B_{i-1}^- + D_i^- + D_{i-1}^+ - D_i^+ - D_{i-1}^- \quad (2.5)$$

The flux directly transmitted to the indoor space and absorbed is S_1 .

$$S_1 = B_1^- - B_1^+ + D_1^- - D_1^+ \quad (2.6)$$

2.3.2.2 Matrix Solution

Matrix manipulation can be used to solve for the complete set of solar flux quantities simultaneously. Equations 2.1 to 2.4 are applied at each gap from i = 1 to i = n-1. Various methods are available to solve the resulting system given by [L][x] = [R], where [L] is the square matrix shown in Figure 2.5, [x] is a column vector whose transpose is

$$[x]^t = (B_1^-, B_1^+, D_1^-, D_1^+, B_2^-, B_2^+, D_2^-, D_2^+ ..... B_{n-1}^-, B_{n-1}^+, D_{n-1}^-, D_{n-1}^+) \quad (2.7)$$

and [R] is a column vector whose transpose is

$$[R]^t = (0,0,0,0,0,0,0,0,.....0,0,0,0,I_{beam},0,I_{diff},0) \quad (2.8)$$

Each dimension of [L], [x] and [R] is $n_L = 4(n-1)$.

2.3.2.3 Sequential Solution

As an alternative, it is also possible to use a sequential process to obtain the solution for all solar flux quantities. This procedure is based on the ideas that (a) the beam flux values result only from the presence of I_{beam} and are not influenced by diffuse radiation and (b) the

diffuse quantities result from the combined influence of I_{diff} and sources of diffuse radiation arising from the interaction of beam radiation with nonspecular layers. This method offers simplicity even to the extent that it can be applied as a hand calculation.

Allowing for the possibility that beam radiation can be converted to diffuse radiation at any given layer, a third set of solar flux variables is defined. The variables C_i^+ and C_i^- describe sources of diffuse radiant flux entering gap i, caused by beam radiation incident at layers i and i+1, respectively. See Figure 2.6. These beam-diffuse source fluxes are given by:

$$C_i^+ = \rho_{f,bd,i} B_i^- + \tau_{b,bd,i} B_{i-1}^+ \tag{2.9}$$

$$C_i^- = \rho_{b,bd,i+1} B_i^+ + \tau_{f,bd,i+1} B_{i+1}^- \tag{2.10}$$

The sequential solution is undertaken in three steps. First, I_{beam} and the bb properties are used to solve for the B_i^+ and B_i^- set. Second, the known values of B_i^+ and B_i^-, and the bd properties, are used to calculate the C_i^+ and C_i^- set. Third, the C_i^+ and C_i^- set along with I_{diff} and the dd properties are used to solve for all D_i^+ and D_i^- values. This step is facilitated by recognizing that Equations 2.9 and 2.10 can be used to simplify Equations 2.3 and 2.4, giving:

$$D_i^+ = \rho_{f,dd,i} D_i^- + \tau_{dd,i} D_{i-1}^+ + C_i^+ \tag{2.11}$$

$$D_i^- = \rho_{b,dd,i+1} D_i^+ + \tau_{dd,i+1} D_{i+1}^- + C_i^- \tag{2.12}$$

Detailed description of the three steps involved in the sequential solution is given in Wright and Kotey (2006).

2.4 Heat Transfer Analysis

The heat transfer in a multi-layer glazing/shading system involves coupled convective and radiative heat transfer (e.g., Wright 2008). Consider the i^{th} layer in the multi-layer system shown in Figure 2.7. The longwave radiative properties of interest are the front emissivity, $\varepsilon_{f,i}$, the back emissivity, $\varepsilon_{b,i}$, and the longwave transmittance, τ_i^{lw}. It is evident, using Kirchoff's law, that the reflectance at the front and back surfaces of the i^{th} glazing layer are, $\rho_{f,i}^{lw} = 1 - \tau_i^{lw} - \varepsilon_{f,i}$ and $\rho_{b,i}^{lw} = 1 - \tau_i^{lw} - \varepsilon_{b,i}$, respectively. The longwave radiative properties are assigned the superscript "lw" to distinguish them from solar optical properties. Longwave properties of coated, uncoated and tinted glazing layers are well documented (e.g., LBNL 2008). The glazing layers are opaque to longwave radiation and hence $\tau^{lw} = 0$ applies to glazing layers whether coated, uncoated or tinted. It is also safe to assume that $\varepsilon_f = \varepsilon_b = 0.84$ for uncoated glazing layers. The longwave properties of shading layers can be estimated using procedures outlined in Chapters 7, 8 and 9.

The indoor and outdoor air temperatures are $T_{a,in}$ and $T_{a,out}$, respectively while the mean radiant temperatures for the participating indoor and outdoor surfaces are $T_{m,in}$ and $T_{m,out}$, respectively. Both indoor and outdoor surfaces are opaque to longwave radiation. Since the

window is small relative to the indoor and outdoor environment, it is safe to assume that the emissivity of the indoor and the outdoor surface is equal to unity.

Having obtained the set of S_i values from the solar-optical analysis, an energy balance is applied at each layer. The energy balance involves the formulation of radiative and convective exchange between the layers with the set of S_i values appearing as source terms. The resulting set of equations is solved for the set of layer temperatures, T_i and radiative and convective heat transfer rates.

Two techniques for modeling the longwave radiant components of heat transfer is described in (Wright 2008). The first technique, a net radiation formulation, is based on the radiant fluxes leaving the front and back surfaces of the each layer, $J_{f,i}$ and $J_{b,i}$, respectively. The net radiant heat flux across a gap can be expressed as the difference between the radiosities of the bounding surfaces. The second technique is a new application of an old approach, the resistance network, which makes it possible to calculate U-factor and SHGC for a system that includes one or more diathermanous layers.

The quantification of convective components of heat transfer relies largely on empirical information. Methods to obtain convective heat transfer coefficients for glazing cavities are well established (e.g., Elsherbiny et al 1982, Wright 1996, Shewen et al 1996). Also available is a method to estimate the convective heat transfer coefficients for a glazing cavity with an enclosed venetian blind (Haung et al. 2006, Wright et al. 2008).

On the other hand, the convective heat transfer coefficients in the vicinity of indoor and outdoor shading layer can be specified by the calling routine (i.e., the building simulation or performance rating program). Values may be specified to differentiate between natural and forced convection. Figure 2.8 shows the resistor network used to model convective heat transfer in the vicinity of the shading layer (Wright et al. 2009). The nodes representing air, shading layer and glass temperatures are T_{air}, T_{shade} and T_{glass}, respectively. The resistors representing convective heat transfer coefficients between shading layer and air, glass and shading layer, and glass and air are h_{s-a}, h_{g-s} and h_{g-a}, respectively. The evaluation of these resistors is beyond the scope of this thesis although details can be found in (Wright 2008). It is worth noting that the resistors representing convective heat transfer coefficients on the outdoor and indoor side exist in parallel with the corresponding resistors that apply to radiant heat transfer. Generally natural convection is likely to occur at the indoor side of the window while forced convection is likely to occur at the outdoor side. For the case of natural convection the radiant mode of heat transfer will be dominant, largely because of the probability that the emissivity of each component will be high.

Established values of convective heat transfer coefficients are available in the limiting cases where the shading layer is spaced well away from the window or where the spacing approaches zero. At the indoor side, a model has been formulated by using an exponential function to make a smooth transition between the established limits so the user can place the shading layer at any distance from the surface of the window. At the outdoor side, much simplified version of the convective heat transfer model is proposed. This is because very

little is known about the influence of spacing between an outdoor shading layer and the window. However, it is clear that the presence of convective heat transfer must be accounted for at both surfaces of the shading layer and the exposed surface of the glass. These simplified convective heat transfer models are documented in (Wright et al. 2009).

2.5 Conclusions

The framework used for the energy analysis of multi-layer glazing/shading systems consisting of specular and/or specular/diffuse glazing and shading layers is presented. This framework involves a two-step analysis, i.e., solar optical and heat transfer analysis. For the solar optical analysis, a method has been devised by which beam and diffuse components of solar radiation can be tracked as they interact with the layers in the system. The solar optical analysis results include all beam and diffuse fluxes, providing full detail concerning the quantities of reflected, transmitted and absorbed radiation – including locations of the absorbed amounts. Solution techniques can be formulated on the basis of either a matrix reduction or a sequential procedure. It is however recognized that the sequential solution technique is rather simple and may be used in the context of hour-by-hour building energy analysis. The heat transfer analysis, on the other hand, involves coupled convective and radiative heat transfer between layers and gaps in the multi-layer system with absorbed solar radiation appearing as source terms. Radiative components of heat transfer are formulated through net radiation equations while convective components of heat transfer relies largely on empirical information. The multi-layer energy analysis can be used to obtain the directly transmitted solar flux as well as the convective and radiative fluxes entering the indoor space

via heat transfer. System performance parameters such as U-factor and SHGC can also be calculated.

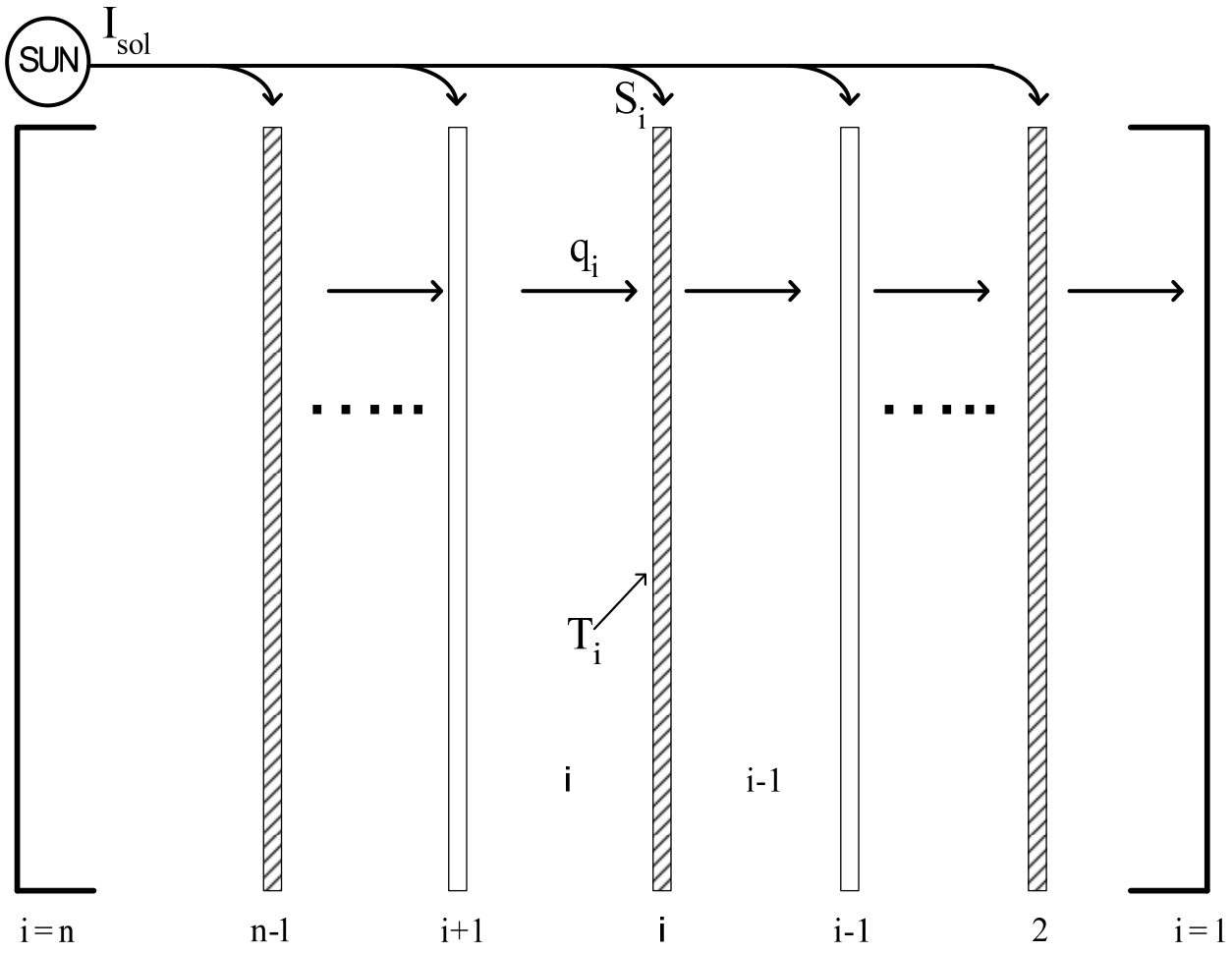

Figure 2.1: Structure of the Multi-layer System Analysis

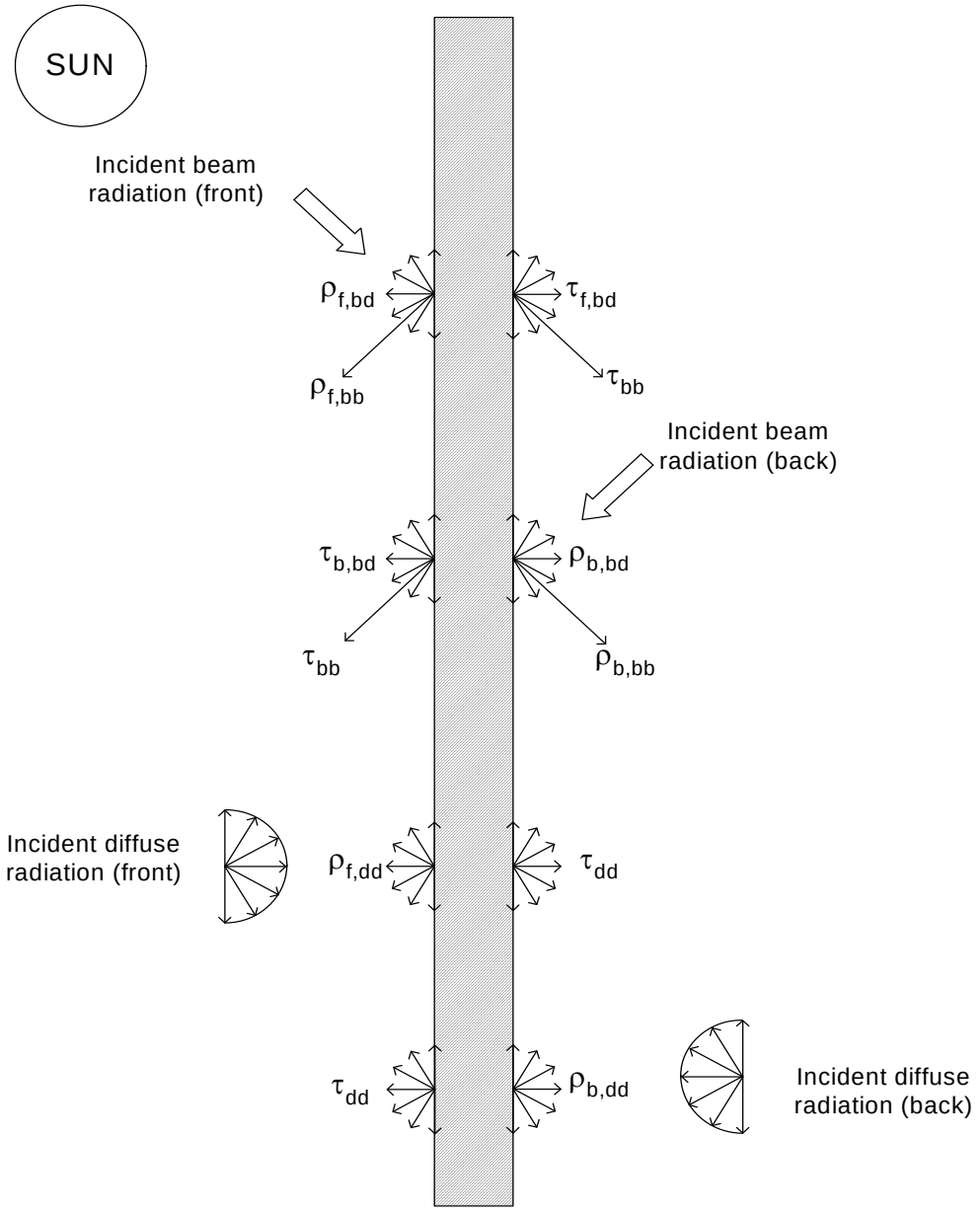

Figure 2.2: Solar Optical Properties of a Single Glazing or Shading Layer

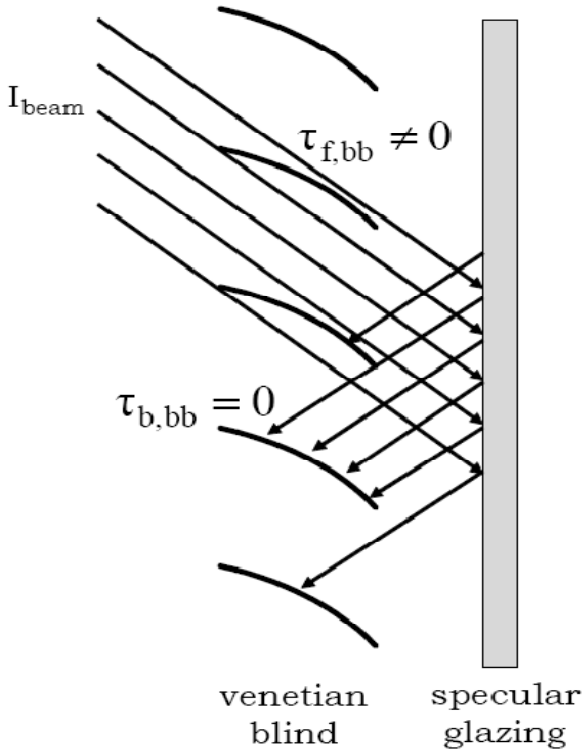

Figure 2.3: Example of a Shading Layer with Unequal Front and Back Beam-Beam Transmittance

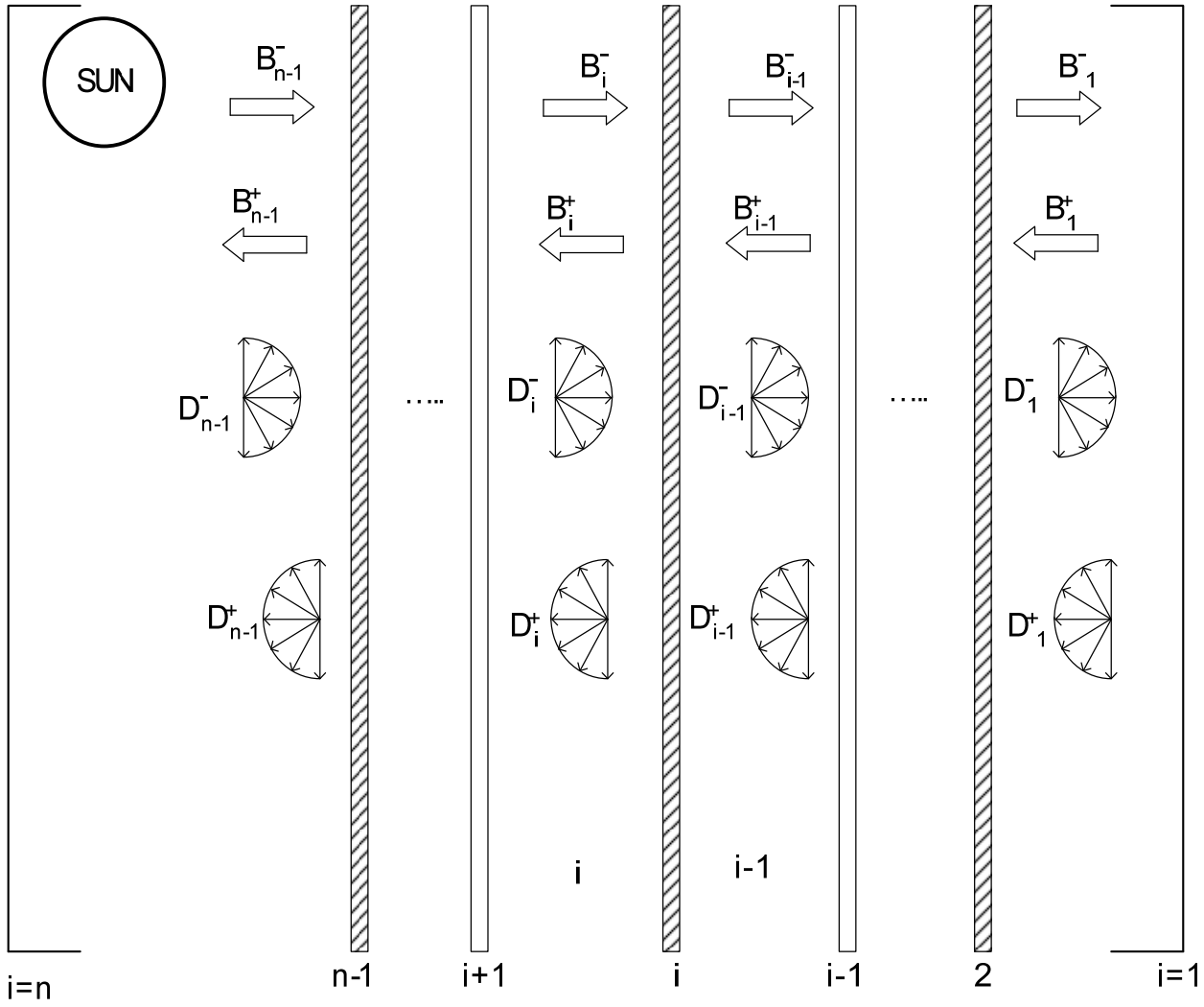

Figure 2.4: Beam and Diffuse Flux Components in a Glazing/Shading Layer Array

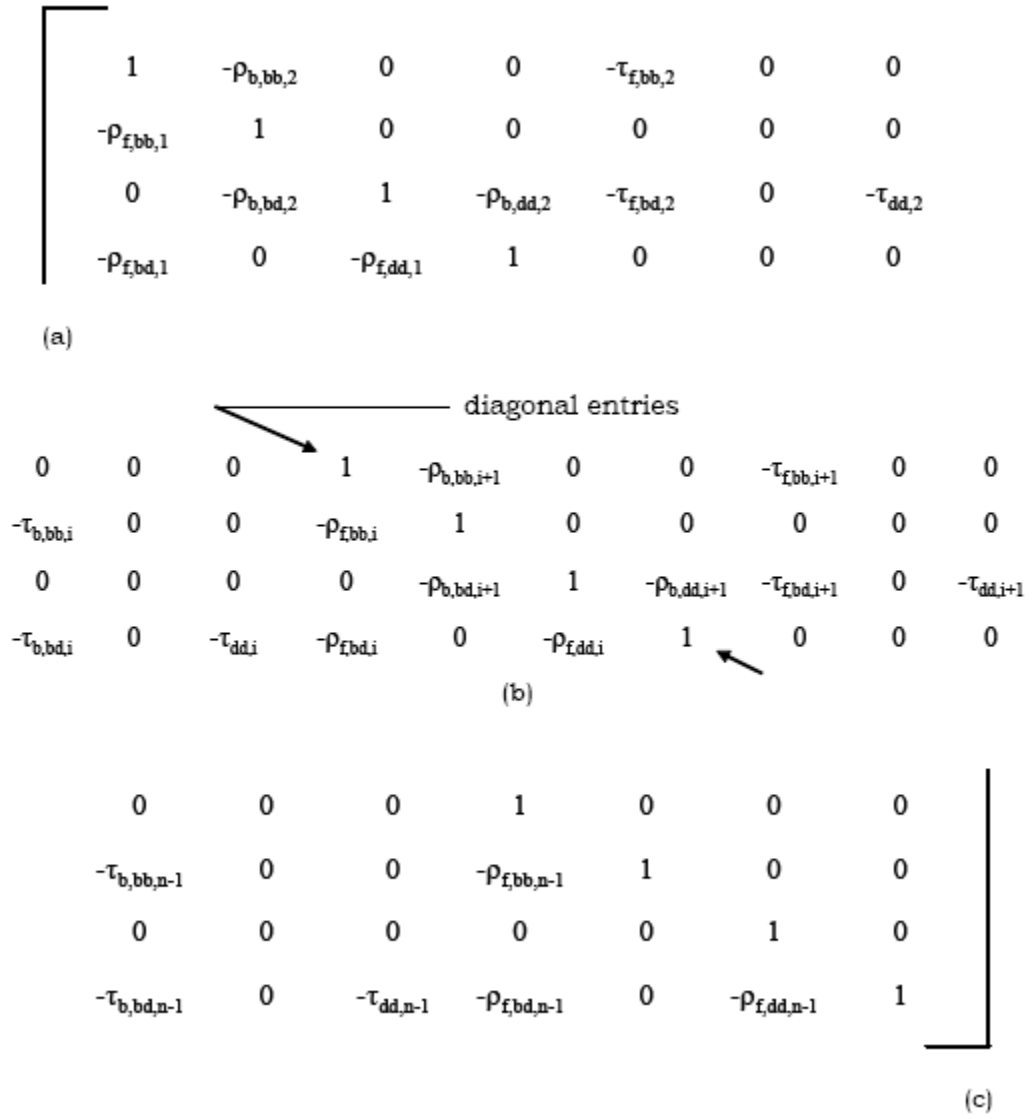

Figure 2.5: The [L] Matrix for Simultaneous Solution of all Beam and Diffuse fluxes: (a) Upper Left Corner, (b) General Expression, and (c) Lower Right Corner

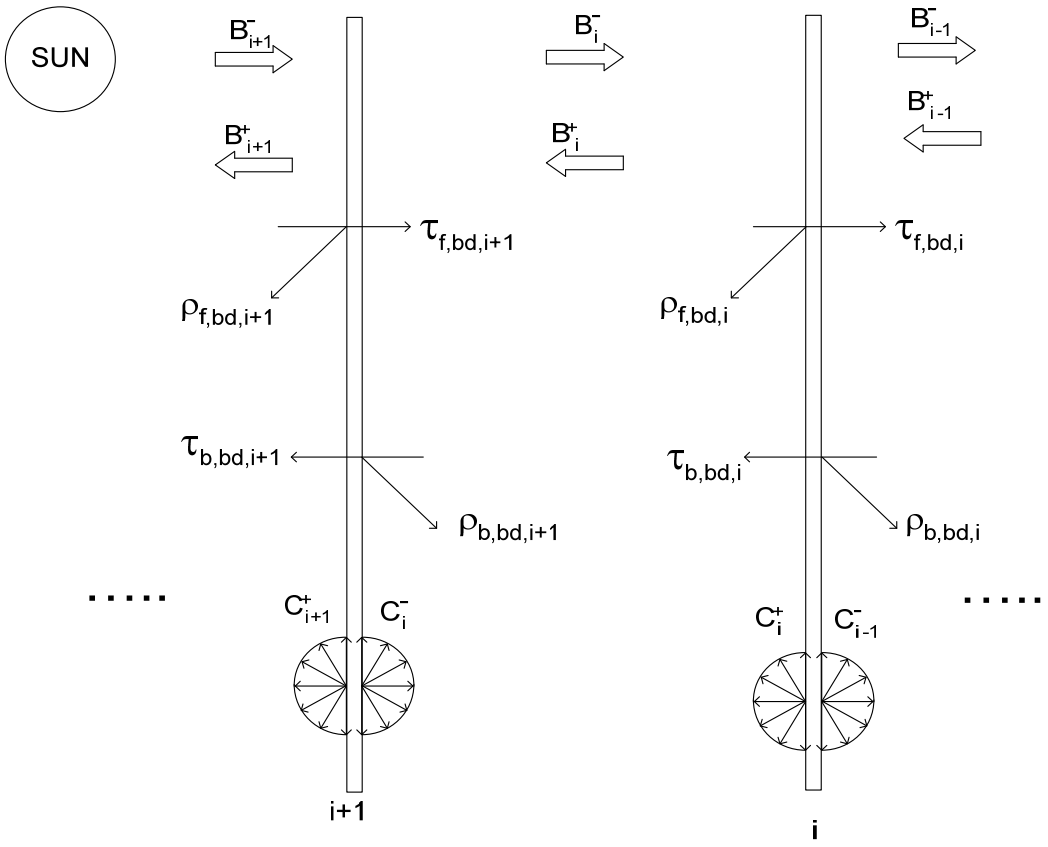

Figure 2.6: Sources of Diffuse Flux Caused by Beam Radiation

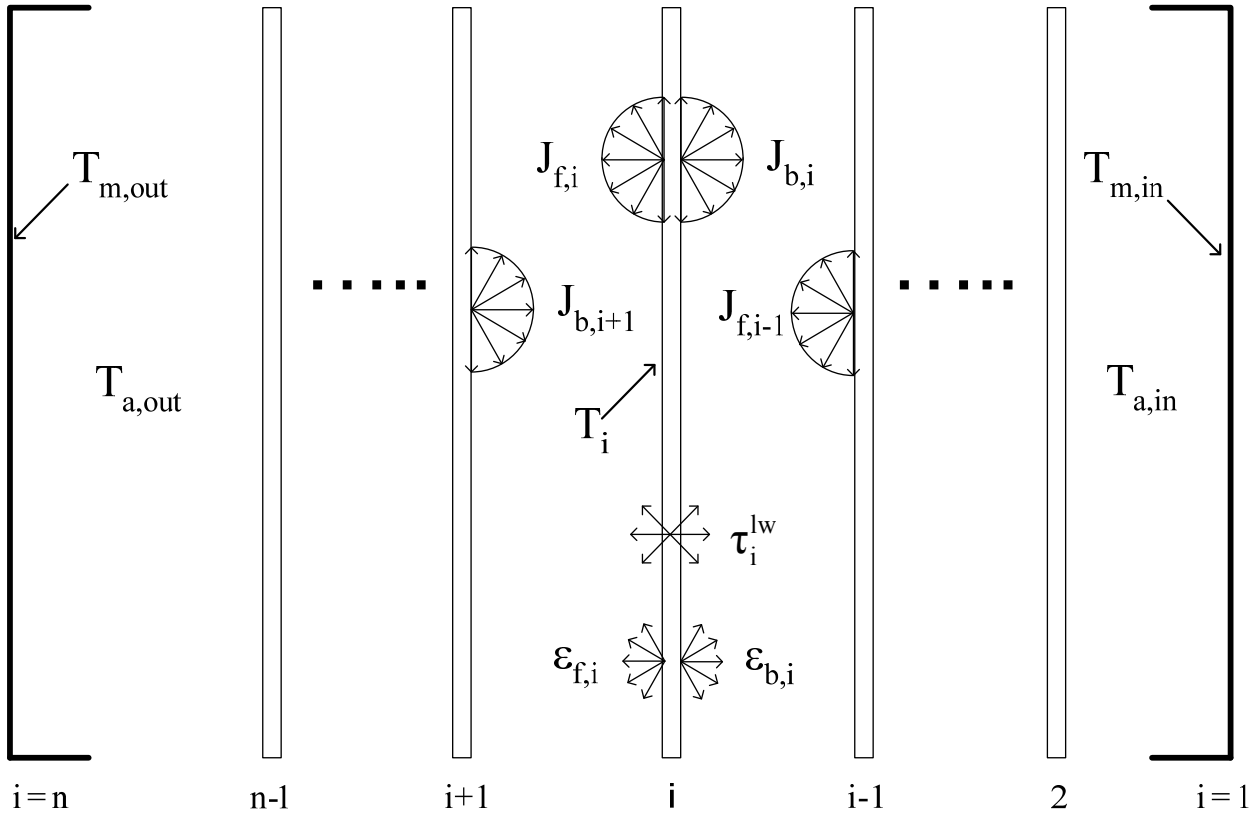

Figure 2.7: Multi-Layer Heat Transfer Model and Longwave Properties

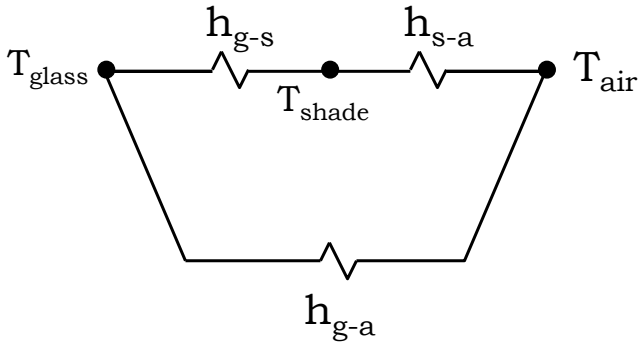

Figure 2.8: Resistor Network for Convective Heat Transfer in the Vicinity of the Shading Layer

CHAPTER 3

MEASURING SOLAR PROPERTIES OF FLAT SHADING MATERIALS

3.1 Introduction

This chapter discusses a unique measurement technique that was used to obtain off-normal solar optical properties of flat shading materials. Special sample holders were designed and fabricated to facilitate measurements using an integrating sphere installed in a commercially available spectrophotometer. The shading materials considered were drapery fabrics, roller blinds and insect screens. For drapery fabrics, measurements were taken for eight of the nine fabric designations documented in the ASHRAE Handbook – Fundamentals. Measurements were also obtained for a sheer fabric which does not fall into any of the customary fabric designations. For roller blinds, six commercially available samples that represent a broad spectrum of roller blinds were selected. For insect screens, measurements were taken on six samples with various mesh sizes and wire reflectances. The off-normal properties obtained from measurements were subsequently used to develop semi-empirical models. The development of these semi-empirical models for fabrics, roller blinds and insect screens are discussed in Chapters 4, 5 and 6, respectively.

3.2 Description of Samples

3.2.1 Fabrics

Fabrics consist of strands of yarn that are woven or knitted. The yarn itself is made up of fibres that are twisted and plied. Strands of yarn can be woven loosely, leaving open areas, or woven tightly with little or no open area. Furthermore, strands of yarn that are loosely twisted and plied could have open areas between the fibres. Keyes (1967), for example, characterised fabrics by yarn color (yarn reflectance) as dark (D), medium (M), and light (L), and by weave as open (I), semi-open (II), and closed (III). See Figure 3.1. A variety of fabrics were obtained with the primary aim of locating samples that fit into each of the nine designations described by Keyes (1967). With the exception of designation IIID which could not be located, all designations were obtained. Also included in the sample set was a sheer fabric which did not fall into any of the customary designations. The thicknesses of the fabric samples ranges from 0.1 mm to 1.0 mm and openness factor, A_o, ranges from 0.01 to 0.44. Figure 3.2 shows the samples considered; and the type, colour and openness of each fabric sample are summarized in Table 3.1.

3.2.2 Roller Blinds

The roller blind samples considered in this study have a general structure similar to the fabrics. A typical roller blind is made up of strands of yarn that can be woven loosely, leaving open areas, or woven tightly with no open areas. There are subtle differences, however, in the material composition of roller blinds and fabrics. The roller blind material,

for example, is usually made from two or more layers of vinyl, fibreglass, PVC and/or polyester. As such, it appears to be more rigid in comparison with a fabric which is typically made from softer materials such as cotton, wool, silk, etc. The differences in material composition generally translate into differences in optical characteristics. The roller blinds tested are grouped into two categories - open weave and closed weave. Six different samples with values of A_o ranging from 0 to 0.13 were selected for testing. This set represents the majority of roller blinds currently in use. Figure 3.3 shows the samples considered; and the description of each sample is summarized in Table 3.2.

3.2.3 Insect Screens

Six different samples of insect screens were considered as summarised in Table 3.3. Each screen is made from stainless steel (SS) wires that are woven to form an orthogonal mesh. The wire diameter and wire spacing are the same in both directions. The wires can be woven loosely, leaving significant open areas, or woven tightly with little openings. The thickness of each sample is equivalent to the wire diameter. See Table 3.3. The screen samples considered represent a wide range of geometry and wire reflectances. For the samples considered, the openness factor ranges from 0.36 to 0.70. Figure 3.4 is a photograph of the samples.

3.3 Preliminary Considerations

A portion of incident beam radiation will pass undisturbed through the openings of the shading material (i.e., fabric, roller blind or insect screen). The remaining portion encounters the structure of the layer and undergoes multiple reflections between the structural material

(e.g., yarn, wires or roller material) as well as possible transmission through the material. The portion of the intercepted radiation that is not absorbed by the material emerges in the forward or backward direction. The undisturbed radiation transmitted through the openings constitutes the beam-beam transmittance (specular transmittance), τ_{bb}. At normal incidence the beam-beam transmittance is equivalent to the openness factor (Keyes 1967), $A_o = \tau_{bb}(\theta = 0)$, which is defined as the ratio of the open area to the total area of the layer. The portion of intercepted/scattered radiation that emerges in the forward direction constitutes beam-diffuse transmittance, τ_{bd}, while the portion that emerges in the backward direction is the beam-diffuse reflectance, ρ_{bd}. These scattered components are assumed to be uniformly diffuse. The beam-total transmittance (directional-hemispherical transmittance), τ_{bt}, is the sum of τ_{bb} and τ_{bd}. It was assumed that the shading layers considered do not exhibit specular reflection, $\rho_{bb} \approx 0$, and this was confirmed experimentally. The beam-total reflectance (directional hemispherical reflectance), ρ_{bt}, is therefore equal to the beam-diffuse reflectance, $\rho_{bt} = \rho_{bd}$. Accordingly, incident diffuse radiation is also assumed to be transmitted and reflected diffusely by the layer. The corresponding diffuse-diffuse properties are τ_{dd} and ρ_{dd}.

3.4 Measurements

3.4.1 Overview of Measurement Technique

The techniques that might be used to measure the off-normal solar optical properties of glazings cannot be applied to flat shading materials. This is due to the fact that shading material surfaces are rough and scatter incident radiation. Nevertheless, the existing techniques can be adapted. To achieve this, special sample holders were designed and fabricated to facilitate the measurement of off-normal solar optical properties of flat shading materials using an integrating sphere installed in a commercially available spectrophotometer (Cary 5000). The integrating sphere is particularly useful because it can resolve the undisturbed and scattered components of transmitted or reflected beam radiation. The sample holders were made from polished aluminium tubes with one end truncated at a known angle, θ. The interior surface of each tube was painted black in order to absorb radiation scattered in reflection during a transmittance measurement or scattered in transmission during a reflectance measurement. A similar technique was used by Pettit (1979) to measure the off-normal transmittance of glazings. Pettit's measurements compared favourably with results obtained from first principles.

Spectral measurements of beam-beam transmittance, beam-diffuse transmittance and beam-diffuse reflectance were obtained at incidence angles, θ, ranging from 0 to 60°. The spectral data showed that flat shading materials are generally not spectrally selective except for variation in the visible region corresponding to the colour of the material. Since the aim of

the current study was to generate solar (spectral-averaged) optical properties for building energy simulation, spectral data are not presented. The solar optical properties were calculated using the 50-point selected ordinate method as described in ASTM E903-96 (1996). A second procedure was devised to repeat the beam-beam transmittance measurements, this time without the integrating sphere and at incidence angle as high as 80°. Having two sets of beam-beam transmittance data offered an opportunity to compare and gain confidence in the new procedures.

3.4.2 Spectrophotometer

The spectrophotometer used in this study is a double beam, direct ratio recording, rapid scanning instrument. It has a resolution of less than 0.05 nm for the ultraviolet and visible spectra (UV-VIS) and less than 0.2 nm for the near infrared spectrum (NIR); a repeatability characteristic of less than 0.025 nm for UV-VIS and less than 0.1 nm for NIR. In operation, two detectors, a Photomultiplier Tube (PMT) and a lead-sulphide (PbS) photoconductive sensor, are illuminated alternately by the sample and the reference beam. The PMT is used in the wavelength, λ, range of $0.17 < \lambda < 0.8$ μm and the PbS detector responds in the $0.8 < \lambda < 3.3$ μm wavelength range. There are a several accessories that can be attached to the spectrophotometer. For the purpose of the current investigation the spectrophotometer was operated, in most cases, with the integrating sphere attachment.

3.4.3 Integrating Sphere

Integrating spheres are designed to measure, and distinguish between, beam and scattered components of transmitted and reflected radiation. Light enters the sphere through a port and reflection from the interior surface must be purely diffuse. Light inside the sphere becomes uniformly distributed over the entire inner surface, eliminating directional or spatial non-uniformity of the incoming radiation, and detectors measure this integrated signal. The detector signal is proportional to the rate at which radiant energy enters at the inlet port and the ratio between the two is called the "response of the sphere". The surface of the sphere must be very highly reflective to maximize the response of the sphere and produce a signal that can be accurately detected. Theory and operating principles can be found in many references (e.g., Edwards et al. 1961, Lovell 1984). A brief review of the integrating sphere theory in given in Appendix A.

A 110 mm diameter sphere with a polytetrafluoroethylene (PTFE) coating was used in this study. The detectors are mounted at the top and are shielded by baffles so that they view only the bottom wall of the sphere. The operational range of the detectors is $0.17 < \lambda < 3.3$ μm but the spectral reflectance characteristic of the PTFE restricts useful measurements to the range of $0.25 < \lambda < 2.5$ μm. Nonetheless, this more limited wavelength range includes almost 98% of the solar spectrum. This particular apparatus was designed for making measurements with incident radiation normal to the surface of the test sample.

Transmittance can be measured by mounting a sample at the transmission port. See Figure 3.5. Reference measurements of the zero and full transmission extremes are made for

calibration. The latter, called the 100% baseline, is obtained with the sample removed while the reflection port is covered with a reference disc that completes the sphere. The 0% baseline is measured by blocking the transmission port with an opaque material while maintaining the reference disc in place. The beam-diffuse transmittance is measured with the sample in place and the reflection port open, allowing the transmitted beam component to escape while trapping the scattered radiation, as shown in Figure 3.5a. The beam-total (beam-beam plus beam-diffuse) transmittance is measured with the reflection port covered. See Figure 3.5b. The beam-beam transmittance is the difference between the two readings.

To measure reflectance radiation is allowed to enter the sphere through the open transmission port and samples are placed at the reflection port. See Figure 3.6. The full-scale baseline is obtained by covering the reflection port with a sample of known reflectance. This reference sample reflects incident radiation diffusely into the sphere. The 0% baseline is measured with the reflection port open, allowing the beam to escape. The test sample is then mounted at the reflection port and radiation reflected from the sample is collected by the sphere. The reflection port has a movable sample positioning cap. To measure the beam-diffuse component the cap is mounted as shown in Figure 3.6a, allowing the incident beam to strike the sample at $\theta = 0$ and causing the beam-beam reflection component to exit through the transmission port. When the cap is mounted as shown in Figure 3.6b, $\theta \approx 3°$, both components remain in the sphere and the detectors measure beam-total reflectance. Again, the beam-beam reflectance is simply the difference between the two readings.

3.4.4 Fixed Sample Holders

Sample holders were designed and fabricated to adapt the integrating sphere for measurement of transmittance and reflectance at off-normal incidence. The sample holders were made from aluminium tubes with one end machined at an angle, θ, with θ ranging from 0 to 60° in 15° steps. Adapters were also built to mount sample holders at the reflection or transmission port. Figure 3.7 shows a set of sample holders and the two adapters. Each sample holder is 40 mm long with internal and external diameters of 13.75 and 15.75 mm. At the transmission port, the incident beam is rectangular in cross-section with dimensions of 13.44 mm x 11.04 mm. Thus, the diagonal of the beam cross-section is 17.39 mm which is greater than the internal diameter of the holder. To ensure that the incident beam would pass through the holder without interference a beam reducer was glued to the outer face of the transmission port adapter. The beam reducer is simply a thin plate with a 12.80 mm diameter hole.

When installed, a fixed sample holder projects into the integrating sphere. Its exterior surface was highly polished to reflect radiation and avoid degrading the response of the sphere. The interior surface was painted black to absorb radiation scattered in reflection during a transmittance measurement or scattered in transmission during a reflectance measurement.

A set of reflectance references were also fabricated. They were made by filling the angled end of sample holders with barium sulphate paste. The paste was pressed against a smooth surface and left to dry. This formed a surface of known reflectance mounted with the same geometry used for flat shading material measurements. Therefore, it was assumed that the

response of the sphere was held constant between calibration and measurement. The corresponding transmission reference is simply an open tube. Again, by calibrating with an open sample holder in place, it was assumed that the response of the sphere was held constant between calibration and measurement.

3.4.5 Rotatable Sample Holder

Transmission measurements were also made without the integrating sphere. A rotatable sample holder made from a piece of aluminium plate and a graduated dial enabled beam-beam transmittance measurements over a wide range of incidence angle. The aluminium plate had an aperture where a sample could be mounted. The incident beam was simply aligned with the detector such that scattered radiation was excluded. Figure 3.8 shows a fabric sample attached to the rotatable sample holder and mounted in the spectrophotometer.

3.4.6 Transmittance Measurement

With the reflection port closed a transmittance reference, a fixed sample holder without any sample attached, was mounted at the transmission port. The 100% baseline readings were taken. The transmission port was blocked and the 0% baseline readings were taken. A sample was attached to the angled end of the sample holder and mounted at the transmission port as shown in Figure 3.9a. With the reflection port closed, spectral readings were taken to obtain $\tau_{bt}(\theta)$. The reflection port was opened and $\tau_{bd}(\theta)$ readings were taken. The 0% and 100% baseline calibration data were applied to the spectral transmittance readings using Equation 3.1 (ASTM, E903-96 1996) producing spectral transmission measurements.

$$\tau(\lambda) = \frac{S_\lambda - Z_\lambda}{F_\lambda - Z_\lambda} \tag{3.1}$$

S_λ is the unadjusted spectrophotometer reading. Z_λ and F_λ are the 0% and 100% baseline readings taken at the same wavelength.

Equation 3.1 was also applied to transmission readings made without the integrating sphere. In this configuration τ_{bb} was measured at θ equal to 15°, 30°, 45°, 60°, 70° and 80°. Baseline readings were taken for 0% and 100% transmission by blocking the beam and by leaving the beam unobstructed, respectively.

3.4.7 Reflectance Measurements with the Integrating Sphere

A reflectance reference with an end angle θ was installed at the reflection port. The transmission adapter was installed at the transmission port to reduce the size of the incident beam. The 100% baseline was recorded. The reflectance reference was replaced with an open sample holder (same θ) and the 0% baseline was recorded.

A sample was attached to the angled end of the sample holder and mounted at the reflection port as shown in Figure 3.9b. Spectral beam-diffuse reflectance readings were taken.

3.4.8 Calculation of Solar Properties

Having obtained the measurements of interest, the solar optical properties were calculated using the 50-point selected ordinate method described in ASTM E903-96 (1996). The solar

spectrum (ASTM E891-87 1987) was divided into 50 equal-energy wavelength intervals. For example, τ_{bb} was calculated as:

$$\tau_{bb} = \frac{1}{50}\sum_{i=1}^{50}\tau_{bb}(\lambda_i) \tag{3.2}$$

where λ_i is the wavelength at the centre of the i^{th} spectral interval.

3.4.9 Measurement Uncertainty

The uncertainty in the beam-total transmittance and beam-total reflectance measurements using the integrating sphere was estimated to be ±0.03 while the uncertainty in the beam-beam transmittance measurements made the integrating sphere was ±0.04. On the other hand, the uncertainty in the beam-beam transmittance measurements made without the integrating sphere was ±0.02. Detailed uncertainty estimation is given in Appendix B.

3.5 Results

The measurement results for fabrics, roller blinds and insect screens are presented in Chapters 4, 5 and 6 respectively, in addition to semi-empirical models that were formulated from the results.

3.6 Conclusions

A novel technique has been developed to measure the off-normal solar optical properties of flat shading materials by adapting an integrating sphere originally designed to measure solar optical properties at normal incidence. The technique involved the design and fabrication of

special sample holders that were attached to the integrating sphere that is used in conjunction with a spectrophotometer. Measurements were then taken at varying incidence angles for a wide variety of flat shading materials (i.e., fabrics, roller blinds and insect screens). The measurements include beam and diffuse components. It was found that flat shading materials are generally not spectrally selective except for variation in the visible region corresponding to the colour of the material. Furthermore, these materials have negligible specular reflectance. The solar properties obtained at off-normal incidence can be used to develop semi-empirical models on the basis of similar properties measured at normal incidence.

Table 3.1: Description of Fabric Samples

Type	Colour	Openness
Sheer	Cream	0.44
Open weave, light coloured (IL)	White	0.24
Semi-open weave, light coloured (IIL)	White	0.01
Closed weave, light coloured (IIIL)	White	0.01
Open weave, medium coloured (IM)	Brown	0.34
Semi-open weave, medium coloured (IIM)	Green	0.02
Closed weave, medium coloured (IIIM)	Blue	0.01
Open weave, dark coloured (ID)	Black	0.20
Semi-open weave, dark coloured (IID)	Black	0.05

Table 3.2: Description of Roller Blind Samples

Type	Colour	Openness
Open weave, vinyl coated fibreglass, 0.55 mm thick	White	0.13
Open weave vinyl coated fibreglass, 0.55 mm thick	Black	0.12
Open weave 25% polyester, 75% PVC on polyester, 0.80 mm thick	Chalk	0.08
Open weave 25% polyester, 75% PVC on polyester, 0.80 mm thick	Ebony	0.06
Closed weave, 12 oz fibreglass, duplex, room darkening, opaque, 0.33 mm thick	Black on one side, white on the other side	0.00
Closed weave, 84% polyester, 16% linen, translucent, 0.35 mm thick	Natural glacier	0.00

Table 3.3: Description of Insect Screen Samples

Type	Colour	Openness
150 mesh 0.0026 in. dia shiny	Grey	0.36
120 mesh 0.0026 in. dia shiny	Grey	0.46
20 mesh 0.016 in. dia shiny	Grey	0.49
60 mesh 0.0045 in. dia shiny	Grey	0.52
20 mesh 0.010 in. dia bluegray	Blue-grey	0.63
26 mesh 0.006 in. dia charcoal	Charcoal-black	0.70
18 mesh 0.009 in. dia charcoal	Charcoal-black	0.62
18 mesh 0.012 in. dia charcoal fiberglass	Charcoal-black	0.58

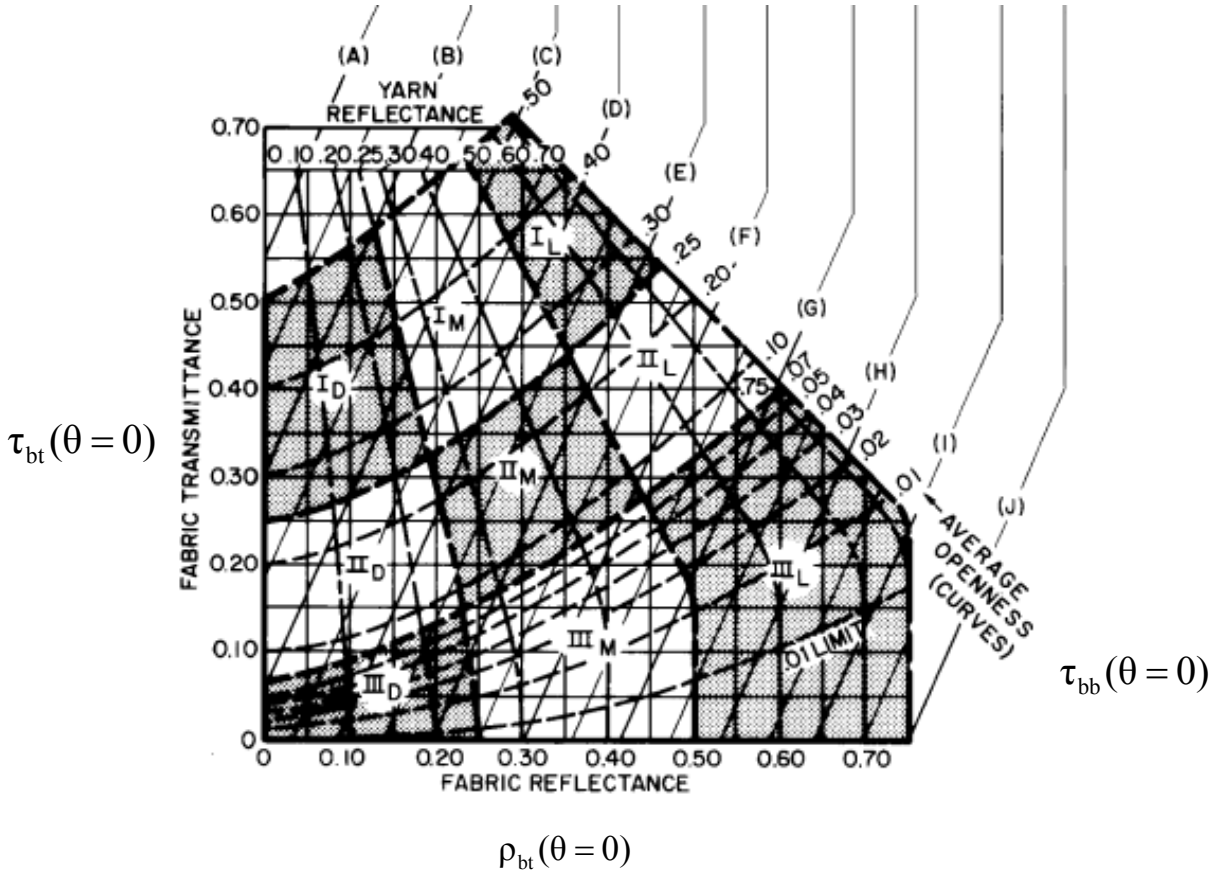

Figure 3.1: Keyes Universal Chart (Adopted from ASHRAE 2005)

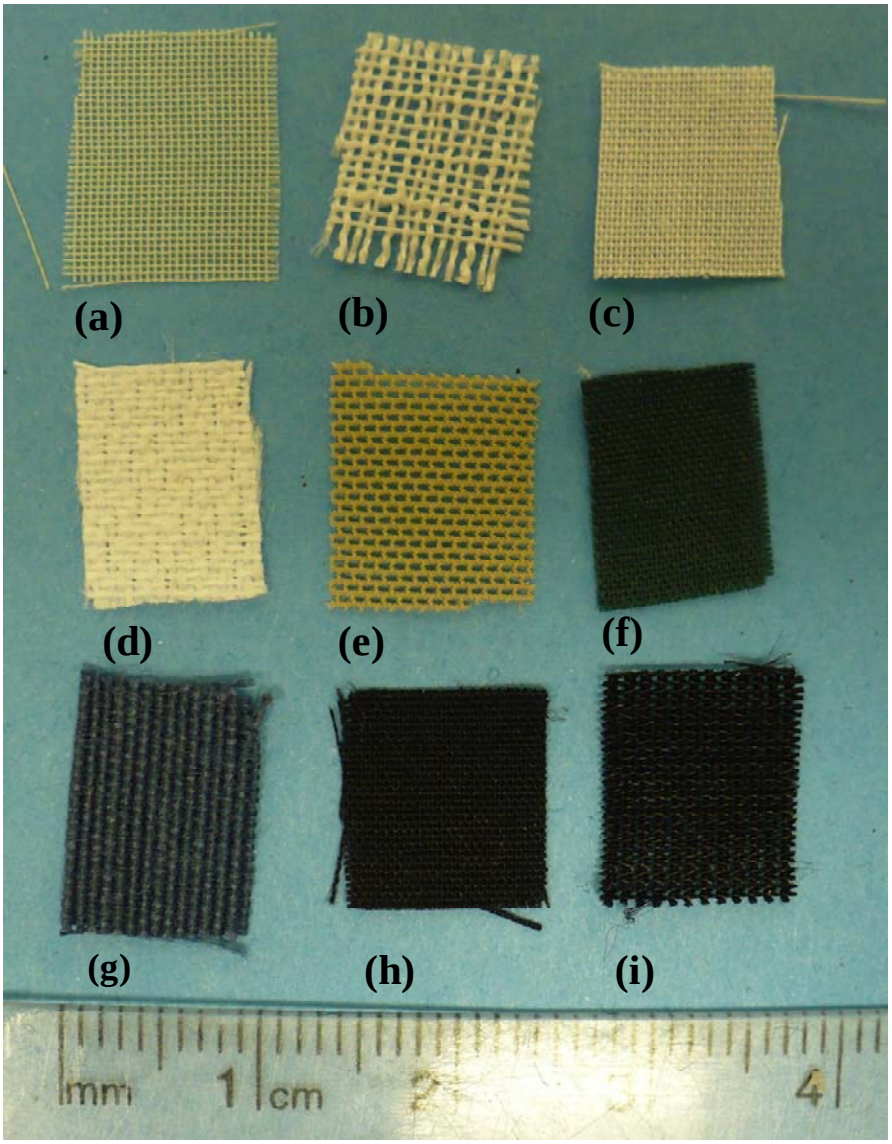

Figure 3.2: Photograph of Fabric Samples (a) Sheer (b) IL (c) IIL (d) IIIL (e) IM (f) IIM (g) IIIM (h) ID (i) IID

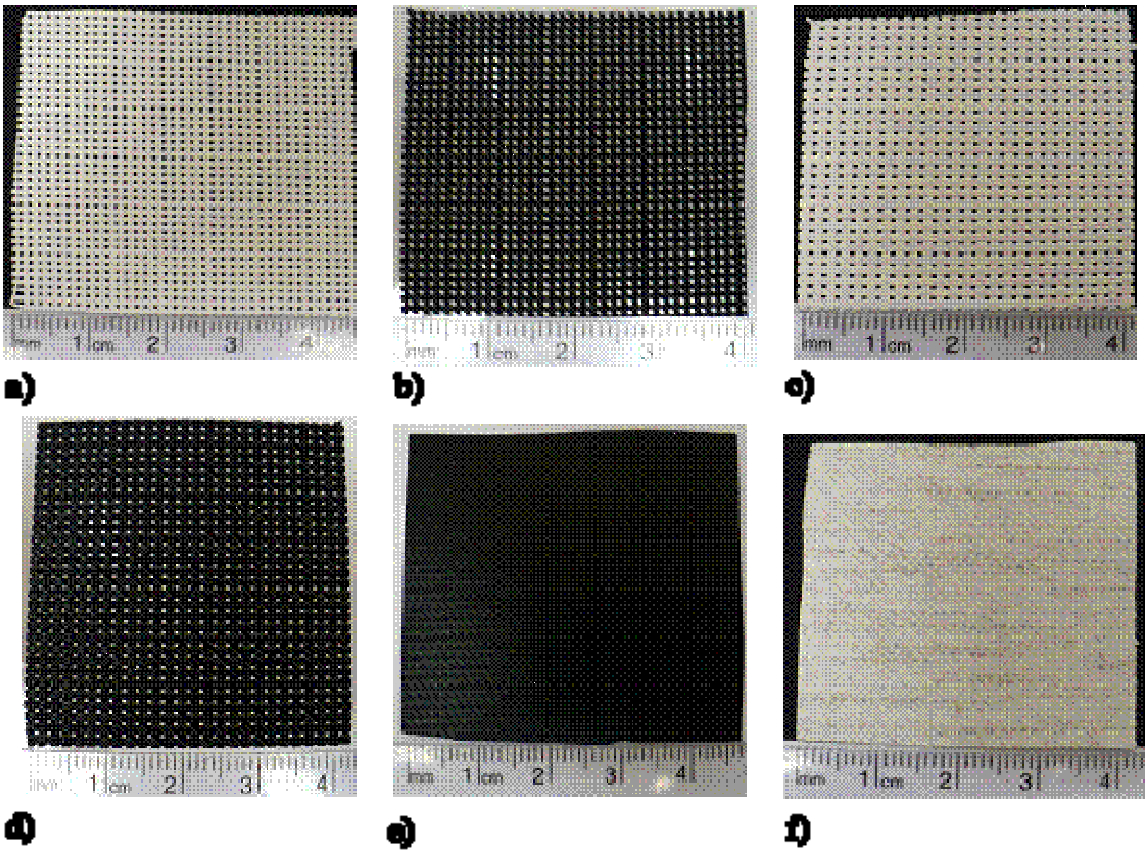

Figure 3.3: Photograph of Roller Blind Samples (a) White_14% (b) Black_14% (c) Chalk_5% (d) Ebony_5% (e) Duplex_black side (f) Glacier

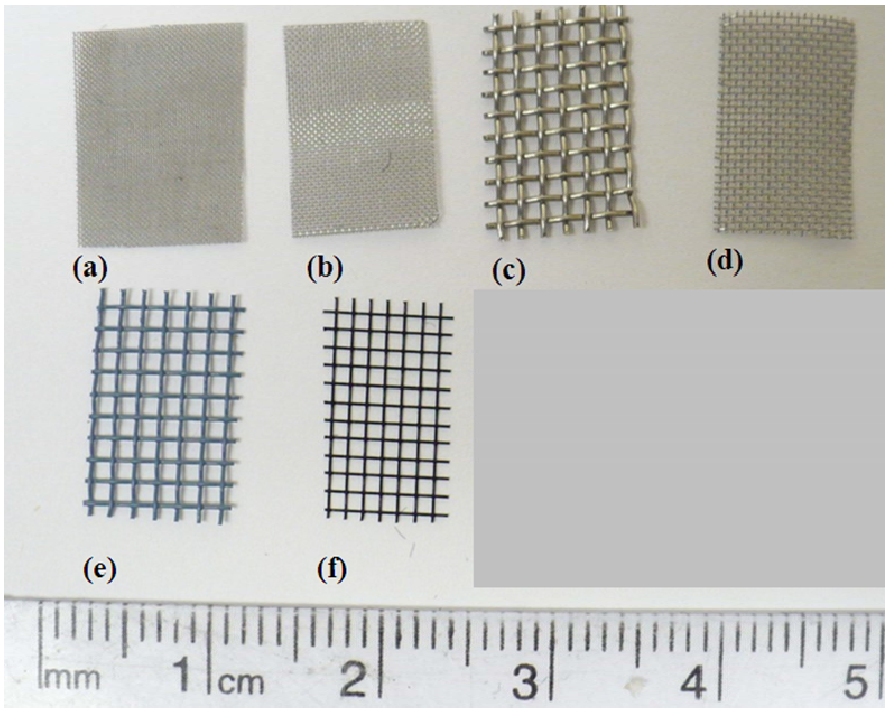

Figure 3.4: Photograph of Insect Screen Samples (a)150 mesh, grey (b) 120 mesh, grey (c) 20 mesh, grey (d) 60 mesh, grey (e) 20 mesh, blue-grey (f) 26 mesh charcoal-black

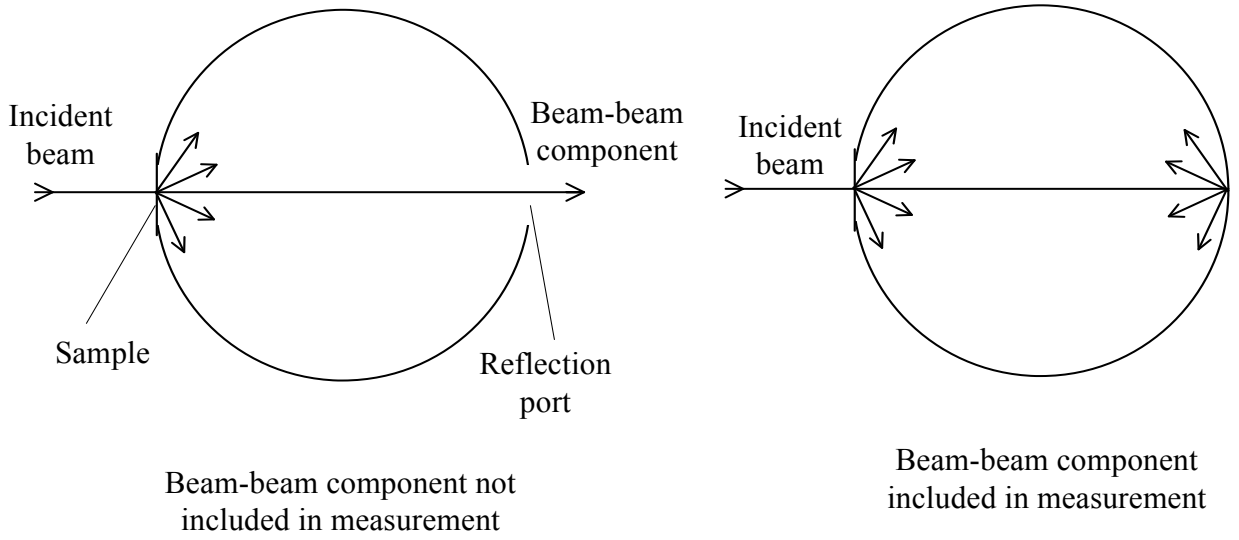

Figure 3.5: a) Beam-Diffuse Transmittance Measurement b) Beam-Total Transmittance Measurement

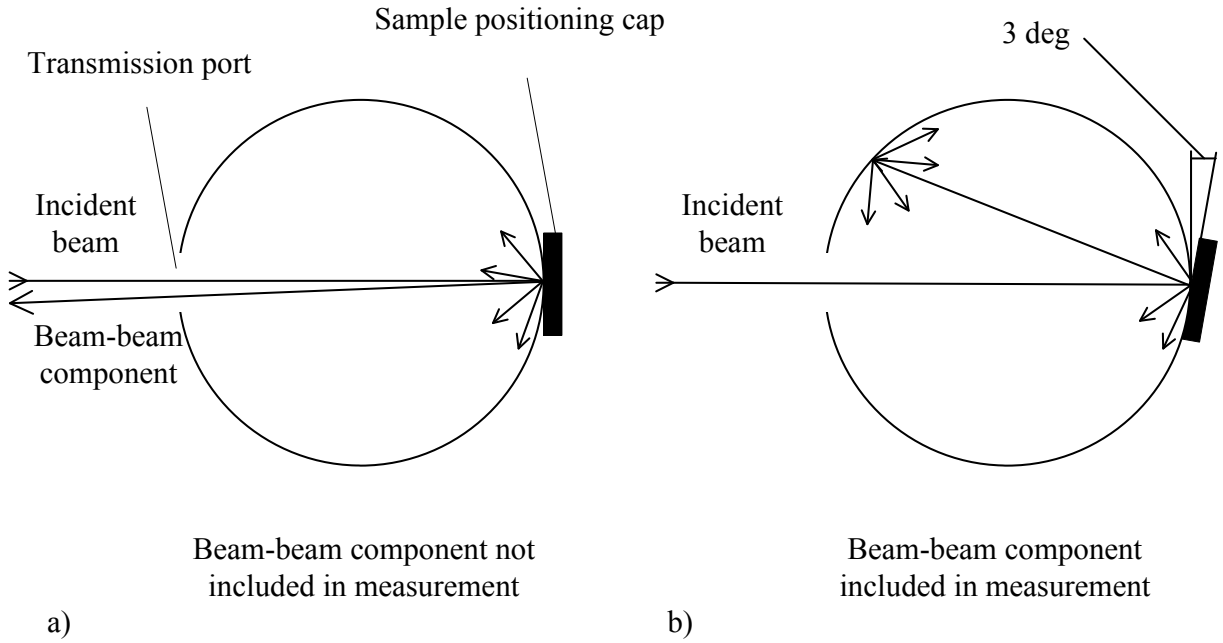

Figure 3.6: a) Beam-Diffuse Reflectance Measurement b) Beam-Total Reflectance Measurement

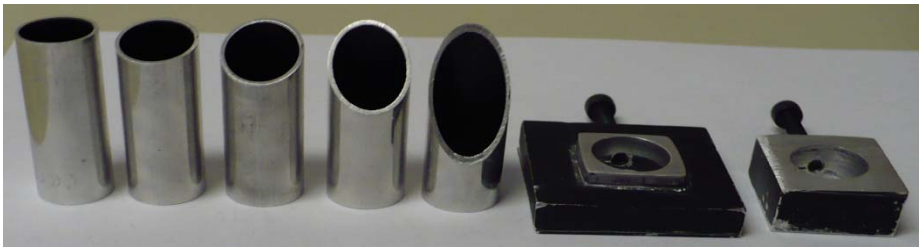

Figure 3.7: A Set of Fixed Sample Holders, Transmission and Reflection Adapters

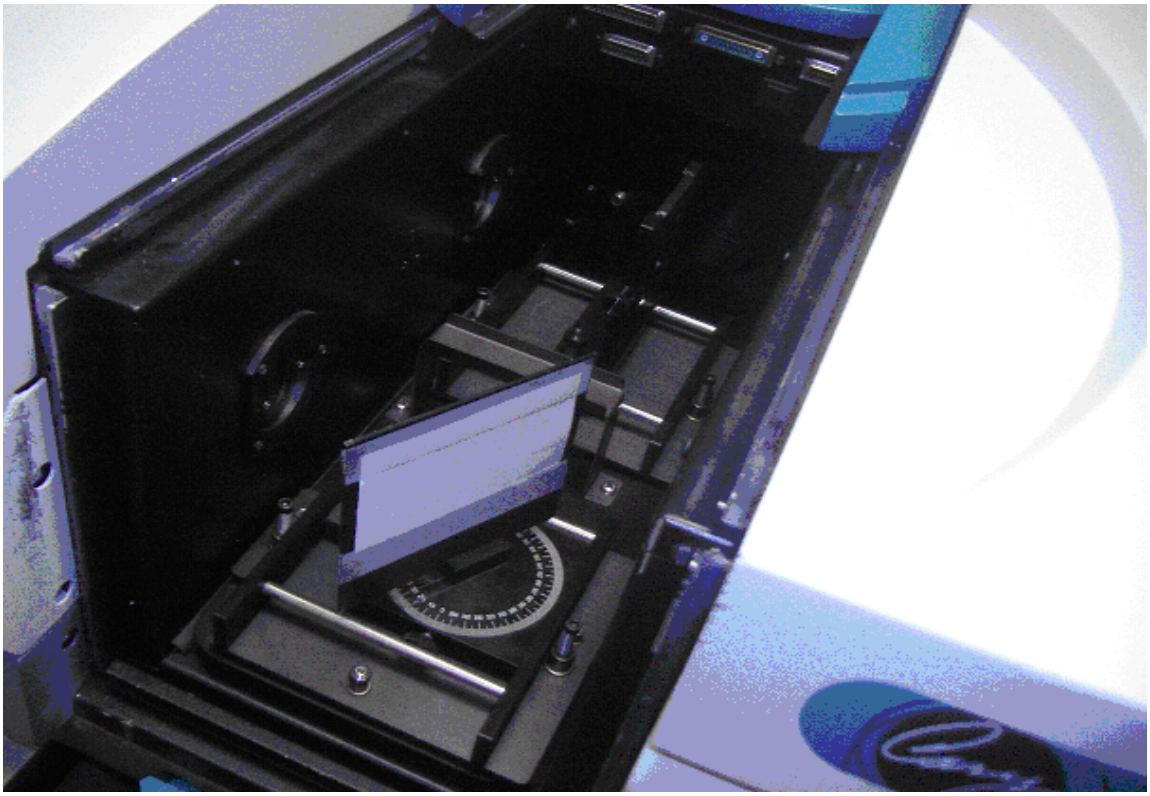

Figure 3.8: Picture of Fabric Sample attached to the Rotatable Sample Holder mounted in the Spectrophotometer

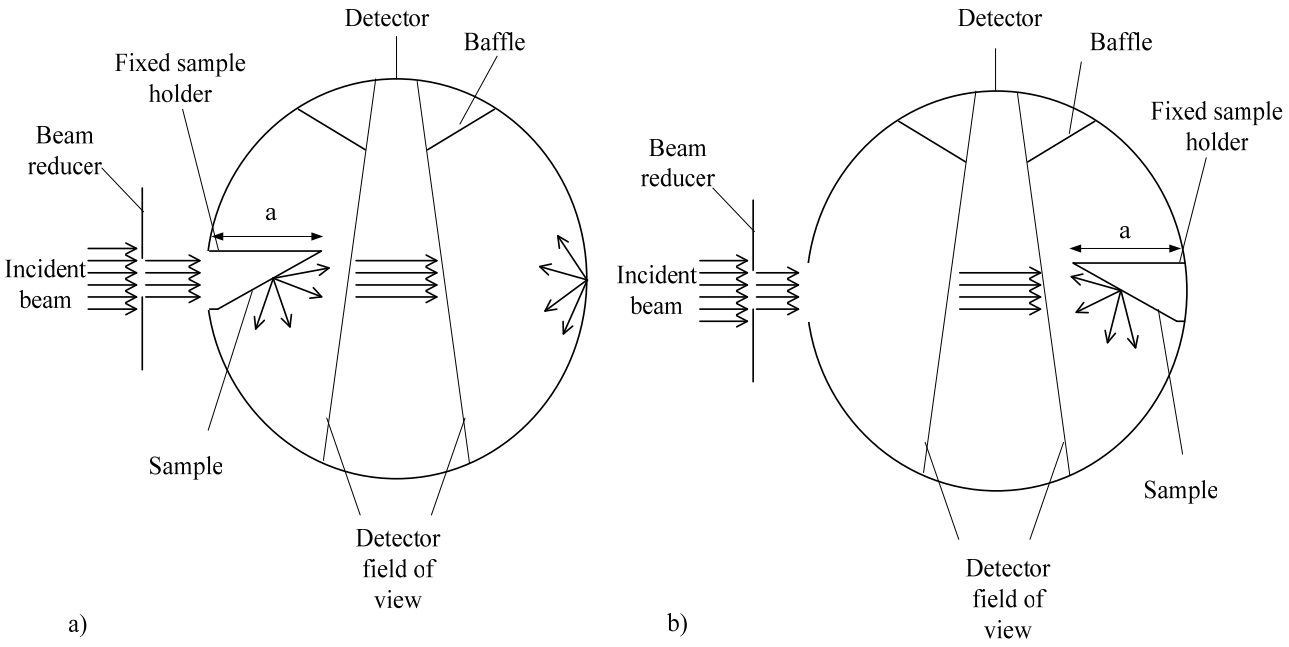

Figure 3.9: Integrating Sphere Measurements with Fixed Sample Holders
a) Transmittance Measurement b) Reflectance Measurement

CHAPTER 4

SOLAR PROPERTIES OF DRAPERY FABRICS

4.1 Introduction

The determination of off-normal solar optical properties of drapery fabrics is particularly useful in modeling the effective solar optical properties of pleated drapes. Chapter 3 outlines the measurement technique that was used to obtain the off-normal properties of flat shading materials including drapery fabrics. This chapter documents the development of semi-empirical models from the measurement data. The semi-empirical models can be used to quantify the variation of solar optical properties with respect to incidence angle ranging from 0 to 90°. Given solar optical properties obtained at normal incidence, these models can be used to characterise the off-normal beam-beam, beam-total and beam-diffuse properties of a drapery fabric. In addition, diffuse-diffuse properties can be obtained from hemispherical integration of beam-total properties. The fabric models comprise useful components of the effective solar optical model of pleated drapes presented in Chapter 8.

4.2 Approach

The direct measurement of off-normal solar optical properties of all drapery fabrics on the market is not a practical option. A realistic approach is to develop models that require a small number of readily obtained measurements as input. Such an approach was used in

determining the off-normal solar optical properties of coated and tinted glazings (e.g., Furler 1991, Roos 1997, Karlsson and Roos 2000). The models developed can be applied as long as the user knows where the fabric is located on Keyes' chart (Keyes 1967), Figure 3.1.

A simple but pragmatic way to characterise fabrics is to assume that transmittance and reflectance data share a common functional dependence with respect to incidence angle. A cosine power function was chosen to represent this dependence. This was done for several reasons, including simplicity. The cosine function is symmetrical, having zero gradient at $\theta = 0$ (normal incidence). It has maximum and minimum values at $\theta = 0$ and at $\theta = 90°$. Also, the shape of the curve can be modified by changing the value of the exponent. Each model component was tuned using a set of integrating sphere measurements and, although the formulation appears to be primarily empirical, it should be noted that an effort was made to incorporate known or expected trends and limiting cases in order to make the resulting models as general and reliable as possible.

4.3 Model Components

4.3.1 Defining Apparent Yarn Reflectance

Consider the reflection of solar radiation at normal incidence. Equation 4.1 can be used to establish the relationship between the beam-total reflectance, ρ_{bt}^{m}, the beam-beam reflectance, ρ_{bb}^{m}, and the beam-diffuse reflectance, ρ_{bd}^{m}.

$$\rho_{bt}^{m}(\theta = 0) = \rho_{bb}^{m}(\theta = 0) + \rho_{bd}^{m}(\theta = 0) \tag{4.1}$$

The superscript "m" is used to denote a property of a fabric (i.e., a material). However, $\rho_{bb}^{m}(\theta = 0) = 0$, so

$$\rho_{bt}^{m}(\theta = 0) = \rho_{bd}^{m}(\theta = 0) \tag{4.2}$$

In order to make an approximate distinction between yarns of different colours (i.e., different solar reflectivity) an apparent yarn reflectance, ρ^{y} is defined. This is done by noting that reflection arises only from the portion of the material that intercepts radiation, $(1 - A_o)$. Note that A_o is equivalent to the beam-beam transmittance of the fabric at normal incidence, $\tau_{bb}^{m}(\theta = 0)$. Thus, the following expression was used to establish a definition of ρ^{y}:

$$\rho_{bd}^{m}(\theta = 0) = \rho^{y}(1 - \tau_{bb}^{m}(\theta = 0)) = \rho^{y}(1 - A_o) \tag{4.3}$$

Combining equations,

$$\rho^{y} = \frac{\rho_{bt}^{m}(\theta = 0)}{1 - \tau_{bb}^{m}(\theta = 0)} \tag{4.4}$$

The apparent yarn reflectance was found to be useful in the development of the off-normal reflectance model.

4.3.2 Beam-Beam Transmittance Model

Values of τ_{bb}^{m} measured without the integrating sphere were plotted with respect to θ. See Figure 4.1. The maximum value of τ_{bb}^{m} is found at $\theta = 0$ and τ_{bb}^{m} decreases as θ increases, approaching zero for most fabrics near $\theta = 80°$.

Comparing the τ_{bb}^{m} measurements made with and without the integrating sphere no appreciable difference was found. The two sets of $\tau_{bb}^{m}(\theta = 0)$ can be found in Table 4.1 and a comparison, at off-normal incidence, for samples with discernable transmission values (category I, open-weave fabrics) is shown in Table 4.2. Generally, discrepancies between the two sets of measurements (diff) are within the stated uncertainty with the exception of the results obtained at $\theta = 15°$ for sample ID. As shown in Appendix B.6.5, beam-beam transmittance results from the integrating sphere were expected to be less reliable because they are obtained by taking the difference between two other measurements but no difficulty was encountered. The observed agreement strengthens the credibility of the measurements made using the fixed sample holders installed in the integrating sphere. At this stage the τ_{bb}^{m} values made without the integrating sphere were set aside and models were developed using only the data measured using fixed sample holders installed in the integrating sphere.

Beam-beam transmittance measurements were normalized according to Equation 4.5.

$$^{norm}\tau_{bb}^{m} = \frac{\tau_{bb}^{m}(\theta)}{\tau_{bb}^{m}(\theta = 0)} \tag{4.5}$$

Measured values of ${}^{norm}\tau_{bb}^{m}$ are shown as data points in Figure 4.2. It was assumed that the normalised data points could be represented by the function shown in Equation 4.6. Curves produced with various values of the exponent, b, are also shown in Figure 4.2.

$$ {}^{norm}\tau_{bb}^{m} = \frac{\tau_{bb}^{m}(\theta)}{\tau_{bb}^{m}(\theta = 0)} = \cos^{b}(\theta) \tag{4.6} $$

Using Figure 4.2 a value of the exponent b was assigned to each fabric while recognising the importance of greater accuracy at intermediate values of θ. The off-normal adjustment should and will have little influence at small values of θ. This is true by default because the cosine function is used. Considerable leeway is available at large values of θ because the incident flux falls to zero as θ approaches 90° . Also take note of the two data points plotted near the upper left corner of Figure 4.2, the open circle and square. These points can safely be omitted because they correspond to fabrics with very little beam-beam transmission. In other words, if $\tau_{bb}^{m}(\theta = 0)$ is small the value of b will have almost no influence on the value of $\tau_{bb}^{m}(\theta)$ produced by the model. Because priorities of this type cannot easily be expressed in a mathematical sense, many of the parameters evaluated in the development of these models were assessed by eye.

Examining Figure 4.2, the relationship between the exponent b and fabric properties is not immediately apparent. Recognizing that values of $\tau_{bb}^{m}(\theta)$ must be the same for the front and back surfaces of the fabric a correlation was sought based on the only input parameter that is free of front/back influence; the openness, $A_o = \tau_{bb}^{m}(\theta = 0)$. Figure 4.3 shows a plot of data

points for b, estimated using Figure 4.2, versus openness. Equation 4.7, also shown in Figure 4.3, can be used to estimate values of the exponent, b.

$$b = \mathrm{Max}\left\{-\frac{1}{2}\ln\left(\mathrm{Max}\left\{\tau_{bb}^{m}(\theta = 0), 0.01\right\}\right), 0.35\right\} \tag{4.7}$$

Rearranging Equation 4.6,

$$\tau_{bb}^{m}(\theta) = \tau_{bb}^{m}(\theta = 0) \cdot \cos^{b}(\theta) \tag{4.8}$$

where b is given by Equation 4.7 and $\tau_{bb}^{m}(\theta = 0)$ is measured or can be equated to A_o.

Ideally, Equation 4.7 would have been formulated in such a way that b approaches zero as $A_o = \tau_{bb}^{m}(\theta = 0)$ approaches unity. In this limit the fabric disappears and Equation 4.7 applies no off-normal adjustment. However, some compromise was needed in order to maintain the simplicity of the model while ensuring that the calculated absorptance of the fabric does not fall below zero for all possible input values.

The data points shown in Figure 4.4 represent the measured values of $\tau_{bb}^{m}(\theta)$ and the lines represent Equation 4.8.

4.3.3 Beam-Total Transmittance Model

Measured values of beam-total transmittance of the fabric, τ_{bt}^{m}, were plotted against θ. See Figure 4.5. These plots show a gradual decrease in τ_{bt}^{m} from its maximum value at $\theta = 0$ as

θ increases. Recognising that τ_{bb}^{m} may decrease more sharply than τ_{bt}^{m} with respect to θ it was anticipated that the diffuse transmission component, τ_{bd}^{m} , might increase with θ . Values of τ_{bd}^{m} are plotted. See Figure 4.6. In fact, the measured values of τ_{bd}^{m} show little variation with θ over the range of measurement.

Having obtained no measurements beyond $\theta = 60°$ the value of $\tau_{bd}^{m}(\theta = 90°)$ is not known. This presents difficulty in the development of a correlation. However, by examining the trends of τ_{bt}^{m}, and also by recognizing that there is some leeway for approximation at high values of θ , it was assumed that

$$\tau_{bt}^{m}(\theta = 90°) = \tau_{bd}^{m}(\theta = 90°) = 0 \tag{4.9}$$

Equation 4.10 was used to normalise τ_{bt}^{m}.

$$^{norm}\tau_{bt}^{m} = \frac{\tau_{bt}^{m}(\theta)}{\tau_{bt}^{m}(\theta = 0)} \tag{4.10}$$

The normalised data points were represented by a function of the form:

$$^{norm}\tau_{bt}^{m} = \cos^{b}(\theta) \tag{4.11}$$

Again, values of b were assessed while recognising the importance of greater accuracy at intermediate values of θ and the following expression, almost identical to Equation 4.7, was developed

$$b = \mathrm{Max}\left\{-\frac{1}{2}\ln\left(\mathrm{Max}\left\{\tau_{bt}^{m}(\theta = 0), 0.01\right\}\right), 0.35\right\} \tag{4.12}$$

Rearranging Equations 4.10 and 4.11,

$$\tau_{bt}^{m}(\theta) = \tau_{bt}^{m}(\theta = 0) \cdot \cos^{b}(\theta) \tag{4.13}$$

The curves shown in Figure 4.5 represent Equation 4.13.

4.3.4 Beam-Diffuse Transmittance Model

At any given value of θ, τ_{bd}^{m} is the difference between τ_{bt}^{m} and τ_{bb}^{m}.

$$\tau_{bd}^{m}(\theta) = \tau_{bt}^{m}(\theta) - \tau_{bb}^{m}(\theta) \tag{4.14}$$

The curves shown in Figure 4.6 represent Equation 4.14.

4.3.5 Beam-Total Reflectance Model

Measured values of ρ_{bt}^{m} are shown in Figure 4.7. As expected, ρ_{bt}^{m} increases with θ but the increase is gradual and $\rho_{bt}^{m}(\theta = 90°)$ could not be measured. Recall that $\rho_{bt}^{m} = \rho_{bd}^{m}$. Observing that $\rho_{bt}^{m}(\theta)$ does not change appreciably over the range of θ used for measurements it was assumed that:

$$\rho_{bt}^{m}(\theta = 90°) \neq 1 \tag{4.15}$$

Noting that all of the incident radiation will strike the yarn, regardless of the degree of openness, as θ approaches 90° an expression was sought to evaluate $\rho_{bt}^{m}(\theta = 90°)$ as a function of yarn reflectance, ρ^{y}. Equation 4.16 was developed by approximately extrapolating the measurements of fabric reflectance at values of θ up to 60°.

$$\rho_{bt}^{m}(\theta = 90°) = \rho_{bt}^{m}(\theta = 0) + \left(1 - \rho_{bt}^{m}(\theta = 0)\right) \cdot \left(0.7\left(\rho^{y}\right)^{0.7}\right) \tag{4.16}$$

The normalised beam-total reflectance is

$$^{norm}\rho_{bt}^{m} = \frac{\rho_{bt}^{m}(\theta) - \rho_{bt}^{m}(\theta = 0)}{\rho_{bt}^{m}(\theta = 90°) - \rho_{bt}^{m}(\theta = 0)} \tag{4.17}$$

The measured values of $^{norm}\rho_{bt}^{m}$ were found to fit a function of the form:

$$^{norm}\rho_{bt}^{m} = 1 - \cos^{b}(\theta) \tag{4.18}$$

In this case the value of the exponent b can be taken as a constant.

$$b = 0.6 \tag{4.19}$$

Finally, rearranging Equations 4.17 and 4.18,

$$\rho_{bt}^{m}(\theta) = \rho_{bt}^{m}(\theta = 0) + \left(\rho_{bt}^{m}(\theta = 90°) - \rho_{bt}^{m}(\theta = 0)\right) \cdot \left(1 - \cos^{b}(\theta)\right) \tag{4.20}$$

The curves plotted in Figure 4.7 represent Equation 4.20.

4.3.6 Diffuse-Diffuse Transmittance and Reflectance Models

The solar optical properties for incident diffuse radiation can be obtained by integrating the beam-total properties over the hemisphere (e.g., Incropera and DeWitt 2001). The diffuse-diffuse transmittance is

$$\tau_{dd}^{m} = 2\int_{0}^{\frac{\pi}{2}} \tau_{bt}^{m}(\theta)\sin(\theta)\cos(\theta)d\theta \tag{4.21}$$

Similarly, the diffuse-diffuse reflectance is:

$$\rho_{dd}^{m} = 2\int_{0}^{\frac{\pi}{2}} \rho_{bt}^{m}(\theta)\sin(\theta)\cos(\theta)d\theta \tag{4.22}$$

Equations 4.21 and 4.22 can readily be evaluated numerically.

4.4 Discussion

The white fabrics fall in the light (L) colour designation while the black fabrics fall in the dark (D) colour designation. The brown, the green and the blue fabrics all fall in the medium (M) colour designation. The cream sheer fabric with a very high τ_{bt}^{m} falls outside the range of Keyes' chart. For each colour designation, the closed weave (III) fabrics have the highest ρ_{bt}^{m} while open weave (I) fabrics have the lowest ρ_{bt}^{m}. This is expected because for a given type of yarn, closed weave fabrics have greater surface area exposed to the radiation. On the other hand, the open weave fabrics have the highest τ_{bt}^{m} followed by the semi-open weave fabrics while the close weave fabrics exhibit the lowest τ_{bt}^{m} in each colour designation.

Comparisons between integrating sphere measurements and the semi-empirical models based on these measurements are shown in Figure 4.4 to Figure 4.7. Generally, the models agree very well with the experimental data. Error bars representing the measurement uncertainty of the beam-total transmittance data are shown on IL and ID in Figure 4.5. Only the open weave fabrics (IL, IM, ID) show appreciable discrepancy. In this case τ_{bb}^{m} in particular would benefit from the use of a cutoff angle but this option was disregarded for the sake of retaining

simplicity – knowing that more leeway regarding the accuracy is available as θ approaches 90°.

Viewing Figure 4.4 through Figure 4.7, the overriding observation is that the proposed models agree very closely with almost all of the measurements. It is also worth noting that in practice the evaluation of off-normal solar properties using these models will be influenced most strongly by the corresponding solar properties measured at normal incidence. The models presented here represent adjustments that will have little influence at small values of θ because the cosine function was used for each formulation. Also the correlations will have little importance at large values of θ, the situation for which few measurements were available and more uncertainty is present, because the incident flux approaches zero. Measured data were available for the intermediate values of θ, the situation where accuracy is most important, and the correlations are expected to work well in this range.

Finally, it is worth noting that the fabric test samples used in this study did not have different front- and back-surface properties. However, the correlations have been formulated in such a way that they can be applied to fabrics that do differ front-to-back and are expected to also work well in this situation. This claim is made because the data required as input will include the front and back solar properties measured at normal incidence and these properties will most directly convey the influence of front/back differences whether these differences are appreciable or not. Remember that A_o and $\tau_{bb}^{m}(\theta)$ are functions of fabric/yarn geometry only, albeit on a very fine scale, and their front/back values must be equal.

4.5 Conclusions

A novel approach has been developed to model the off-normal solar optical properties of drapery fabrics. By taking measurements with special sample holders attached to an integrating sphere of a spectrophotometer, it was found that solar properties at off-normal incidence, including beam and diffuse components, can be predicted on the basis of similar properties measured at normal incidence. Correlations were formulated by fitting a cosine power function to the measured data. The proposed models offer significant value for computing the effective solar properties of pleated drapes.

In general, the agreement between integrating sphere measurements and the resulting correlations was remarkably good. However, some discrepancy was noted with respect to the beam-beam transmittance of open weave fabrics at high incidence angle. If greater accuracy is desired it is recommended that the models developed in the current study be re-evaluated using a larger set of fabric samples in a set of measurements that extend to a higher range of incidence angle.

Table 4.1: Summary of Measured Solar Optical Properties at Normal Incidence

		Measurement with Integrating Sphere				Measurement without the Integrating Sphere
Fabric colour	**Fabric Designation**	**Beam-Total Reflectance**	**Beam-Total Transmittance**	**Beam-Diffuse Transmittance**	**Beam-Beam Transmittance**	**Beam-Beam Transmittance**
Cream	Sheer	0.19	0.80	0.36	0.44	0.45
White (1)	IL	0.42	0.56	0.32	0.24	0.26
White (2)	IIL	0.56	0.43	0.42	0.01	0.01
White (3)	IIIL	0.68	0.30	0.29	0.01	0.01
Brown	IM	0.23	0.64	0.30	0.34	0.33
Green	IIM	0.32	0.28	0.26	0.02	0.02
Blue	IIIM	0.38	0.20	0.19	0.01	0.01
Black (1)	ID	0.15	0.32	0.12	0.20	0.23
Black (2)	IID	0.21	0.23	0.18	0.05	0.05

Table 4.2: Comparison Between Beam-Beam Transmittance Measurements with and without Integrating Sphere

	ID			IM			IL		
Incidence Angle	**Measurement with Integrating Sphere**	**Measurement without Integrating Sphere**	**Diff**	**Measurement with Integrating Sphere**	**Measurement without Integrating Sphere**	**Diff**	**Measurement with Integrating Sphere**	**Measurement without Integrating Sphere**	**Diff**
0	0.23	0.20	0.03	0.32	0.33	-0.01	0.26	0.24	0.02
15	0.23	0.19	0.04	0.32	0.33	-0.01	0.25	0.24	0.01
30	0.21	0.18	0.03	0.31	0.32	-0.01	0.23	0.23	0.00
45	0.14	0.11	0.03	0.27	0.27	0.00	0.18	0.18	0.00
60	0.02	0.01	0.01	0.18	0.19	-0.01	0.09	0.11	-0.02

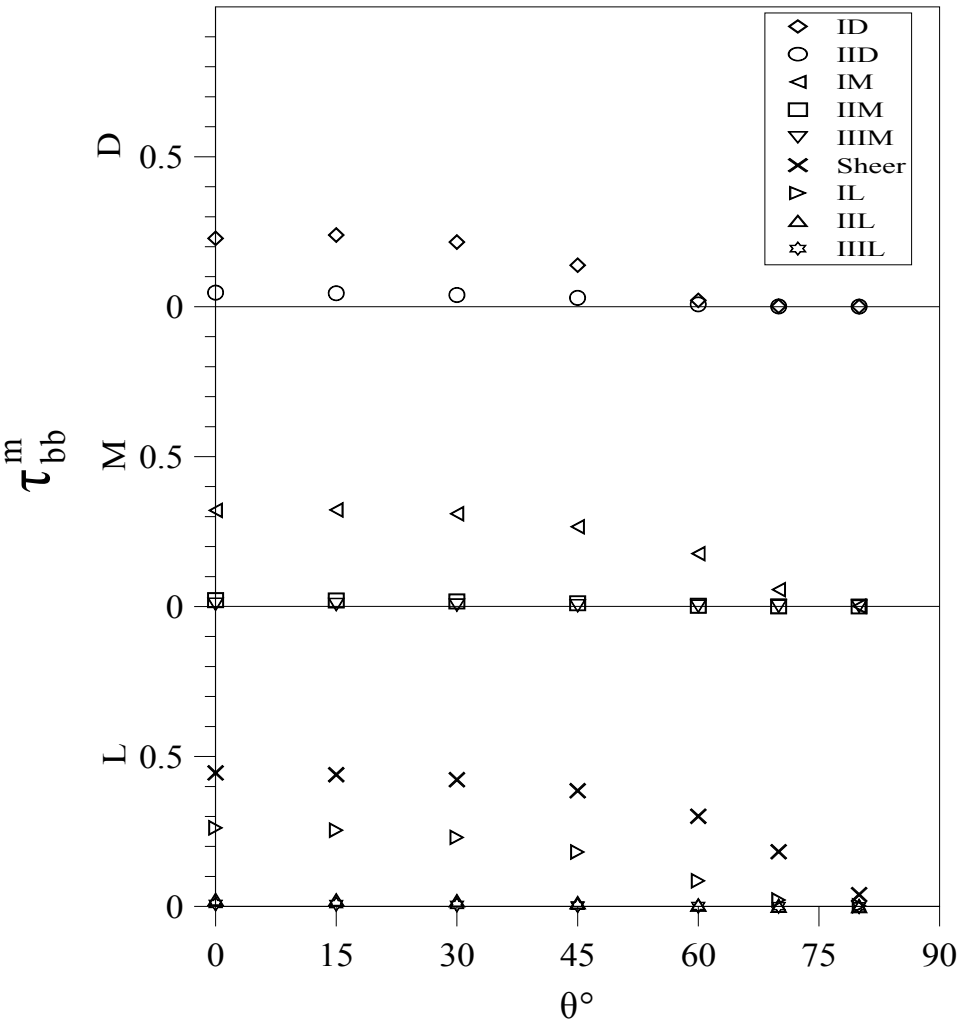

Figure 4.1: Beam-Beam Transmittance versus Incidence Angle
(From Measurements without Integrating Sphere)

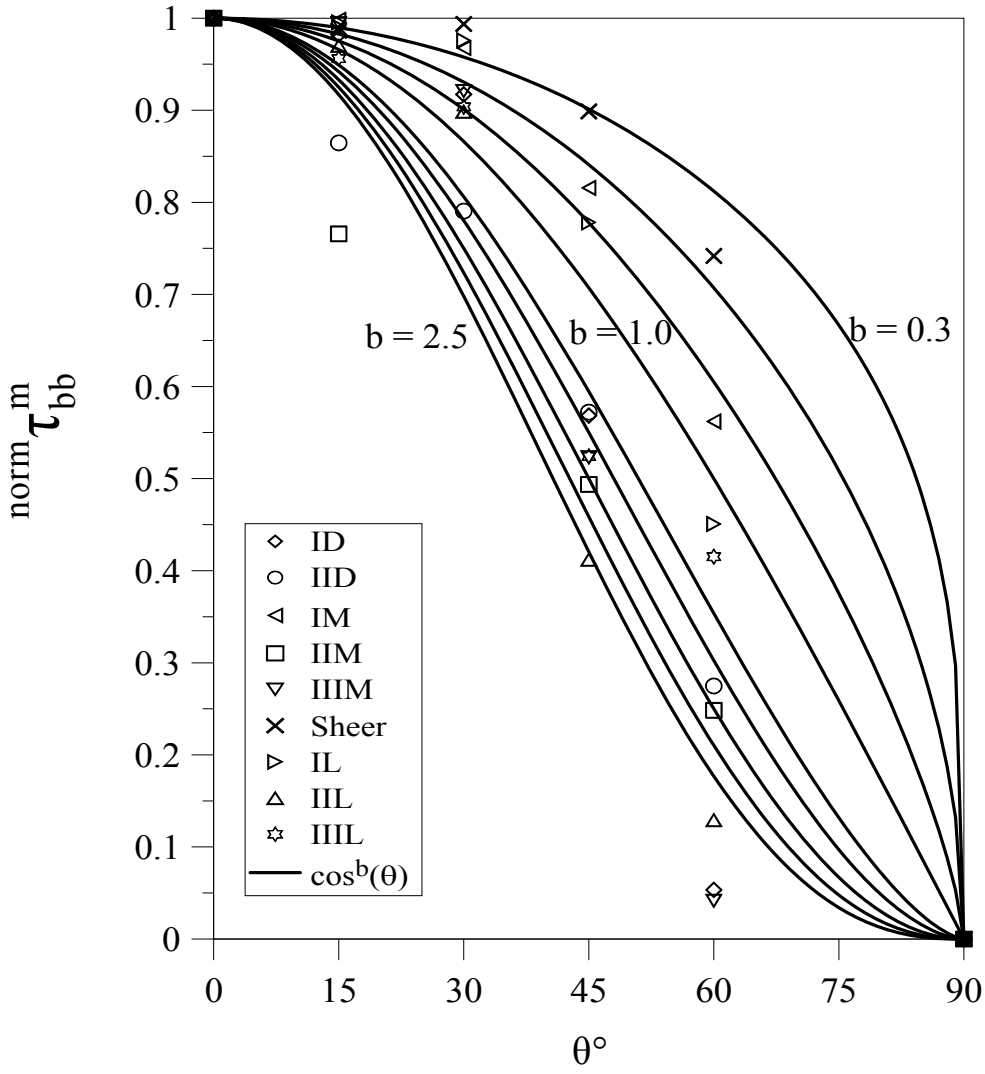

Figure 4.2: Normalised Beam-Beam Transmittance versus Incidence Angle (From Measurements with Integrating Sphere)

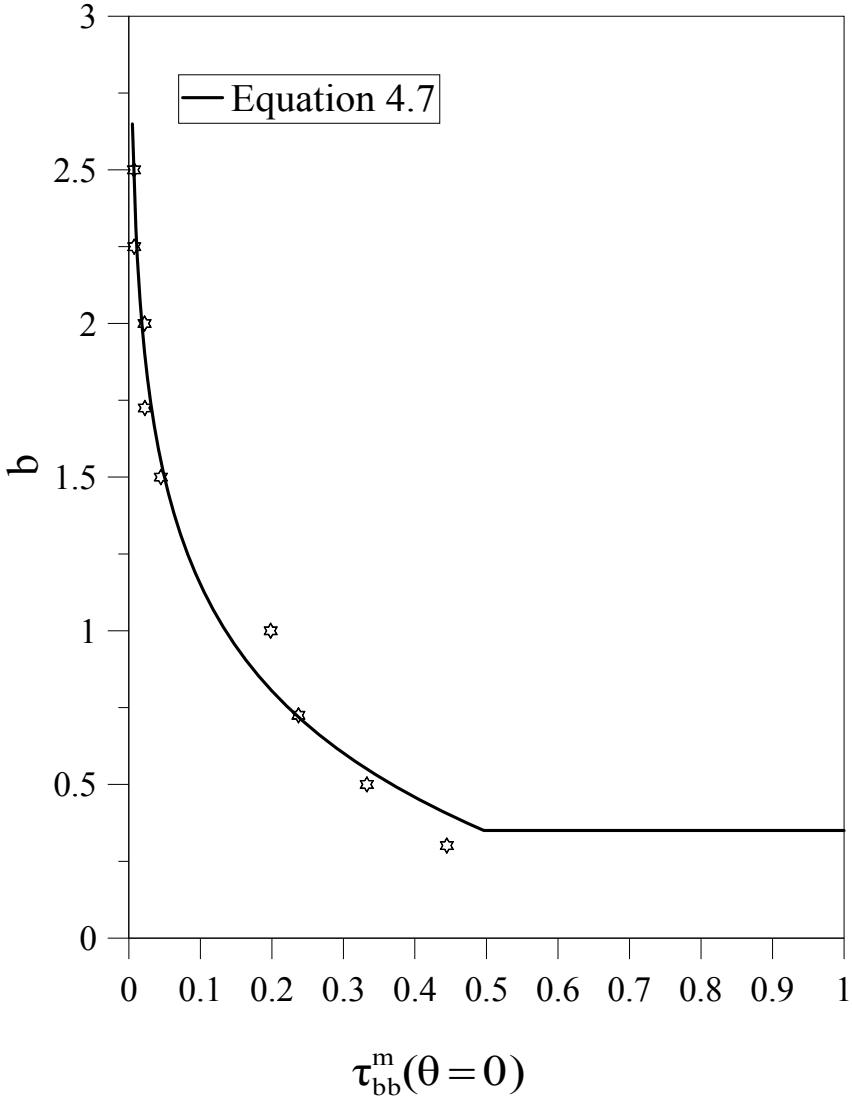

Figure 4.3: Exponent b versus $\tau_{bb}^{m}(\theta = 0)$, for Equation 4.8

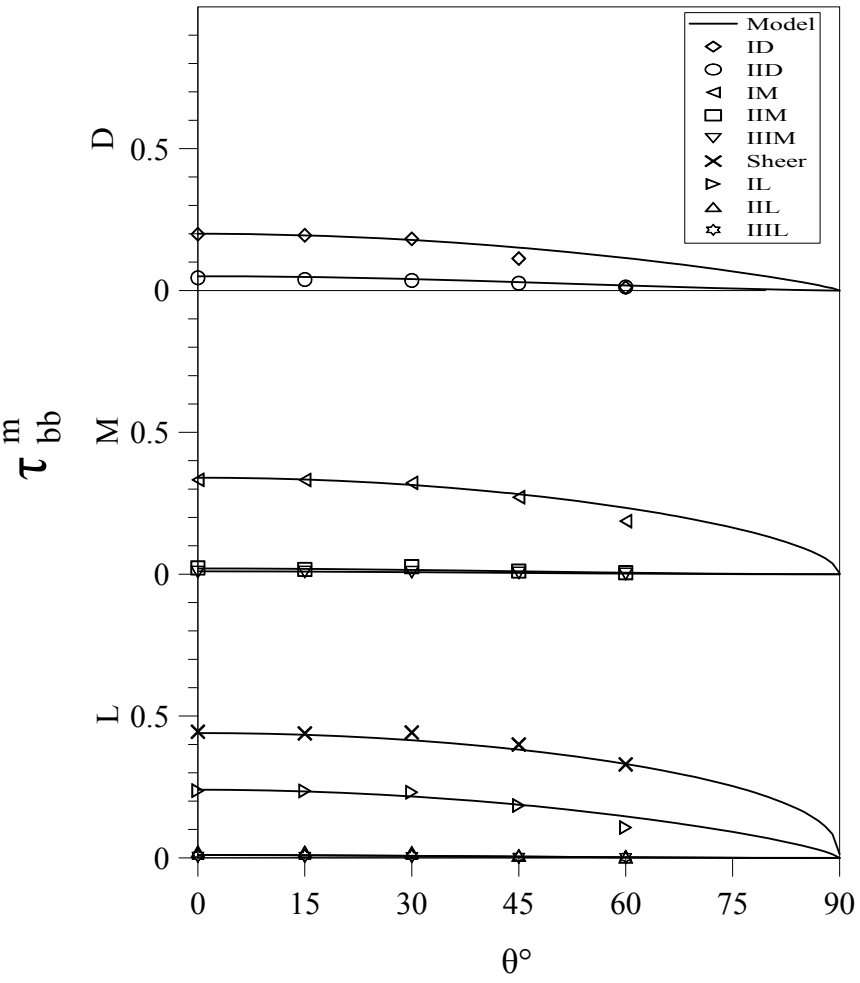

Figure 4.4: Beam-Beam Transmittance versus Incidence Angle

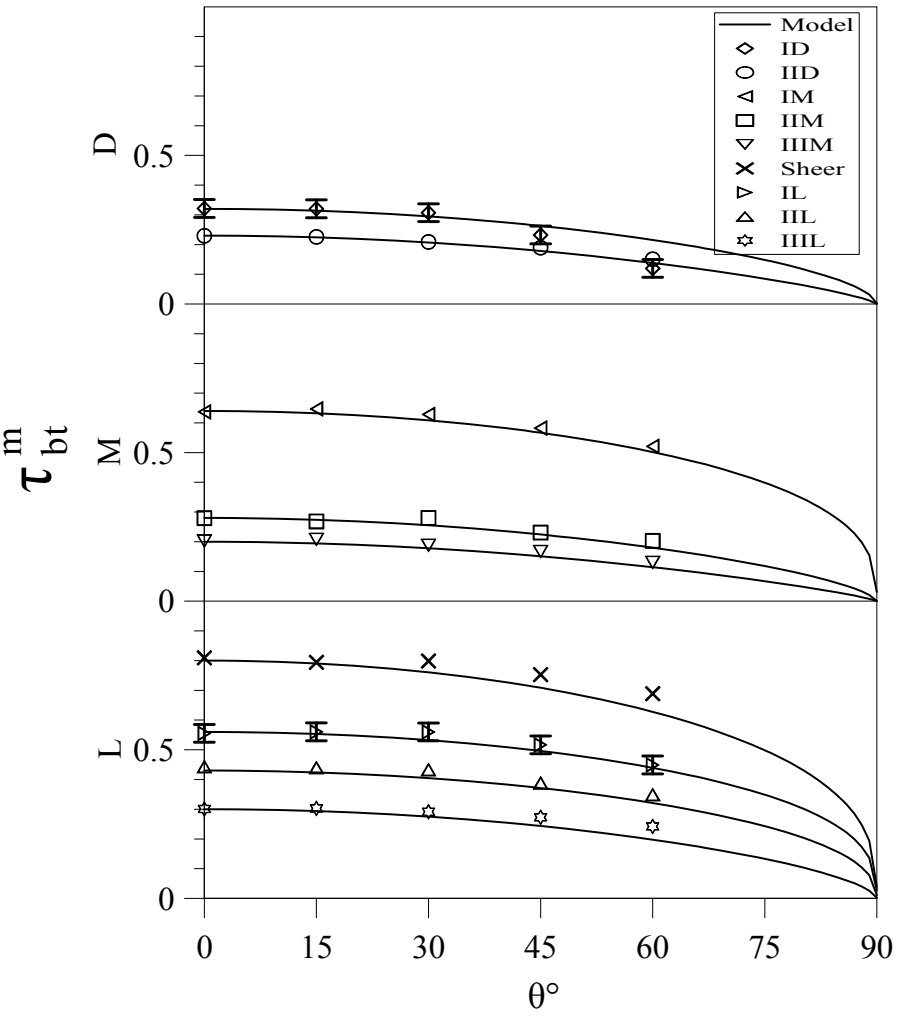

Figure 4.5: Beam-Total Transmittance versus Incidence Angle

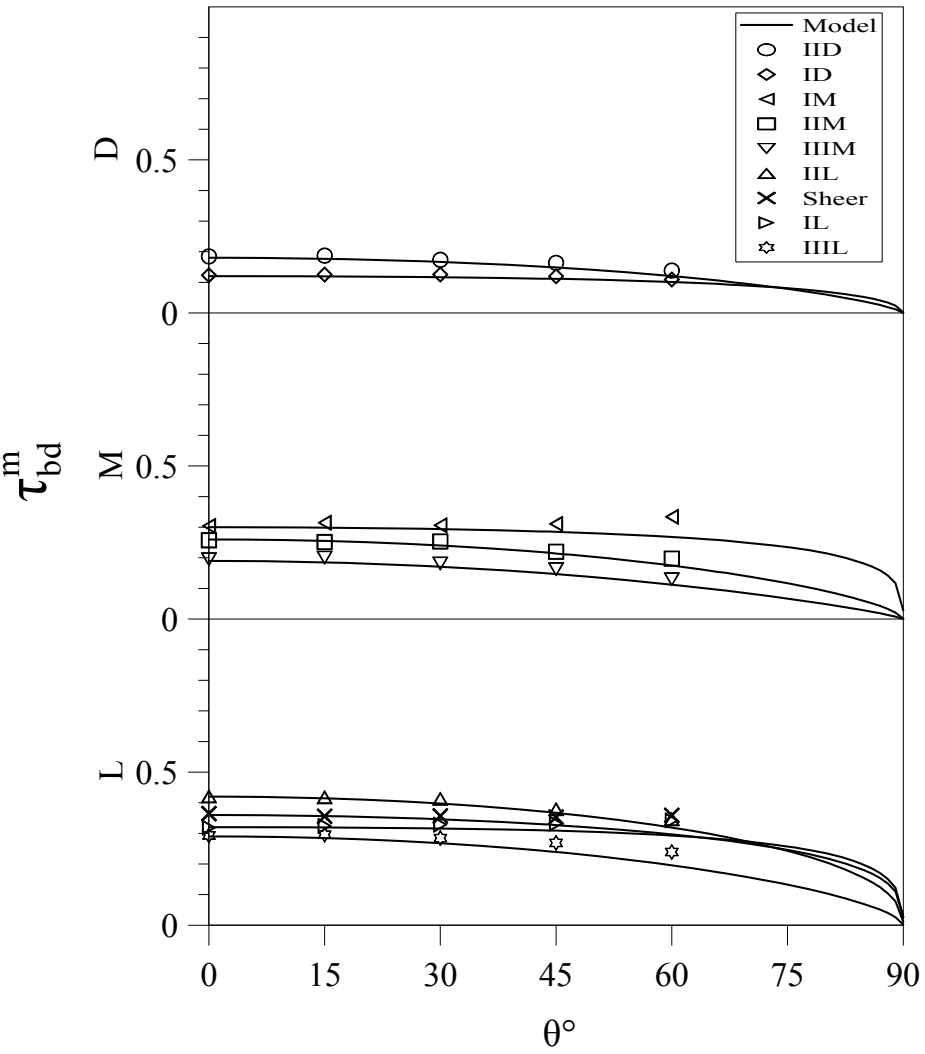

Figure 4.6: Beam-Diffuse Transmittance versus Incidence Angle

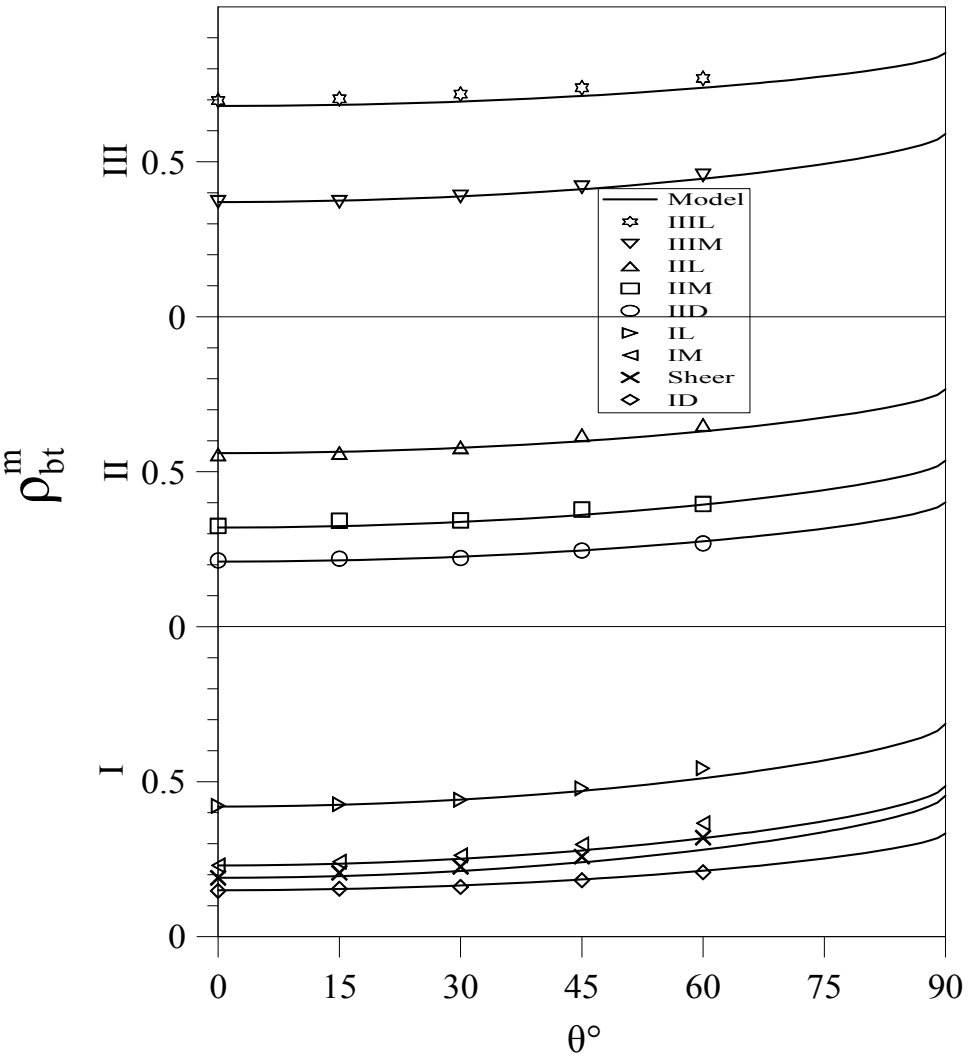

Figure 4.7: Beam-Total Reflectance versus Incidence Angle

CHAPTER 5

SOLAR PROPERTIES OF ROLLER BLINDS

5.1 Introduction

The formulation of solar optical property models for commercially available roller blinds is presented in this chapter. Off-normal solar property data for six typical roller blind samples were obtained with special sample holders attached to an integrating sphere (IS) of a spectrophotometer. The test samples and the measurement procedure are described in Chapter 3. The measurement data, in turn, were used to develop semi-empirical models for the off-normal beam-beam, beam-total and beam-diffuse properties of the roller blinds. The models provide a means to calculate off-normal properties by adjusting known values of beam-beam transmittance, beam-total transmittance and beam-total reflectance measured at normal incidence. The properties that apply to normal incidence can be readily obtained. In addition, diffuse-diffuse properties are obtained from hemispherical integration of beam-total properties.

5.2 Approach

A similar approach to fabric model development as outlined in Chapter 4 was adopted in generating off-normal properties of roller blinds. Again, a cosine power function was chosen to represent the functional dependence of only the normalised transmittance data with respect

to incidence angle, as roller blind reflectance appears to be independent of incidence angle. The cosine power function was chosen for the same reasons as presented in Chapter 4, i.e., having zero gradient at $\theta = 0$ (normal incidence), having maximum and minimum values at $\theta = 0$ and at $\theta = 90°$, respectively, and being able to modify the shape of the curve by changing the value of the exponent. Again, each transmittance model component was tuned using a set of measurement data while an effort was made to incorporate known or expected trends and limiting cases.

5.3 Model Components

5.3.1 Beam-Total Reflectance Model

From the measurement data obtained using techiques outlined in Chapter 3, a plot of ρ_{bt} versus θ revealed an insignificant variation of ρ_{bt} with respect to θ for each sample considered. See Figure 5.1. In the absence of measurements at $\theta > 60°$, and noting that the reflectance of a rough surface might realistically be independent of incidence angle, the beam-total reflectance is considered to be constant.

$$\rho_{bt}(\theta) = \rho_{bt}(\theta = 0) \tag{5.1}$$

5.3.2 Beam-Beam Transmittance Model

The measured values of τ_{bb} were normalized according to the definition shown in the left hand section of Equation 5.2. The resulting values of ${}^{norm}\tau_{bb}$ appear in Figure 5.2.

$$^{norm}\tau_{bb} = \frac{\tau_{bb}(\theta)}{\tau_{bb}(\theta = 0)} = \cos^{b}\left(\frac{\theta}{\theta_{cutoff}} \cdot \frac{\pi}{2}\right) \qquad \theta \le \theta_{cutoff} \quad (5.2)$$

It was observed that τ_{bb} diminished to zero at $\theta \approx 65°$ in each case. Measurements carried out by Look (1986) on three different awning fabrics with A_o = 6% also revealed that τ_{bb} fell to zero at $\theta \approx 65°$. Two parameters, θ_{cutoff} and b, as shown in Equation 5.2, were used to characterise off-normal beam-beam transmission through all roller blind materials. As seen in Figure 5.2, by choosing b = 0.6 and $\theta_{cutoff} \approx 65°$, Equation 5.2 closely represents the measurements. However, it should also be recognized that as A_o approaches unity, the structure of the roller blind disappears, the requirements that $b \to 0$ and $\theta_{cutoff} \to 90^{\circ}$ must be satisfied to obtain 100% transmission and to remove any influence of incidence angle in this limit. Noting also that b and θ_{cutoff} do not vary appreciably in the range over which measurements were performed, $0 \le A_o \le 0.14$, Equations 5.3 and 5.4 are proposed.

$$b = 0.6 \cos^{0.3}\left(A_o \frac{\pi}{2}\right) \quad (5.3)$$

$$\theta_{cutoff} = 65° + (90° - 65°) \cdot \left(1 - \cos\left(A_o \frac{\pi}{2}\right)\right) \quad (5.4)$$

Several points can be made regarding Equations 5.3 and 5.4.

- In choosing a value for the exponent, b, little emphasis was placed on the data for the ebony sample because b will have virtually no influence on the calculation of $\tau_{bb}(\theta)$ for roller blind materials with such low solar transmission ($\tau_{bb}(\theta = 0) = 0.06$).

- The exponent used in Equation 5.3 was chosen to ensure that τ_{bd} remains greater than zero for all values of A_o and θ (i.e., $\tau_{bt}(\theta) \geq \tau_{bb}(\theta)$ must always be true). This condition would be violated for materials where $\tau_{bb}(\theta = 0)$ approaches $\tau_{bt}(\theta = 0)$ if a larger exponent were used.

- The exponent used in Equation 5.4 (i.e., unity) is based on insect screen measurements where values of $\tau_{bb}(\theta)$ were available at much higher values of A_o.

5.3.3 Beam-Total Transmittance Model

Figure 5.3 shows the beam-total transmittance measurements, normalized according to the left-hand portion of Equation 5.5.

$$^{norm}\tau_{bt} = \frac{\tau_{bt}(\theta)}{\tau_{bt}(\theta = 0)} = \cos^{b}(\theta) \tag{5.5}$$

Examining Figure 5.3 it appears that a cutoff angle is needed near $\theta = 65°$, but only for the dark coloured samples. However, a cutoff angle was not used. This decision was made for two reasons. First, some diffuse transmission might be expected, however small, as $\theta \to 90°$ for most roller blind material. Second, dark samples create very little scattered

reflection or transmission. Therefore, there is some freedom to place more emphasis on the data for light coloured samples.

The beam-total transmittance will be influenced not only by A_o (This influence is clearly seen in the model for $\tau_{bb}(\theta)$) but also by the way in which the structure of the material transmits solar radiation. Thus, noting that the portion of incident radiation intercepted by the structure is $1 - A_o = 1 - \tau_{bb}(\theta = 0)$ and also noting that the structure only produces diffuse transmission, the apparent transmittance of the roller blind structure, τ^{str}, is defined.

$$\tau^{str} = \frac{\tau_{bd}(\theta = 0)}{A_o} = \frac{\tau_{bt}(\theta = 0) - \tau_{bb}(\theta = 0)}{1 - \tau_{bb}(\theta = 0)} \tag{5.6}$$

An expression for b was developed by choosing $b \approx 2$ for values of τ^{str} corresponding to the dark roller blind samples and $b \approx 0.28$ for values of τ^{str} corresponding to the light roller blind samples. Recalling also that as A_o approaches unity we expect $b \to 0$, Equations 5.7a and 5.7b were developed.

$$b = 0.133\left(\tau^{str} + 0.003\right)^{-0.467} \qquad \left(0 \le \tau^{str} \le 0.33\right) \tag{5.7a}$$

$$b = 0.33\left(1 - \tau^{str}\right) \qquad \left(0.33 < \tau^{str} \le 1\right) \tag{5.7b}$$

In formulating Equation 5.7a little emphasis was placed on the data for the two dark coloured samples measured at $\theta = 60°$. This can be seen in Figure 5.3. This was done because b will

have virtually no influence on the calculation of $\tau_{bt}(\theta)$ for roller blind materials with such low solar transmission, particularly at higher values of θ.

5.3.4 Beam-Diffuse Transmittance Model

At any given value of θ, the beam-diffuse transmittance is the difference between the beam-total and beam-beam transmittance values.

$$\tau_{bd}(\theta) = \tau_{bt}(\theta) - \tau_{bb}(\theta) \tag{5.8}$$

5.3.5 Diffuse-Diffuse Transmittance and Reflectance Models

The solar optical properties for incident diffuse radiation can be obtained by integrating the beam-total properties over the hemisphere. The diffuse-diffuse transmittance and reflectance are respectively given by

$$\tau_{dd} = 2\int_0^{\pi/2} \tau_{bt}(\theta)\cdot\cos(\theta)\cdot\sin(\theta)\,d\theta \tag{5.9}$$

$$\rho_{dd} = 2\int_0^{\pi/2} \rho_{bt}(\theta)\cdot\cos(\theta)\cdot\sin(\theta)\,d\theta \tag{5.10}$$

Noting that ρ_{bt} is taken to be constant for any given roller blind material, Equation 5.10 reduces to

$$\rho_{dd} = \rho_{bt}(\theta = 0) \tag{5.11}$$

Equation 5.9 can be evaluated numerically.

5.4 Results and Discussion

The solar optical properties measured at normal incidence are summarized in Table 5.1. The data include measurements made with and without the IS. Several observations can be made:

- The two sets of $\tau_{bb}(\theta = 0)$ measurements, with and without the IS agree to within ±0.01 even though τ_{bb} was indirectly measured as the difference between τ_{bt} and τ_{bd} when the IS was used. This observation strengthens confidence in the validity of the measurements.

- The openness factor, A_o, reported by the manufacturer closely matches the experimentally determined $\tau_{bb}(\theta = 0)$.

- Generally, the light coloured roller blinds have high values of $\rho_{bt}(\theta = 0)$ while the dark coloured roller blinds exhibit very low values of $\rho_{bt}(\theta = 0)$. Since reflection and diffuse transmission are attributed primarily to multiple reflections within the structure of the material a connection can be observed between $\tau_{bt}(\theta = 0)$ and $\rho_{bt}(\theta = 0)$ for roller blind materials with non-zero transmission.

A comparison between τ_{bb} measurements, obtained with and without the IS, at various angles of incidence is shown in Table 5.2. The differences between the two sets of measurements are also listed (diff). With a maximum difference of 0.02, the two sets of

measurements agree within experimental uncertainty. Again, this agreement adds confidence in the instrument and calibration procedure.

Turning to the effect of θ, plots of τ_{bb}, τ_{bt} and τ_{bd} are shown in Figure 5.4, Figure 5.5 and Figure 5.6, respectively. Each plot includes measured data points plus curves representing the semi-empirical models developed in this chapter. Each figure is subdivided according to openness in order to display overlapping results more clearly.

$\tau_{bb}(\theta)$ consistently decreases as θ increases as shown in Figure 5.4. Clearly, there is a good agreement between the model and the measurements, to some extent because τ_{bb} is always small. Note the cutoff angle, $\theta_{cutoff} \approx 65°$. The data for closed weave roller blinds ($\tau_{bb}(\theta) = 0$) are not shown in the Figure 5.4.

Figure 5.5 shows beam-total transmission data. Again close agreement between measurement and the semi-empirical model is demonstrated. Also shown in Figure 5.5 are the error bars representing the uncertainty for measurements made with the Black-14% sample. For all roller blinds τ_{bt} decreases as θ increases.

The variation of τ_{bd} with θ shows an interesting trend among the various roller blinds as seen in Figure 5.6. For the closed weave roller blind with $\tau_{bb} = 0$, τ_{bd} is simply equal to τ_{bt} and decreases with an increase in θ. The light coloured, open weave roller blinds (White-14% and Chalk-5%) have similar beam-diffuse characteristics. They both show a gradual increase in τ_{bd} to a maximum value before decreasing as θ increases. Little can be

said about dark coloured, open weave roller blinds (Black-14% and Ebony-5%) with very small values of τ_{bd} over the entire range of θ.

The test samples used in this study represent the range of products used in common practice. However, these samples all have relatively little openness, $A_o \leq 14\%$ and some restrictions may apply to the models presented here. For example, it is clear that Equation 5.2 can safely be used for small values of A_o, say $A_o \leq 20\%$, and for the unlikely situation of large values of A_o, say $A_o > 80\%$ (because of the limits accomodated by Equation 5.3 and Equation 5.4), but some uncertainty can be expected at intermediate values of A_o.

Finally, it should be noted that all of the non-opaque test samples were optically symmetric. The models presented here are trivial when used to characterise opaque roller blinds (zero transmission and constant reflectance) and therefore can be safely applied to asymmetric opaque materials such as the black/white material included in this study. In contrast, it is not clear how well the models apply to asymmetric materials that allow some diffuse transmission. This is not a serious limitation. Certainly the current models will work well for asymmetric materials that have little diffuse transmission ($\tau_{bt}(\theta = 0) \approx \tau_{bb}(\theta = 0)$). Regardless, the vast majority of roller blinds are optically symmetric. The extension of the current models, if necessary at all, will be the subject of future research.

5.5 Conclusions

A set of models for generating off-normal solar optical properties of roller blinds are presented. The models provide a means to calculate off-normal properties by adjusting known values of beam-beam and beam-total transmittance values measured at normal incidence. No such adjustment is required for reflectance since measurements revealed an insignificant variation of reflectance with respect to incidence angle for each sample considered. The models are based on experiments made with special sample holders attached to an integrating sphere of a spectrophotometer. Models for roller blind transmittance were obtained by fitting curves that closely matched the experimental data. Given solar optical properties obtained at normal incidence, the proposed models can be used to characterise the off-normal transmittance of any roller blind including blinds with a moderate amount of openness. The off-normal models can be integrated to obtain the diffuse properties. The models have also been formulated so that they can be applied to both optically symmetric and assymetric roller blind materials.

Table 5.1: Summary of Measured Solar Optical Properties at Normal Incidence

		Measurements with IS				Measurements without IS
Identification	**Classification**	**Beam-Total Reflectance**	**Beam-Total Transmittance**	**Beam-Diffuse Transmittance**	**Beam-Beam Transmittance**	**Beam-Beam Transmittance**
White_14%	Open weave	0.64	0.30	0.17	0.13	0.14
Black_14%	Open weave	0.03	0.13	0.01	0.12	0.12
Chalk_5%	Open weave	0.75	0.16	0.08	0.08	0.09
Ebony_5%	Open weave	0.03	0.07	0.01	0.06	0.07
Duplex_opaque (black side)	Closed weave	0.05	0.00	0.00	0.00	0.00
Duplex_opaque (white side)	Closed weave	0.84	0.00	0.00	0.00	0.00
Glacier_translucent	Closed weave	0.65	0.24	0.24	0.00	0.00

Table 5.2: Comparison Between Beam-Beam Transmittance Measurements with and without the Integrating Sphere

	White_14%			**Black_14%**			**Chalk_5%**			**Ebony_5%**		
Incidence Angle	**With IS**	**Without IS**	**Diff**	**With IS**	**Without IS**	**Diff**	**With IS**	**Without IS**	**Diff**	**With IS**	**Without IS**	**Diff**
0	0.14	0.13	0.01	0.12	0.12	0.00	0.09	0.08	0.01	0.07	0.06	0.01
15	0.14	0.13	0.01	0.12	0.11	0.01	0.08	0.08	0.00	0.06	0.06	0.00
30	0.12	0.11	0.01	0.11	0.10	0.01	0.07	0.07	0.00	0.05	0.05	0.00
45	0.11	0.09	0.02	0.08	0.07	0.01	0.05	0.05	0.00	0.03	0.03	0.00
60	0.05	0.03	0.02	0.04	0.02	0.02	0.02	0.02	0.00	0.00	0.00	0.00

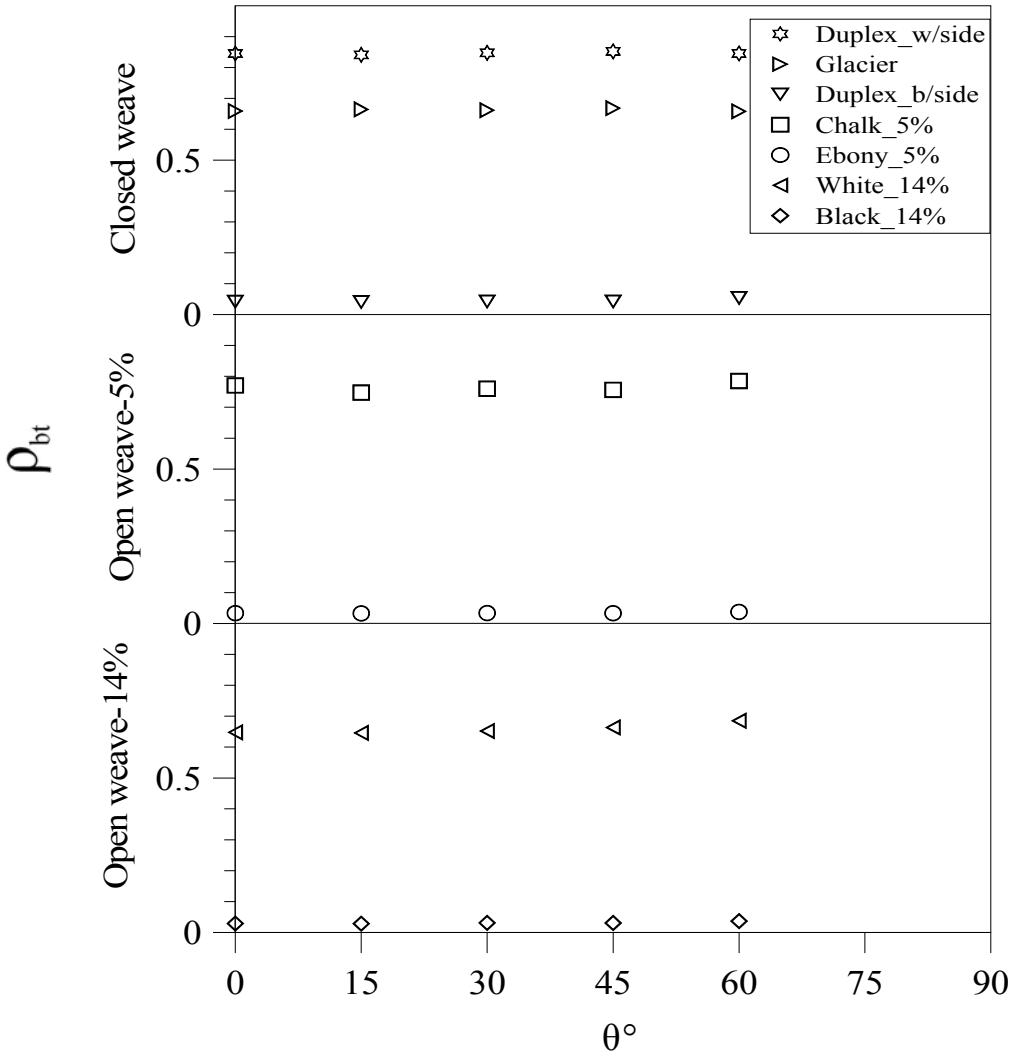

Figure 5.1: Beam-Total Reflectance versus Incidence Angle

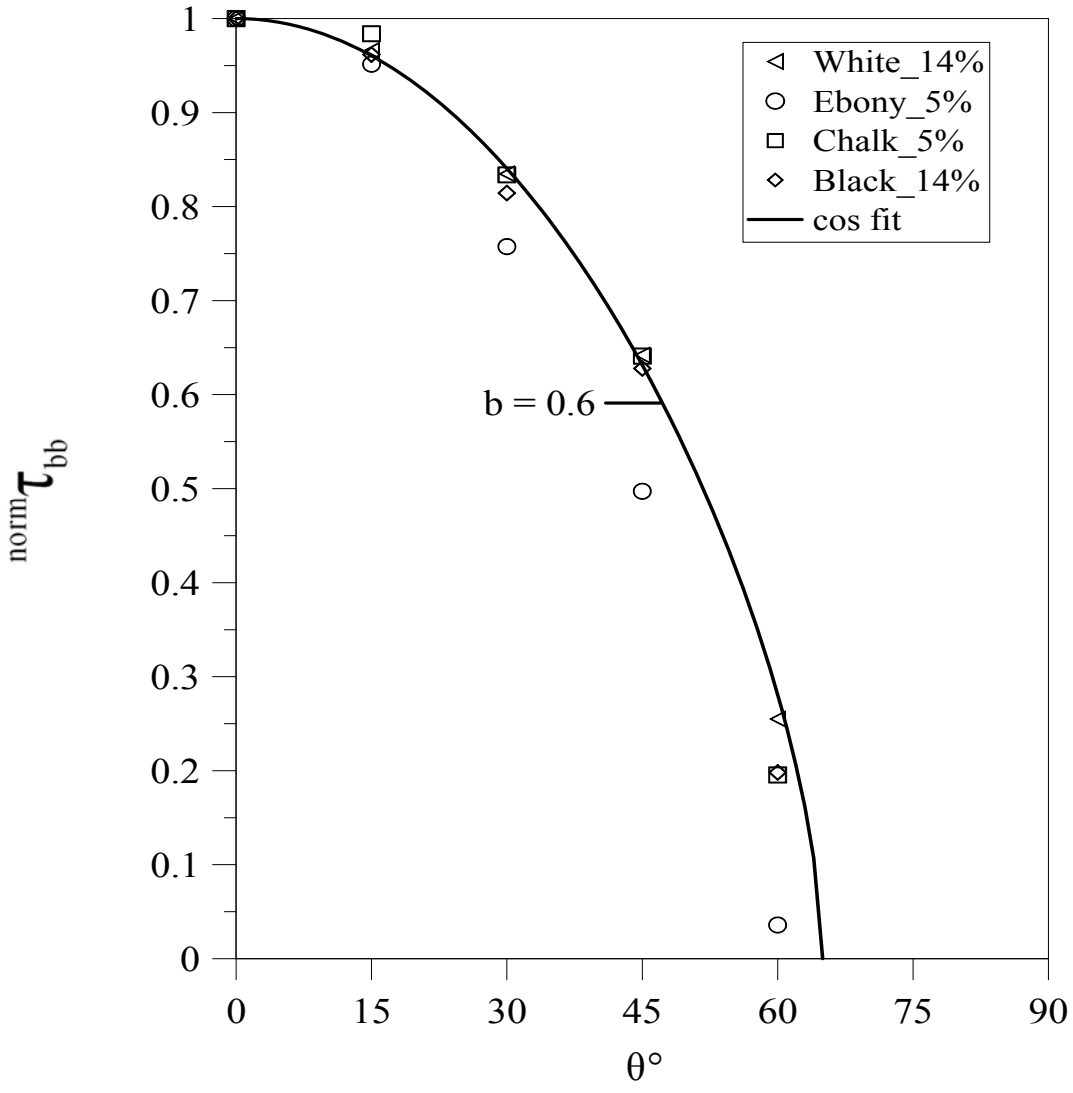

Figure 5.2: Normalised Beam-Beam Transmittance versus Incidence Angle

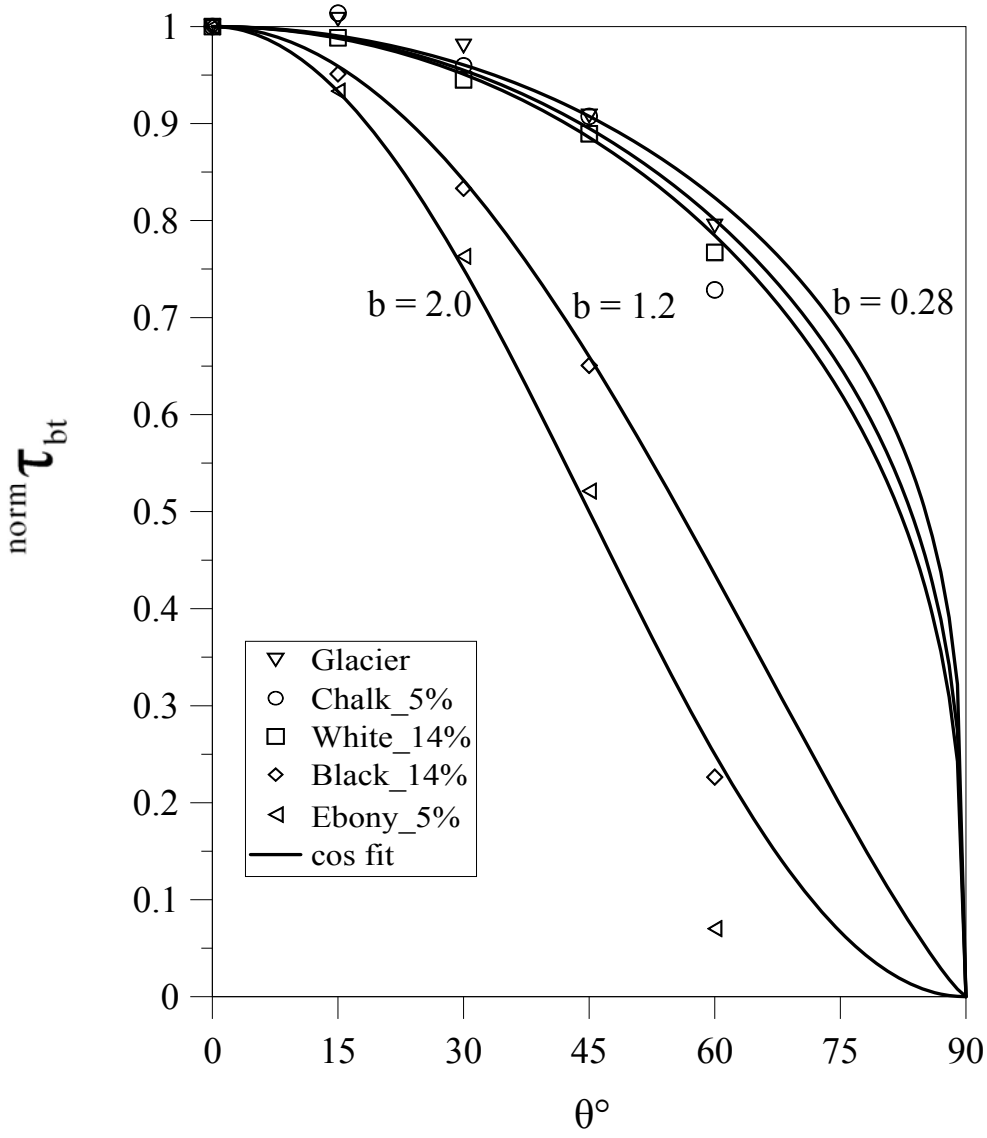

Figure 5.3: Normalised Beam-Total Transmittance versus Incidence Angle

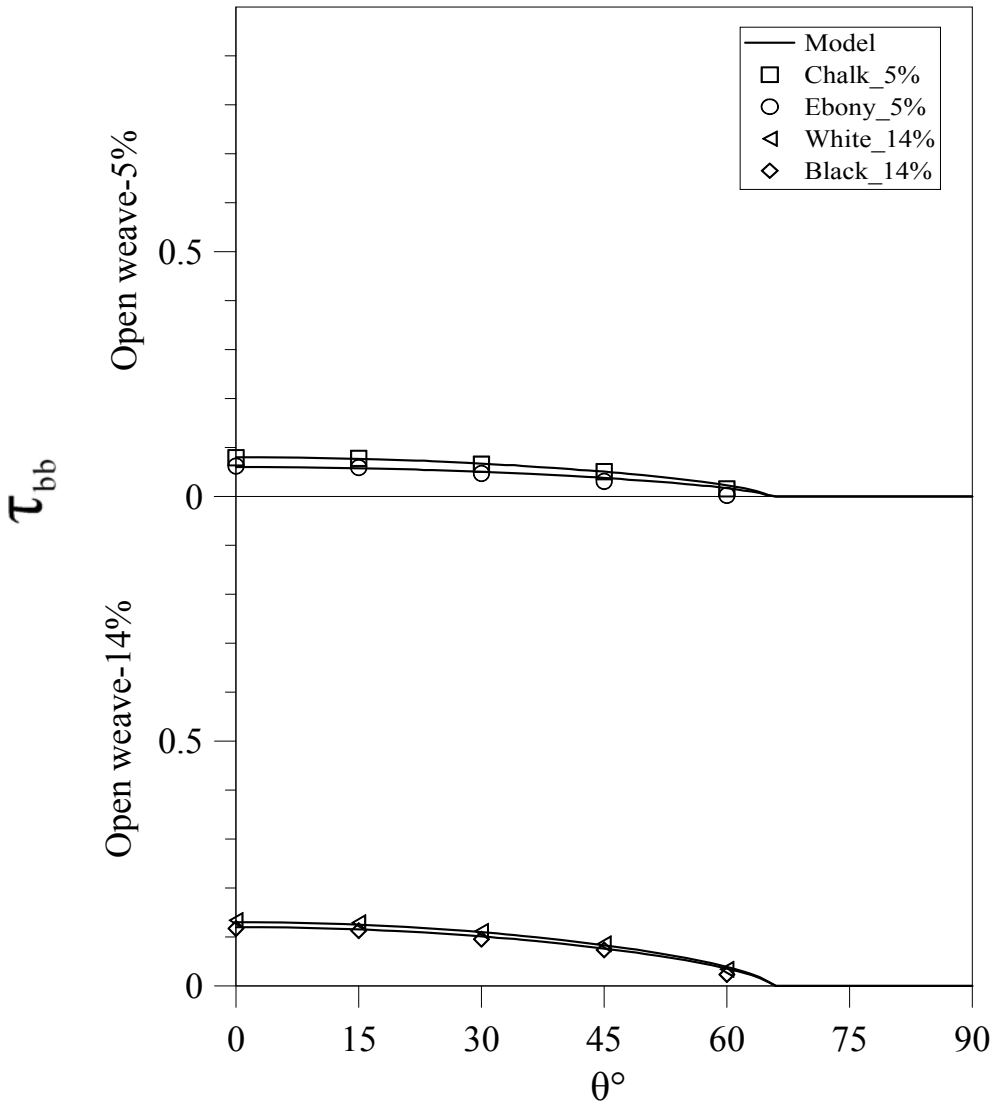

Figure 5.4: Beam-Beam Transmittance versus Incidence Angle

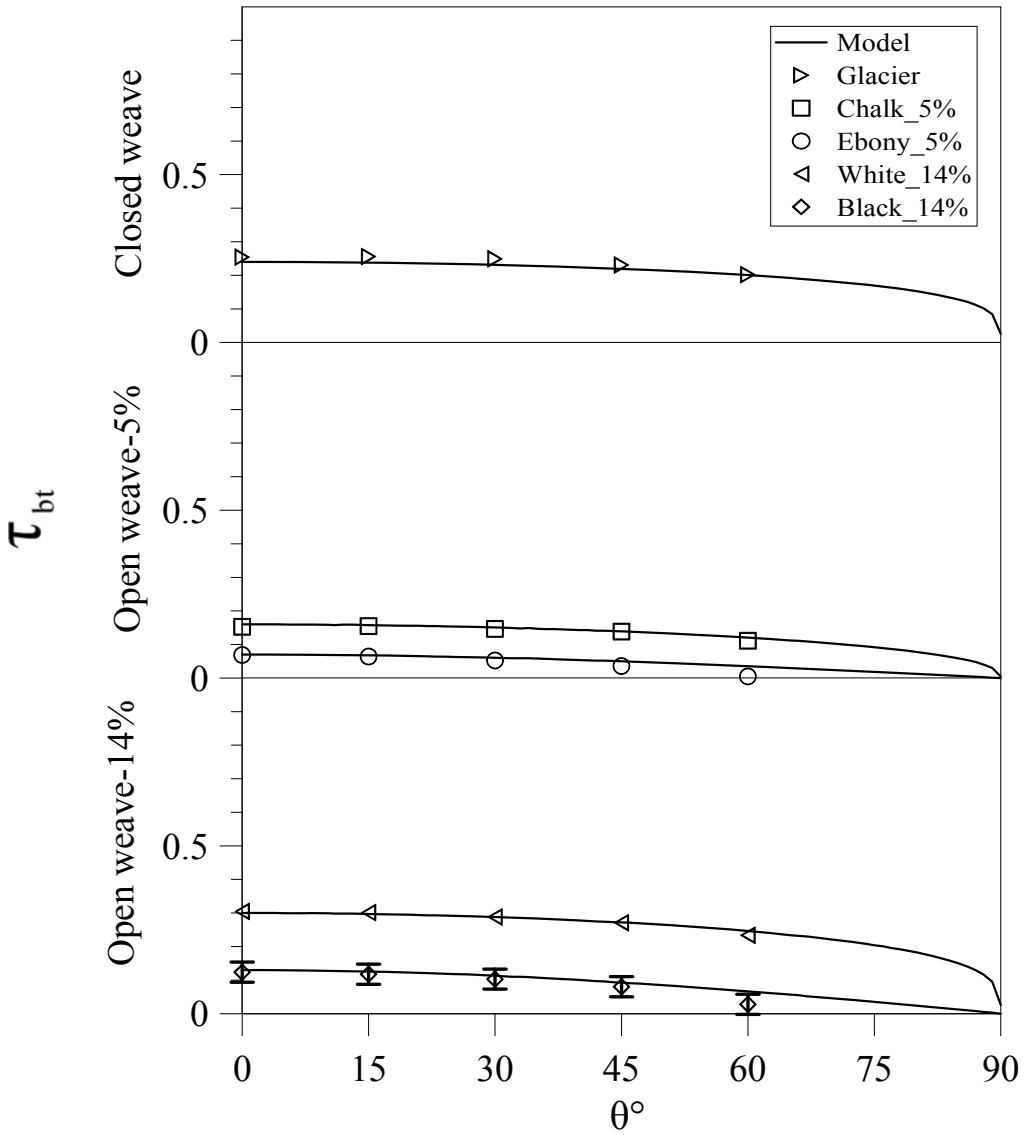

Figure 5.5: Beam-Total Transmittance versus Incidence Angle

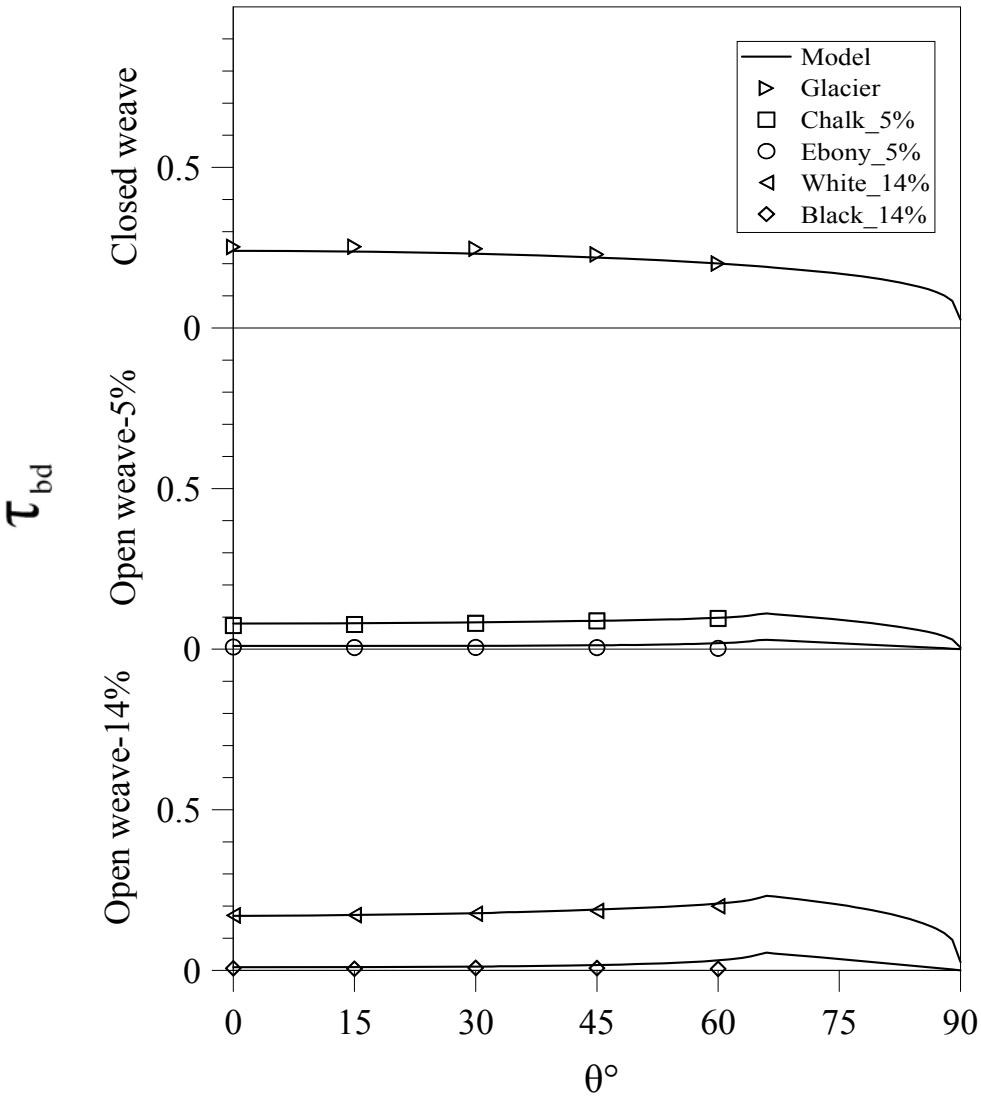

Figure 5.6: Beam-Diffuse Transmittance versus Incidence Angle

CHAPTER 6

SOLAR PROPERTIES OF INSECT SCREENS

6.1 Introduction

The development of solar optical property models for insect screens is presented. The models are formulated using off-normal measurement data obtained with special sample holders attached to an integrating sphere of a spectrophotometer. Measurements were taken on six samples with various mesh sizes and wire reflectances as described in Chapter 3. The models are formulated such that solar optical properties obtained at normal incidence can be used to calculate off-normal beam-beam, beam-total and beam-diffuse properties. Diffuse-diffuse properties are subsequently obtained from hemispherical integration of beam-total properties. To further demonstrate the reliability of the measurement procedure, the results are compared with analytical models recently developed from geometry and a ray tracing technique (EnergyPlus 2005).

6.2 Model Components

6.2.1 Beam-Beam Transmittance Model

The geometric configuration of a screen is relatively simple and can be represented by orthogonal crossed wires with known wire diameter, D, and centre-to-centre spacing, S as shown in Figure 6.1. Assuming D and S are the same in both directions, the openness, A_o, is

$$A_o = \frac{(S-D)^2}{S^2} \tag{6.1}$$

The value of A_o can either be determined from geometry or by simply measuring $\tau_{bb}(\theta = 0)$

Another parameter of practical importance is the incidence angle beyond which direct beam transmission is cut off, θ_{cutoff}. From geometry, θ_{cutoff} can be estimated as:

$$\cos(\theta_{cutoff}) = \frac{D}{S} \tag{6.2}$$

This analysis establishes the endpoints of a curve that represents the beam-beam transmittance model. To obtain the shape of the curve a cosine power function with an exponent is selected to match the experimental data. A similar approach has been used in Chapters 4 and 5 to formulate off-normal property models for fabrics and roller blinds, respectively, and this well established method is documented in (Kotey et al. 2009a, 2009b and 2009c).

A convenient way to normalise τ_{bb} is given by Equation 6.3:

$$^{norm}\tau_{bb} = \frac{\tau_{bb}(\theta)}{\tau_{bb}(\theta = 0)} = \cos^{b}\left(\frac{\theta}{\theta_{cutoff}} \cdot 90°\right) \tag{6.3}$$

For a given sample, a unique value of b allows the empirical function to match the experimental data as shown in Figure 6.2. Assuming that b is a function of $\tau_{bb}(\theta = 0)$, a graph of b versus $\tau_{bb}(\theta = 0)$ can be represented by a curve as shown in Figure 6.3. The equation that represents the curve in Figure 6.3 is:

$$b = -0.45\ln\left(MAX\left(\tau_{bb}(\theta = 0), 0.01\right)\right) + 0.1 \tag{6.4}$$

Ideally, Equation 6.4 would be formulated such that b approaches zero as openness approaches 100%. In this limit, the insect screen disappears and Equation 6.3 applies no off-normal adjustment. However, some compromise was needed in order to retain the simplicity of the model and to retain the realism that absorptivity of the screen remains between zero and unity for all possible input values.

More formally, Equations 6.1 through 6.4, can be used to calculate $\tau_{bb}(\theta)$ as a function of $\tau_{bb}(\theta = 0)$ using:

$$\tau_{bb}(\theta) = \tau_{bb}(\theta = 0)\cos^{b}\left(\frac{\theta}{\theta_{cutoff}} \cdot 90°\right) \qquad \theta < \theta_{cutoff} \tag{6.5a}$$

$$\tau_{bb}(\theta) = 0 \qquad \theta \geq \theta_{cutoff} \tag{6.5b}$$

6.2.2 Beam-Total Transmittance Model

The beam-total transmittance, τ_{bt} is the sum of τ_{bd} and τ_{bb}. A recent analytical model of screens (EnergyPlus 2007) reveals that τ_{bd} increases monotonically to a maximum value at θ_{cutoff} and then decreases sharply to zero at $\theta = 90°$. Since $\tau_{bb} = 0$ at $\theta_{cutoff} < 90°$ and $\tau_{bd} = 0$ at $\theta = 90°$, it implies that $\tau_{bt} = 0$ at $\theta = 90°$. Using the cosine power function, the normalised form of τ_{bt} can be represented with a function given by Equation 6.6:

$$^{norm}\tau_{bt} = \frac{\tau_{bt}(\theta)}{\tau_{bt}(\theta = 0)} = \cos^{b}(\theta) \tag{6.6}$$

By inspection, the desired values of b can be obtained by working with Equation 6.6. Assuming b is a function of $\tau_{bt}(\theta = 0)$, a relation between b and $\tau_{bt}(\theta = 0)$ can also be represented by the curve:

$$b = -0.65\ln(\mathrm{MAX}(\tau_{bt}(\theta = 0), 0.01)) + 0.1 \tag{6.7}$$

Similar to the way in which Equation 6.4 was formulated, some compromise was accepted in order that the model would provide realistic results in the extreme cases of insect screens with very high openness and very low reflectance.

Rearranging Equation 6.6,

$$\tau_{bt}(\theta) = \tau_{bt}(\theta = 0)\cos^{b}(\theta) \tag{6.8}$$

6.2.3 Beam-Diffuse Transmittance Model

At any given θ, τ_{bd} is the difference between τ_{bt} and τ_{bb}, i.e.,

$$\tau_{bd}(\theta) = \tau_{bt}(\theta) - \tau_{bb}(\theta) \tag{6.9}$$

6.2.4 Beam-Total Reflectance Model

Measurements showed that the beam-total reflectance of the screen, ρ_{bt}, includes no specular component; thus, $\rho_{bt} = \rho_{bd}$.

In order to make an approximate distinction between wires of different reflectance values, an apparent wire reflectance, ρ^{w}, was defined such that:

$$\rho_{bt}(\theta = 0) = \rho^{w}(1 - A_o) \tag{6.10}$$

The reflectance model described by Equation 6.10 considers reflection at the surface of the wire as well as multiple reflections between the wires. Rearranging Equation 6.10,

$$\rho^{w} = \frac{\rho_{bt}(\theta = 0)}{1 - A_o} \tag{6.11}$$

Equation 6.12 was used to define normalised beam-total reflectance:

$$^{norm}\rho_{bt}(\theta) = \frac{\rho_{bt}(\theta) - \rho_{bt}(\theta = 0)}{\rho_{bt}(\theta = 90°) - \rho_{bt}(\theta = 0)} \tag{6.12}$$

A model was then developed by comparing measurements with the function shown in Equation 6.13. Knowing only the openness of the screen and $\rho_{bt}(\theta = 0)$, the off-normal reflectance of the screen can be calculated as follows:

$$^{norm}\rho_{bt}(\theta) = 1 - \cos^{b}(\theta) \tag{6.13}$$

where

$$\rho_{bt}(\theta = 90°) = \rho_{bt}(\theta = 0) + \left(1 - \rho_{bt}(\theta = 0)\right) \cdot 0.35\rho^{w} \tag{6.14}$$

The exponent b was estimated for each set of experimental data by inspection, similar to the way in which values of b were found for $\tau_{bb}(\theta)$, and was found to correlate well with respect to ρ^{w}:

$$b = -0.45\ln(\rho^{w}) \tag{6.15}$$

Finally, $\rho_{bt}(\theta)$ was obtained by rearranging Equation 6.12 and 6.13:

$$\rho_{bt}(\theta) = \rho(\theta = 0) + (\rho(\theta = 90°) - \rho(\theta = 0))\,(1 - \cos^{b}(\theta)) \tag{6.16}$$

6.2.5 Diffuse-Diffuse Transmittance and Reflectance Models

The solar optical properties for incident diffuse radiation can be obtained by integrating the beam-total properties over the hemisphere. The diffuse-diffuse transmittance is

$$\tau_{dd} = 2\int_{0}^{\frac{\pi}{2}} \tau_{bt}(\theta)\sin(\theta)\cos(\theta)d\theta \tag{6.17}$$

Similarly, the diffuse-diffuse reflectance is:

$$\rho_{dd} = 2\int_0^{\frac{\pi}{2}} \rho_{bt}(\theta)\sin(\theta)\cos(\theta)d\theta \tag{6.18}$$

Numerical integration can be used to evaluate the integrals in Equations 6.17 and 6.18.

6.3 Discussion

Table 6.1 gives a summary of the measured normal incidence solar optical properties of screens considered. The results in Table 6.1 include measurements with and without the IS as well as A_o calculated from geometry. As expected, $\tau_{bb}(\theta = 0)$ obtained from measurements compared favourably with A_o. This observation clearly demonstrates the reliability of measuring A_o using a spectrophotometer.

Figure 6.4 through Figure 6.7 show the variation of the solar optical properties with respect to θ. The symbols represent measurements while the solid lines represent the semi-empirical models. Clearly, there is a good agreement between measured and calculated results. Also shown in Figure 6.5 are the error bars representing the uncertainty for measurements made with the 60 mesh screen. As seen in Figure 6.4, τ_{bb} decreases as θ increases and falls to zero at θ_{cutoff} which is directly dependent on D and S as given by Equation 6.2. Figure 6.5 also shows a decrease in τ_{bt} as θ increases and in this case the semi-empirical model predicts a complete attenuation of τ_{bt} at $\theta = 90°$. On the other hand, τ_{bd} changes very little

with respect to θ until $\theta \approx 60°$ as seen in Figure 6.6. Beyond $\theta \approx 60°$, τ_{bd} increases to a maximum value which occurs at $\theta = \theta_{cutoff}$. At $\theta > \theta_{cutoff}$, τ_{bd} decreases sharply to zero at $\theta = 90°$. Turning to the variation of ρ_{bt} with θ, it is evident from Figure 6.7 that ρ_{bt} remains almost constant with respect to θ until $\theta \approx 60°$. Beyond $\theta \approx 60°$, ρ_{bt} increases slightly to a maximum value at $\theta = 90°$.

6.3.1 Comparison with EnergyPlus Model

The most recent characterisation of screens is reported in the EnergyPlus (2007) Reference Manual. Off-normal solar property models were developed for building energy simulation using analytical and ray tracing techniques. The models are based on the orthogonal crossed cylinder geometry with known wire diameter, wire centre-to-centre spacing and wire reflectance. It is assumed that the wire diameter and wire spacing are the same in both directions. For a unit of incoming beam radiation with known direction, the models account for both undisturbed flux going through the openings of the screen and intercepted flux. The beam-diffuse transmittance model was "empirically" formulated by curve-fitting results from an optical ray tracing algorithm. The ray tracing algorithm is based on the assumption that the wire reflectance is diffuse. The beam-diffuse reflectance is a function of the beam-beam transmittance, the wire reflectance and the beam-diffuse transmittance. The diffuse-diffuse transmittance and reflectance models are simply hemispherical integrations of the beam-total transmittance and beam-diffuse reflectance, respectively.

To compare the experimental results with the EnergyPlus model, the experimental results for the 20-mesh, 0.006 in. blue-gray screen were plotted on the same graph with model curves as shown in Figure 6.8. The models are in good agreement with the experimental results except for an obvious underprediction of τ_{bd} in the range of $0 < \theta < 45°$. This underprediction is very small with a maximum value of 2% in absolute terms at $\theta = 0$. Nonetheless, it can be explained by considering the accuracy of the model. As stated in EnergyPlus (2007), τ_{bb} was derived from pure geometry and as such is only influenced by the geometrical properties of the screen and θ. However, τ_{bd} was formulated by curve-fitting results from an optical ray tracing algorithm that modeled ρ^{w} as diffuse. More specifically generalised curves were fitted to accommodate ray tracing results for $0.2 \le D/S \le 0.8$ and $0.2 \le \rho^{w} \le 0.8$. Since the curve-fitted model generally underpredicts the optical ray tracing results for most screens with modest values of D/S and ρ^{w} (McCluney 2006), a similar trend between the curve-fitted model and results obtained from the measurements is expected. It is imperative to note that the agreement between EnergyPlus models and the measurement results for all other screens considered in this study was good.

6.4 Conclusions

The formulation of semi-empirical models that approximate the off-normal solar optical properties of insect screens is reported. The models were developed from the experimental results obtained with special sample holders attached to an integrating sphere of a

spectrophotometer. Given solar optical properties obtained at normal incidence, the proposed semi-empirical models can be used to obtain the off-normal properties of practically any screen that can be attached to a window. To further demonstrate the reliability of the measurement technique, the experimental results were compared to analytical and ray tracing model recently developed for building energy simulation. In general, there was very good agreement between the two sets of results.

Table 6.1: Summary of Solar Optical Properties at Normal Incidence

Item	Measurements with IS				Measurements without IS	Calculated Openness, Ao
	$\rho_{bt}(\theta=0)$	$\tau_{bt}(\theta=0)$	$\tau_{bd}(\theta=0)$	$\tau_{bb}(\theta=0)$	$\tau_{bb}(\theta=0)$	
150 mesh 0.0026 in. dia shiny	0.23	0.44	0.08	0.36	0.38	0.37
120 mesh 0.0026 in. dia shiny	0.19	0.54	0.08	0.46	0.47	0.48
20 mesh 0.016 in. dia shiny	0.18	0.54	0.05	0.49	0.48	0.48
60 mesh 0.0045 in. dia shiny	0.18	0.60	0.08	0.52	0.54	0.54
20 mesh 0.010 in. dia bluegray	0.07	0.65	0.02	0.63	0.64	0.65
26 mesh 0.006 in. dia charcoal	0.01	0.71	0.01	0.70	0.73	0.73

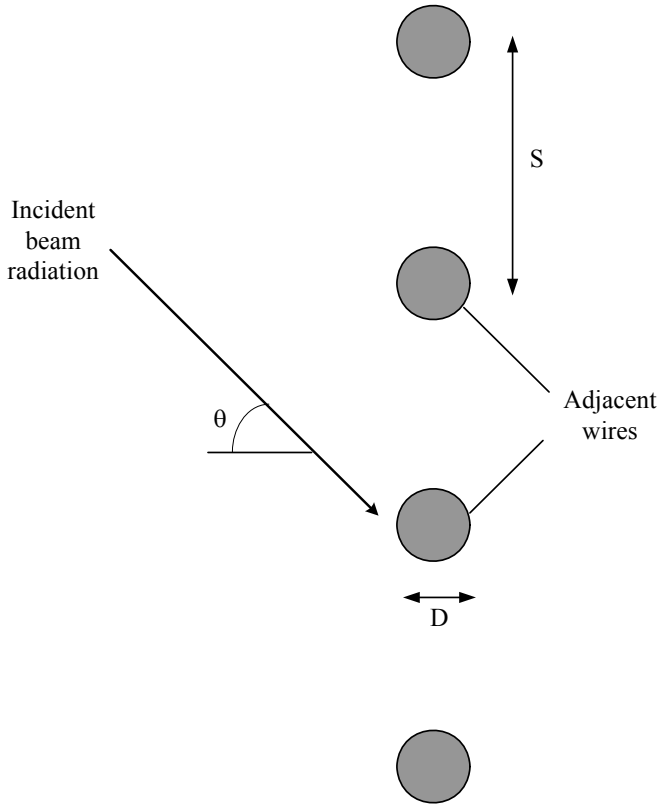

Figure 6.1: Geometry used for Insect Screens

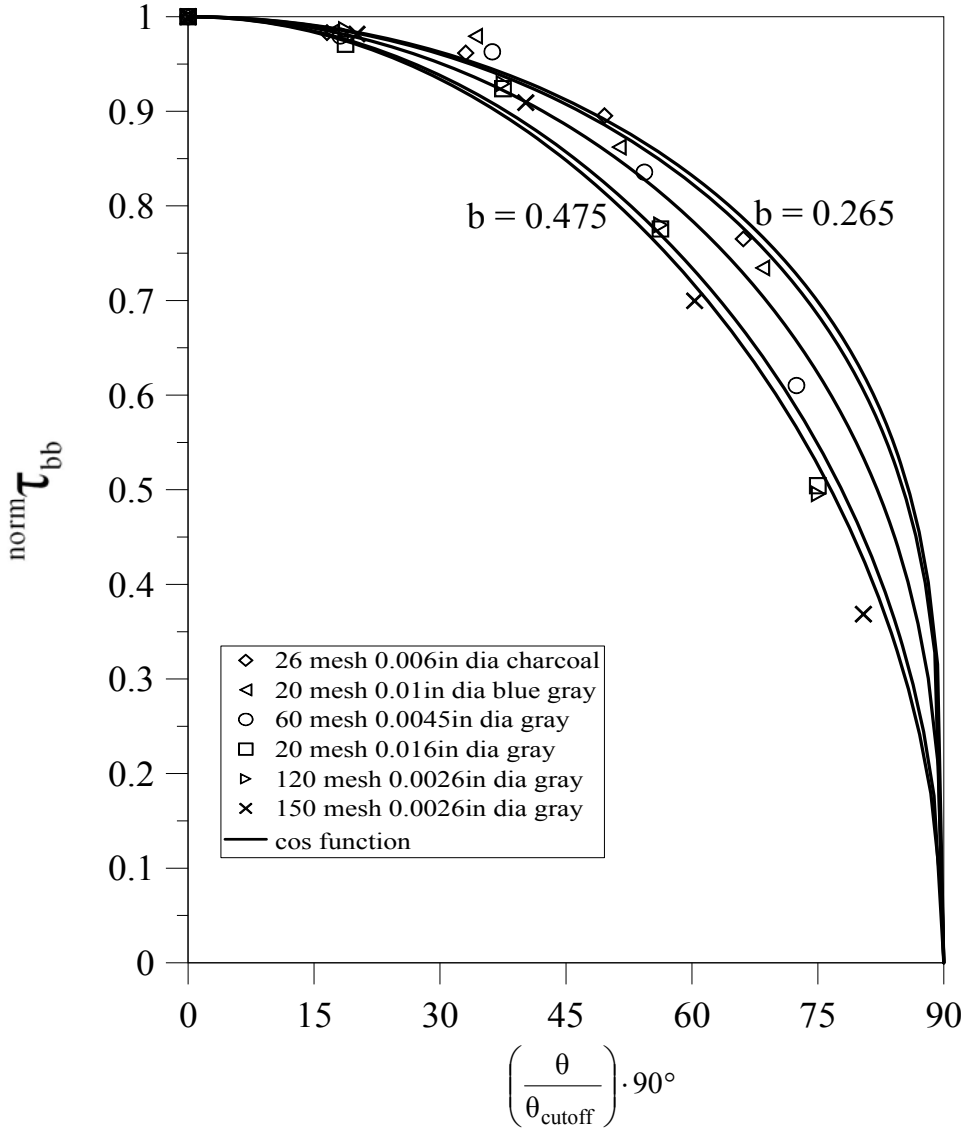

Figure 6.2: Normalised Beam-Beam Transmittance Versus Incidence Angle (From Measurements with Integrating Sphere)

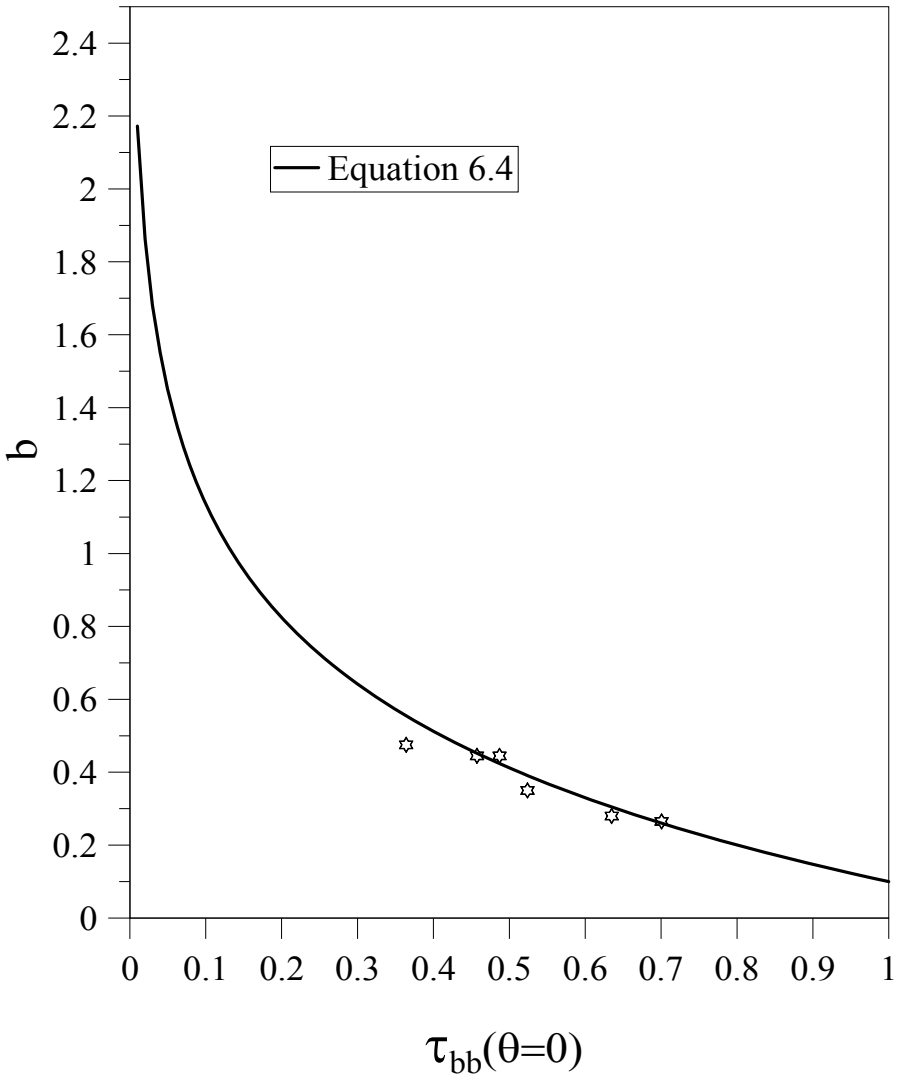

Figure 6.3: Graph of b Versus $\tau_{bb}(\theta = 0)$

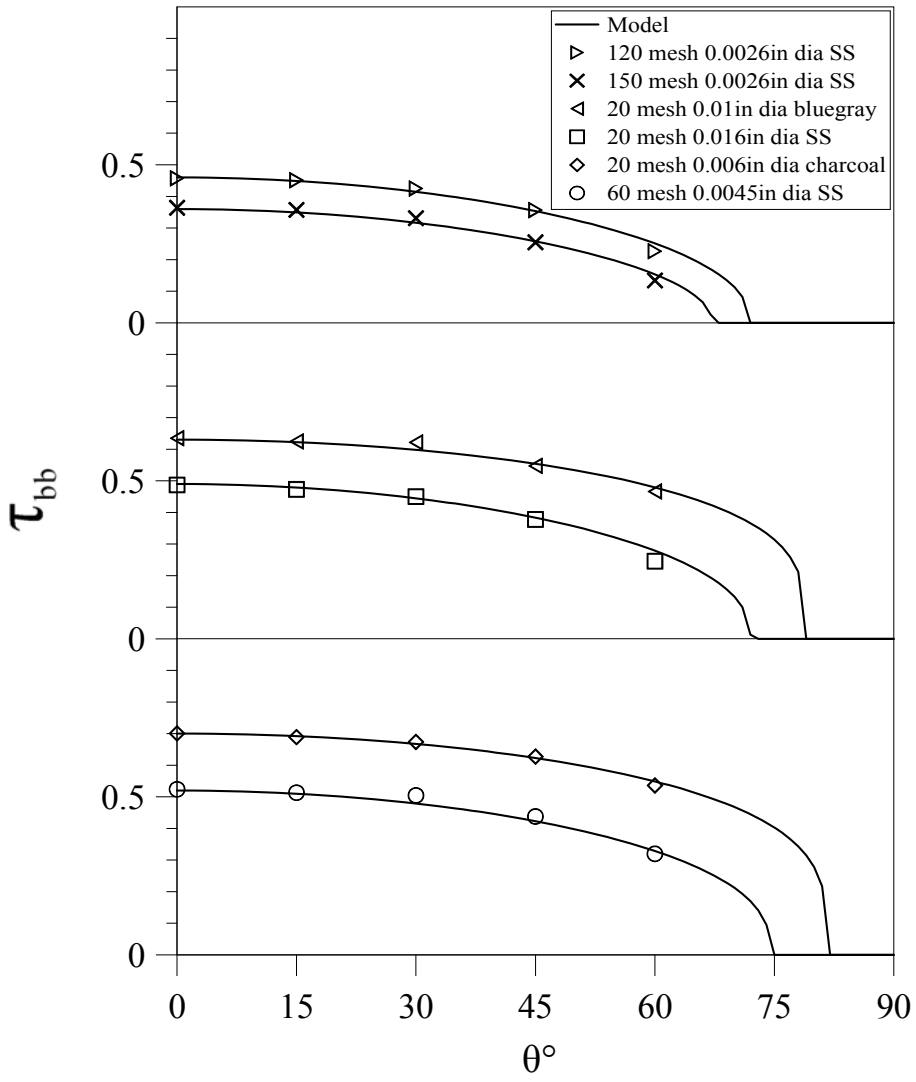

Figure 6.4: Beam-Beam Transmittance Versus Incidence Angle

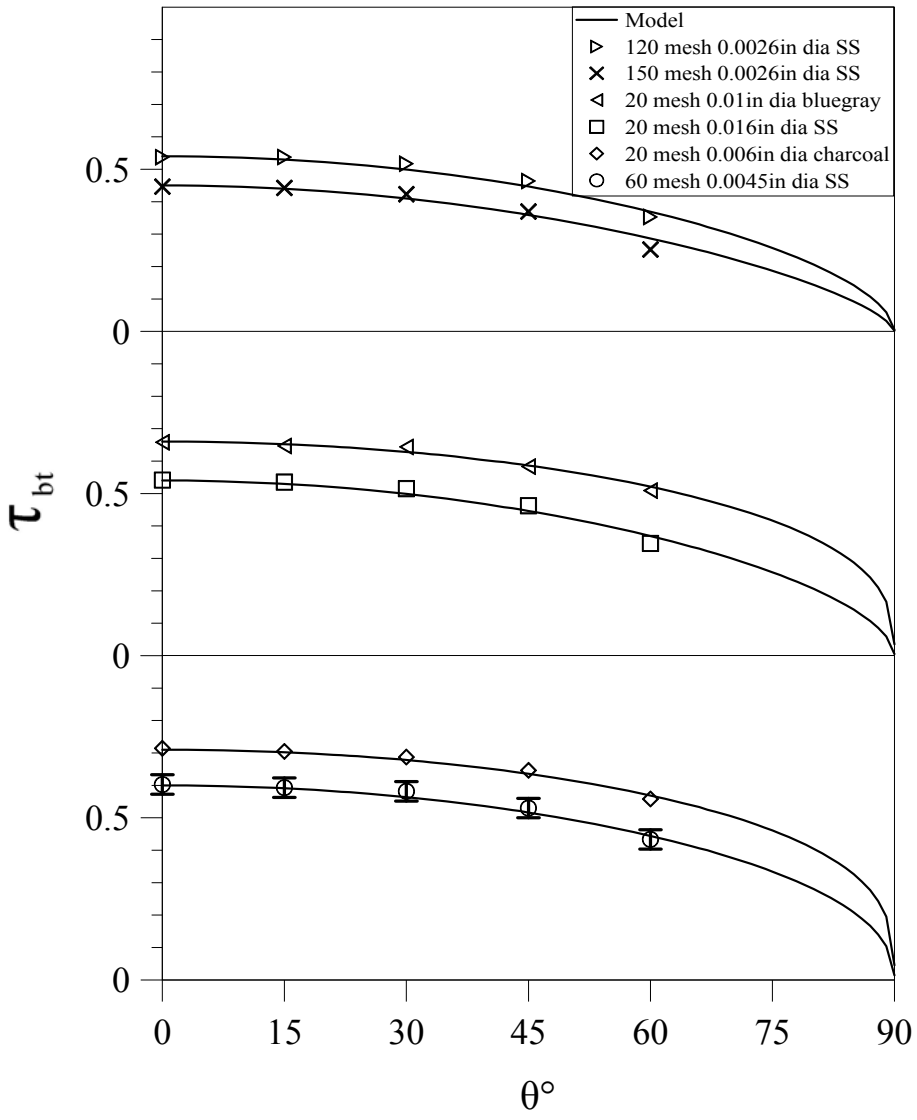

Figure 6.5: Beam-Total Transmittance Versus Incidence Angle

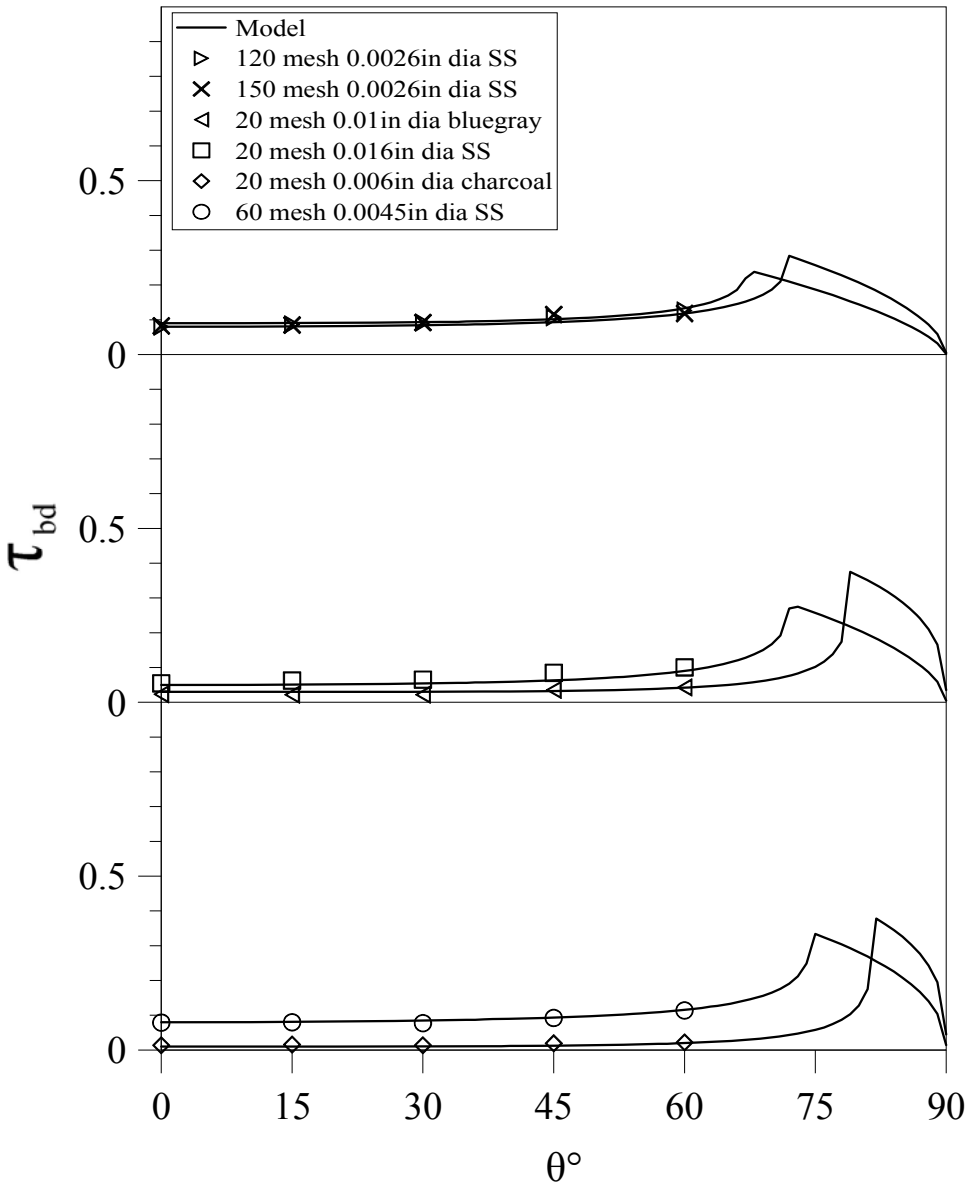

Figure 6.6: Beam-Diffuse Transmittance Versus Incidence Angle

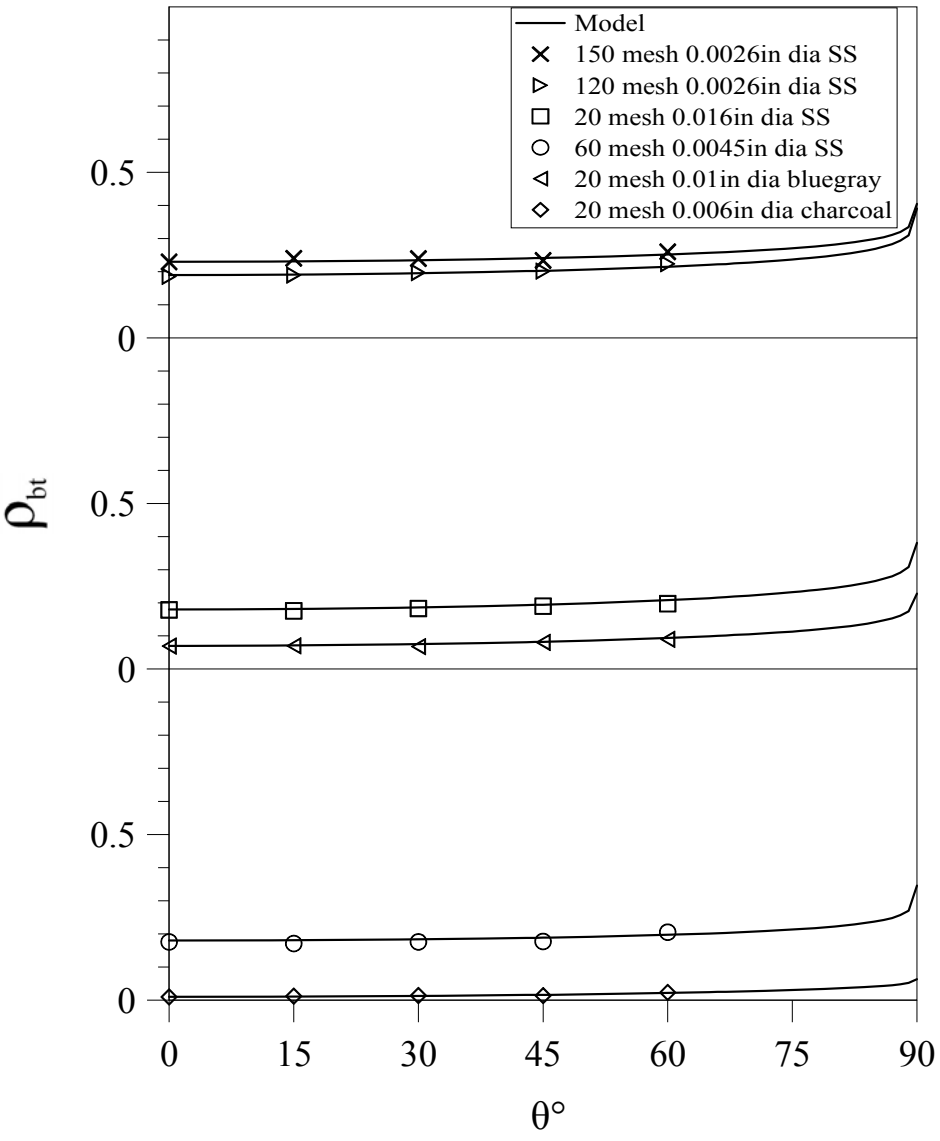

Figure 6.7: Beam-Total Reflectance Versus Incidence Angle

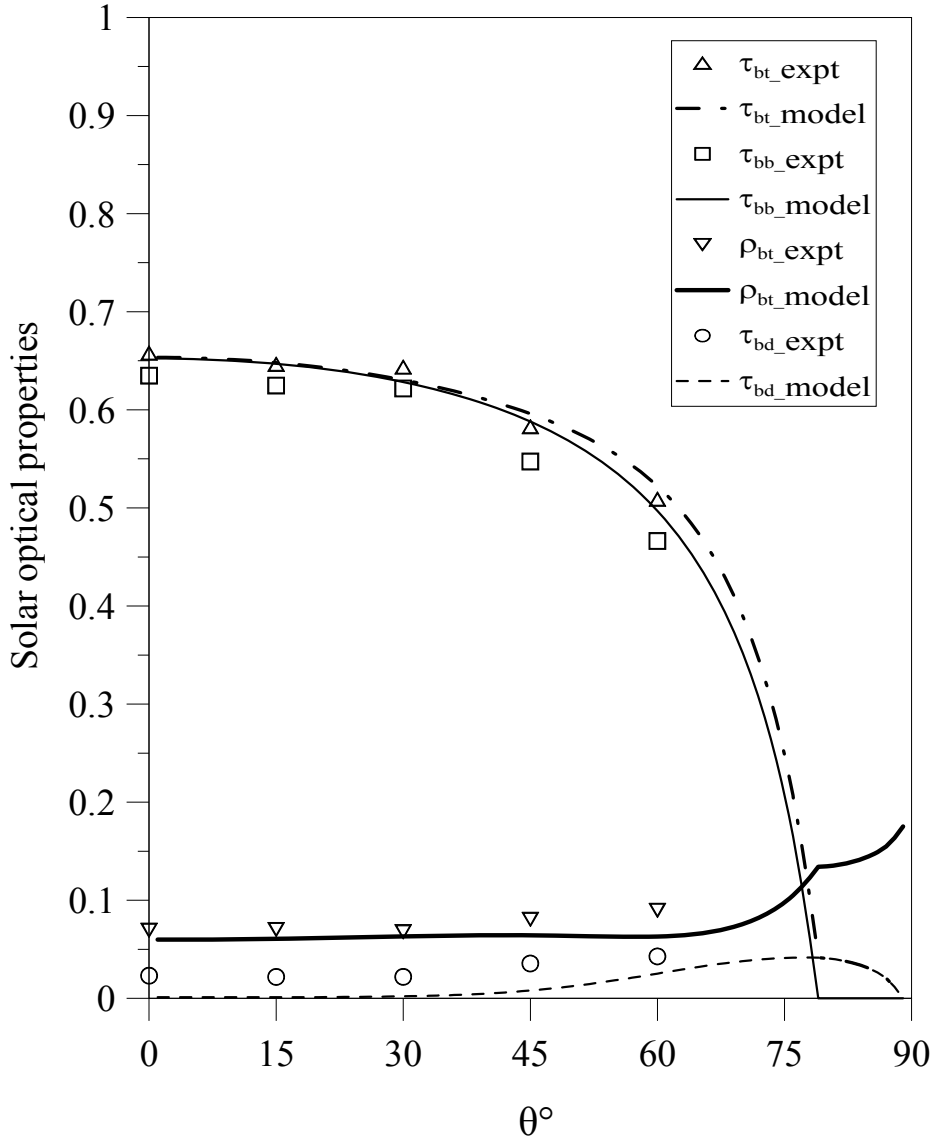

Figure 6.8: Comparison between Experimentally Determined Solar Optical Properties and EnergyPlus Models for 20-Mesh-Blue-Grey Screen

CHAPTER 7

LONGWAVE PROPERTIES OF FLAT SHADING MATERIALS

7.1 Introduction

The chapter discusses the determination of longwave properties of flat shading materials. The shading materials considered were drapery fabrics, insect screens and roller blinds. Each of these materials consists of a structure (i.e., yarn, wire, sheet) that is opaque with respect to longwave radiation and each material is likely to have some openness. Material emittance and longwave transmittance measurements were taken with an infrared reflectometer using two backing surfaces. The results show emittance and longwave transmittance of the shading material to be simple functions of openness, emittance and longwave transmittance of the structure. This is especially useful because openness can be determined from solar transmittance measurements (see Chapter 3) while emittance and longwave transmittance of the structure was found to be constant for each category of shading material. The models that describe the longwave properties of roller blinds and insect screens can be used directly in the multi-layer analysis. On the other hand, the model that describes the longwave properties of fabrics comprises a useful component of the effective longwave properties model for pleated drapes and, in turn, an input to the multi-layer analysis.

7.2 Approach

Spectral measurements of longwave reflectance and transmittance were obtained for each category of flat shading material using an infrared reflectometer. The spectral data showed that the shading materials are generally not spectrally selective. Since the aim was to generate total (spectral-averaged) properties for building energy simulation, no spectral data are presented. The total properties, including emittance, were calculated with respect to the blackbody spectrum at a room temperature (ASTM E408-71 1971). The procedure entailed the solution of two simultaneous equations resulting from the reflectance measurements with the sample backed by two surfaces with different reflectance values. A similar procedure was used by Christie and Hunter (1984) to determine the longwave properties of thin diathermanous films using a DB-100 Infrared Reflectometer.

7.3 Test Samples

A wide variety of commercially available shading materials was selected for testing. This includes samples of drapery fabrics, roller blinds and insect screens. The dimensions of each sample were 5 cm by 5 cm. For each category of shading material, values of $A_o = \tau_{bb}^{m}(\theta = 0)$ were obtained from spectrophotometer measurements (Kotey et al. 2009a, 2009b and 2009c). The description of the shading materials tested is given in Chapter 3.

7.4 Instrumentation

A commercially available FTIR (Fourier Transform Infrared Spectroscopy) reflectometer, SOC 400T, was used to obtained the measurements. It is a portable, self calibrating instrument with a reflectance repeatability of ±0.01 and a spectral resolution selectable from 4 to 32cm^{-1}. The reflectometer is designed to measure normal-hemispherical reflectance of an opaque surface in the wavelength range of $2.0 < \lambda < 25.0$ μm (infrared region). The instrument collects many infrared spectra over a short period of time. The infrared spectra are automatically averaged and integrated with respect to the back body spectrum at selectable temperature range. Emittance values are evaluated from the integrated values of the spectral reflectance. Detailed description and the operating principles of the SOC 400T is documented by Surface Optics Corporation (2002) and Jaworske and Skowronski (2000).

The SOC 400T is the current state-of-the-art instrument that may be offered as a substitute for the well known Gier Dunkle DB-100 infrared reflectometer. This is because the SOC 400T has the capability to measure reflectance over a large spectral range and subsequently evaluates emittance over a large temperature range. The Gier Dunkle DB-100, on the other hand, measures total reflectance in the vicinity of 9.7 μm while emittance can only be evaluated at room temperature. Another remarkable difference between the two instruments is that the DB-100 measures hemispherical-normal reflectance whereas the SOC 400T measures normal-hemispherical reflectance.

7.5 Measurement Procedure

The SOC 400T is designed to measure infrared reflectance of samples that are opaque to infrared radiation. However, by following the general theory and measurement procedure documented by Christie and Hunter (1984), the reflectometer can be adapted to measure both infrared reflectance and transmittance of diathermanous samples. Emittance is easily estimated from the reflectance and the transmittance measurements.

The SOC 400T was calibrated by first leaving the measurement port uncovered while the room was scanned and the zero spectrum recorded. Care was taken not to obstruct the field of view of the measurement port. A specular gold disk was then placed over the measurement port and the reference spectrum recorded. The gold disk has a constant reflectance value of 0.98 in the wavelength range of $2.0 < \lambda < 25.0$ μm. To confirm this reflectance value, a reflectance measurement was obtained after calibration while the gold disk was still in place. This confirmation was necessary since the gold disk also served as a backing surface. As such, its reflectance value needed to be known accurately. The reflectance of a second backing surface (black surface) was also measured and found to be 0.07.

Having obtained the calibration spectra and the reflectance values of the two backing surfaces, two sets of spectral reflectance measurements were taken for each sample. The first set of measurements was obtained by placing the sample over the measurement port with the gold surface backing it. The second set of measurements was obtained by replacing the gold surface with the black surface. In both cases, the total emittance of the opaque surface

formed by the sample and the backing surface were computed from the spectral reflectance measurements at temperatures ranging from 290 to 300 K.

7.6 Estimation of Emittance and Longwave Transmittance

Consider longwave radiation incident on the surface of a given sample. Assuming the sample is grey, the longwave reflectance, ρ^{lw}, the longwave transmittance, τ^{lw} and the emittance, ε, are related by principle of energy conservation and Kirchoff's law,

$$\rho^{lw} = 1 - \tau^{lw} - \varepsilon \tag{7.1}$$

For an opaque sample, $\tau^{lw} = 0$ and

$$\rho^{lw} = 1 - \varepsilon \tag{7.2}$$

The SOC 400T measures the spectral reflectance of an opaque surface, integrates the spectral data with respect to black body spectrum at a given temperature and computes ε. The value of ρ^{lw} can subsequently be calculated from Equation 7.2.

To estimate ε and τ^{lw} of a diathermanous sample, we resort to the procedure outlined by Christie and Hunter (1984). Christie and Hunter used theory to derive reflectance equations by considering radiation incident on a thin diathermanous film backed by two different surfaces. The system (i.e., the diathermanous film together with the backing surface) reflectance in each case is dependent on the film and the backing surface reflectance values

as well as the film transmittance. Given the reflectance values of the backing surfaces, the film reflectance, ρ^{lw} and the film transmittance, τ^{lw} were obtained as

$$\rho^{lw} = \frac{(\rho_{B1}/\rho_{B2})\rho_{M2} - \rho_{M1}}{(\rho_{B1}/\rho_{B2}) + \rho_{B1}(\rho_{M2} - \rho_{M1}) - 1} \tag{7.3}$$

and

$$\tau^{lw} = \sqrt{\frac{(\rho_{M1} - \rho^{lw})(1 - \rho^{lw}\rho_{B1})}{\rho_{B1}}} \tag{7.4}$$

where ρ_{M1} and ρ_{M2} are the system reflectance values with backing surfaces 1 and 2 in place while ρ_{B1} and ρ_{B2} are the reflectance values of backing surfaces 1 and 2. Having obtained ρ^{lw} and τ^{lw}, ε can be calculation from Equation 7.5:

$$\varepsilon = 1 - \tau^{lw} - \rho^{lw} \tag{7.5}$$

Typical uncertainties associated with the values ρ^{lw}, τ^{lw} and ε were estimated to be ±0.016, ±0.024, and ±0.028, respectively. Details of the uncertainty analysis are discussed in the Appendix B.

Equations 7.4 and 7.5 are subsequently used to calculate the values of τ^{lw} and ε for the shading materials. The following subsections describe the functional dependence of τ^{lw} and ε on A_o for each category of shading material.

7.6.1 Drapery Fabrics

To establish a relationship between ε and A_o, measured values of ε were plotted against $1 - A_o$ as shown in Figure 7.1a. Note that values of A_o were obtained from solar optical measurements (Kotey et al. 2009a). Equation 7.6 is the result of a regression fit (goodness of fit, R-squared = 0.94) obtained from the measured data.

$$\varepsilon = 0.87(1 - A_o) \tag{7.6}$$

The straight line shown in Figure 7.1a represents Equation 7.6. Clearly, there is a strong correlation between ε and $1 - A_o$. The regression fit was set to pass through the origin since in the limit where $A_o \to 1$ (i.e., the fabric disappears) $\varepsilon \to 0$ and Equation 7.6 correctly satisfies this limiting case.

A similar relationship was established between τ^{lw} and A_o by plotting values of $1 - \tau^{lw}$ against $1 - A_o$. See Figure 7.1b. Equation 7.7 is the result of a regression fit (goodness of fit, R-squared = 0.95) obtained from the plot.

$$1 - \tau^{lw} = 0.95\,(1 - A_o) \tag{7.7}$$

Again, there exists a strong correlation between τ^{lw} and A_o as seen in Figure 7.1b. The straight line shown in Figure 7.1b, representing Equation 7.7, passes through the origin since

in the limit where $A_o \to 1$, $\tau^{lw} \to 1$. Substituting $1 - A_o$ from Equation 7.7 into Equation 7.6 gives the desired relationship between ε and τ^{lw}, i.e.,

$$\varepsilon = 0.92\left(1 - \tau^{lw}\right) \tag{7.8}$$

To confirm this relationship, measured values of ε were plotted against $1 - \tau^{lw}$ as shown in Figure 7.1c. A regression fit (goodness of fit, R-squared = 0.99) given by Equation 7.8 was indeed realised. Such a strong correlation further validates the relationships established between longwave properties and openness.

7.6.2 Roller Blinds

The measured values of ε were plotted against $1 - A_o$. See Figure 7.2a. Values of A_o were again obtained from solar optical measurements reported by Kotey et al. (2009b). The best possible regression fit that passes through the origin is given by

$$\varepsilon = 0.91\left(1 - A_o\right) \tag{7.9}$$

To establish a relationship between τ^{lw} and A_o, values of $1 - \tau^{lw}$ were plotted against $1 - A_o$ as shown in Figure 7.2b. Again, a linear regression fit was obtained as given by Equation 7.10.

$$1 - \tau^{lw} = 0.95\left(1 - A_o\right) \tag{7.10}$$

Again, substituting $1 - A_o$ from Equation 7.10 into Equation 7.9 gives the desired relationship between ε and τ^{lw}, i.e.,

$$\varepsilon = 0.96\left(1-\tau^{lw}\right) \tag{7.11}$$

A plot of the values of ε against $1-\tau^{lw}$ fall on the straight line represented by Equation 7.11 and confirms the relationship between ε and τ^{lw}. See Figure Figure 7.2c.

7.6.3 Insect Screens

Once again, values of ε were plotted against $1-A_o$ in order to establish a relationship between ε and A_o. See Figure 7.3a. Values of A_o were again obtained from solar optical measurements reported by Kotey et al. (2009c). For a given range of A_o, it is seen from Figure 7.3a that dark screens showed consistently higher values of ε compared to grey screens. It was therefore logical to distinguish between dark and grey screens in the subsequent analysis.

Two different regression fits deduced from the plots in Figure 7.3a are Equation 7.12 for dark screens and Equation 7.13 for grey screens, i.e.,

$$\varepsilon = 0.93\left(1-A_o\right) \quad \text{(dark screens)} \tag{7.12}$$

$$\varepsilon = 0.32\left(1-A_o\right) \quad \text{(grey screens)} \tag{7.13}$$

Although the regression fits were not ideal, they represented the measured data with reasonable accuracy.

Turning consideration to the relationship between τ^{lw} and A_o, measured values of $1-\tau^{lw}$ were plotted against $1-A_o$ as shown in Figure 7.3b. Again, there was a discernible difference between the data set obtained for dark and grey screens. The correlation between $1-\tau^{lw}$ and $1-A_o$ for dark and grey screens as established by regression fits are given by Equations 7.14 and 7.15, respectively.

$$1-\tau^{lw} = 0.98\left(1-A_o\right) \qquad \text{(dark screens)} \qquad (7.14)$$

$$1-\tau^{lw} = 0.81\left(1-A_o\right) \qquad \text{(grey screens)} \qquad (7.15)$$

The straight lines representing these correlations are also shown in Figure 7.3b.

Finally, it can readily be shown that for dark and grey screens, ε is directly related to τ^{lw} via Equations 7.16 and 7.17, respectively, i.e.,

$$\varepsilon = 0.95\left(1-\tau^{lw}\right) \qquad \text{(dark screens)} \qquad (7.16)$$

$$\varepsilon = 0.40\left(1-\tau^{lw}\right) \qquad \text{(grey screens)} \qquad (7.17)$$

To reaffirm this relationship, values of ε were plotted against $1-\tau^{lw}$ as shown in Figure 7.3c. Again, regression fits established by Equations 7.16 and 7.17 show a strong correlation between ε and τ^{lw}.

7.7 Discussion

The coefficients in Equations 7.6, 7.9, 7.12 and 7.13 may be considered to be the total hemispherical emittance of the structure making up the fabric, the roller blind, the dark screens and the grey screens, respectively. This is because when $A_o = 0$, the emittance of the shading material is simply equal to the emittance of the structure. The measurements show that irrespective of the colour of the fabric, the emittance of the fabric structure may be considered to be constant. The same observation is apparent for the emittance of the roller blind structure. Insect screens, on the other hand, show two distinct structure emittance values depending on the surface finish. The structure emittance of a dark screen is much higher than that of a grey screen.

Table 7.1 summarises the estimated total hemispherical emittance, transmittance and reflectance of the structure of each shading material. Also shown in Table 7.1 are the total normal emittance values of typical opaque surfaces at specified temperatures (Modest 1993, Siegel and Howell 1993, Incropera and DeWitt 2001). For smooth surfaces, the hemispherical emittance can be estimated from the normal emittance values. Materials with high emittance tend to behave like dielectrics and therefore have a hemispherical emittance that is 3 to 5% greater than the normal emittance. On the other hand, metals generally have a hemispherical emittance that is 3 to 10% greater than the normal emittance (Modest 1993, Hollands 2004). Note that the aforementioned conversion factors were not applied since the shading materials generally have rough surfaces and the normal to hemispherical emittance conversion is not applicable.

From the literature survey, it can be seen that a typical fabric made from dyed cloth has a high emittance which is independent of the colour of the dye (paint). Furthermore, roller blinds which are generally made from plastics and paint also have high emittance independent of the colour of the paint. The same observation can be made for the high emittance of dark screens. However, the emittance of grey screens is attributed to the emittance of the stainless steel. Since metals generally have low emittance, the grey stainless steel screens also exhibit low emittance.

Consideration will now turn to the behaviour of longwave transmittance of the shading materials when $A_o = 0$. From Equations 7.7, 7.10, 7.14 and 7.15, it is evident that the τ^{lw} value of a shading material does not necessarily drop to zero under such circumstances. Substituting $A_o = 0$, the aforementioned equations give the τ^{lw} values of the structure. The results are summarised in Table 7.1. The finite value of τ^{lw} when $A_o = 0$ may be attributed to multiple reflections between structural members of each shading material (i.e., yarn, wire, sheet) and subsequent transmission through the interstices of the structure. To further substantiate this argument, the ρ^{lw} value of the structure was estimated from Equation 7.1 given the values of τ^{lw} and ε. The results are also included in Table 7.1. It is clearly seen from Table 7.1 that fabrics, roller materials and dark screens with low values of ρ^{lw} have low values of τ^{lw}. On the other hand, grey screens with relatively high value of ρ^{lw} have a high value of τ^{lw}.

7.8 Conclusions

A method of estimating the longwave radiative properties of flat shading materials like drapery fabrics, roller blinds and insect screens is outlined in this chapter. The method involves the use of a portable infrared reflectometer originally designed to measure the emittance of opaque surfaces. The shading materials considered consists of a structure (i.e., yarn, wire, sheet) that is opaque with respect to longwave radiation and each material is likely to have some openness. It was found that the emittance and longwave transmittance of the materials are simple functions of openness as well as the emittance and longwave transmittance of the structure. The results are particularly useful since openness can be determined from solar transmittance measurements while emittance and longwave transmittance of the structure was found to be constant for each category of shading material.

Table 7.1: Summary of Longwave Properties

Experimental Results				Results from Literature Survey		
Shading Material	**Estimated hemispherical emittance of structure at 300 K**	**Estimated hemispherical transmittance of structure**	**Estimated hemispherical reflectance of structure**	**Opaque surfaces**	**Surface temp (K)**	**Typical total normal emittance**
Fabrics	0.87	0.05	0.08	Paint (all colours)	300	0.92-0.98
Roller blinds	0.92	0.05	0.03	Cloth	293	0.77-0.78
Dark (painted stainless steel) screens	0.93	0.02	0.05	Plastics	291	0.84-0.95
Grey (unpainted stainless steel) screens	0.32	0.19	0.49	Stainless steel (various types)	368	0.27-0.42

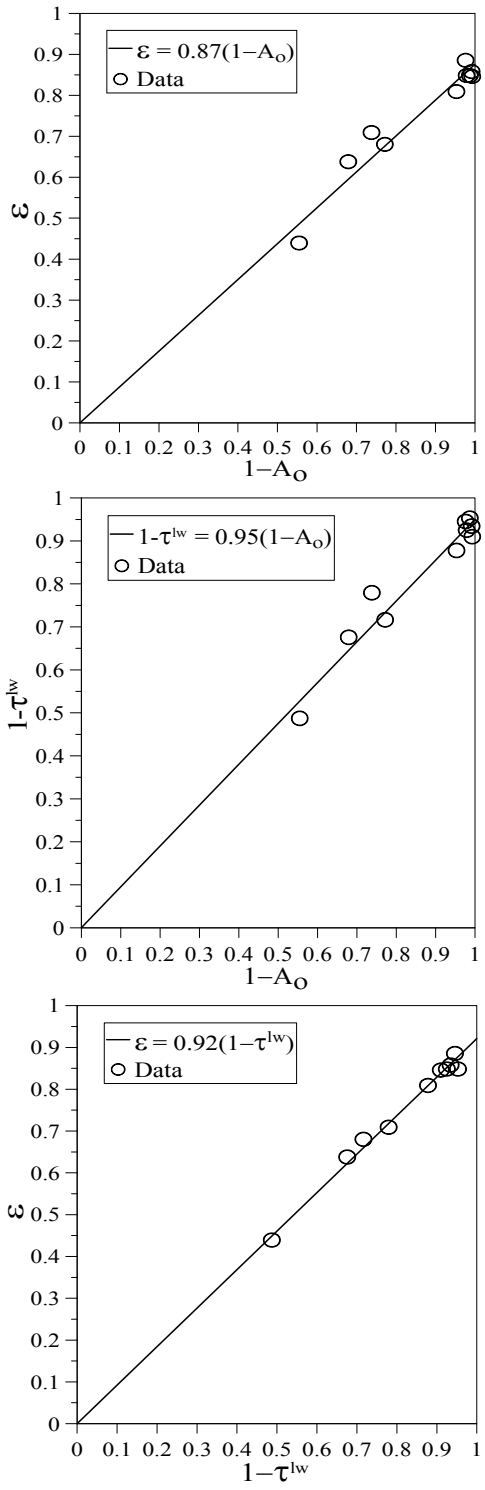

Figure 7.1: Longwave Radiative Properties of Drapery Fabrics (a) ε versus $1 - A_o$ (b) $1 - \tau^{lw}$ versus $1 - A_o$ (c) ε versus $1 - \tau^{lw}$

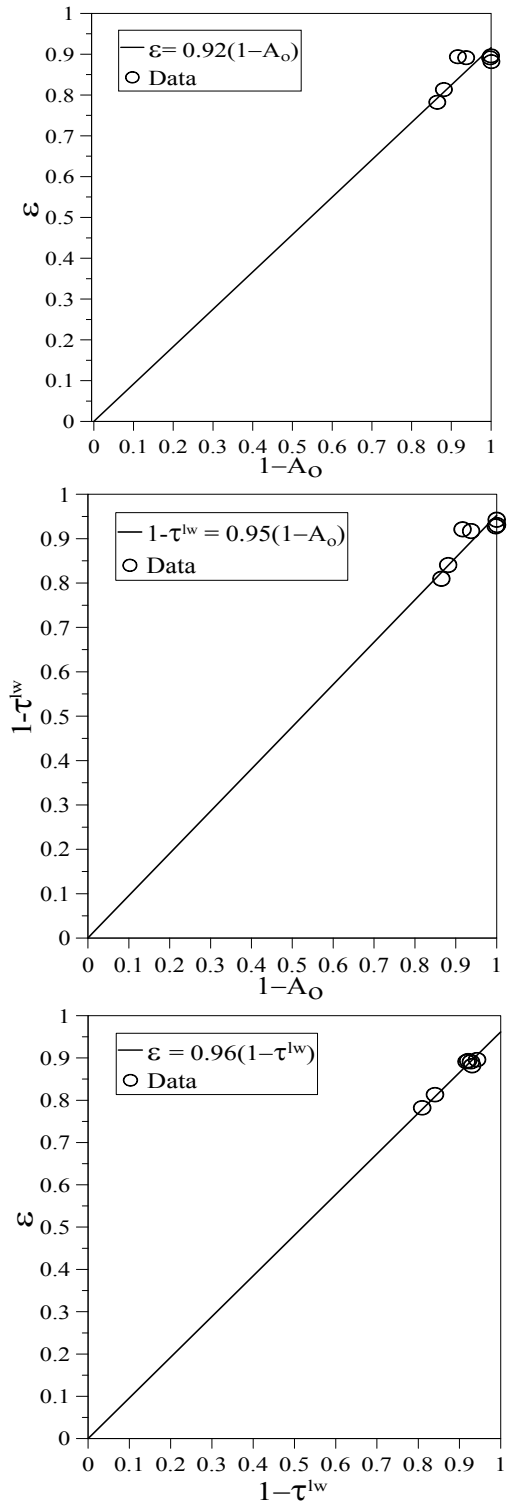

Figure 7.2: Longwave Radiative Properties of Roller Blinds (a) ε versus $1 - A_o$ (b) $1 - \tau^{lw}$ versus $1 - A_o$ (c) ε versus $1 - \tau^{lw}$

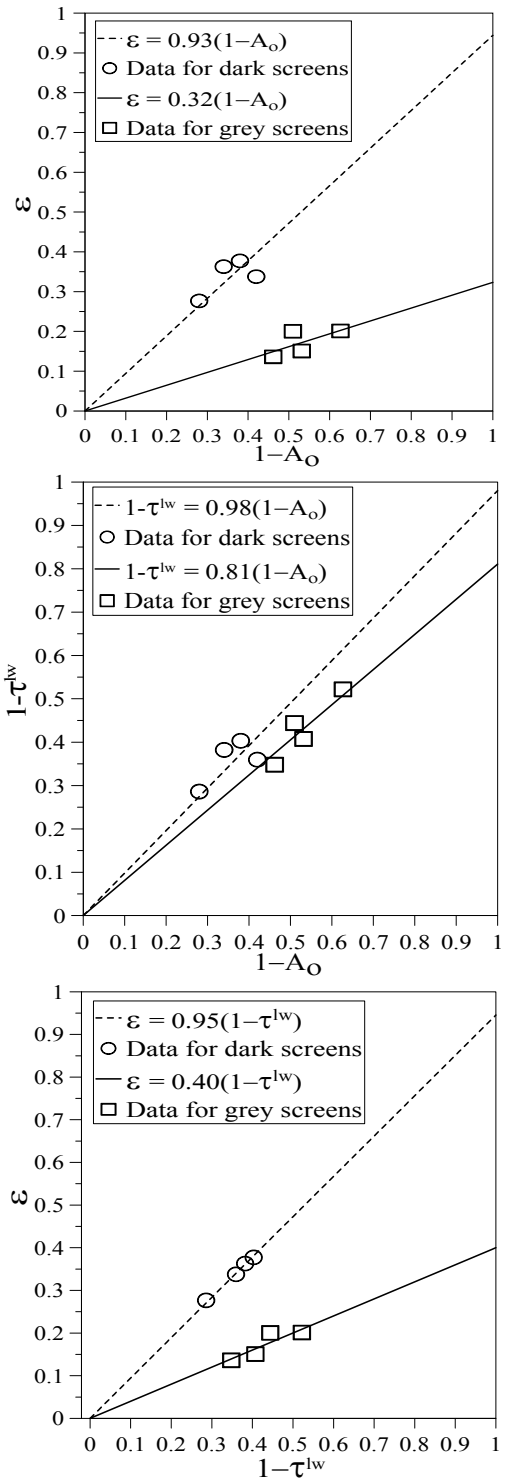

Figure 7.3: Longwave Radiative Properties of Insect Screens (a) ε versus $1 - A_o$ (b) $1 - \tau^{lw}$ versus $1 - A_o$ (c) ε versus $1 - \tau^{lw}$

CHAPTER 8

EFFECTIVE PROPERTIES OF PLEATED DRAPERIES

8.1 Introduction

A detailed model to determine the effective properties of pleated draperies is presented in this chapter. The model approximates a drapery layer as a series of uniformly arranged rectangular pleats. The effective properties of the drapery are then determined by considering a representative enclosure. The effective beam-beam and beam-diffuse solar properties of the pleated drapery are determined by tracking both radiation components, for a given direction of incident solar radiation, through various interactions with the fabric pleats. Angle dependent solar properties of the fabric and the effect of beam and diffuse components, in both reflection and transmission are included in the analysis. The effective diffuse-diffuse solar properties of the pleated drapery are evaluated using a much simpler net-radiation analysis with conventional shape factors to track radiant exchange between surfaces. The effective solar optical model can be applied to fabrics with differing front and back properties. The analysis presented in this chapter is mainly focused on the determination of effective solar properties since effective longwave properties can readily be obtained from the diffuse-diffuse solar model with fabric longwave properties replacing corresponding fabric diffuse-diffuse solar properties. The pleated drapery model therefore offers new possibilities in calculating the effective properties of draperies made with practically any

fabric. The effective properties of pleated draperies are required in the multi-layer analysis to quantify the reduction of solar gain when pleated draperies are attached to windows.

8.2 Previous Studies

Researchers have used several ways to quantify the reduction of solar gain when draperies are present. Keyes (1967), for example, characterised fabrics by yarn colour (yarn reflectance) as dark (D), medium (M), and light (L), and by weave as open (I), semi-open (II), and closed (III). Keyes then developed a chart that expressed measured shading coefficient (SC), defined as the ratio of solar gain through a window to the solar gain through a standard layer of clear glass, as a function of yarn reflectance and weave openness when a drapery was combined with both regular plate and heat-absorbing glass. If the solar optical properties of the fabric are not well known, the Keyes method can still be used to obtain an approximate SC of the glass-drapery combination.

Having acknowledged that fabric colour and weave openness alone were not sufficient to accurately determine the SC of the glass-drapery combination, Moore and Pennington (1967) developed a chart that expressed the SC as a function of fabric solar optical properties. They measured the solar optical properties of fabrics, draperies, and glass-drapery combinations using various techniques. They also measured the SC using a solar calorimeter. Furthermore, they developed equations to calculate the SC using solar optical properties as inputs. The effective solar properties of the drapery were estimated by applying a multiplicative factor to the solar properties of the fabric at normal incidence. This factor accounted for the effect of

folding and the variation of incidence angle. Their calculations agreed well with experimentally determined SC values.

By careful analysis of fabric transmittance and reflectance, yarn reflectance, and openness factor, Keyes (1967) was able to reconcile the yarn reflectance-openness chart with the fabric reflectance-transmittance chart. The Keyes (1967) universal chart is the basis of the interior attenuation coefficient (IAC) data for glass-drapery combinations found in the *2005 ASHRAE Handbook—Fundamentals* (ASHRAE 2005). This chart correlates measured optical properties with eye-observed values to determine the IAC, thus making it a convenient tool for designers. However, optical properties measurements carried out by Moore and Pennington (1967) revealed that the solar properties could differ from the visible properties. In such situations, using visual judgment to predict shading effects could give inaccurate results.

The first attempt to quantify the cumulative effect of folding (or pleating) and the directional nature of incident radiation on the solar gain through draperies was carried out by Ozisik and Schutrum (1960). To determine the effectiveness of 100% fullness draperies (width of drapery is twice the width of fabric) in reducing solar gain, Ozisik and Schutrum tested draperies of different fabrics in combination with regular and heat-absorbing glass using a solar calorimeter. Their results were presented in terms of the solar heat transfer factor, K, defined as the ratio of the solar gain to insolation. Note that K is identical to the solar heat gain coefficient (SHGC) currently used. They showed that K was independent of incidence angle for incidence angles ranging from 0° to 50°. For incidence angles greater than 50°, they

suggested a decrease in K by 10% for each 10° increase in incidence angle. They also proposed a reduction of 10% in K for incident diffuse radiation. Furthermore, they presented the variation of K with solar optical properties of fabrics at normal incidence and observed that the reflectance was the dominant property influencing solar gain. In addition to the solar gain tests, they performed a series of tests to investigate the effect of pleating on the solar optical properties of draperies. They measured the angular transmittance and reflectance of both fabrics and draperies with a pyrheliometer. Their results showed that the transmittance of the drapery at normal incidence was almost the same as that of the fabric. However, at 45° incidence, the transmittance of the drapery was 20% lower. For incident diffuse radiation, both transmittance and reflectance of the drapery were 20% lower than the fabric values.

Yellot (1965) determined experimentally the solar heat gain factor (SHGF), defined as solar gain through a standard clear glass, and the SC of draperies using an outdoor solar calorimeter. He also measured the solar optical properties of fabrics as well as glass-fabric combinations using a custom-made instrument. The measurements were taken at incidence angles ranging from 26° to 90°. His experiments showed that the SHGF for a typical glass-fabric combination decreased as the incidence angle increased, although the SC remained nearly constant. To explore the effects of varying surface solar azimuth on reflectance, Yellot used a reflectometer to measure the reflectance of a typical light coloured fabric and drapery. His results showed that although the reflectance of both fabric and drapery varied with surface solar azimuth, there was very little difference between the two reflectances for a given surface solar azimuth.

The results of the preceding studies (Keyes 1967; Moore and Pennington 1967; Ozisik and Schutrum 1960; Yellot 1965) are useful in predicting the solar gain through windows with draperies. However, they were limited to single-glazed windows.

Few data can be found in the literature for comparison against results of the current research. The work of Farber et al. (1963) is of particular interest because it includes a model to determine the effective solar optical properties of draperies using a simplified rectangular configuration. Farber et al. (1963) assumed that the fabric is diffusely reflecting and diffusely transmitting, and that the reflectance and transmittance for beam radiation vary with incidence angle. Their calculation involved a separate treatment of the front and the cavity portions of the pleated drapery with the front portion having the same optical properties as the fabric. The solutions of the cavity portion and the front portion were averaged to give the effective optical property of the drapery. Farber et al. used results published by Sparrow and Johnson (1962) to estimate the apparent (i.e., effective) reflectivity of the cavity portion of the drapery, noting that these results were obtained by means of "long and tedious numerical computer techniques."

It was also asserted, without explanation, that the abnormal transmittance of the pleated drapery follows the same pattern as the abnormal reflectance. In addition, examining the work of Sparrow and Johnson (1962), it can be seen that the reflectance of the cavity portion of the drapery (with respect to beam insolation) was estimated on the assumption that each groove is infinitely deep. However, by examining Figure 7 of Sparrow and Johnson (1962), it

is apparent that this assumption is not valid. Pennington et al. (1964), while using the model of Farber et al. to compare against measurements, mention that:

"If a zero deg horizontal projection angle had been assumed for the rectangular configuration of the theoretical analysis, then the curves of absorptance, reflectance and transmittance versus incidence angle would have been identical to that of a flat drapery."

This statement offers additional insight regarding the limitations of the Farber et al. model. The Farber et al. model is unable to account for the effect of pleating when solar radiation is incident normal, or near normal, to the window. To validate the theoretical analysis carried out by Farber et al. (1963), Pennington et al. (1964) performed a series of experiments with an outdoor solar calorimeter. They used a pyrheliometer installed in the calorimeter to measure the solar optical properties of fabrics, draperies, and glass-drapery combinations at various incidence (or profile) angles. Regarding the results for pleated draperies, Pennington et al. note that:

"In general, the two methods show good agreement on transmittance. Their agreement, however, on reflectance and absorptance leaves much to be desired."

These discrepancies are not surprising given the range of assumptions used by Farber et al. and the method used to account for the interaction of solar radiation with the groove portion of the drapery. These researchers were clearly hampered by limitations in theory and computational power available at the time. Nonetheless, calculated results from Farber et al. (1963) are subsequently presented and compared with the model developed in this chapter.

A recent study by Kotey et al. (2007) modeled a drapery layer as a series of rectangular pleats with diffusely transmitting and diffusely reflecting fabric. The model presented in Kotey et al. (2007) assumed that the fabric solar optical properties were independent of the angle of incidence and did not allow for direct beam transmission of solar radiation through openings in the fabric. The effective solar optical properties of the drapery were then determined as a function of drapery geometry and solar profile angle. This simplified approach has been extended in this chapter to include several additional effects. In particular, the pleated drapery model presented here makes use of fabric properties that are determined as a function of incidence angle, these properties include detail regarding beam and diffuse components of reflection and transmission. It is assumed that these properties are available with respect to both beam and diffuse insolation. The methods for determining all of these fabric solar properties have been developed in Chapters 3 and 4.

8.3 Modeling

The effective solar optical properties of a drapery are dependent on many things, including the colour of the yarn, the openness of the fabric, the pleat geometry, and the direction of the incident solar radiation. The model presented in this chapter was developed in an attempt to account for all of these influences. Pleat geometry is approximated as rectangular and self shading and, along with the directional characteristics of the fabric, has an important influence on the effective properties of the pleated drape. The solar properties of a fabric are dependent on the openness of the weave as well as the colour of the yarn and the directional nature of the incoming radiation. For a given fabric, experiments show that the solar optical

properties pertaining to beam radiation at off-normal incidence can be determined using properties measured at normal incidence. Solar optical properties pertaining to incident diffuse radiation can also be determined. Details of the experimental procedure and the resulting fabric property models are given in Chapters 3 and 4, respectively.

8.3.1 Drape Geometry and Solar Angles

A drapery consists of a series of fabric pleats that are non-uniform. Similar to the approach used by Farber et al. (1963), rectangular pleats have been used as an approximation. See Figure 8.1. Consider beam radiation incident on the drapery. The interception of the beam radiation by fabric surfaces is dependent on the angle of incidence, θ. In addition, the perpendicular surfaces of the drapery can produce considerable blockage. The blockage is influenced by pleat geometry and horizontal profile angle, Ω_H (equivalent to the surface solar azimuth). The fabric properties are also influenced by (local) incidence angle so the vertical profile angle, Ω_V, also comes into play. The relationship between θ, Ω_H, and Ω_V is well documented (e.g., ASHRAE 2005). For fabric surfaces parallel and perpendicular to the window, it can be shown that

$$\cos(\theta_{PARL}) = \cos\left(\tan^{-1}(\tan\Omega_V \cos\Omega_H)\right) \cdot \cos\Omega_H \tag{8.1}$$

and

$$\cos(\theta_{PERP}) = \cos\left(\tan^{-1}(\tan\Omega_V \sin\Omega_H)\right) \cdot \sin\Omega_H \tag{8.2}$$

where θ_{PARL} and θ_{PERP} are the incidence angles on the parallel and perpendicular surfaces, respectively.

Since the pleats are repetitive, an enclosure formed by two consecutive pleats will represent the entire drapery. A cross-section of such an enclosure is shown in Figure 8.2a. The representative enclosure is made up of two sub-enclosures with pleat width, w, and pleat spacing, s. Fictitious surfaces at the front and back openings complete the enclosure.

The solar optical properties of the drapery are influenced by pleat geometry, which can be described in terms of folding ratio, Fr, or percent fullness. The folding ratio is defined as the total length of the fabric divided by the length of the drapery, L. When the length of the fabric is twice that of the drapery, Fr = 2, the drapery is described as having 100% fullness. Figure 8.2 shows draperies with different values of Fr and fullness. The geometry of Figure 8.2 gives Fr = 1 + w / s.

8.3.2 Solar Optical Properties of Fabric

Solar optical properties of a fabric are determined by considering what happens when beam or diffuse radiation is incident on the fabric. For radiation incident on the front surface of the fabric, the properties pertaining to transmittance are the front beam-beam transmittance, $\tau^{m}_{f,bb}$, the front beam-diffuse transmittance, $\tau^{m}_{f,bd}$, and the front diffuse-diffuse transmittance, $\tau^{m}_{f,dd}$. The sum of $\tau^{m}_{f,bb}$ and $\tau^{m}_{f,bd}$ gives the front beam-total transmittance, $\tau^{m}_{f,bt}$. The superscript m is used to designate a fabric (i.e., material) property as opposed to

the corresponding effective solar optical property of the pleated drapery. Similarly, the properties pertaining to reflectance are the front beam-beam reflectance, $\rho^{m}_{f,bb}$, the front beam-diffuse reflectance, $\rho^{m}_{f,bd}$ and the front diffuse-diffuse reflectance, $\rho^{m}_{f,dd}$. However, $\rho^{m}_{f,bb}$ is assumed to be zero and hence the front beam-total reflectance, $\rho^{m}_{f,bt}$ is equal to $\rho^{m}_{f,bd}$. The corresponding properties for radiation incident on the back surface of the fabric are designated by replacing subscript f in the aforementioned nomenclature with subscript b. Refer to Chapters 3 and 4 for more detail.

8.3.3 Incident Beam Radiation

Beam radiation incident on a drapery is transmitted undisturbed through fabric openings or, after multiple reflections, emerges in the forward direction as beam-diffuse transmission and in the backward direction as beam-diffuse reflection. To simplify the calculation, beam-beam transmission is considered only when beam radiation is incident on the fabric for the first time. Subsequent transmission of incident beam radiation is considered to be diffuse. This simplification is reasonable since multiple transmissions of beam radiation will entail incidence on alternating parallel or perpendicular surfaces, and one of the two (or both) incidence angles is likely to be high. At such high incidence angles, fabric beam-beam transmittance is small and the overall beam transmission will be very small.

Note that the following sections include diagrams that show only positive values of profile angle, Ω_H. Recognizing the symmetry of the pleated drapery it is apparent that the same effective properties should be obtained for positive or negative values of Ω_H. In fact, the models presented include only the absolute value of Ω_H and because of this apply to all values of Ω_H ranging from -90° to +90°.

8.3.4 Effective Beam-Beam Solar Optical Properties of Drapery

Consider beam radiation incident on the front (i.e., outdoor facing surface) of the drapery. The front beam-beam reflectance of the drapery, $\rho_{f,bb}$, is zero, and the front beam-beam transmittance, $\tau_{f,bb}$, can be determined by considering the three cases shown in Figure 8.3. The different cases are realized by considering the length of the illuminated portion of the bottom sub-enclosure, bc, relative to the width of drapery, w.

Case I ($bc \leq w$; $bc \leq ab$)

The value of Ω_H is such that surface bc is illuminated directly by incident beam radiation. Surface de is illuminated indirectly by beam radiation passing through fabric surface cd. The length of surface de is equal to the length of surface bc. Note that because of the repetitive nature of the pleats, illuminated surface bc at the bottom sub-enclosure is the same as the illuminated surface bc at the top sub-enclosure. Furthermore, incident beam radiation passing through surface bc illuminates surface ef. Since surfaces de and ef are

illuminated by beam radiation that has passed through the fabric at least once, subsequent transmission of beam radiation through de and ef is considered to be diffuse. No beam radiation passes through the drapery for this case so $\tau_{f,bb} = 0$. The condition of $\tau_{f,bb} = 0$ continues to hold as the length of bc increases until bc becomes equal to ab.

Case II ($bc \leq w$; $bc > ab$)

As Ω_H decreases and surface bc lengthens, a portion of the beam radiation passing through surface bc emerges from fictitious surface ag (see top sub-enclosure, Figure 8.3, Case II). The value of $\tau_{f,bb}$ is proportional to the ratio of the distance, s_1, and the width $2 \cdot s \cdot \cos\Omega_H$, which represents the area of incident radiation. Since the outgoing beam radiation passes through surface bc before leaving the enclosure, its strength is reduced by $\tau^m_{f,bb}$ of surface bc. Thus,

$$\tau_{f,bb} = \frac{s_l}{2 \cdot s \cdot \cos\Omega_H} \cdot \tau^m_{f,bb}(\theta_{PERP}) \tag{8.3}$$

It can be shown that

$$\tau_{f,bb} = \frac{(bc - eg) \cdot \sin|\Omega_H|}{2 \cdot s \cdot \cos\Omega_H} \cdot \tau^m_{f,bb}(\theta_{PERP}) \tag{8.4}$$

where

$$bc = s\left|\frac{\cos\Omega_H}{\sin\Omega_H}\right| \tag{8.5}$$

and

$$eg = w - bc \tag{8.6}$$

The condition for one-pass beam-beam transmission continues to hold as Ω_H decreases and as bc increases until bc becomes equal to w.

Case III (bc > w)

When surface bc is greater than w, more beam radiation emerges from the enclosure, as shown in Figure 8.3, Case III. For the top sub-enclosure, beam radiation emerges from fictitious surface ag, some having passed through fabric surfaces ac and some through cd. For the bottom sub-enclosure, beam radiation is directly transmitted through fabric surface am. Note that the strength of the beam radiation on areas s_2, s_3 and s_4 are reduced by $\tau_{f,bb}^m$. Fabric surfaces cd and ag are both parallel to the window with $\tau_{f,bb}^m(\theta) = \tau_{f,bb}^m(\theta_{PARL})$, whereas fabric surface ac is perpendicular to the window with $\tau_{f,bb}^m(\theta) = \tau_{f,bb}^m(\theta_{PERP})$. The value of $\tau_{f,bb}$ in this case is given by

$$\tau_{f,bb} = \frac{s_2 \cdot \tau_{f,bb}^m(\theta_{PERP}) + (s_3 + s_4) \cdot \tau_{f,bb}^m(\theta_{PARL})}{2 \cdot s \cdot \cos\Omega_H} \tag{8.7}$$

which can be expressed as

$$\tau_{f,bb} = \frac{2 \cdot (bc - w) \cdot \sin|\Omega_H| \cdot \tau_{f,bb}^m(\theta_{PARL}) + \left(s \cdot \cos\Omega_H - (bc - w) \cdot \sin|\Omega_H|\right) \cdot \tau_{f,bb}^m(\theta_{PERP})}{2 \cdot s \cdot \cos\Omega_H} \tag{8.8}$$

8.3.5 Beam-Diffuse Solar Optical Properties of Drapery

Beam radiation that is intercepted by yarn and then emerges as transmitted or reflected diffuse radiation can be traced as shown in Figure 8.4. As seen in the previous section, the calculation can be subdivided into three cases, depending on the value of Ω_H . In all, a total of ten different surfaces can be realized between the three cases, although a minimum of seven and a maximum of nine surfaces are actually needed to analyze an individual case.

The radiant analysis can be performed with the following definitions in mind:

J_i = radiosity of surface i

G_i = irradiance at surface i

$Z_{i,bb}$ = flux of beam radiation from surface i caused by beam insolation

$Z_{i,bd}$ = flux of diffuse radiation from surface i caused by beam insolation

The following equations are applied:

$$J_{1b} = \rho^{m}_{b,dd} G_{1b} + \tau^{m}_{f,dd} G_{1f} \tag{8.9}$$

$$J_{2b} = Z_{2b,bd} + \rho^{m}_{b,dd} G_{2b} + \tau^{m}_{f,dd} G_{2f} \tag{8.10}$$

$$J_{3b} = Z_{3b,bd} + \rho^{m}_{b,dd} G_{3b} \tag{8.11}$$

$$J_{4b} = Z_{4b,bd} + \rho^{m}_{b,dd} G_{4b} + \tau^{m}_{f,dd} G_{4f} \tag{8.12}$$

$$J_{5b} = Z_{5b,bd} + \rho^{m}_{b,dd} G_{5b} + \tau^{m}_{f,dd} G_{5f} \tag{8.13}$$

$$J_{6b} = \rho^{m}_{b,dd} G_{6b} + \tau^{m}_{f,dd} G_{6f} \tag{8.14}$$

$$J_{1f} = \rho^{m}_{f,dd} G_{1f} + \tau^{m}_{b,dd} G_{1b} \tag{8.15}$$

$$J_{2f} = Z_{2f,bd} + \rho^{m}_{f,dd} G_{2f} + \tau^{m}_{b,dd} G_{2b} \tag{8.16}$$

$$J_{4f} = Z_{4f,bd} + \rho^{m}_{f,dd} G_{4f} + \tau^{m}_{b,dd} G_{4b} \tag{8.17}$$

$$J_{5f} = Z_{5f,bd} + \rho^{m}_{f,dd} G_{5f} + \tau^{m}_{b,dd} G_{5b} \tag{8.18}$$

$$J_{6f} = \rho^{m}_{f,dd} G_{6f} + \tau^{m}_{b,dd} G_{6b} \tag{8.19}$$

$$J_{7f} = \rho^{m}_{f,dd} G_{7f} \tag{8.20}$$

$$J_{8f} = Z_{8f,bd} + \rho^{m}_{f,dd} G_{8f} \tag{8.21}$$

Surfaces not illuminated by beam radiation do not generate a diffuse source term and, hence, Z_{bd} is zero for those surfaces. Also, the radiosities of the two fictitious surfaces ag and cd (i.e., J_{9b} and J_{10f}) are zero. It can be shown that for a given incident beam flux, I_{beam}, the beam source terms after first transmission through fabric surfaces bc and cd are as follows:

$$Z_{2b,\,bb} = \tau^{m}_{f,\,bb}(\theta_{PERP}) \cdot \frac{s}{bc} I_{beam} \tag{8.22}$$

$$Z_{3b,\,bb} = \tau^{m}_{f,\,bb}(\theta_{PARL}) \cdot I_{beam} \tag{8.23}$$

Similarly, the diffuse source terms from fabric surfaces due to I_{beam} are as follows:

$$Z_{2b,\,bd} = \tau^{m}_{f,\,bd}(\theta_{PERP}) \cdot \frac{s}{bc} I_{beam} \tag{8.24}$$

$$Z_{3b,bd} = \tau^{m}_{f,bd}(\theta_{PARL}) \cdot I_{beam} \tag{8.25}$$

$$Z_{4b,bd} = Z_{3b,bb} \cdot \rho^{m}_{b,bt}(\theta_{PERP}) \cdot \frac{s}{bc} \tag{8.26}$$

$$Z_{5b,\,bd} = Z_{2b,\,bb} \cdot \rho^{m}_{b,\,bt}(\theta_{PERP}) \tag{8.27}$$

$$Z_{2f,bd} = \rho^{m}_{f,bt}(\theta_{PERP}) \cdot \frac{s}{bc} I_{beam} \tag{8.28}$$

$$Z_{4f,bd} = Z_{3b,bb} \cdot \tau^{m}_{b,bt}(\theta_{PERP}) \cdot \frac{s}{bc} \tag{8.29}$$

$$Z_{5f,bd} = Z_{2b,bb} \cdot \tau^{m}_{b,bt}(\theta_{PERP}) \tag{8.30}$$

The diffuse irradiance on each surface of the top or bottom sub-enclosure is given by

$$G_i = \sum_j F_{ij} J_j \tag{8.31}$$

The view factor, F_{ij}, is the fraction of diffuse radiation leaving surface i that is intercepted by surface j. The values of F_{ij} can be determined by Hottel's crossed string rule (e.g., Hollands (2004)). Since all of the surfaces are flat, $F_{ii} = 0$. Likewise, F_{ij} from one surface to another surface on the same fabric segment is zero. Note that subscripts i and j are applied to the given number of surfaces in each sub-enclosure for each particular case considered. For example, the irradiance on back of surface ac of the top sub-enclosure for Case III will be

$$G_{2b} = F_{2b2b}J_{2b} + F_{2b3b}J_{3b} + F_{2b4b}J_{4b} + F_{2b9b}J_{9b} \tag{8.32}$$

Equations 8.9 to 8.31 apply to all the cases shown in Figure 8.4. Consideration will now turn to each specific case.

Case I ($bc \leq w$; $bc \leq ab$)

As shown in Figure 8.4, Case I, beam radiation incident on surface bc is transmitted and reflected diffusely into the enclosure. In addition, beam radiation is transmitted diffusely through fabric surface cd. A portion of the beam radiation incident on surfaces bc and cd is transmitted directly and subsequently falls on surfaces ef and de, respectively, where it gets transmitted and reflected diffusely. Since surfaces ab, ag, and fg are shaded, no

beam-to-diffuse conversion exists at these locations. Diffuse radiation in the enclosure is transmitted and reflected diffusely by all fabric surfaces. From the definitions of J, G, and Z_{bd}, a complete radiant analysis can be performed for beam-diffuse radiation using Equations 8.9 to 8.20 with the appropriate diffuse source terms specified in Equations 8.24 to 8.30. The radiosity-irradiance equation set so obtained is linear and can be solved by matrix reduction for any given I_{beam}. However, with I_{beam} set to unity, the values of $\tau_{f,bd}$ and $\rho_{f,bd}$ can be calculated as

$$\tau_{f,bd} = \frac{sG_{9b} + s\tau_{f,dd}^{m} G_{7f}}{2sI_{beam}} \tag{8.33}$$

which simplifies to:

$$\tau_{f,bd} = \frac{G_{9b} + \tau_{f,dd}^{m} G_{7f}}{2} \tag{8.34}$$

and

$$\rho_{f,bd} = \frac{s\rho_{f,bt}^{m}(\theta_{PARL})\, I_{beam} + s\tau_{b,dd}^{m} G_{3b} + sG_{10f}}{2s\, I_{beam}} \tag{8.35}$$

which simplifies to

$$\rho_{f,bd} = \frac{\rho_{f,bt}^{m}(\theta_{PARL}) + \tau_{b,dd}^{m} G_{3b} + G_{10f}}{2} \tag{8.36}$$

Case II ($bc \leq w$; $bc > ab$)

As Ω_H decreases, the length of the directly illuminated surface bc increases, and the length of the indirectly illuminated surface de also increases. A portion of the beam radiation passing through surface bc escapes the enclosure through fictitious surface ag, thus leaving a smaller portion of beam radiation to fall on surface eg, as shown in Figure 8.4, Case II. Surface dg therefore becomes completely illuminated, while surfaces ab and ag remain shaded. A radiant analysis can be performed with the relevant equations extracted from Equations 8.9 to 8.20 with the corresponding diffuse source terms as specified in Equations 8.24 to 8.30. The set of linear equations generated can be solved by matrix reduction again with I_{beam} set to unity. Again, the values of $\tau_{f,bd}$ and $\rho_{f,bd}$ are calculated using Equations 8.34 and 8.36, respectively.

Case III ($bc > w$)

When surface bc becomes greater than w, surfaces ac and dg become completely illuminated by beam radiation. A portion of fabric surface ag, (i.e., surface $8f$) is also illuminated directly by beam radiation. The only surface that is shaded is mg. A significant portion of the beam radiation passing through fabric surfaces ac and cd and fictitious surface cd escapes the enclosure as beam radiation. With the relevant relations extracted from Equations 8.9 to 8.21 and the appropriate diffuse source terms as specified in Equations

8.24 to 8.30, the set of linear equations so generated can be solved. Again, with I_{beam} set to unity, the value of $\tau_{f,bd}$ is calculated as

$$\tau_{f,bd} = \frac{s\ G_{9b} + \tau^{m}_{f,dd} \cdot (gm \cdot G_{7f} + am \cdot G_{8f}) + am \cdot \tau^{m}_{f,bd}(\theta_{PARL})}{2} \tag{8.37}$$

where

$$gm = w\left|\frac{\sin\Omega_H}{\cos\Omega_H}\right| \tag{8.38}$$

and

$$am = s - gm \tag{8.39}$$

Likewise, the value of $\rho_{f,bd}$ can be calculated from Equation 8.36.

8.3.6 Diffuse-Diffuse Solar Optical Properties of Drapery

Consider diffuse radiation, I_{diff}, incident on the front of the drapery layer. See Figure 8.5. Diffuse radiation within the enclosure remains diffuse as it interacts with the surfaces before finally emerging in the forward (transmission) and backward (reflection) direction. The values of $\tau_{f,dd}$ and $\rho_{f,dd}$ can be determined by considering the representative geometry (w and s). In this particular situation, the calculations are independent of θ and Ω_H. The following equations are applied:

$$J_{2b} = \rho^{m}_{b,dd} G_{2b} + \tau^{m}_{f,dd} G_{2f} \tag{8.40}$$

$$J_{3b} = \tau^{m}_{f,dd} I_{diff} + \rho^{m}_{b,dd} G_{3b} \tag{8.41}$$

$$J_{4b} = \rho^{m}_{b,dd} G_{4b} + \tau^{m}_{f,dd} G_{4f} \tag{8.42}$$

$$J_{2f} = \rho^{m}_{f,dd} G_{2f} + \tau^{m}_{b,dd} G_{2b} \tag{8.43}$$

$$J_{4f} = \rho^{m}_{f,dd} G_{4f} + \tau^{m}_{b,dd} G_{4b} \tag{8.44}$$

$$J_{8f} = \rho^{m}_{f,dd} G_{8f} \tag{8.45}$$

The radiosity of fictitious surface cd is $J_{10f} = I_{diff}$, while the radiosity of fictitious surface ag is $J_{9b} = 0$. The irradiance on each surface of either sub-enclosure can be calculated using Equation 8.31, with the subscripts i and j applied to the given number of surfaces in that sub-enclosure. Once again, Equations 8.40 to 8.45 are linear and can be solved by matrix reduction with I_{diff} set to unity. The values of τ_{dd} and $\rho_{f,dd}$ are as follows:

$$\tau_{dd} = \frac{G_{9b} + \tau^{m}_{f,dd} G_{8f}}{2} \tag{8.46}$$

$$\rho_{f,dd} = \frac{\rho^{m}_{f,dd} + \tau^{m}_{b,dd} G_{3b} + G_{10f}}{2} \tag{8.47}$$

8.3.7 Back Solar Optical Properties of Drapery

In the preceding sections, models were described for the calculation of front effective solar optical properties of a pleated drape. The corresponding back-surface properties can be calculated using the same models by interchanging the front and back fabric properties.

8.3.8 Longwave Radiative Properties of Drapery

Longwave radiative properties of a drapery are calculated using the diffuse-diffuse solar optical properties model. First, fabric diffuse-diffuse solar properties in Equations 8.40 to 8.45 are replaced with the corresponding fabric longwave properties and the set of equation solved by matrix reduction. The effective longwave properties of the pleated drapery are subsequently obtained from Equations 8.46 and 8.47 by replacing diffuse-diffuse solar properties with the corresponding longwave properties. The method for determining fabric longwave properties is outlined in Chapter 7 and also documented in Kotey et al. (2008).

8.4 Results and Discussion

8.4.1 The Present Model

Nominal property data for the nine fabric designations presented in Keyes's chart (Keyes 1967; ASHRAE 2005) were obtained from Keyes (1967). These data are listed in Table 8.1. It is assumed that front and back properties are equal, so the subscripts f and b have been dropped for simplicity. At normal incidence, $\tau_{bb}^{m}(\theta = 0)$ is equivalent to the openness

factor, A_o (Keyes 1967). The value of $\tau_{bd}^{m}(\theta = 0)$ corresponds to radiation redirected by the yarn in the forward direction. The sum of the two, the total transmittance of the fabric, $\tau_{bt}^{m}(\theta = 0)$, corresponds to the vertical axis in Keyes's chart. As expected, the closed-weave fabrics have negligible τ_{bb}^{m}, while the open and semi-open weave fabrics allow some beam-beam transmission. Furthermore, in each openness category, the light-coloured fabrics have the highest ρ_{bt}^{m} followed by the medium-coloured fabrics while the dark-coloured fabrics have the lowest ρ_{bt}^{m}.

The effective solar properties of the drapery were calculated for both incident beam and incident diffuse radiation. The results are shown in Figure 8.6, grouped into open-weave (I), semi-open-weave (II), and closed-weave (III) categories. Subgroupings show transmittance and reflectance for light (L), medium (M), and dark (D) coloured draperies. Figure 8.6a shows the variation of the τ_{dd} and ρ_{dd} with Fr for all nine fabric designations. Note that for w = 0 (Fr = 1), the drape is flat and the effective properties of the drape correspond to the properties of the fabric.

It can be seen that τ_{dd} for draperies with open and semi-open fabrics decreases with increasing Fr while the value of τ_{dd} for draperies with closed weave fabrics remains nearly constant. This trend is found in all three colour designations. It is to be expected that pleating will consistently decrease solar transmission because there is more opportunity for

radiation to be absorbed in the fabric because of the inter-reflection that arises if the fabric can view itself.

The calculated ρ_{dd} data reveal another interesting phenomenon. For open weave, light coloured drapery (I_L), pleating causes ρ_{dd} to increase at Fr < 3. Again, this is due to self-viewing. Some of the radiation that passes through the front surface of the drape (fabric surface cd) will encounter one of the perpendicular surfaces (dg or ac) where a portion will transmit to the adjacent cavity and a portion of this radiation will exit through the opening (fictitious surface cd), either directly or by intermediate reflection. This effect is most prevalent in fabrics with higher values of A_o and yarn reflectance. Open weave, medium coloured drapery (I_M) shows a slight decrease in ρ_{dd} while for open weave, dark coloured drapery (I_D) ρ_{dd} remains almost constant at a small value. For semi-open and closed weaved draperies, ρ_{dd} decreases with increasing Fr irrespective of the colour of the drapery.

Now consider the effect of Ω_H on the solar properties of draperies. To investigate this effect Ω_V was fixed at zero and Fr = 2 (100% fullness) was chosen. The results are shown in Figure 8.6b. Clearly, τ_{bb} for open and semi-open weave draperies always decreases with increasing Ω_H. At $\Omega_H = 63.4°$, the cutoff angle that marks the transition from Case II to Case III for the 100% fullness drapery, τ_{bb} is completely eliminated. An increase in Ω_H beyond this cutoff angle results in only beam-diffuse transmission through the drapery. It should be noted that a small amount of beam-beam transmission through a drapery would be

realised with Ω_H greater than the cutoff angle if multiple beam-beam transmissions through the fabric pass were considered. For closed weave drapes (type III) $\tau_{bb}^{m}(\theta = 0) \approx 0$ and τ_{bb} is very close to zero for all values of Ω_H. Generally τ_{bd} for open weave drapery (type I) shows a weak increase to a local maximum at the cutoff angle and then decreases as Ω_H increases further. On the other hand, τ_{bd} for semi-open and closed weave drapery (type II and III) decreases gradually with an increase in Ω_H over the full range of Ω_H.

Turning to the variation of ρ_{bd} with Ω_H, note that draperies in all nine fabric designations exhibit an increase in ρ_{bd} as Ω_H increases. This increase in ρ_{bd} happens for two reasons. First, the solar reflectance of the exposed front surface of the drapery, surface 3f, increases as Ω_H increases. Second, as Ω_H increases the illuminated portion of the lower cavity, surface 2f, moves closer to the front face of the pleated drapery and more of the solar radiation reflected from this section of fabric will exit through the front opening as reflection from the pleated drapery.

8.4.2 Comparison with Farber et al. Model

Farber et al. (1963) produced curves of effective reflectance versus Fr for incident diffuse radiation. Figure 8.7a shows curves reproduced from Farber et al. (1963) for values of ρ_{dd}^{m} ranging from 0.1 to 0.5. Since no information was given to the contrary, it is assumed that these fabrics were opaque. The curves clearly show a decrease in ρ_{dd} as Fr increases. This

is the expected trend for fabrics with low solar transmittance. The curves also show that the higher the value of ρ_{dd}^{m}, the stronger the influence of Fr. Results generated with the present model, Figure 8.7b, compare favourably with Figure 8.7a. Both models predict $\rho_{dd} = \rho_{dd}^{m}$ at Fr = 1 which corresponds to a pleatless (flat) drape. At high values of Fr, the present model predicts slightly lower values of ρ_{dd} especially for fabrics with high values of ρ_{dd}^{m}. In general, and particularly for the most practical cases at $Fr \leq 2$, the agreement is very good.

Now compare the two models for incident beam radiation. Farber et al. generated curves of effective transmittance and absorptance for 100% fullness drapery versus θ. They considered three different shades of drapery; dark coloured (tan), medium coloured (grey) and light coloured (white). The solar optical properties of the three shades of fabric at normal incidence are summarised in Table 8.2. The transmittance and reflectance values shown in Table 8.2 should be interpreted as $\tau_{bt}^{m}(\theta = 0)$ and $\rho_{bt}^{m}(\theta = 0) = \rho_{bd}^{m}(\theta = 0)$. The Farber et al. model uses the assumption that the fabrics transmit and reflect diffusely; $\tau_{bb}^{m} = 0$, $\tau_{bt}^{m} = \tau_{bd}^{m}$ and $\rho_{bb}^{m} = 0$. In contrast, the current model allows for the possibility of direct beam transmission through openings in the fabric but a value for $\tau_{bb}^{m}(\theta = 0) = A_o$ must also be supplied. Noting that the light, medium and dark fabrics in question have approximately the same solar reflectance it must be concluded that they have different amounts of openness. The values of A_o used in the current model are also listed in Table

8.2. These A_o values were read from Keyes (1967) chart using the given values of $\tau_{bt}^{m}(\theta = 0)$ and $\rho_{bt}^{m}(\theta = 0)$.

The Farber et al. model required input data describing the variation of fabric reflectance and transmittance with respect to θ. See Figure 8.8a, reproduced from Farber et al. (1963). To compare the Farber et al. drapery model with the present model, the corresponding reflectance curves for the three fabrics were generated using the fabric model documented in (Kotey et al. 2009) and in Chapter 4. The results are shown in Figure 8.8b. With the exception of the grey fabric, there is good agreement between the two sets of fabric reflectance curves. No information was given as to how Farber et al. obtained the curves shown in Figure 8.8a.

Figure 8.9a, Figure 8.10a and Figure 8.11a show calculated values of effective absorptance and transmittance versus θ for tan, grey and white draperies, reproduced from Farber et al. (1963). Results from the present model are shown for comparison in Figure 8.9b, Figure 8.10b and Figure 8.11b. In producing Figure 8.9, Figure 8.10, and Figure 8.11, the horizontal projection angle was fixed at $\Omega_H = 0$ so $\theta = \Omega_V$.

In general, the agreement is quite good given the limitations of the Farber et al. model. Results for the dark coloured drapery agree very well. The results for the medium coloured drapery agree well at $\theta = 0$ but a significant discrepancy in absorptivity is seen at off-normal incidence. This is clearly due to the unusual off-normal property curve shown in Figure 8.8a for the grey fabric and possibly the inability of the Farber et al. model to account

for openness (A_o = 0.12). Figure 8.11 shows noticeable discrepancies between the two models for light coloured drapes. Various reasons can be offered to explain these differences, including the openness of the white fabric (A_o = 0.16) but the comparison is probably not legitimate in this case. Examining Figure 8.11a, the Farber et al. model predicts a transmittance of 42% for a pleated drape made from fabric with 35% transmittance. These data indicate a problem because pleating will always reduce solar transmittance, as shown in Figure 8.6a. It is not clear whether the Farber et al. model was applied incorrectly for the white drape or if perhaps the labels (α and τ) should be interchanged in Figure 8.11a.

To further explore the effect of pleat geometry, the current model was used to generate results for the three fabrics examined by Farber et al. Solar properties were calculated for pleated drapes with 100% fullness and properties for both drape (solid lines) and fabric (dashed lines) are shown with respect to horizontal projection angle ($\Omega_V = 0$ and $\Omega_H = \theta$) in Figure 8.12. Compared to a flat fabric, a pleating causes the incident radiation to interact with the fabric surfaces via multiple reflections and transmissions. This interaction generally gives rise to higher absorptance, lower reflectance and lower transmittance (as asserted above regarding Figure 8.11a of a pleated drape compared to the flat fabric). Figure 8.12 shows these relations to be true, for the three fabrics examined, over virtually the full range of incidence angle.

On a more general note, Moore and Pennington (1967) acknowledged difficulty in measuring the effective solar properties of draperies. Given the solar properties of a fabric at normal incidence, they proposed constants that could be used to scale down the solar properties of

the fabric in order to obtain the effective solar optical properties of the drapery. Their scaling constants were based on experiments performed with several fabrics. The present results however show that the solar properties of a pleated drape do not necessarily decrease by a constant factor with respect to Fr and/or θ. Depending on the combination of fabric properties, Fr and θ, the effective solar properties of the drape could be greater than the corresponding properties of the fabric.

8.5 Conclusions

A detailed model has been developed to calculate the effective properties of pleated drapes. The model approximates a drape as a series of uniform rectangular pleats. To calculate the effective solar optical properties, the pleated drape model uses angle-dependent properties of the flat fabric (Kotey et al. 2009) in conjunction with drapery geometry and solar angles to calculate the effective solar properties for both incident beam and diffuse radiation. The model is general enough to handle open-weave fabrics, allowing for beam-beam transmission. The present model compares favorably with models documented in the literature. The results obtained from the present model also show that the solar optical properties of a drapery do not always decrease by a factor with respect to folding ratio and/or incidence angle as suggested by previous researchers. To calculate the effective longwave properties, the effective diffuse-diffuse solar model is used with fabric longwave properties replacing corresponding fabric diffuse-diffuse solar properties. The method for determining fabric longwave properties is outlined in Chapter 7 and also documented in (Kotey et al. 2008).

Table 8.1: Nominal Solar Properties of Drapery Fabrics

Fabric Designation	Fabric Description	Beam-Beam Transmittance	Beam-Diffuse Transmittance	Beam-Total Transmittance	Beam-Total Reflectance
I_D	Open weave, dark-coloured	0.35	0.04	0.39	0.07
II_D	Semi-open weave, dark-coloured	0.15	0.03	0.18	0.10
III_D	Closed weave, dark-coloured	0.01	0.04	0.05	0.14
I_M	Open weave, medium-coloured	0.35	0.14	0.49	0.25
II_M	Semi-open weave, medium-coloured	0.15	0.14	0.29	0.32
III_M	Closed weave, medium-coloured	0.01	0.10	0.11	0.38
I_L	Open weave, light-coloured	0.35	0.23	0.58	0.36
II_L	Semi-open weave, light-coloured	0.15	0.26	0.41	0.48
III_L	Closed weave, light-coloured	0.01	0.16	0.17	0.63

Table 8.2: Solar Optical Properties for Dark-, Medium-, and Light-Coloured Fabrics, Normal Incidence (Farber et al. 1963)

Fabric Description	Transmittance	Reflectance	Absorptance	Openness
Dark coloured (tan)	0.14	0.35	0.51	0.03
Medium coloured (grey)	0.23	0.30	0.47	0.12
Light coloured (white)	0.35	0.39	0.26	0.16

* *Note:* Openness estimated using Keyes (1967) chart (ASHRAE 2005).

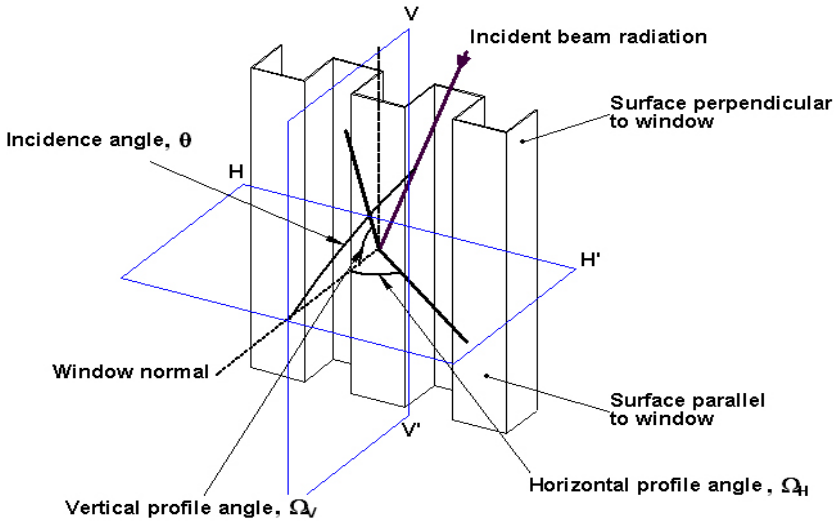

Figure 8.1: Configuration of Drapery Model Showing Solar Angles.

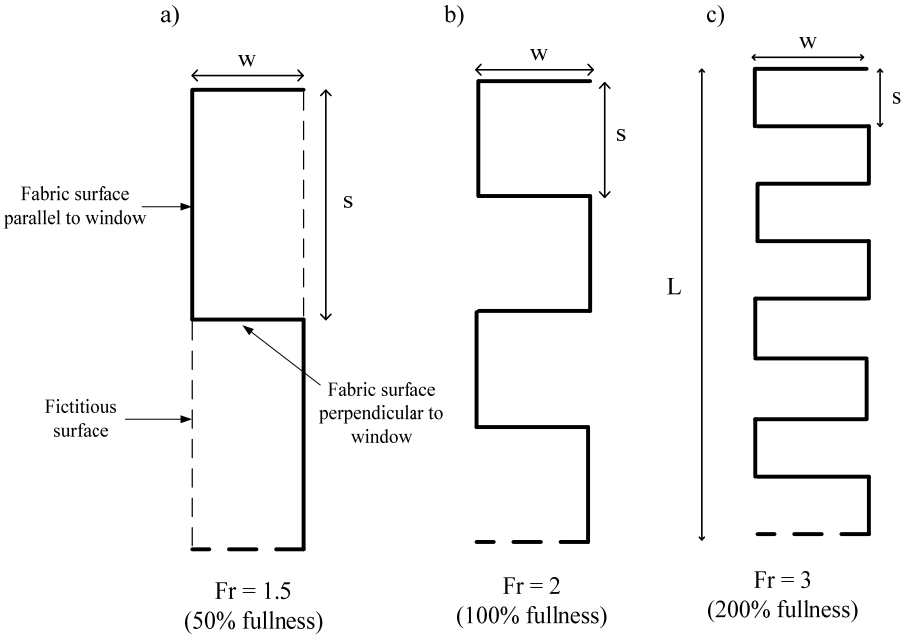

Figure 8.2: Cross-Section of Drapery Pleats with Different Values of Folding Ratio and Percent Fullness.

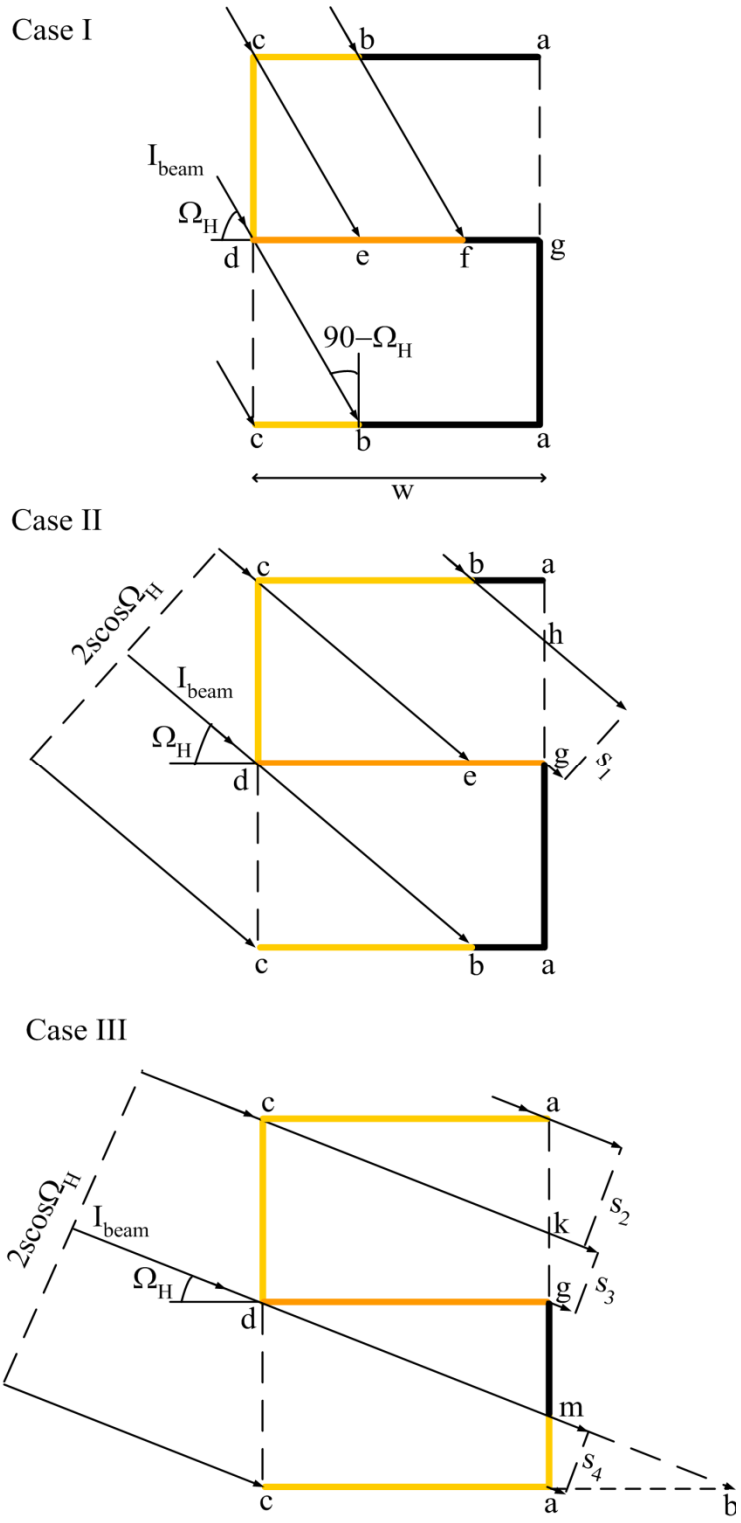

Figure 8.3: Calculating Beam-Beam Effective Solar Transmittance of Pleated Drape

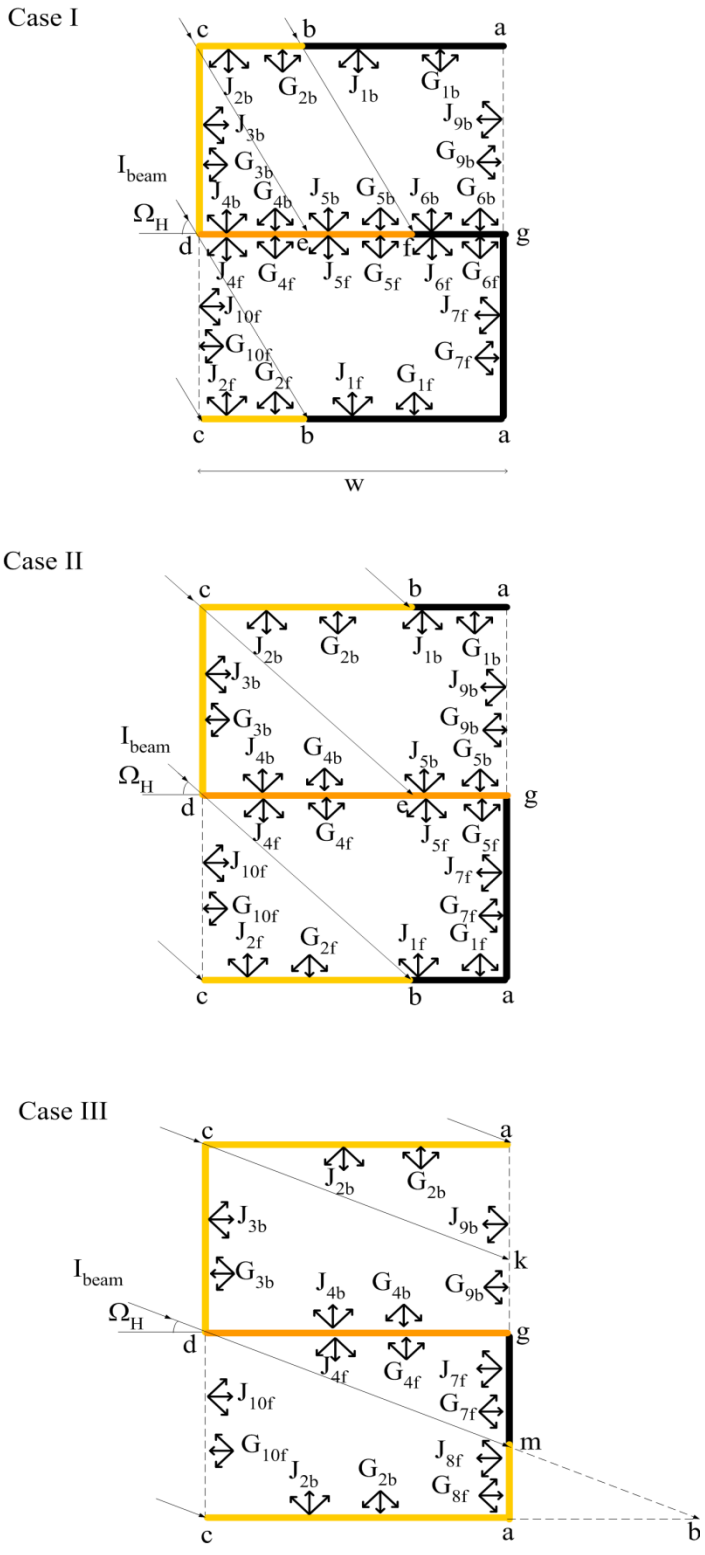

Figure 8.4: Calculating Beam-Diffuse Effective Solar Properties of Pleated Drape.

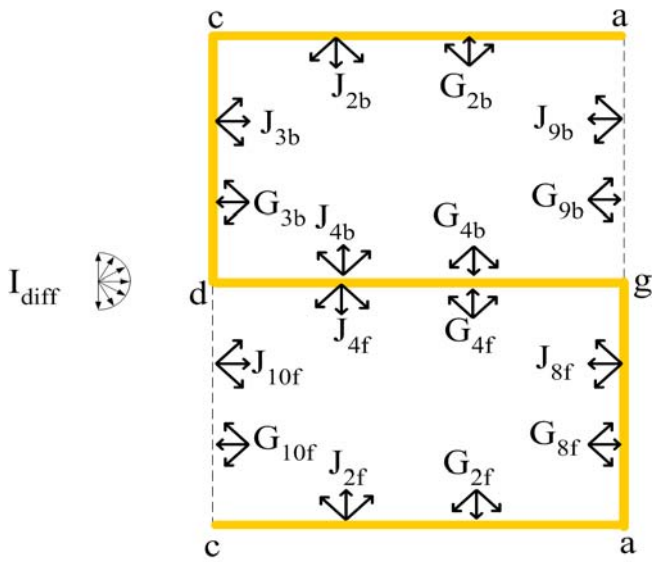

Figure 8.5: Calculating Diffuse-Diffuse Effective Solar Properties of Pleated Drape

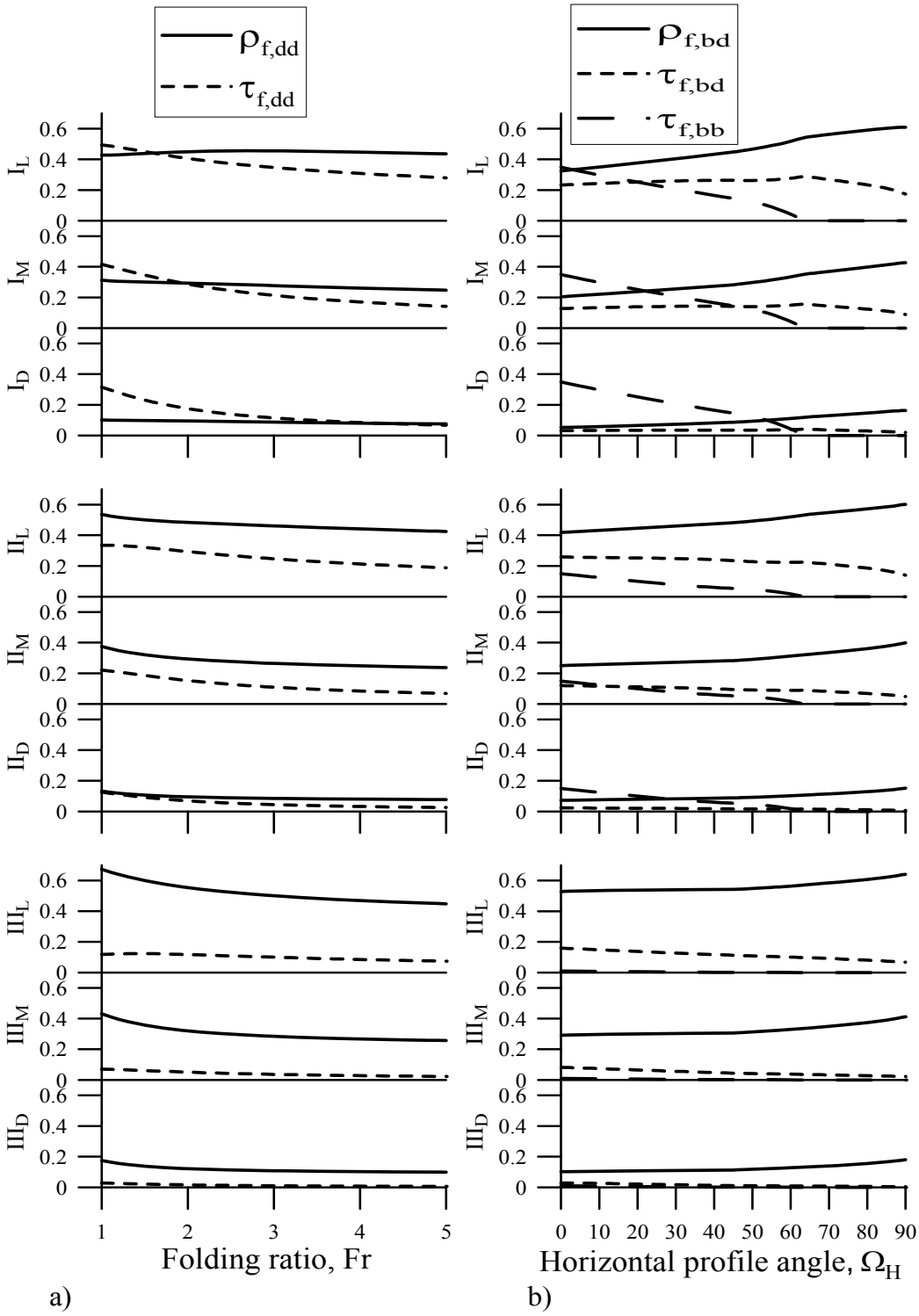

Figure 8.6: Effective Solar Properties of Pleated Drapes: (A) Diffuse, (B) Beam, 100% Fullness.

a)

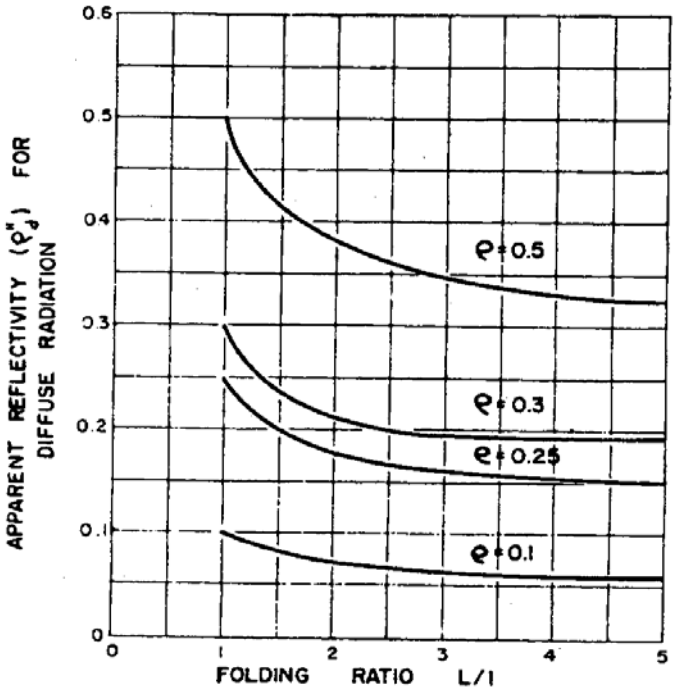

b)

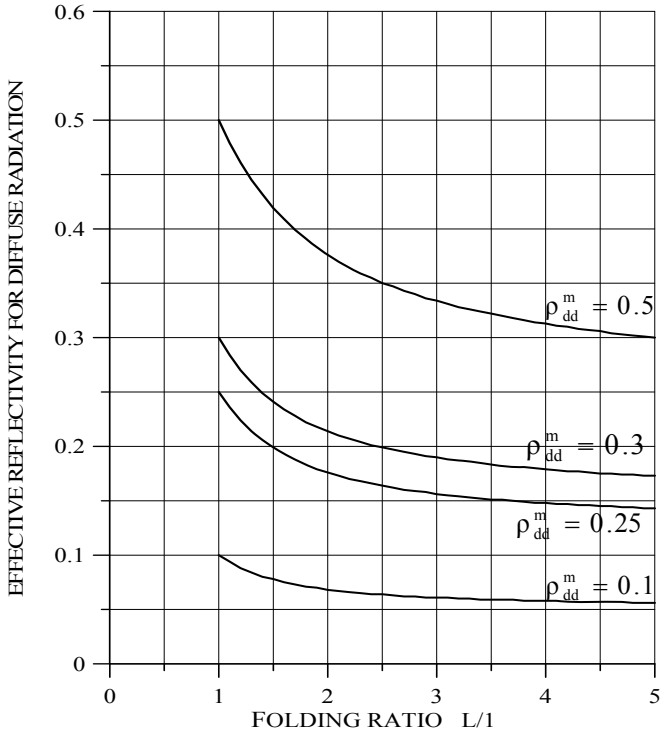

Figure 8.7: Effective Diffuse-Diffuse Reflectance of Pleated Drape: (a) Farber et al. (1963) Model; (b) The Present Model

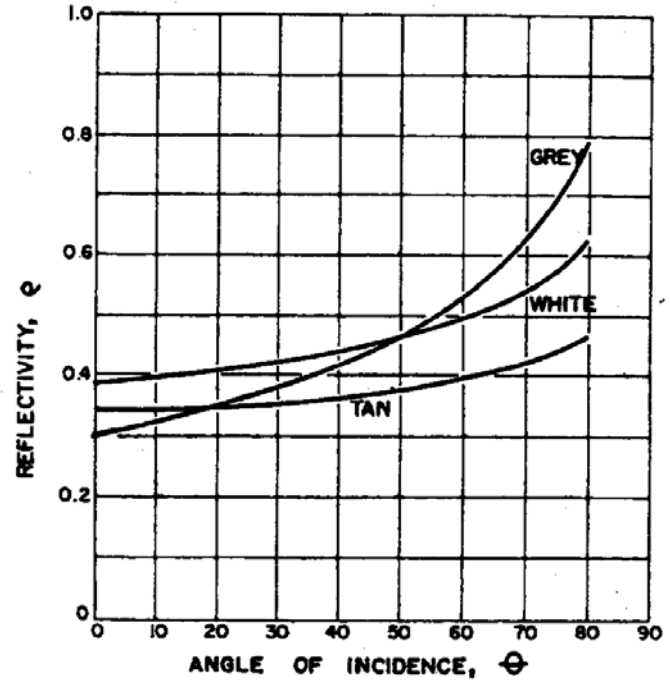

a)

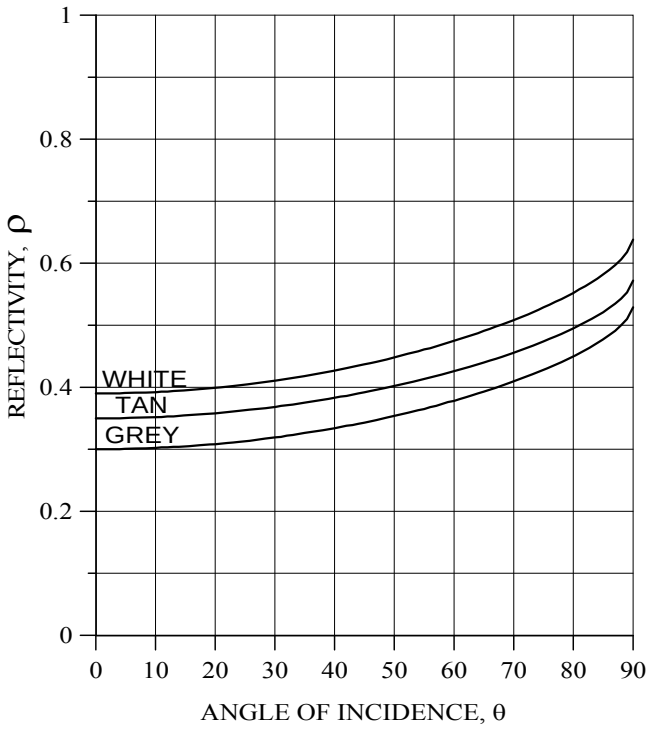

b)

Figure 8.8: Reflectivity of Fabrics versus Angle of Incidence: (a) Farber et al. (1963) Model; (b) Kotey et al. (2009) Model.

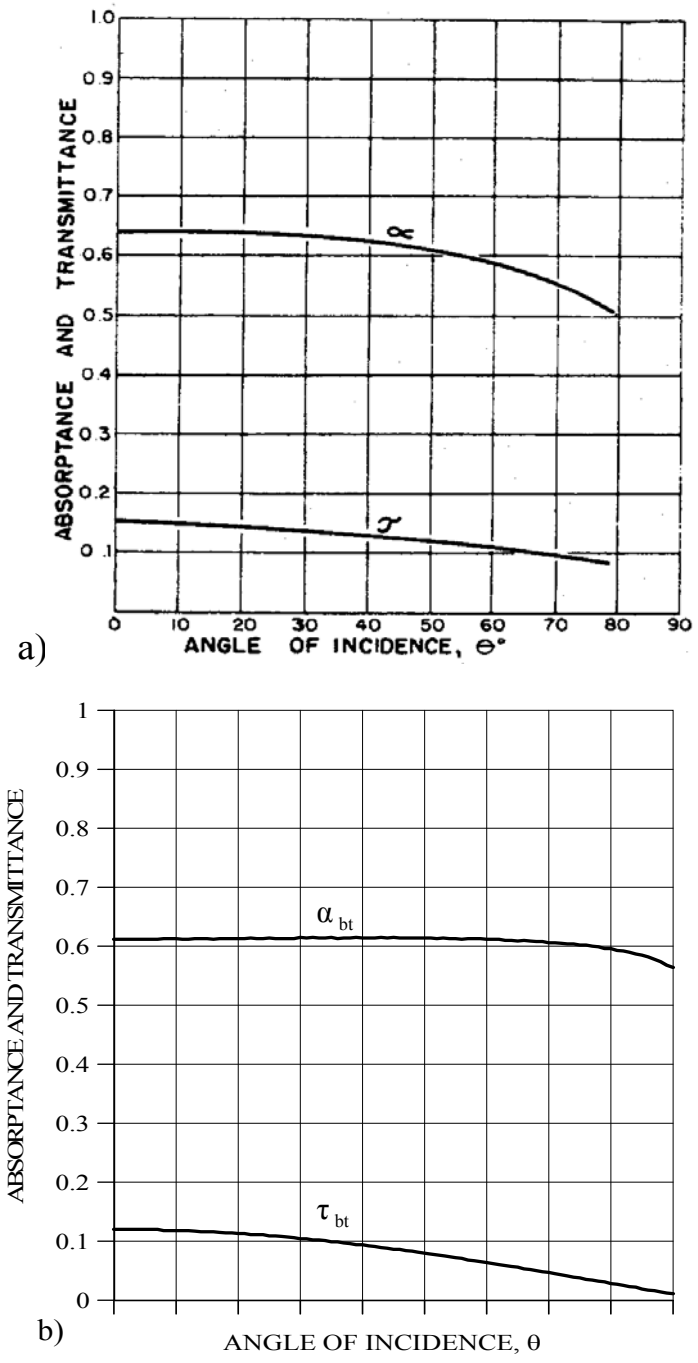

Figure 8.9: Effective Transmittance and Absorptance of Dark-Coloured (Tan) Drape versus Angle of Incidence $\theta = \theta_V$: (a) Farber et al. (1963) Model; (b) The Present Model.

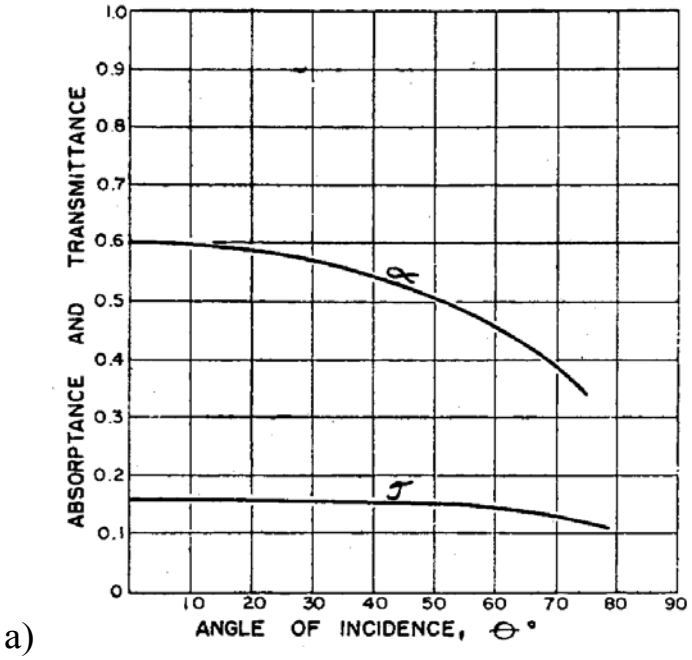

a)

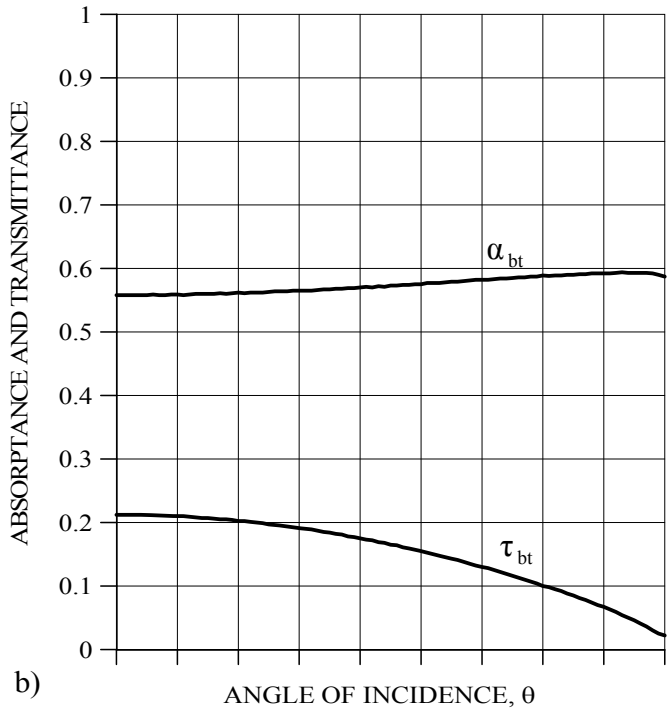

b)

Figure 8.10: Effective Transmittance and Absorptance of Medium-Coloured (Grey) Drape versus Angle of Incidence $\theta = \theta_V$: (a) Farber et al. (1963) Model; (b) The Present Model.

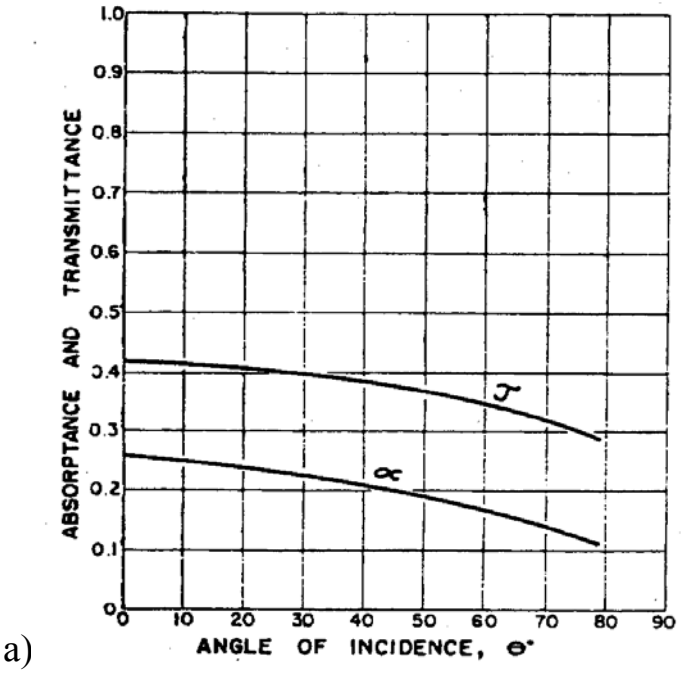

a)

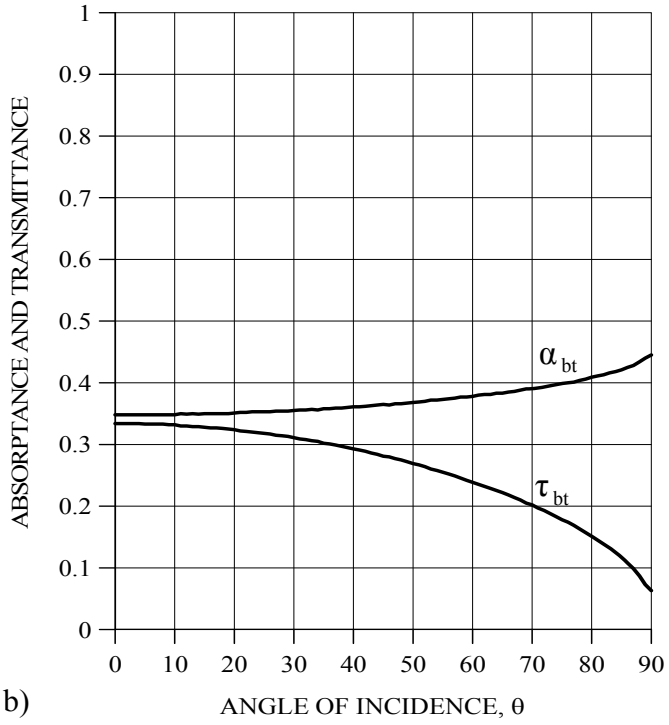

b)

Figure 8.11: Effective Transmittance and Absorptance of Light-Coloured (White) Drape versus Angle of Incidence $\theta = \theta_V$: (a) Farber et al. (1963) Model; (b) The Present Model.

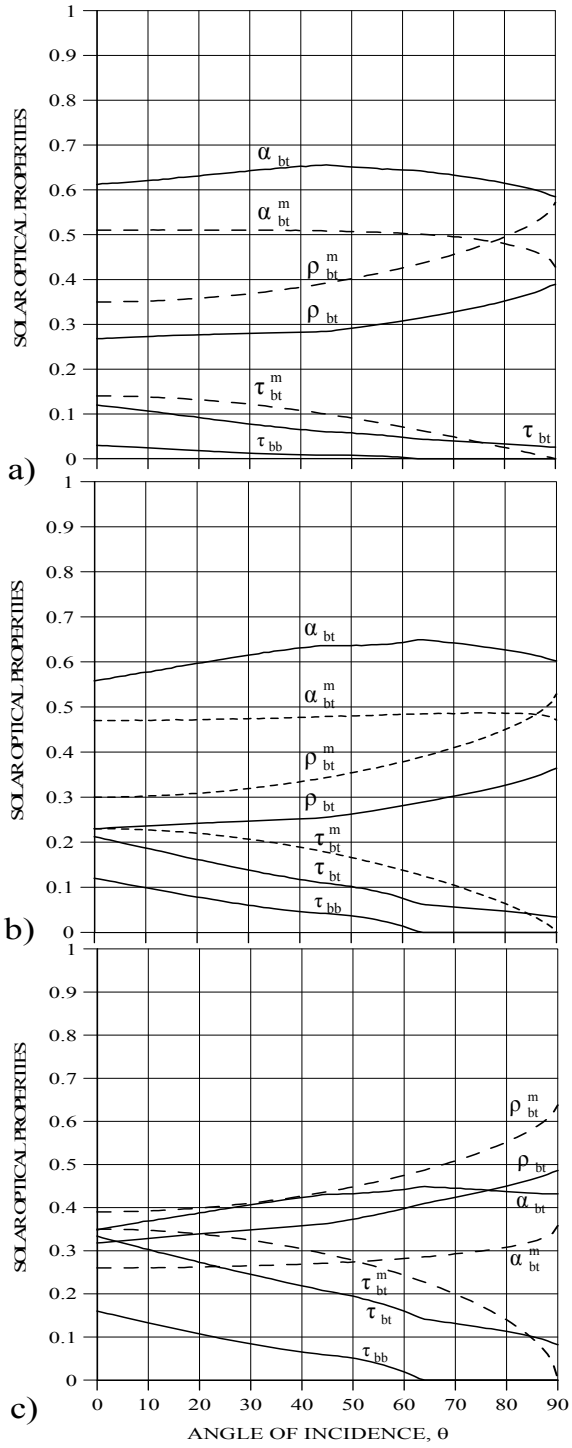

Figure 8.12: Solar Properties of Pleated Drapes and Fabrics versus Incidence Angle ($\Omega_V = 0$ and $\Omega_H = \theta$) for Yarn Colours (a) Tan, (b) Grey, and (c) White

CHAPTER 9

EFFECTIVE PROPERTIES OF VENETIAN BLINDS

9.1 Introduction

A simplified method for calculating the effective properties of venetian blinds is presented in this chapter. The effective properties of an entire blind layer are dependent on slat geometry and slat material properties. For beam solar radiation, the effective beam-beam and beam-diffuse solar properties of the blind are determined by tracking both radiation components, for a given direction of incident solar radiation, through various interactions with the slats. The slat material solar optical properties are assumed to be independent of the angle of incidence, and the slats are assumed to transmit and reflect beam radiation diffusely. As a first approximation, the slats are assumed to be flat with negligible thickness. A correction is then developed and applied to account for the curvature of the slat. For diffuse solar radiation, the effective diffuse-diffuse solar properties of the blind are evaluated using net-radiation analysis with conventional shape factors to track radiant exchange between slat surfaces. The analysis presented in this chapter is mainly focused on the determination of effective solar properties since effective longwave properties can readily be obtained from the diffuse-diffuse solar model with slat longwave properties replacing corresponding slat diffuse-diffuse solar properties. The results of the flat and curved slat models are compared with experimental data for commercially available venetian blinds.

9.2 Previous Studies

Several solar optical models in the literature consider the effective properties of slat-type shading layers (e.g., Parmelee and Aubele 1952, Pfrommer et al. 1996, Rosenfeld et al. 2000, Breitenbach et al. 2001). Parmelee and Aubele (1952), for example, presented a mathematical method for the determination of layer specific absorptance, reflectance, and transmission for the shading layer. Properties were determined as a function of solar position with respect to the glazing system, the optical properties of the shading material, and slat geometry (slat width, angle, and pitch ratio) and results were presented for both direct and diffuse solar radiation. It was assumed in that analysis that the slats were flat and diffusely reflecting.

Yahoda and Wright (2005a) developed a set of optical property models for venetian blinds. Their method requires the slat geometry and knowledge of slat surface reflectance as well as its beam-diffuse split. Furthermore, the method requires separate treatment of incident beam and diffuse radiation. For incident beam radiation, the method generates both beam-beam and beam-diffuse optical properties. The beam-beam calculations involve tracing the specularly reflected portion of incidence beam radiation until it emerges from the blind layer. Only two specular reflections were permitted by this model, after which, the ray becomes a diffuse source. This particular ray tracing technique is computationally intensive as algorithms are required to determine the fraction of incident radiation undergoing a certain number of reflections coupled with a series of geometric conditions imposed on each ray. The beam-diffuse calculations, on the other hand, involve net radiation analysis which accounts for

diffuse reflections at the slat surfaces. The models can be used to calculate solar optical properties pertaining to incident beam and incident diffuse radiation, and can also be used to obtain both direct-normal and off-normal optical properties of venetian blinds at various slat angles.

9.3 Objectives

In this chapter, the solar optical property models developed by Yahoda and Wright (2005a) are reevaluated. The primary intention is to eliminate the computationally intensive ray tracing techniques inherent in those models. It is anticipated that the simplified models developed in this chapter will be valuable to building energy simulation which places a strong requirement for speed on any of its sub-models. In this regard, the slats are assumed to be perfect diffusers and hence transmit and reflect diffusely any beam solar radiation that is incident on a slat. As a first approximation, the slats are assumed to be flat with negligible thickness. A secondary goal, therefore, is to increase the accuracy of the results by adding a curvature correction. Such a correction should prevent the model from over-predicting directly transmitted radiation when the profile and slat angles are aligned. A more recent comparison between flat and curved slat models to experimental data by Platzer (2005) further suggests an increase in accuracy of curved slat models.

9.4 Methodology

Solar optical properties of a venetian blind layer are determined by considering an enclosure which is representative of an entire blind layer. Figure 9.1a shows a typical enclosure of a

venetian blind where s is the slat spacing, w is the slat width and ϕ is the slat angle. The optical properties of the venetian blind are functions of the slat geometry and the slat material optical properties. Optical properties pertaining to beam radiation are also dependent on the vertical solar profile angle, Ω_V. Some simplifications are incorporated in the models by making the following assumptions:

- The slats are flat with negligible thickness
- Incident diffuse radiation is isotropic

The following observations and inherent features of the slats lead to further simplifications of the models:

- The slats reflect beam radiation diffusely.
- The slats transmit beam radiation diffusely if at all.

The optical property models for the venetian blind pertaining to incident beam radiation require the beam-diffuse reflectance of the upward-facing and downward-facing slat surfaces ($\rho^s_{u,bd}$ and $\rho^s_{d,bd}$) as well as the beam-diffuse transmittance of the slats (τ^s_{bd}). For incident diffuse radiation, the diffuse-diffuse reflectance values of the upward-facing and downward-facing slat surfaces are required ($\rho^s_{u,dd}$ and $\rho^s_{d,dd}$) as well as the diffuse-diffuse transmittance of the slats (τ^s_{dd}). From the assumption that slats are perfect diffusers, it follows that $\rho^s_{u,bd}$, $\rho^s_{d,bd}$ and τ^s_{bd} are independent of the angle of incidence and hence

$\rho^s_{u,bd} = \rho^s_{u,dd}$, $\rho^s_{d,bd} = \rho^s_{d,dd}$ and $\tau^s_{bd} = \tau^s_{dd}$. Moreover, since there is no beam-beam transmission or reflection, $\tau^s_{bb} = 0$, $\rho^s_{u,bb} = 0$ and $\rho^s_{d,bb} = 0$. Consequently, the only slat material optical properties required as inputs to the blind model are $\rho^s_{u,bd}$, $\rho^s_{d,bd}$ and τ^s_{bd}.

9.4.1 Beam-Beam Solar Optical Properties

The beam-beam transmittance is the ratio between the beam radiation that passes through the slat openings and the incident beam radiation. This is purely a geometric property. From Figure 9.1a, the front beam-beam transmittance is

$$\tau_{f,bb} = \frac{s-h}{s} \tag{9.1}$$

It can be shown that the front beam-beam transmittance is also given by the expression,

$$\tau_{f,bb} = \frac{de-w}{de} \tag{9.2}$$

where

$$de = s\left|\frac{\cos(\Omega_v)}{\sin(\Omega_v+\phi)}\right| \tag{9.3}$$

Equations 9.1 to 9.3 are based on the assumption that the slat thickness is zero. A similar calculation can be used to obtain the back beam-beam transmittance, $\tau_{b,bb}$, by considering beam radiation incident on the back surface of the venetian blind layer. However, by

symmetry, $\tau_{b,bb}$ is readily obtained by using the same formulae for calculating $\tau_{f,bb}$ with a negative slat angle.

9.4.2 Beam-Diffuse Solar Optical Properties

The beam-diffuse calculation is subdivided into two categories depending on whether the slats are fully or partially illuminated. For fully illuminated slats, the representative enclosure comprises four surfaces as shown in Figure 9.1a. Partially illuminated slat surfaces on the other hand give rise to a six-surface enclosure as shown in Figure 9.1b.

9.4.2.1 Four-Surface Model

As shown in Figure 9.1a, beam radiation incident on surface w_4 is reflected diffusely. Furthermore, a portion of the beam radiation incident on surface w_4 is diffusely transmitted. Diffuse radiation present within the enclosure will also be transmitted and reflected diffusely by the slats. The following definitions apply:

J_i = radiosity of surface i

G_i = irradiance at surface i

Z_i = the diffuse source term due to incident beam radiation on surface i

The following balances apply:

$$J_3 = Z_3 + \rho^s_{d,bd} G_3 + \tau^s_{bd} G_4 \tag{9.4}$$

$$J_4 = Z_4 + \tau^s_{bd} G_3 + \rho^s_{u,bd} G_4 \tag{9.5}$$

$$G_i = \sum_{j=1}^{4} F_{ij} J_j \quad \text{for } i = 1 \text{ to } 4 \tag{9.6}$$

The view factor, F_{ij}, is the fraction of diffuse radiation leaving surface i that is intercepted by surface j and can be determined by Hottel's crossed string rule.

Since there is no incident diffuse radiation at the front and back surfaces of the enclosure, $J_1 = J_2 = 0$. The diffuse source terms, Z_3 and Z_4 can be computed for two different cases:

If incident beam radiation, I_{beam}, hits the upward-facing slat surfaces, then

$$Z_3 = \tau^s_{bd} \frac{s}{de} I_{beam} \tag{9.7}$$

$$Z_4 = \rho^s_{u,bd} \frac{s}{de} I_{beam} \tag{9.8}$$

If incident beam radiation hits downward-facing slat surfaces, then

$$Z_3 = \rho^s_{d,bd} \frac{s}{de} I_{beam} \tag{9.9}$$

$$Z_4 = \tau^s_{bd} \frac{s}{de} I_{beam} \tag{9.10}$$

Equations 9.4 to 9.6 are solved to obtain all the radiosities J_j. In these equations, I_{beam} is set to unity and the front beam-diffuse transmittance and reflectance of the blind layer are

$$\tau_{f,bd} = G_2 \tag{9.11}$$

$$\rho_{f,bd} = G_1 \tag{9.12}$$

9.4.2.2 Six-Surface Model

Each slat surface is divided into two segments in order to distinguish between the illuminated and shaded portions of the slat with respect to beam radiation. Following a similar methodology described for the four-surface model, the following equations are written for the six-surface model:

$$J_3 = Z_3 + \rho^s_{d,bd} G_3 + \tau^s_{bd} G_4 \tag{9.13}$$

$$J_4 = Z_4 + \tau^s_{bd} G_3 + \rho^s_{u,bd} G_4 \tag{9.14}$$

$$J_5 = Z_5 + \rho^s_{d,bd} G_5 + \tau^s_{bd} G_6 \tag{9.15}$$

$$J_6 = Z_6 + \tau^s_{bd} G_5 + \rho^s_{u,bd} G_6 \tag{9.16}$$

$$G_i = \sum_{j=1}^{6} F_{ij} J_j \quad \text{for } i = 1 \text{ to } 6 \tag{9.17}$$

Because there is no incident diffuse radiation on the front and back surfaces of the enclosure, $J_1 = J_2 = 0$. Also, for the configuration shown in Figure 9.1b, surfaces w_5 and w_6 are

shaded from beam radiation and therefore the source terms, $Z_5 = Z_6 = 0$. The diffuse source terms, Z_3 and Z_4 are computed using Equations 9.7 to 9.10. After solving Equations 9.13 to 9.17 for all the J_j terms, the front beam-diffuse transmittance and reflectance are calculated from Equations 9.11 and 9.12.

A similar analysis is used to determine the back beam-diffuse transmittance and reflectance of the blind by considering beam radiation incident on surface w_2 in Figure 9.1b. However, by symmetry, $\tau_{b,bd}$ and $\rho_{b,bd}$ are readily obtained by using the same formulae for calculating $\tau_{f,bd}$ and $\rho_{f,bd}$ with a negative slat angle.

9.4.3 Diffuse-Diffuse Solar Optical Properties

The diffuse-diffuse transmittance and reflectance of the blind are calculated using the four-surface model shown in Figure 9.1c. For diffuse radiation incident on the front surface of the enclosure, I_{diff}, the following equations can be written:

$$J_1 = I_{diff} \tag{9.18}$$

$$J_2 = 0 \tag{9.19}$$

$$J_3 = \rho^s_{d,dd} G_3 + \tau^s_{dd} G_4 \tag{9.20}$$

$$J_3 = \rho^s_{d,dd} G_3 + \tau^s_{dd} G_4 \tag{9.21}$$

$$G_i = \sum_{j=1}^{4} F_{ij} J_j \quad \text{for } i = 1 \text{ to } 4 \tag{9.22}$$

Equations 9.18 to 9.22 are solved to obtain all the radiosities. In solving these equations, I_{diff} is set to unity and the front diffuse-diffuse transmittance and reflectance are:

$$\tau_{dd} = G_2 \tag{9.23}$$

$$\rho_{f,dd} = G_1 \tag{9.24}$$

Recall that $\rho^s_{u,bd} = \rho^s_{u,dd}$, $\rho^s_{d,bd} = \rho^s_{d,dd}$ and $\tau^s_{bd} = \tau^s_{dd}$.

The back diffuse-diffuse reflectance is calculated in a similar manner by setting $J_2 = I_{diff} = 1$ and $J_1 = 0$. However, by symmetry, $\rho_{b,bd}$ is readily obtained by using the same formulae for calculating $\rho_{f,bd}$ with a negative slat angle.

9.4.4 Curvature Correction

One deficiency inherent in solar optical models for venetian blinds is the flat-slat, zero-thickness assumption. Under this assumption, there is 100% transmission as Ω_V and ϕ come into line (i.e., as $\Omega_V + \phi$ approaches zero). In reality, most aluminum, steel and polymer-based venetian blinds have slats that are curved to provide longitudinal rigidity and this curvature blocks some solar radiation.

Figure 9.2 shows the effect of slat curvature for cases where $\Omega_V + \phi > 0$. In the upper diagram, the blockage of both the flat and curved slats would be identical. While slat

curvature will effect reflected-thru radiation, the projected cross section of the slat is identical in both cases. In the lower diagram, there will be a significant difference in the projected cross section. Between the two angles shown in the upper and lower diagrams, the curvature should provide some additional blockage of incident radiation.

The effect of the flat-slat zero-thickness combination on the blind's properties is clearly demonstrated by comparing model results to experiments (Jiang and Collins 2008). The model predicts 100% transmission when $\Omega_V + \phi = 0$, and comes into better agreement with experimental results as $\Omega_V + \phi$ moves away from zero. When $\Omega_V + \phi$ is sufficiently large, the flat-slat, zero-thickness assumption no longer has a significant impact on the predicted results. In comparing the experiments of Jiang and Collins (2008) and the model results of Kotey and Wright (2006), model predictions can be as much as 10% greater than measurements when $\Omega_V + \phi = 0$. This translates into higher solar gain predictions by models having flat slat assumption built into them. Practically, this over prediction applies over a range of about $\Omega_V + \phi = \pm 13°$.

In developing a curvature correction, the slat is first assumed to be a perfect arc of radius, r, and included angle, θ_s, as shown in Figure 9.3. The radius and included angle can be determined in a number of ways. It is suggested, however, that the slat crown, c, and the actual width, w, be measured. The values of θ_s and r can then be solved using

$$r\sin(\theta_s/2) = w/2 \quad \text{and} \quad r\cos(\theta_s/2) = r - c \tag{9.25}$$

The first step in developing a curvature correction is to determine when the slat curvature has an effect on the slat's blockage. The assumption of the slat as a perfect arc makes this calculation relatively easy. As can be seen in Figure 9.3, the curvature of the slat will have an impact when $\Omega_V + \phi$ is between $\pm \theta_s/2$. Mathematically

$$\left|\Omega_V + \phi\right| < \theta_s/2 \tag{9.26}$$

Once the need for a curvature correction is confirmed, the second step is to locate the x and y coordinates for a number of intermediate calculation points A to F as shown in Figure 9.4. The need for these points will be demonstrated. The coordinate system is defined such that the x-direction is always along the slat (AB) while the y-direction is perpendicular to it. The origin is located at the centre of the circle that would be created if the slat arc continued for 360^o. In keeping with this coordinate system, intermediate points A to F can be obtained as follows:

Point A is the leading edge of the slat (side towards the irradiation). It is located at

$$x_A = r\sin(-\theta_s/2) \quad \text{and} \quad y_A = r\cos(-\theta_s/2) \tag{9.27}$$

Point B is the trailing edge of the slat (side away from the irradiation). It is located at

$$x_B = r\sin(\theta_s/2) = -x_A \quad \text{and} \quad y_B = r\cos(\theta_s/2) = y_A \tag{9.28}$$

Point C is the point where the ray is tangent to the slat surface. It is located at

$$y_C = r\cos(\phi + \Omega_V)$$

$$x_C = \sqrt{r^2 - y_C^2} \quad \text{for } \Omega_v + \phi \geq 0 \tag{9.29}$$

$$x_C = -\sqrt{r^2 - y_C^2} \quad \text{for } \Omega_v + \phi < 0$$

Point D is the intersection of a ray that passes point A (top lit: $y = mx + b_A$) or B (bottom lit: $y = mx + b_B$) and the radial line from point C ($y = -x/m$). In the case of a top-lit slat, therefore,

$$x_D = \frac{y_A - mx_A}{-\frac{1}{m} - m} \quad \text{and} \quad y_D = mx_D + b_A = -\frac{1}{m}x_D \tag{9.30}$$

where $m = -x/y$ is the slope of the incident ray with respect to the coordinate axis. For a bottom-lit slat,

$$x_D = \frac{y_B - mx_B}{-\frac{1}{m} - m} \quad \text{and} \quad y_D = mx_D + b_B = -\frac{1}{m}x_D \tag{9.31}$$

and $m = x/y$. To avoid a division by zero error, when $m = 0$ (at $\Omega_v + \phi = 0$), $x_D = 0$ and $y_D = y_A$.

Point E is found in the same way as point D, except that a ray passing Point B is used in the top-lit case, and a ray passing point A is used in the bottom-lit case. For the top-lit slat, therefore,

$$x_E = \frac{y_B - mx_B}{-\frac{1}{m} - m} \quad \text{and} \quad y_E = mx_E + b_B = -\frac{1}{m}x_E \tag{9.32}$$

where $m = -x/y$. For a bottom-lit slat,

$$x_E = \frac{y_A - mx_A}{-\frac{1}{m} - m} \tag{9.33}$$

and $m = x/y$. To avoid a division by zero error, when $m = 0$, $x_E = 0$ and $y_E = y_A$.

Point F is the intersection of a ray passing point E, and the slat itself. For a top-lit slat

$$x_F = x_B - |x_B - x_E| \cdot 2 \quad \text{and} \quad y_F = \frac{x_F}{m} \tag{9.34}$$

where $m = -x/y$. For a bottom-lit slat,

$$x_F = x_A + |x_A - x_E| \cdot 2 \quad \text{and} \quad y_F = -\frac{x_F}{m} \tag{9.35}$$

It is desirable to continue to use the existing solution engine (flat slat model) in an adapted form. To do so, however, some further understanding of the existing solution engine is required. In the original calculation, the length of the region that is directly irradiated along the slat, de, is determined. In applying the curved assumption, it is first necessary to 'flatten' the irradiated portion of the curved slat. The coordinate definition presented in Figure 9.5 makes this a relatively simple process. The length de is approximately the Δx of the lit surface. In doing this, it is assumed that the effect of curvature on the first diffuse reflection is not significant. A more significant concern is the physical meaning of de in the original

model. When de is less than w, the beam-beam transmission is set to zero. Likewise, when de is greater than w, beam-beam transmission is (de-w)/de. Due to the curved slat, however, de can be less than w, while beam-beam transmission still exists. Two measures are required to account for this. A beam-beam transmission can still be calculated based on the projected thickness of the slat in a plane perpendicular to the direction of irradiation. More significantly, however, is that for de < w, the original calculation assumes 100% of the irradiation is on the slat. Therefore, when sending a value of de that is less than w, knowing that beam-beam transmission still exists, it is a simple matter of multiplying the results of the solution routine by the percentage of irradiation that actually falls on the slat.

As shown in Figure 9.4 and Figure 9.5 for a top-lit slat, the aforementioned modifications are fairly simple to implement. When $\Omega_v + \phi \geq 0$

$$de = x_C - x_A \tag{9.36}$$

$$\tau_{f,bb} = \frac{s\cos(\Omega_V) - L_{CD}}{s\cos(\Omega_V)} \tag{9.37}$$

$$\Lambda = \frac{L_{CD}}{s\cos(\Omega_V)} \tag{9.38}$$

All results from the solution routine, fed with de, are subsequently multiplied by weighting, Λ. L_{CD} is the distance between Points C and D, and is given by

$$L_{CD} = \sqrt{(x_C - x_D)^2 + (y_C - y_D)^2} \tag{9.39}$$

A bottom-lit slat is slightly more complex due to the fact that it will be irradiated both on the top and bottom of the slat surface. In this case, Equations (9.37) and (9.39) can still be used to determine beam-beam transmission. For the irradiation on the slat top, de_1 is still given by Equation (9.36), and the weighting factor becomes

$$\Lambda_1 = \frac{L_{CE}}{s\cos(\Omega_V)} \tag{9.40}$$

For the irradiation falling on the underside of the slat,

$$de_2 = x_B - x_F \tag{9.41}$$

$$\Lambda_2 = \frac{L_{DE}}{s\cos(\Omega_V)} \tag{9.42}$$

Here, L_{DE} and L_{CE} are the distance between points D and E, and C and E respectively, and are calculated in a similar manner to which L_{CD} was determined. Further, the results that come from the solution engine are multiplied by the associated weighting factor, and then summed. The beam-diffuse transmission, for example, is given by

$$\tau_{f,bd} = \Lambda_1 \tau_{f,bd,1} + \Lambda_2 \tau_{f,bd,2} \tag{9.43}$$

where $\tau_{f,bd,1}$ and $\tau_{f,bd,2}$ are the values output from the original solution engine.

At high slat angles (venetian blind in an almost closed position), double blockage could occur when curvature correction is applied to the flat slat model as $\Omega_v + \phi$ approaches zero. Under such conditions, curvature correction gives negative values for beam-beam

transmission as well as meaningless values for beam-diffuse transmission and reflection. The problem is easily remedied by setting the beam-beam transmission to zero and using the flat slat model to calculate the beam-diffuse transmission and reflection.

9.4.5 Longwave Radiative Properties

Longwave radiative properties of venetian blinds are calculated using the diffuse-diffuse solar optical properties model. First, slat diffuse-diffuse solar properties in Equations 9.20 and 9.21 are replaced with the corresponding slat longwave properties and the set of equations solved by matrix reduction. The effective longwave properties of the venetian blind are subsequently obtained from Equations 9.23 and 9.24. Longwave properties of slats can easily be obtained.

9.5 Results and Discussion

The simplified solar optical models were used to calculate the effective solar optical properties of a light-colored venetian blind. The slat width, the slat spacing, the slat crown and the slat angle are w = 15.0 mm, s = 12.5 mm, c = 2.0 mm and $\phi = 45°$, respectively. The slat surface reflectance ($\rho^{s}_{u,bd}$ and $\rho^{s}_{d,bd}$) is 0.673 while the slat transmittance, τ^{s}_{bd} is zero (Jiang and Collins 2008).

Figure 9.6 shows plots of front effective solar optical properties versus Ω_V. With the exception of the beam-beam reflectance which is assumed to be equal to zero, all the optical properties are dependent on Ω_V. As seen in Figure 9.6, the peak value of the beam-beam

transmittance occurs at Ω_V = -45° when the edges of the slats are aligned with the incident beam radiation and $\Omega_V + \phi = 0$. For a model which assumes that the slats are flat with negligible thickness, this peak value of transmittance would be equal to 1.0. However, by correcting for slat curvature, the peak value was estimated to be 0.92. The beam-diffuse transmittance and the beam-diffuse reflectance, on the other hand, approach zero at Ω_V = -45° as expected. This is because when the edges of the slats are aligned with the incident beam radiation, only small portions of the projected surface area of the curved slats are illuminated. Hence the net radiation that leaves the blind enclosure both in the forward direction (transmitted) and the backward direction (reflected) are expected to be very small. The beam-diffuse transmittance peaks at two values of Ω_V corresponding to a beam-beam transmittance of zero as seen in Figure 9.6.

Figure 9.7 shows the variation of the front effective optical properties with slat angle, ϕ, for incident diffuse radiation. As expected, the effective diffuse-diffuse reflectance of the blind increases with increasing ϕ while the diffuse-diffuse transmittance decreases with increasing ϕ. The maximum reflectance is obtained when $\phi = \pm 90^o$. Since the slats are opaque, it is expected that the effective diffuse-diffuse transmittance of the blind goes to zero at $\phi = \pm 90^o$. However, the four-surface model considered gives a false effective diffuse-diffuse transmittance because the slats overlap when $\phi = \pm 90^o$. This false diffuse-diffuse transmittance can easily be remedied by using a six-surface model as observed by Yahoda and Wright (2005b). Nonetheless, a four-surface model with inherent simplifications will produce the desired accuracy for building energy simulation since commercially available

blinds cannot be closed beyond $\phi \geq \pm 75^{o}$. The minimum value of the effective diffuse-diffuse reflectance is obtained when the blind is fully opened ($\phi = 0$) with a correspondingly high diffuse-diffuse transmittance.

Consideration will now turn to the comparison between experimental results and the simplified models. The experiments were performed using the Broad Area Illumination – Integrating Sphere (BAI-IS) shown in Figure 9.8 (Jiang and Collins 2008). The BAI-IS operates in a similar manner to other integrating spheres with a few key differences. The test sample is typically far larger than the sphere aperture and is fully illuminated by the light source. The sphere itself is 50 cm in diameter and has a 5 cm diameter aperture. With these modifications, it is possible to test materials that have relatively large scale non-homogeneity. Full details of the BAI-IS and test methodology can be found in Jiang (2005), Jiang and Collins (2008) and Milburn and Hollands (1994).

Slats from a commercially available mini-blind were employed for this experiment. Again, the slat width, the slat spacing, the slat crown and the slat angle are w = 15.0 mm, s = 12.5 mm, c = 2.0 mm, respectively. To cover a broader range of cases, a black and a white venetian blind were chosen. The black slats represent an extreme condition, and it was used solely to test the capabilities of the model. The reflectance values of the black and white slats are 0.13 and 0.67, respectively. Details of the test samples can be found in Jiang (2005), Jiang and Collins (2008).

Figure 9.9 shows the results of the curvature correction applied to the total transmittance through the blinds. It is imperative to note that the total transmittance used in this context is

the sum of the beam-beam and the beam-diffuse transmittance. In all cases, the predicted total transmittance using the curved slat model falls more closely in line with experimentally determined results than the flat slat model.

9.6 Conclusions

In this chapter, simplified models are used to calculate the effective solar optical properties of venetian blinds by considering an enclosure which is representative of the entire blind layer. The slats are assumed to transmit and reflect beam radiation diffusely. In addition, the optical properties of the slats are assumed to be independent of the angle of incidence. As a first approximation, the slats are assumed to be flat with negligible thickness. A curvature correction is then applied to the flat slat model. The results of the flat slat and the curved slat models are compared with experimental results on commercially available venetian blinds. The curved slat model matches the experimental results more closely than the flat slat model over the entire range of profile angle.

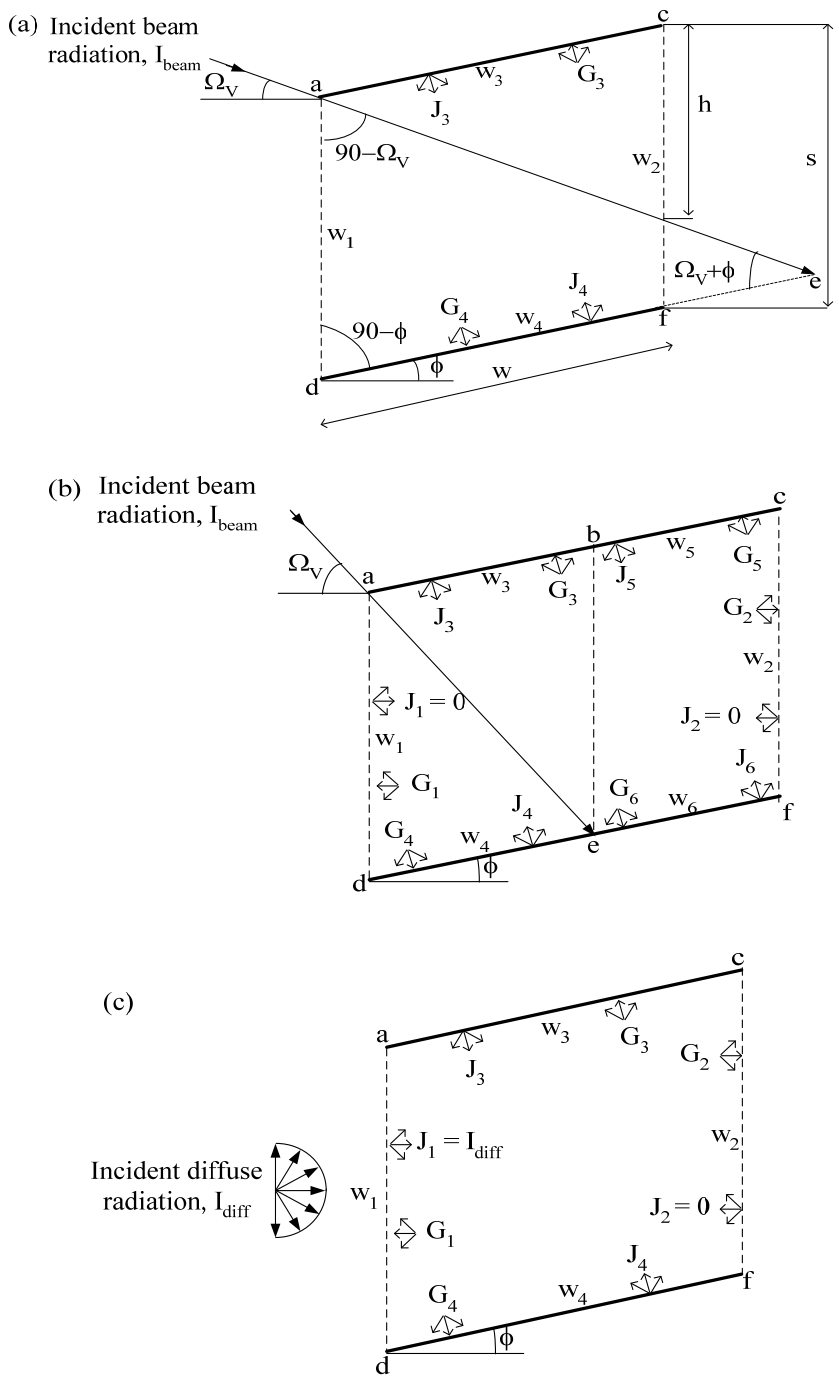

Figure 9.1: Enclosure Geometry for Calculating Venetian Blind Layer Optical Properties (a) Incident Beam Radiation (Four-Surface Model) (b) Incident Beam Radiation (Six-Surface Model) (c) Incident Diffuse Radiation

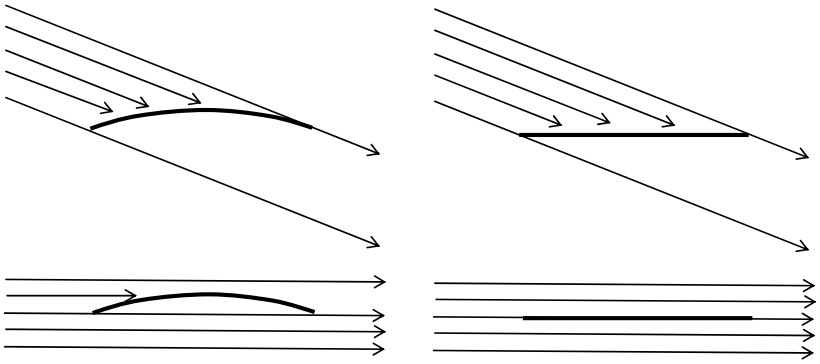

(a) (b)

Figure 9.2: Differing Effects of Slat Curvature on Blockage of Incident Beam Radiation Curved Slats (b) Flat Slats

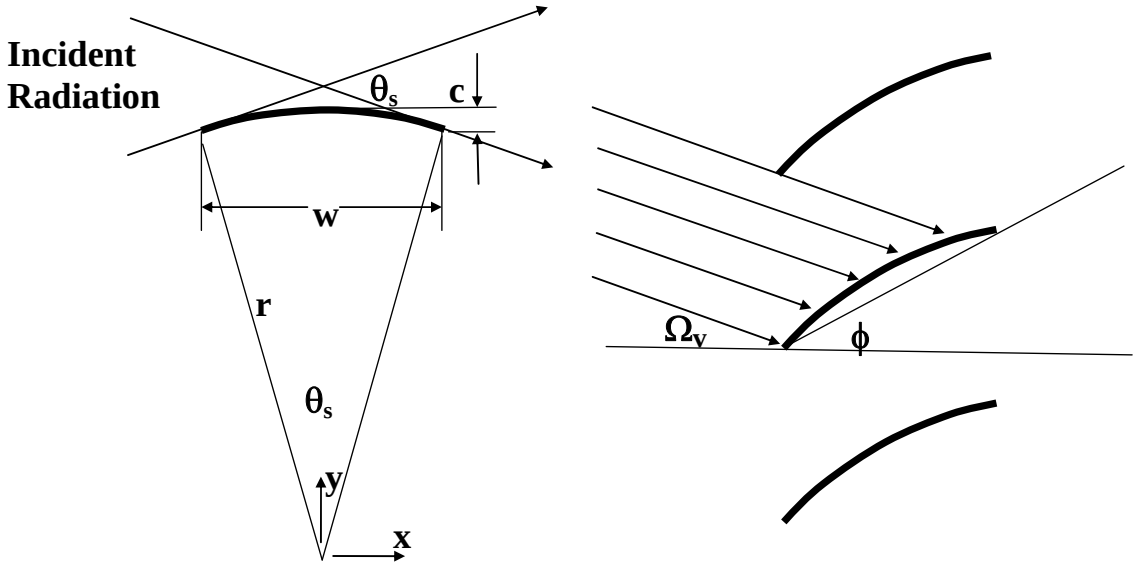

Figure 9.3: Angular conditions under which slat curvature is a factor

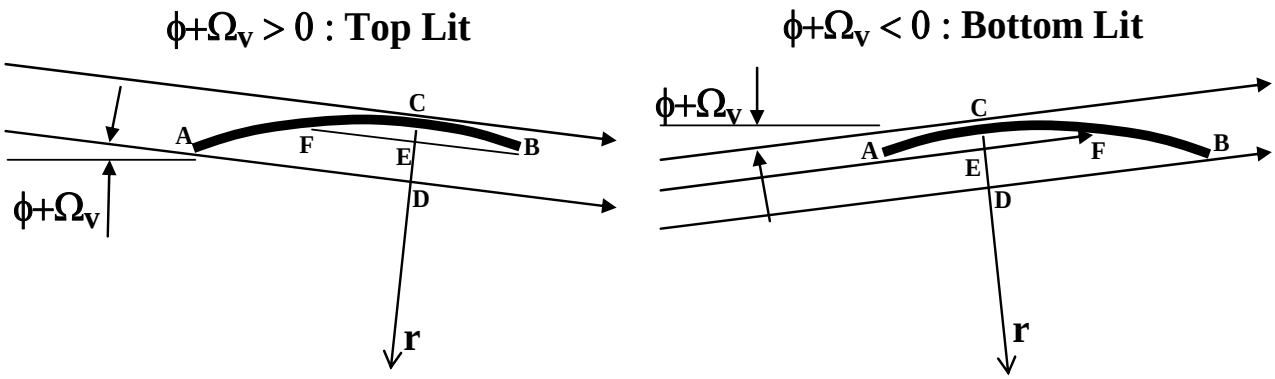

Figure 9.4: Locations of intermediate points

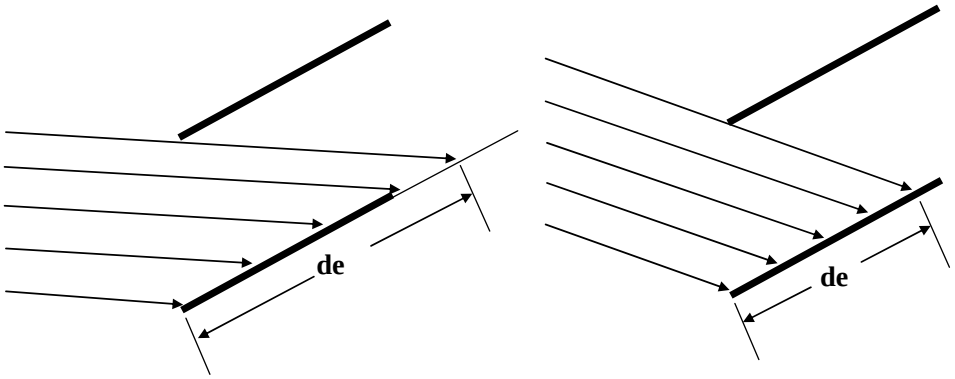

Figure 9.5: Irradiation cases considered in original model (top-lit only)

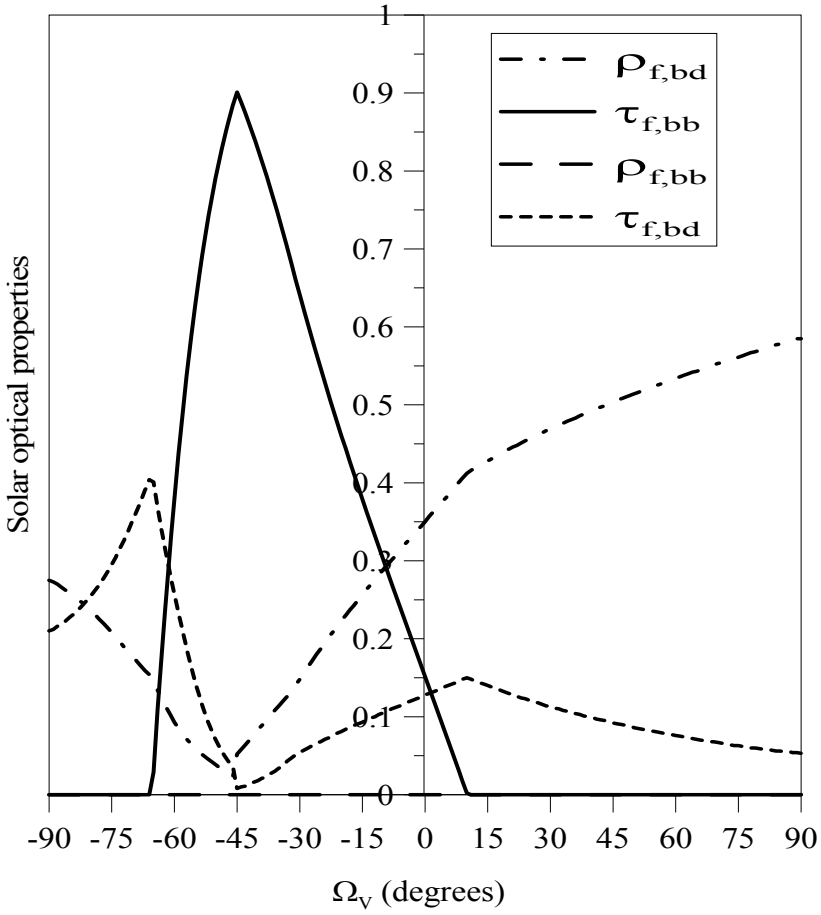

Figure 9.6: Front Effective Solar Optical Properties versus Ω_V

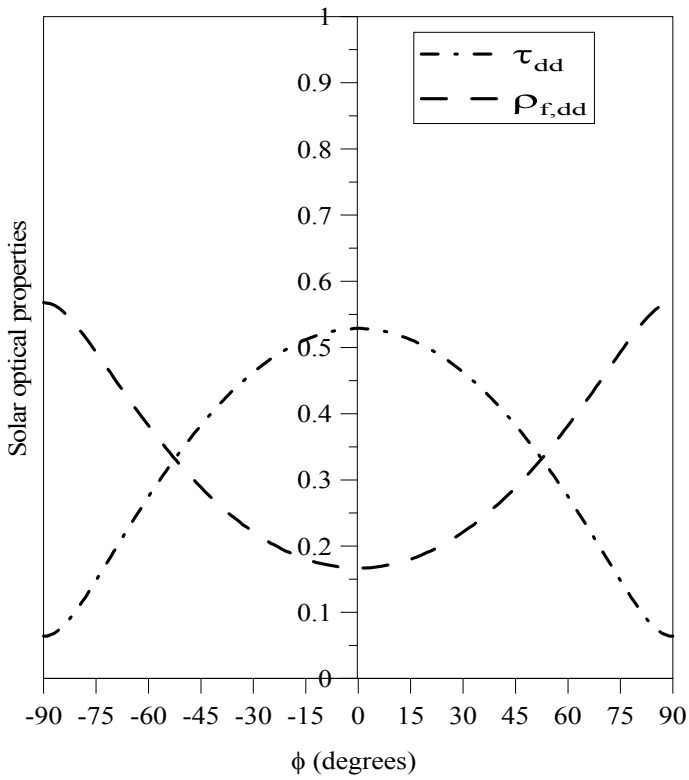

Figure 9.7: Effective Solar Optical Properties Versus ϕ for Incident Diffuse Radiation

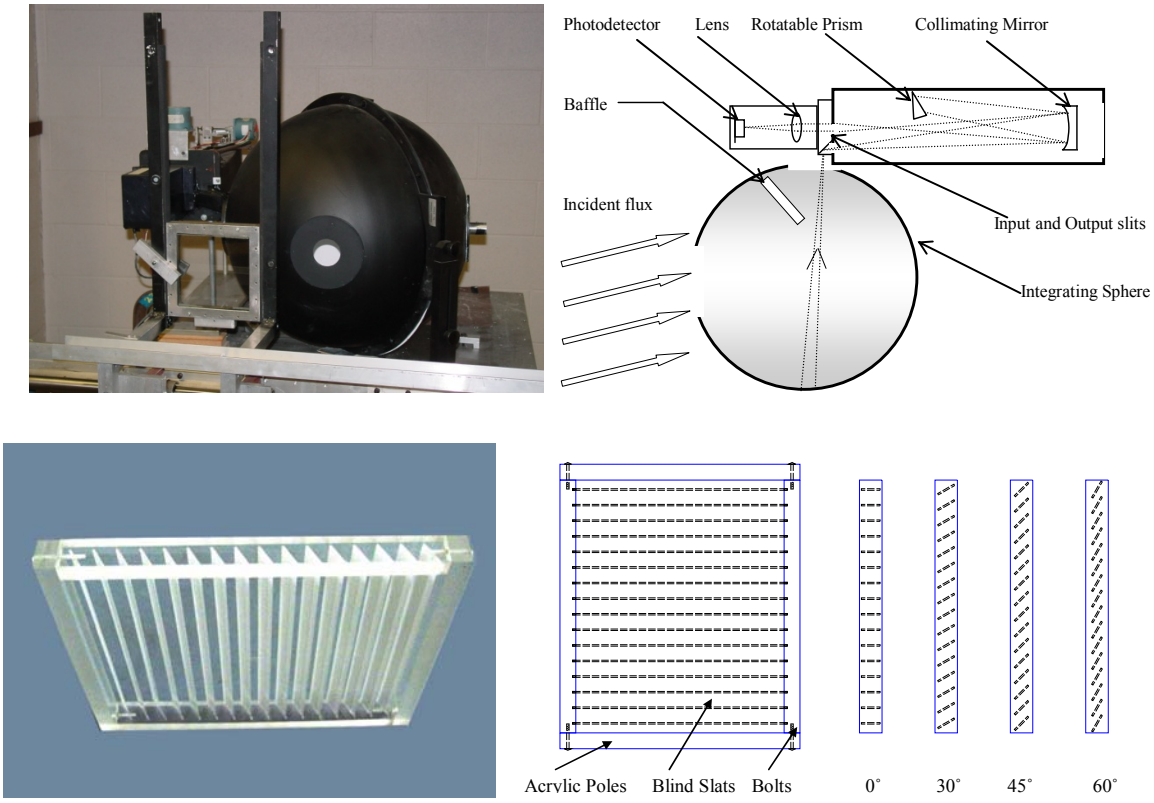

Figure 9.8: The BAI-IS and the Experimental Model (from Jiang and Collins 2008)

(a)

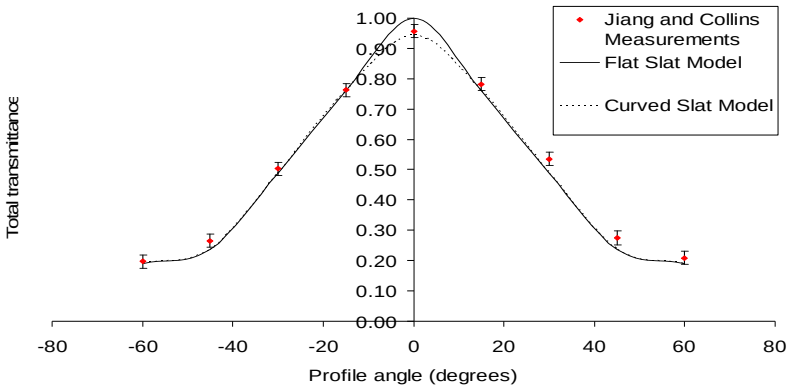

(b)

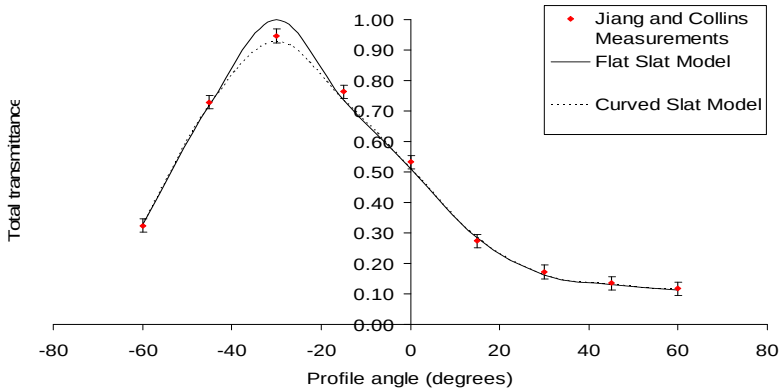

(c)

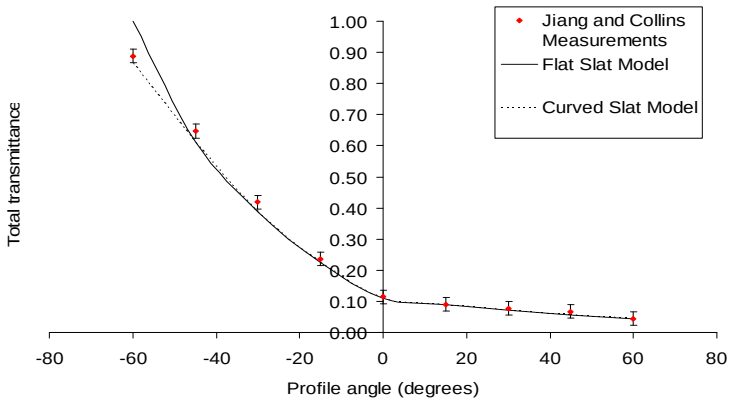

Figure 9.9: Comparison Between Experimental Data, Flat Slat Model, and Curved Slat Model for Three Slat Angles: (a) $\phi = 0^o$, (b) $\phi = 30^o$, and (c) $\phi = 60^o$

CHAPTER 10

VALIDATION OF SOLAR-THERMAL MODELS

10.1 Introduction

This chapter presents a system validation of solar-thermal models developed in the preceding chapters. Solar gain through various shading devices attached to a conventional double glazed (CDG) window was measured using the NSTF solar simulator and solar calorimeter. The shading devices include dark and light coloured venetian blinds, a medium coloured roller blind, a medium coloured pleated drape, and a dark coloured fiberglass insect screen. More specifically, performance parameters including SHGC, IAC and system solar transmittance, τ_{sys}, were obtained for the CDG window as well as various CDG/shading layer combinations. The performance parameters were also obtained for the same measurement conditions using the ASHRAE Toolkit simulations that incorporate the currently developed solar-thermal models. Finally, the measurement and simulation results were compared.

10.2 Performance Parameters

As discussed in Chapter 1, a portion of the solar radiation incident on a fenestration system will be directly transmitted to the indoor space while other portions are absorbed by the

individual layers, some of which is redirected to the indoor space by heat transfer. For a given fenestration system, the solar gain is characterised by the SHGC which is the ratio of the solar gain to the solar irradiance. In a multi-layer fenestration system consisting of n layers, the SHGC can be expressed as

$$\mathrm{SHGC} = \tau_{\mathrm{sys}} + \sum_{i=1}^{n} N_i \cdot A_i \tag{10.1}$$

where τ_{sys} is the system solar transmittance; A_i and N_i are respectively the absorbed portion of incident solar radiation and the inward flowing fraction of that absorbed solar radiation in the i^{th} layer.

A shading attachment will generally reduce solar gain and this effect may be conveniently represented by the IAC.

$$\mathrm{IAC} = \frac{\mathrm{SHGC}_{\mathrm{cfs}}}{\mathrm{SHGC}_{\mathrm{g}}} \tag{10.2}$$

where $\mathrm{SHGC}_{\mathrm{cfs}}$ and $\mathrm{SHGC}_{\mathrm{g}}$ are SHGC values for the shaded and unshaded glazing system, respectively. Historically, IAC has been presented as a constant depending only on glazing and shading layer properties (e.g., ASHRAE 2005). However, IAC also depends on solar incidence angle, especially for shading layers having non-uniform geometry (e.g., venetian blinds and pleated drapes). The IAC is an important parameter since it is required to determine solar gain using cooling load calculation procedures such as ASHRAE's Radiant Time Series (RTS) method.

10.3 Measurements

10.3.1 Facility

The measurements were taken using the NSTF solar simulator and solar calorimeter. This measurement facility is capable of measuring the SHGC and the U-factor of a full scale window with or without shading layers. Figure 10.1 is a schematic of the measurement apparatus. Measurements can be carried out under a variety of imposed weather conditions using a solar simulator arc-lamp source and a solar calorimeter positioned in a large environmentally-controlled chamber. The lamp, in combination with an optical reflector system, provides a uniform irradiance over the test area with a spectral irradiance distribution that approximates the ASTM AM1.5 solar spectrum (ASTM E891-87 1987). The intensity of the incident flux at the test section can be adjusted from 100 to 1100 W/m^2. The angle of incidence can be varied from 0 to 30° above the horizontal.

The calorimeter comprises an outer and an inner cell with an absorber plate within the inner cell. The outer cell is designed to provide a stable temperature environment for the inner cell while the absorber plate adds or removes heat from the inner cell. The rate of energy entering or leaving the inner cell can be accurately measured using the heat exchanger loop connected to the absorber plate.

The environmental chamber can be maintained at temperatures ranging from -20 to +50°C. The temperature set point in the chamber can be maintained within ±1°C. A variable speed fan incorporated in the chamber's air-circulating system provides wind with speeds ranging

from 0.5 to 4.0 m/s. The wind direction is normal to the plane of the test sample. A detailed description of the theory and the operating principles of the NSTF solar simulator and solar calorimeter can be found in several references (e.g., Harrison and Dubrous 1990, CANMET 1993, van Wonderen 1995)

10.3.2 Procedure

Measurements were taken using the window in combination with various shading devices. The test method is similar to the method prescribed by CSA A440.2-98 (1998).

First, the window was mounted in the mask wall of the calorimeter test cell. The test cell was then placed inside the environmental chamber with the mask wall facing the solar simulator. Test conditions including solar irradiance, G_{inc}, indoor air temperature, T_{in}, and outdoor air temperature, T_{out} were maintained at steady state while the net energy transfer through the window, Q_{net}, was measured. During each test a still air condition was maintained on the indoor side of the window with a small fan mounted near the top of the inner cell to eliminate stratification. A turbulent flow condition, with steady wind speed of 2.9 m/s perpendicular to the window was maintained at the outdoor side of the window. The experiment was carried out with solar irradiance at normal incidence. In subsequent experiments, shading devices were attached to the window and the test was repeated. Table 10.1 summarises the glazing/shading system test combinations and associated test conditions.

10.3.3 Estimation of Surface Convective Heat Transfer Coefficients

Previous experiments under similar convective conditions using a Calibration Test Standard (CTS) without a shading attachment gave a total (i.e., including convective and radiative) indoor surface coefficient of $h_{tot,in} = 9.6 \pm 1.9\ W/m^{2\,o}C$ and a total outdoor surface coefficient of $h_{tot,in} = 16.5 \pm 5.3\ W/m^{2\,o}C$ (van Wonderen 1995). Given the indoor surface temperature of the CTS glass, $T_{g,in}$, and the indoor mean radiant temperature, T_{in} (assumed equal to the air temperature), the indoor radiative heat transfer coefficient, $h_{r,in}$, was estimated by treating the window as a small object in a large enclosure . See Equation 10.3.

$$h_{r,in} = \varepsilon_g \sigma (T_{g,in}^2 + T_{in}^2)(T_{g,in} + T_{in}) \tag{10.3}$$

where σ is the Stefan-Boltzmann constant and $\varepsilon_g = 0.84$ is the emissivity of glass. The outdoor radiative heat transfer coefficient, $h_{r,out}$, was estimated in a similar manner.

$$h_{r,out} = \varepsilon_g \sigma (T_{g,out}^2 + T_{out}^2)(T_{g,out} + T_{out}) \tag{10.4}$$

In this case $T_{g,out}$ and T_{out} are respectively the outdoor surface temperature of the CTS glass and the outdoor mean radiant temperature (again assumed equal to the air temperature). The temperatures obtained during calibration, i.e., T_{in}, $T_{g,in}$, $T_{g,out}$ and T_{out} are listed in Table 10.2. Since the total surface coefficient, h_{tot}, is the sum of the radiative and the

convective components, the values of $h_{c,in}$ and $h_{c,out}$ were estimated from Equations 10.5 and 10.6:

$$h_{c,in} = h_{tot,in} - h_{r,in} \tag{10.5}$$

$$h_{c,out} = h_{tot,out} - h_{r,out} \tag{10.6}$$

giving $h_{c,in} = 4.6\ W/m^2\ °C$ and $h_{c,out} = 10.1\ W/m^2\ °C$. These convective heat transfer coefficients are needed as input to the simulation models.

10.3.4 Test Samples

The window used was a pre-fabricated insulated glazing unit (IGU) mounted in a fixed wooden frame. The shading devices that were attached to the window include commercially available insect screen, pleated drape, venetian blinds and roller blind. Note that the indoor shading devices were attached such that convective air could flow vertically through the space between shading device and the window. The distance between glazing/shading layers is given in Table 10.3. The window and shading devices are described below and detail is also provided in Table 10.4.

Insulated Glazing Unit and Frame

The air-filled IGU consists of two 3 mm layers of clear glass separated by a commercially produced edge seal comprising foam spacer and butyl sealant to give an air gap of 12.7 mm. The IGU was mounted in a wooden frame (unpainted pine). The frame design enabled easy

attachment of shading devices. Figure 10.2 shows a cross-section of the window and the mounting details in the mask wall of the solar calorimeter.

The projected area of the window was divided into three sub-areas: the centre glass area, A_{cg}, the edge glass area, A_{eg}, and the frame area, A_{fr}. The centre glass area is defined as that part of the view area more than 6.35 cm from the sight line (e.g., CSA A440.2-98 1998, ASHRAE 2005) and the edge glass area consists of the remaining part of the view area. The frame area consists of the portion lying outside the sight line. Figure 10.2 also shows the sub-areas of the window. The total projected window area, A_w, is the sum of A_{cg}, A_{eg} and A_{fr} while the total glass area (view area), A_g, is sum of A_{cg} and A_{eg}. The dimensions of A_w were 1665 mm x 1665 mm and the dimensions of A_g were 1590 mm x 1590 mm.

Insect Screen

The insect screen selected was a fiberglass cloth, black screen. It had 18 x 16 mesh per square inch and a strand diameter of approximately 0.38 mm giving it an openness factor of 0.58. During testing, the insect screen was attached to the frame at the outdoor side of the window with the aid of staples. This arrangement sealed the screen at its perimeter. The distance between the outdoor glazing and the screen was approximately 20 mm.

Pleated Drape

A beige colour, closed weave, pleated drape was selected for testing. To obtain 100% fullness the width of the flat fabric was twice the width of the pleated drape. During testing

the drape was mounted at the indoor side of the window with the aid of a curtain rod affixed to the frame. The drape covered the entire width of the window when installed in its pleated configuration. The distance between convex pleat surfaces and the window was about 100 mm. The pleats were regularly arranged with an approximately sinusoidal cross-section. There were approximately ten pleats with an average pleat width and spacing of 127 and 178 mm, respectively.

Venetian Blinds

Two venetian blinds were selected for testing. The first blind had black painted slats while the second had white painted slats. The slats were metallic having curved surfaces with 24.5 mm slat width, 19.1 mm slat spacing and 2.3 mm slat crown. These blinds were mounted at the indoor side of the window. In the fully opened position, the distance between the indoor glazing and the tip of the slats was approximately 42 mm. Both blinds were tested at a slat angle of 60°. The white blind was tested with slats at three additional positions, fully opened (slat angle = 0°), closed (slat angle = 75°) and partially opened (slat angle = 30°). At each slat angle other than zero, the convex slat surfaces faced the outdoor side and the slat tips nearer the outdoor side were oriented downward.

Roller Blind

An open weave, grey, vinyl roller blind was selected for testing. The thickness of the blind was 0.80 mm and its openness factor was 0.10. The roller blind was mounted on the indoor

side of the window at a distance of 72 mm from the indoor glazing and the edges were left unsealed so that room air could circulate between the blind and glazing.

10.3.5 Solar and Longwave Properties of Glazing and Shading Materials

Table 10.5 lists the normal incidence solar and longwave properties of the glazing and shading materials. The solar properties include beam-total transmittance, τ_{bt}, beam-total reflectance, ρ_{bt}, beam-diffuse transmittance, τ_{bd}, and beam-beam transmittance, τ_{bb}. The longwave properties are the emissivity, ε, and the longwave transmittance, τ^{lw}. Each material is symmetrical with respect to solar and longwave properties so there is no need to distinguish between front and back properties. To obtain the solar properties, spectral measurements were taken at normal incidence using a commercially available spectrophotometer as discussed in Chapter 3 (Kotey et al. 2009a, b and c). The spectral data showed that the shading materials are generally not spectrally selective except for variation in the visible wavelength band corresponding to the colour of the material. The solar properties were calculated using the 50-point selected ordinate method as described in ASTM E903-96 (1996). The longwave properties were measured with a commercially available infrared reflectometer as discussed in Chapter 7 (Kotey et al. 2008). The measured longwave properties of shading materials are included in Table 10.5. However, the measured longwave properties of drapery fabric, roller blind material and the insect screen were not needed because empirical relations included in the simulation models (Kotey et al. 2008) were used to estimate the longwave properties of these materials.

10.3.6 Determination of Solar Heat Gain Coefficient

An energy balance on the window gives the net heat gain, Q_{net}, as the difference between the solar gain, Q_{solar}, and the heat loss, Q_{ht}, due to the temperature difference across the window, i.e.,

$$Q_{net} = Q_{solar} - Q_{ht} \tag{10.7}$$

By definition, Q_{solar} can be expressed as

$$Q_{solar} = SHGC_w \cdot G_{inc} \cdot A_w \tag{10.8a}$$

giving

$$SHGC_w = \frac{Q_{solar}}{A_w \cdot G_{inc}} \tag{10.8b}$$

where $SHGC_w$ is the solar heat gain coefficient of the window, A_w is the total projected window area and G_{inc} is the solar irradiance.

During testing, G_{inc} was measured with a pyranometer mounted on the mask wall while Q_{net} was measured based on an energy balance over the control volume of the inner cell. The net energy flow through the window comprised energy absorbed by the absorber plate, Q_{abs}, heat loss through the calorimeter mask wall, Q_{mw}, heat loss due to air leakage, Q_{al} and electrical power inputs to the calorimeter, Q_{inp}.

$$Q_{net} = Q_{abs} + Q_{mw} + Q_{al} - Q_{inp} \tag{10.9}$$

All terms on the right hand side of Equation 10.9 are well defined in (CANMET 1993, Brunger et al. 1999) and were determined accordingly. Note that the more significant terms in Equation 10.9 are Q_{abs} and Q_{inp}. Generally, the magnitudes of Q_{mw} and Q_{al} are such that they can be neglected.

The value of Q_{abs} was determined from the product of the mass flow rate of the circulating fluid, $\dot{m}$, its specific heat, C_p, and the temperature rise across the absorber plate, ΔT_{abs}.

$$Q_{abs} = \dot{m} C_p \Delta T_{abs} \tag{10.10}$$

The value of Q_{inp} includes the electrical power supply to the absorber plate recirculation pump, Q_{pump}, and the power supply to the air-circulation fan, Q_{fan}.

$$Q_{inp} = Q_{pump} + Q_{fan} \tag{10.11}$$

By definition, Q_{ht} can be expressed as

$$Q_{ht} = U_w \cdot A_w \cdot \Delta T_w \tag{10.12}$$

where U_w is the overall window heat transfer coefficient and ΔT_w is the temperature difference across the window.

To obtain $SHGC_w$ from Equation 10.8, ΔT_w was maintained close to zero during the experiments (e.g., Harrison and van Wonderen 1994). This was achieved by holding the temperature within the calorimeter (indoor) and the environmental chamber (outdoor) at 20 ± 1°C. Since zero temperature difference was not realised, the small temperature difference across the window was accounted for by estimating Q_{ht} and subsequently using the value of Q_{ht} to calculate Q_{solar}. See Equation 10.7. However, this adjustment was very small and influences the value of $SHGC_w$ typically in the third decimal place. A similar procedure has been used to obtain SHGC of windows with shading devices (Harrison and van Wonderen 1998 and Brunger et al. 1999).

In addition, the solar heat gain coefficient of the total glass area, $SHGC_g$ was obtained from $SHGC_w$ using an area-based calculation, i.e.,

$$SHGC_g = \frac{A_w}{A_g} SHGC_w \qquad (10.13)$$

Equation 10.13 is based on the assumption that the solar heat gain coefficient of the frame, $SHGC_{fr}$ is negligible (Wright and McGowan 1999). The SHGC values reported in Table 10.6 are the values for $SHGC_g$.

The IAC, as defined by Equation 10.2, was subsequently obtained. The measured IAC values are also listed in Table 10.6. The uncertainty associated with the SHGC values of each test

condition ranges from ±0.02 to ±0.04. Details of the uncertainty analysis are discussed in the Appendix B (CANMET 1993).

10.3.7 Determination of System Solar Transmittance

The value of τ_{sys} was determined by Equation 10.14.

$$\tau_{sys} = \frac{G_{trans,1}}{G_{inc}} \tag{10.14}$$

where $G_{trans,1}$, is the indoor-side pyranometer reading adjusted for distance. The distance adjustment is necessary because the rays of incident radiation are not perfectly parallel. Therefore, the indoor-side pyranometer should have been mounted very close to the test sample at location 1. See Figure 10.1. However, it was mounted at location 2, a distance of 0.43 m from the indoor surface of the shading layer. At location 2, the pyranometer was able to view a representative area of the shading layer. Such an arrangement reduces the uncertainty in the transmittance measurements associated with non-homogeneous shading layers by eliminating the need to take several readings at different locations in the vertical plane. Nevertheless, the readings from the indoor-side pyranometer required adjustment to compensate for the decreased irradiance with distance.

Prior measurements of irradiance, G, with distance, D, from the solar simulator revealed an inverse power relation of the form:

$$G = \text{constant}\left(\frac{1}{D}\right)^{1.83} \tag{10.15}$$

Given the irradiance at location 2, $G_{trans,2}$, the irradiance at location 1, $G_{trans,1}$ was calculated as

$$G_{trans,1} = G_{trans,2}\left(\frac{D_2}{D_1}\right)^{1.83} \tag{10.16}$$

where D_1 and D_2 are the distances from the solar simulator to locations 1 and 2, respectively. See Figure 10.1. The $G_{trans,1}$ value, as calculated from Equation 10.16 was subsequently substituted into Equation 10.14 to estimate τ_{sys}. The values of τ_{sys} are included in Table 10.6. The uncertainty associated with the measured τ_{sys} values ranges from 0 to ±0.05. Details of the uncertainty analysis are discussed in Appendix B.

10.4 Simulation

The simulation entails a multi-layer analysis where each glazing/shading multi-layer system is treated as a series of parallel layers separated by gaps (Wright and Kotey 2006, Wright 2008). Chapter 2 discusses the multi-layer analysis that was employed in the simulation.

The same test conditions summarised in Table 10.1 were input to the current version of the ASHRAE Loads Toolkit (Barnaby et al. 2004, Pedersen et al. 2001) that incorporates the solar-thermal models. The mean radiant temperatures were assumed to be equal to the air

temperatures. Solar, longwave and geometric properties of the individual layers including the distance between glazing/shading layers were also supplied to the simulation program.

A wide variety of output parameters such as layer temperature, heat flux values, absorbed solar radiation, τ_{sys}, $SHGC_{cg}$, IAC and U-factor could be extracted from the simulation. However, for the current investigation, only τ_{sys}, $SHGC_{cg}$, IAC and U-factor were examined. See Table 10.7. Note that the value of $SHGC_{cg}$ is routinely equated to $SHGC_g$. Thus the SHGC values listed in Table 10.7 are those of $SHGC_g$. The U-factors listed in Table 10.6 are the centre glass U-factors, i.e., U_{cg}. The window U-factor, U_w, was required to make a small adjustment in determining the measured $SHGC_w$. See Equations 10.7, 10.8a and 10.12. However, for a large window having a smaller edge glass and frame area fractions, U_{cg} is approximately equal to U_w, and this approximation was used.

10.5 Discussion

10.5.1 Effect of Shading Devices on Solar Gain

The measurement and simulation results are summarised in Table 10.6 and Table 10.7, respectively. Generally, the shading devices reduce solar gain; SHGC values for the shaded window are lower than the corresponding value for the unshaded window. The reduction in solar gain by shading devices is also evident from IAC values with lower IAC values corresponding to greater reduction in solar gain.

The white venetian blind in the closed position gives the largest reduction in solar gain. This can be attributed to high solar reflectance of the white slats. Higher solar reflectance will result in greater rejection of insolation. Furthermore, there is complete blockage of beam insolation by the closed slats. Thus, amongst the indoor shading devices considered, the white venetian blind has the greatest potential to reduce cooling loads. On the other hand, the lowest reduction in solar gain was achieved when the white venetian blind was fully opened. This is because in the fully opened position the slats are aligned with the beam and intercept only a small portion of the insolation. The partially opened white blind (slat angle = 30°, 60°) gives IAC values in between the fully opened and closed positions with the 30° slat position recording a higher IAC than the 60° slat position. This is due to the fact that the 60° slat position blocks more beam insolation as compared to the 30° slat position. The variation in IAC demonstrated by these results attests to the suitability of venetian blinds as operable solar control devices.

Considering the black venetian blind with slat angle = 60°, it is interesting to note a fairly low reduction in solar gain compared to the white venetian blind with the same slat angle. This observation is primarily due to a much lower reflectance of black slats compared to white slats. In addition, the black blind absorbs more solar energy than the white blind. Given that both blinds are located at the indoor side of the window, a much higher flux of absorbed energy is redirected to the indoor side by heat transfer from the black blind.

Another interesting observation is that the indoor mounted pleated drape has about the same effect as the outdoor mounted insect screen. Table 10.5 reveals that the insect screen has a

much higher solar transmittance compared to the drape fabric. On the other hand, the drape fabric has a higher solar reflectance. Note that the drape in its pleated form will have slightly lower effective solar reflectance and transmittance values in comparison with the fabric from which it is made. This observation is clearly demonstrated in Chapter 8 and Kotey et al. 2009d. The insect screen might be expected to deliver more solar gain since it has a higher solar transmittance and a much lower solar reflectance. However, because the screen was located on the outdoor side, the absorbed solar energy was mostly dissipated to the outdoor air.

On a more general note, it is worth mentioning that the potential for any given shading device to control solar gain (i.e., its IAC) is influenced by the glazing system to which it is attached. Consider two categories of glazing systems.

1. High-SHGC: A simple glazing system consisting of one or two layers of clear glass will produce high solar gain. The solar gain will consist almost entirely of transmitted solar radiation and this is evident because the system solar transmittance of the glazing system will be only slightly less than its SHGC value (i.e., the ratio τ_{sys}/SHGC will be high, close to unity).

2. Low-SHGC: A more sophisticated glazing system that includes tinted glass and/or one or more coatings will generally produce low solar gain. In this case less of the solar gain will consist of transmitted solar radiation. A large portion of the solar gain will result from absorbed solar radiation that makes its way to the indoor space by

means of heat transfer. The system solar transmittance of the glazing system will be much less than its SHGC value (i.e., the ratio τ_{sys}/SHGC will be low, close to zero).

If a glazing system is in the high-SHGC category the solar gain can be controlled effectively using an indoor attachment with high solar reflectance. It is widely acknowledged that solar reflectance is the most important performance characteristic of a shading device. The challenge of controlling solar gain is largely a matter of solar optics in this case and this is demonstrated in the comparison between white and black venetian blinds.

In contrast, if the glazing system is in the low-SHGC category the solar reflectance of an indoor attachment will have little influence because most of the solar gain arrives by means of heat transfer. In addition, examining the U-factors listed in Table 10.7, it can be seen that the shading attachments have very little influence on thermal resistance. Therefore, indoor shading attachments offer little potential for controlling the solar gain produced by low-SHGC glazing systems. However, the solar gain of any glazing system can be controlled by locating the shading device on the outdoor side of the building. This arrangement allows the solar radiation to be intercepted, either absorbed or reflected, before it can be absorbed or transmitted by the glazing system. This point is demonstrated by the comparison between the pleated drape and the outdoor insect screen.

10.5.2 Comparison between Measurement and Simulation Results

The comparison of NSTF measurements and simulation results is shown graphically in Figure 10.3 through Figure 10.6.

Figure 10.3 shows very good agreement between NSTF measurements of τ_{sys} and the simulation models. With an average difference of 0.02 and a maximum difference of 0.04 there is remarkably good agreement between the two sets of results. The discrepancy, expressed as a percentage, is appreciable only for systems with very low values of τ_{sys}. With the exception of the fully opened white venetian blind and black venetian blind (slat angle = 60°), the difference between the measurement and simulation results is well within measurement uncertainty.

The comparison of measured and simulated SHGC is shown in Figure 10.4. The average difference between the two sets is 0.04. In most cases, the difference is within measurement uncertainty. The white venetian blind (slat angle = 30°) and black venetian blind (slat angle = 60°) give the best agreement while the roller blind shows a difference of 0.07. Again, there is good agreement but the simulated SHGC is consistently greater than the measured SHGC. As a result of this observation some additional investigation was undertaken.

Noting that there is very little bias in the τ_{sys} data as seen in Figure 10.3, it was concluded that the bias seen in Figure 10.4 must be caused by some aspect of the heat transfer process. The most likely cause is the assignment of convective heat transfer coefficients for surfaces exposed to the environment. The indoor and outdoor convective heat transfer coefficients used to produce Figure 10.4 were $h_{c,in} = 4.6\ W/m^2{}^oC$ and $h_{c,out} = 10.1\ W/m^2{}^oC$. In order to test the sensitivity of SHGC with respect to these coefficients the simulations were

re-run with heat transfer coefficients more typical of the ASHRAE summer design conditions, $h_{c,in} = 4.0\ W/m^2{}^oC$ and $h_{c,out} = 15.0\ W/m^2{}^oC$, and again the simulation results were compared against NSTF measurements. See Figure 10.5. In the new comparison the agreement between simulation and NSTF results has improved with an average difference of only 0.02 and the bias is virtually gone. The white venetian blind gives a perfect correlation both in the closed and slat angle = 60° position while the pleated drape records a maximum difference of 0.04. The point of this exercise is not necessarily to assert that the heat transfer coefficients supplied for the NSTF facility are wrong. It is more informative to note that the uncertainties attached to the total surface heat transfer coefficients are high (recall $h_{tot,in} = 9.6 \pm 1.9\ W/m^2{}^oC$ and $h_{tot,out} = 16.5 \pm 5.3\ W/m^2{}^oC$). This is primarily because the CTS was not calibrated (van Wonderen 1995). The modified heat transfer coefficients used to produce Figure 10.5 actually fall within the range of those uncertainties. The modified comparison simply highlights the idea that the SHGC is mildly sensitive to the surface convective heat transfer coefficients and that this might be a suitable topic for future research if higher accuracy is desired.

Finally, measured and simulated IAC values were compared as shown in Figure 10.6. Again the agreement is very good. The average difference between the two sets of results is 0.03 and a maximum difference of 0.06 is observed for the pleated drape and the roller blind. Note that regardless of whether the SHGC data shown in Figure 10.4 or Figure 10.5 are used, the resulting values of simulated IAC and Figure 10.6 are virtually unchanged. In other words, although some sensitivity in SHGC has been demonstrated, the sensitivity of IAC with

respect to the surface convective coefficients is weak. There are several reasons for this insensitivity including the ideas that (a) the τ_{sys} is unaffected by convection and (b) changes in the convective heat transfer will influence the shaded and unshaded window in a similar fashion – causing a similar increase or decrease in the SHGC of both.

On a more general note, the uncertainty associated with the measured values of SHGC was estimated to range from ±0.02 to ±0.04. Small differences between the measured and simulated SHGC values may also be attributed to uncertainty in the measured input values used in the simulation. For example, the solar properties obtained from the spectrophotometer (Kotey et al. 2009a, b and c) have an uncertainty of ±0.03. Furthermore, minor differences in the SHGC values may also be attributed to the approximations in the simulation models in particular the convection models associated with open-channel attachment (Wright et al. 2009). However, it is difficult to pinpoint all sources of discrepancy because the agreement is very good.

In summary, very good agreement between the measured and the simulated solar gain is clearly demonstrated in Figure 10.3 through Figure 10.6 since the absolute difference in most cases is within 0.05.

10.6 Conclusions

A comparison between measured and simulated solar gain in windows with shading devices is presented. The measurements were taken using the NSTF solar simulator and solar calorimeter. The shading devices investigated include two venetian blinds, a roller blind, a

pleated drape and an insect screen. The calculations were obtained from a comprehensive fenestration/shading model which was developed for building energy simulation and performance rating. In general, there is very good agreement between the measured and simulated values of SHGC, IAC and τ_{sys}. In most cases the discrepancy between measurement and simulation is well below 0.05. The differences between the two sets offer little insight regarding shortcomings of either technique because the agreement is very good. However, this study provides more insight into the effect of different types of shading devices, their colour and their location on the solar gain in windows.

Table 10.1: Summary of Glazing/Shading Systems Test Combinations and Associated Test Conditions

Sample Description	Location	G_{inc} (W)	T_{in} (°C)	T_{out} (°C)
CDG window	NA	306	20.3	19.7
CDG window + black insect screen	Outdoor	512	20.4	19.9
CDG window + beige pleated drape (100% fullness)	Indoor	374	20.6	19.8
CDG window + white venetian blind (closed)	Indoor	299	19.9	19.9
CDG window + white venetian blind (fully opened)	Indoor	254	20.3	20.2
CDG window + white venetian blind (slat angle = 30^0)	Indoor	305	21.4	20.8
CDG window + white venetian blind (slat angle = 60^0)	Indoor	281	20.6	20.8
CDG window + grey roller blind	Indoor	295	21.1	20.8
CDG window + black venetian blind (slat angle = 60^0)	Indoor	223	20.8	20.7

Table 10.2: Temperatures obtained from CTS Measurements (from van Wonderen 1995)

T_{in} (°C)	$T_{g,in}$ (°C)	T_{out} (°C)	$T_{g,out}$ (°C)
21.2	26.7	47.5	50.7

Table 10.3: Distance between Glazing/Shading Layers

Glazing/Shading Layers	L (mm)
Two glazings	12.7
Glazing and insect screen	20.0
Glazing and venetian blind	42.0
Glazing and roller blind	72.0
Glazing and pleated drape	100.0

Table 10.4: Description of Window and Shading Devices

Sample	Description
Window	IGU, two 3 mm clear glass, 12.7 mm air gap, butyl rubber spacer, wood frame, 1665 mm x 1665 mm (total window area), 1590 mm x 1590 mm (total glass area)
Insect Screen	Black, fiberglass, 60% openness, 18 x 16 mesh per square inch, 0.015 in strand diameter
Pleated drape	Beige fabric, closed weave, 100% fullness
Venetian blind (1)	White, curved, metallic slats, 24.5 mm slat width, 19.1 mm slat spacing, 2.3 mm slat crown
Venetian blind (2)	Black, curved, metallic slats, 24.5 mm slat width, 19.1 mm slat spacing, 2.3 mm slat crown
Roller blind	Grey, vinyl mesh, 10% openness, 0.80 mm thick

Table 10.5: Solar and Longwave Properties of Glazing and Shading Materials

	Normal incidence solar properties				Longwave properties	
Glazing/shading material	τ_{bt}	ρ_{bt}	τ_{bd}	τ_{bb}	ε	τ_{LW}
3 mm clear glass	0.83	0.08	0.00	0.83	0.84	0.00
Beige drapery fabric	0.24	0.55	0.22	0.02	0.89	0.06
Grey roller blind	0.13	0.29	0.02	0.11	0.80	0.17
Dark fiberglass insect screen	0.60	0.03	0.01	0.59	0.35	0.62
Venetian blind slat (black)	0.00	0.06	0.00	0.00	0.86	0.00
Venetian blind slat (white)	0.00	0.68	0.00	0.00	0.87	0.00

Table 10.6: Summary of Measurement Results

Sample Description	SHGC	IAC	τ_{sys}
CDG window	0.73	1.00	0.67
CDG window + black insect screen	0.43	0.59	0.40
CDG window + beige pleated drape (100% fullness)	0.43	0.59	0.18
CDG window + white venetian blind (closed)	0.40	0.55	0.03
CDG window + white venetian blind (fully opened)	0.69	0.95	0.59
CDG window + white venetian blind (slat angle = 30^0)	0.63	0.86	0.38
CDG window + white venetian blind (slat angle = 60^0)	0.46	0.64	0.08
CDG window + grey roller blind	0.51	0.70	0.09
CDG window + black venetian blind (slat angle = 60^0)	0.67	0.92	0.02

Table 10.7: Summary of Simulation Results

Sample Description	SHGC	IAC	τ_{sys}	U-factor
CDG window	0.76	1.00	0.69	2.76
CDG window + black insect screen	0.47	0.61	0.42	2.77
CDG window + beige pleated drape (100% fullness)	0.49	0.65	0.17	2.49
CDG window + white venetian blind (closed)	0.43	0.56	0.05	2.49
CDG window + white venetian blind (fully opened)	0.74	0.97	0.63	2.63
CDG window + white venetian blind (slat angle = 30^0)	0.64	0.83	0.35	2.62
CDG window + white venetian blind (slat angle = 60^0)	0.49	0.64	0.10	2.54
CDG window + grey roller blind	0.58	0.76	0.10	2.56
CDG window + black venetian blind (slat angle = 60^0)	0.68	0.90	0.00	2.54

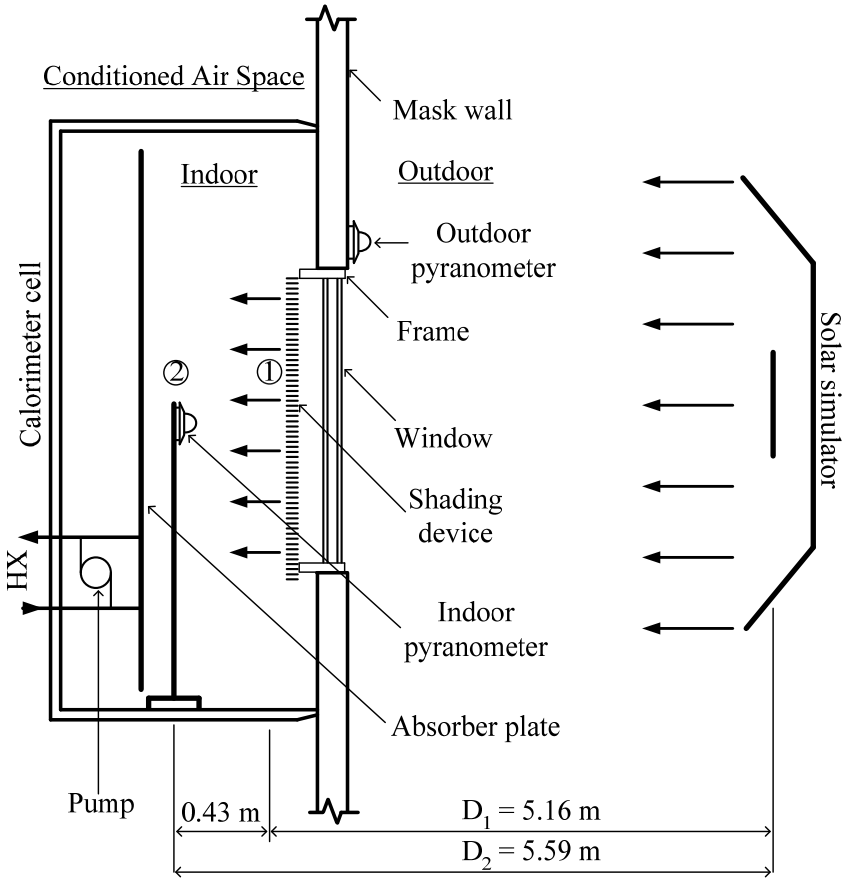

Figure 10.1: Schematic of Measurement Apparatus

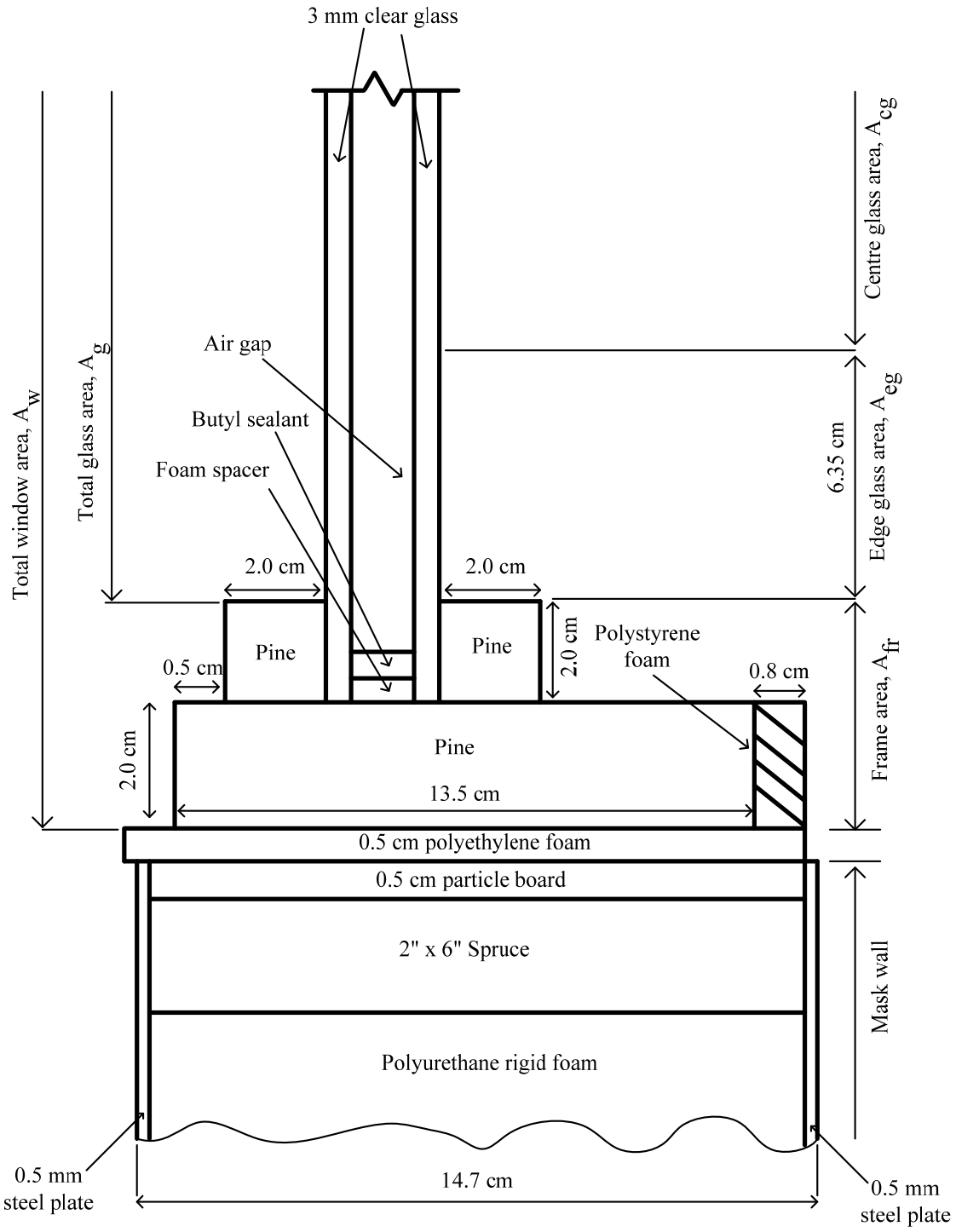

Figure 10.2: Cross-Sectional Details of Window and Mask Wall Mounting

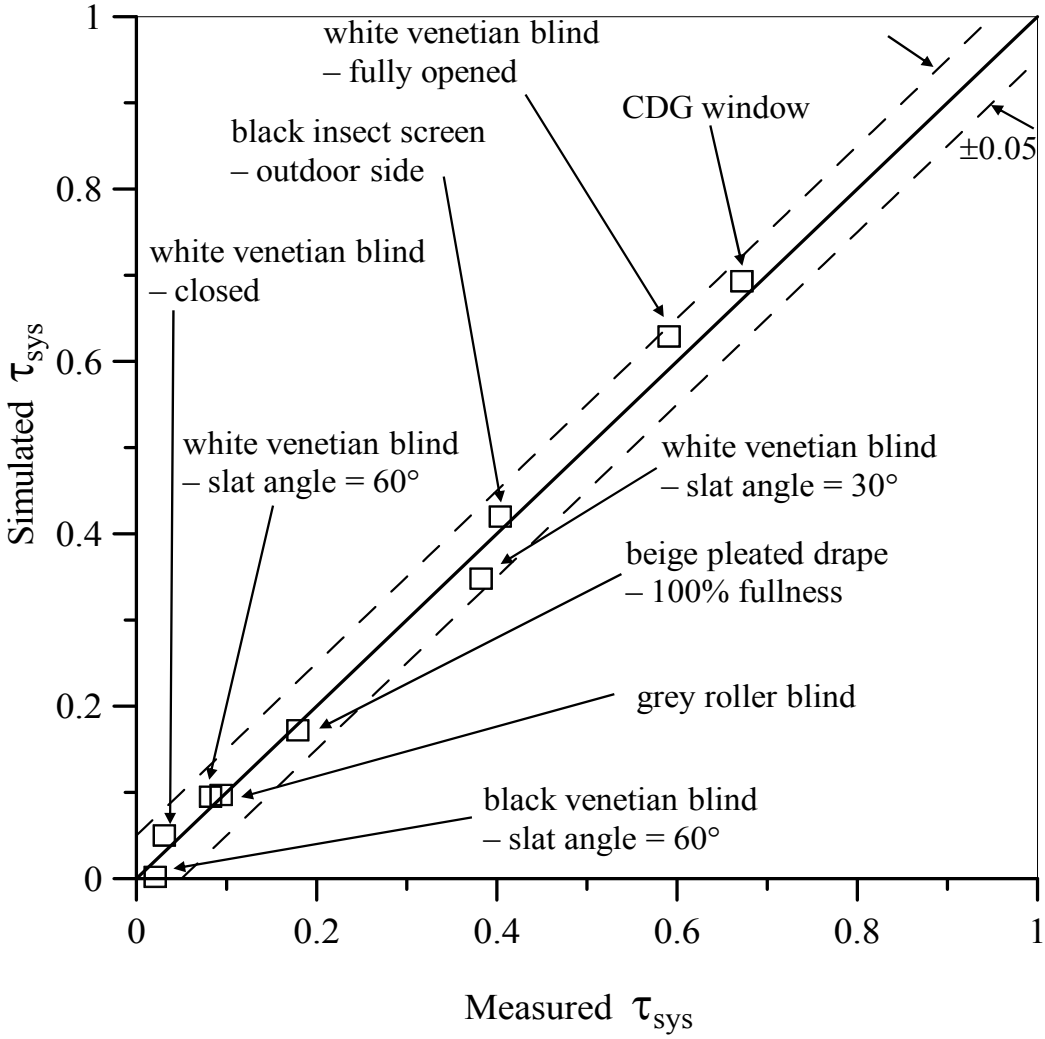

Figure 10.3: Comparison of Centre-Glass τ_{sys} Values, Simulation versus Measurements, Normal Incidence, Various Shading Layers attached to CDG Window

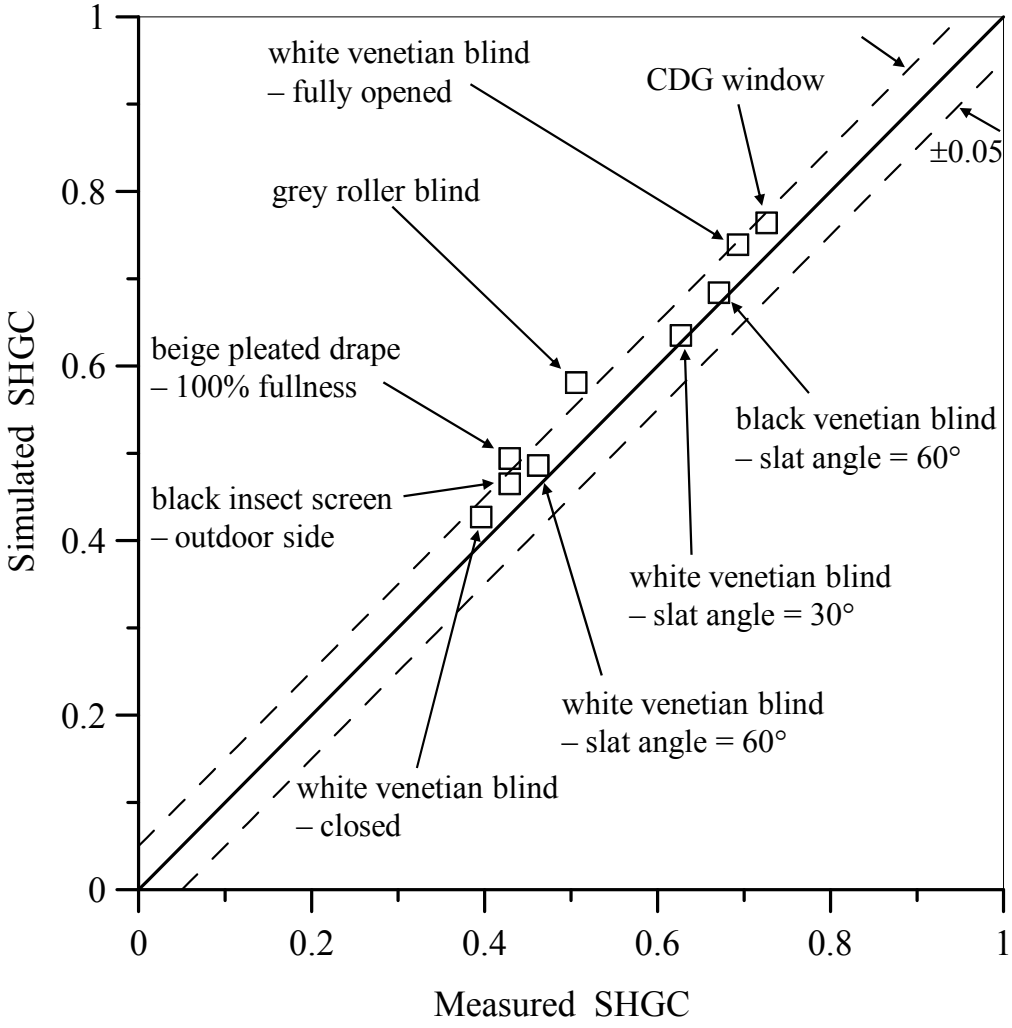

Figure 10.4: Comparison of Centre-Glass SHGC Values, Simulation versus Measurements, Normal Incidence, Various Shading Layers attached to CDG Window

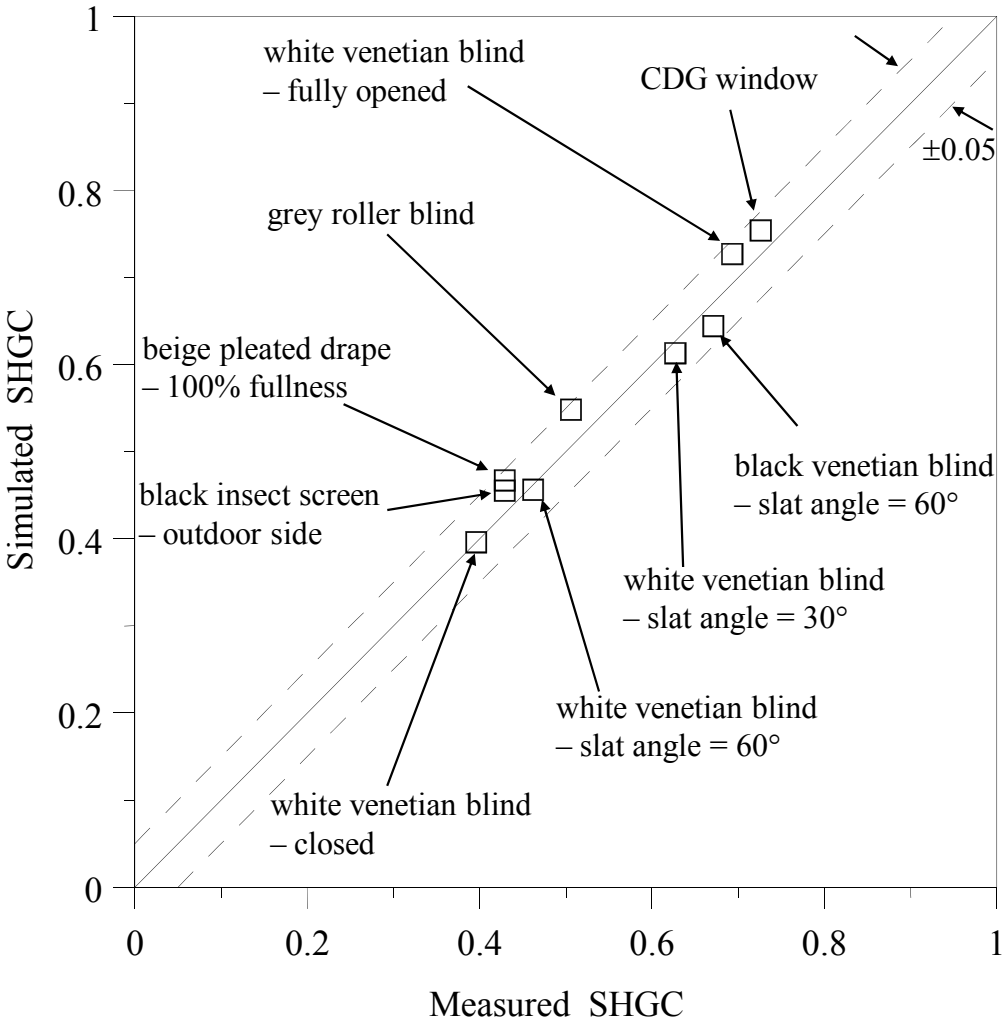

Figure 10.5: Comparison of Recalculated and Measured Centre-Glass SHGC Values, Normal Incidence, Various Shading Layers attached to CDG Window

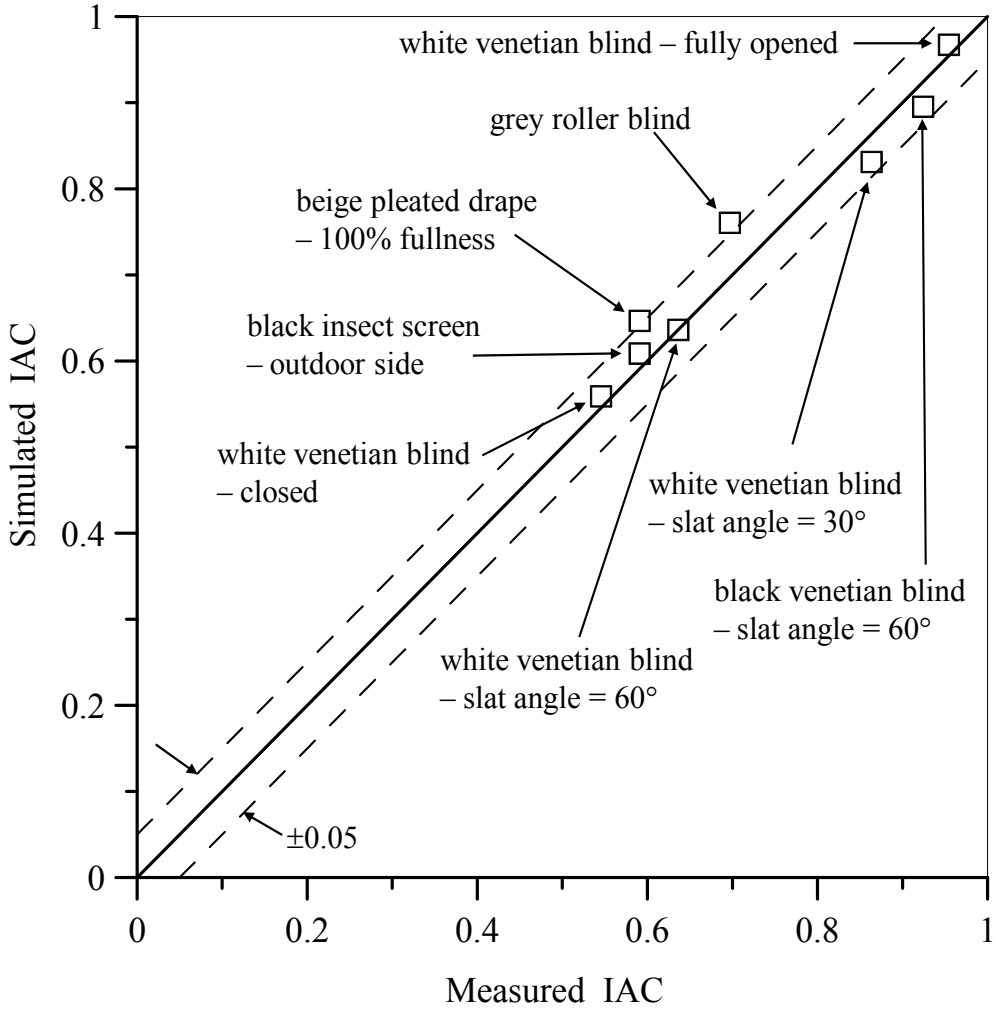

Figure 10.6: Comparison of Centre-Glass IAC values, Simulation versus Measurements, Normal Incidence, Various Shading Layers attached to CDG window

CHAPTER 11

SUMMARY, CONCLUSIONS AND RECOMMENDATIONS

11.1 Summary and Conclusions

Solar gain through a window represents the most variable heat gain imposed on the indoor space. It is also likely to represent the largest heat gain. Therefore, window solar gain can strongly influence building energy consumption and peak cooling load. Shading devices such as venetian blinds, roller blinds and drapes are routinely used to control solar gain since they offer the potential for significant energy savings. In addition, insect screens are frequently attached to windows, particularly in residential building and recent studies have revealed that insect screens have a significant influence on solar gain. Thus, there is a strong need for models that allow shading layers to be included in glazing system analysis.

In the current research, the energy performance of windows with shading devices was modeled using a two step procedure. In the first step, solar radiation was considered. A multi-layer solar optical model was developed by extending existing model for systems of specular glazing layers to include the effect of layers that create scattered, specifically diffuse, radiation in reflection and/or transmission. Spatially-averaged (effective) optical properties were used to characterise shading layers, including their beam-diffuse split. Using effective optical properties and a beam/diffuse split of solar radiation at each layer, the framework

used to represent multi-layer systems provides virtually unlimited freedom to consider different types of shading layers. The multi-layer solar optical model estimates the system solar transmission and absorbed solar components. The absorbed solar components appear as energy source terms in the second step – the heat transfer analysis. The heat transfer analysis involves the formulation of energy balance equations and requires both effective longwave properties and convective heat transfer coefficients as input. The simultaneous solution of the energy balance equations yields the temperature as well as the convective and radiative fluxes.

To obtain the effective solar optical properties of flat materials like drapery fabrics, roller blinds and insect screens a new measurement technique was developed. Special sample holders were designed and fabricated to facilitate measurements using an integrating sphere installed in a commercially available spectrophotometer. Semi-empirical models were then developed to quantify the variation of solar optical properties with respect to incidence angle. In turn, effective layer properties of venetian blinds and pleated drapes were modeled using a more fundamental net radiation scheme.

To obtain the effective longwave properties of flat materials, measurements were taken with an infrared reflectometer using two backing surfaces. The results showed emittance and longwave transmittance to be simple functions of openness, emittance and longwave transmittance of the structure. In turn, effective longwave properties of venetian blinds and pleated drapes were modeled using a net radiation scheme. Convective heat transfer correlations were obtained from the literature.

To validate the newly developed models, solar gain through various shading devices attached to a double glazed window was measured using the NSTF solar simulator and solar calorimeter. Solar gain results were also obtained from simulation software that incorporated the models. There was very good agreement between the measured and the simulated results thus strengthening confidence in the models.

The wealth of new information is most evident in the rate of technical publication. Ten refereed technical papers including seven journal and three conference papers have been published on topics related to this research.

11.2 Innovative Contribution to Window Research

Several findings that represent significant contribution to this window research include:

- a multi-layer solar optical analysis that can accommodate beam and diffuse radiation components

- a method to measure off-normal, beam and diffuse components of solar reflection and transmission for drapery fabric, roller blind material and insect screens

- correlations with which the off-normal solar optical properties of drapery fabric, roller blind material and insect screens can be calculated

- models with which the off-normal solar optical properties of venetian blinds and pleated drapes can be calculated

- a simple method to estimate longwave properties of flat shading layer materials

The multi-layer framework also offers the possibility for the development of additional shading layer models with relatively little effort. The set of shading layers considered represents a comprehensive shading capability that is suitable for time-step building energy analysis and has been incorporated in the ASHRAE Toolkit.

11.3 Recommendations for Future Research

Several suggestions for future research include:

- extending off-normal solar optical measurements to a higher range of incidence angle.

- developing a more general theory regarding off-normal solar properties of drapery fabrics, roller blinds and perhaps insect screens

- expanding the set of shading layer models as demand arises - many innovative devices are being brought to market (e.g., sheer blinds)

- implementing recently developed window/shading models within the framework of building energy simulation tools like the Environmental Systems Performance-research (ESP-r) software

- examining the impact of different types of shading devices, their location and their optical characteristics on peak cooling load and annual energy consumption

- exploring different control strategies for shading devices to admit or reject solar energy

APPENDIX A
INTEGRATING SPHERE THEORY

A.1 Introduction

This appendix outlines the integrating sphere theory. As stated in Chapter 3, an integrating sphere is an optical device that is primarily used to spatially integrate radiant flux. It is simply a hollow sphere with its inner surface coated with a material with high and uniformly diffuse reflectance. It has an inlet port to admit light and an exit port where the light may leave the sphere. Radiation detectors attached to small openings on the sphere wall receive an integrated signal. In principle, integrating sphere theory is based on the following assumptions (ANSI/ASHRAE 74-1988):

- The sphere coating is uniform in reflectance over the entire inner surface of the sphere
- The sphere coating is a perfectly lambertian reflector
- For incoming beam radiation, none of the reflected flux reaches the detector without being reflected at least twice by the sphere wall.
- For incoming diffuse radiation, none of the reflected flux reaches the detector without being reflected at least once by the sphere wall.

Although none of the above assumptions can be achieved in practice, measurement error can significantly be minimized through proper design.

A.2 Radiation Exchange between Elemental Areas within a Diffusing Sphere

Integrating sphere theory can be explained by considering radiation exchange between elemental areas within a diffusing sphere (e.g., Labsphere 1998). For a sphere with radius, R, and elemental areas dA_1 and dA_2 at a distance S apart as seen in Figure A.1, it can be shown that the fraction of radiation leaving dA_1 that arrives at dA_2 is given by

$$dF_{A1-A2} = \frac{dA_2}{4\pi \cdot R^2} \tag{A1}$$

dF_{A1-A2} is also known as the exchange factor. It is evident from Equation A1 that the exchange factor does not depend on the view angle as well as the location and distance between the two elemental areas. Thus, the fraction of radiation leaving a point on the sphere that is received by another point is the same regardless of the location of the two points. Diffuse radiation leaving any part of the sphere is uniformly distributed over the entire sphere surface.

If elemental areas dA_1 and dA_2 are replaced by finite areas A_1 and A_2 it can be shown that

$$F_{A1-A2} = \frac{A_2}{A_S} \tag{A2}$$

where $A_S = 4\pi \cdot R^2$, is the surface area of the sphere. Equation A2 states that the fraction of radiation received by A_2 is equal to the fraction of the surface area it occupies in the sphere.

A.3 Response of the Integrating Sphere

Consider an integrating sphere with an inlet port with area, A_{in}, and a sphere surface area, A_S, as shown in Appendix Figure A.2. Let I_{in} be the incoming flux while J_∞^{ref} is radiosity at any point on the inner surface of the sphere. For this analysis, consider J_∞^{ref} to be within the field of view of the detector as shown in the figure. By definition, the response of the sphere is the ratio of J_∞^{ref} and I_{in}. Thus for a unit value of I_{in}, the response of the sphere is simply equal to J_∞^{ref}.

To determine the value of J_∞^{ref} we consider multiple reflections within the sphere. If ρ is the reflectance of the sphere wall then neglecting losses through the ports, the flux leaving the sphere wall after the first reflection, J_1 is given by:

$$J_1 = I_{in} \frac{A_{in}}{A_S} \rho \tag{A3}$$

By the same token, the flux leaving the sphere wall after the second reflection, J_2, is:

$$J_2 = J_1\rho = I_{in}\frac{A_{in}}{A_S}\rho^2 \tag{A4}$$

It follows that after infinite reflections, the total flux leaving any point on the sphere wall is simply the sum of all the fluxes, i.e.,

$$J_\infty^{ref} = I_{in}\frac{A_{in}}{A_S}\rho + I_{in}\frac{A_{in}}{A_S}\rho^2 + I_{in}\frac{A_{in}}{A_S}\rho^3 + ... \tag{A5a}$$

$$J_\infty^{ref} = I_{in}\frac{A_{in}}{A_S}\rho\left(1 + \rho + \rho^2 + \rho^3 + ...\right) \tag{A5b}$$

Since $|\rho| < 1$, the sum of this geometric series is

$$J_\infty^{ref} = I_{in}\frac{A_{in}}{A_S}\rho\left(\frac{1}{1-\rho}\right) \tag{A6}$$

Again, for I_{in} equal to unity, the response of the sphere is given by

$$J_\infty^{ref} = \frac{A_{in}}{A_S}\rho\left(\frac{1}{1-\rho}\right) \tag{A7}$$

Equation A7 shows that the response of the sphere is a function of the sphere geometry and the reflectance of the sphere wall. Since $(1-\rho) < \rho$, the response of the sphere is magnified as a result of multiple reflections.

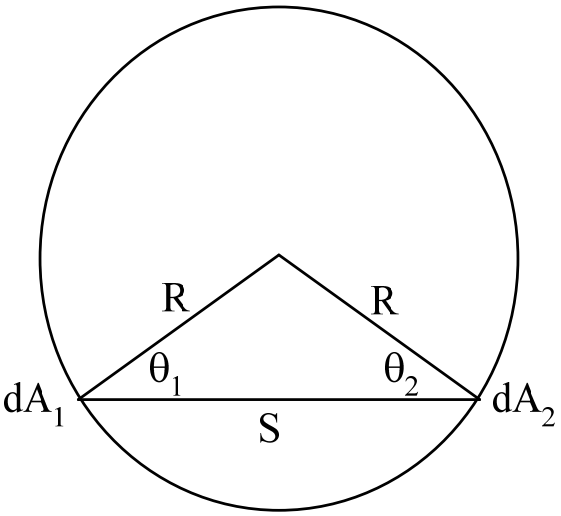

Appendix Figure A.1: Radiation Exchange in a Spherical Enclosure

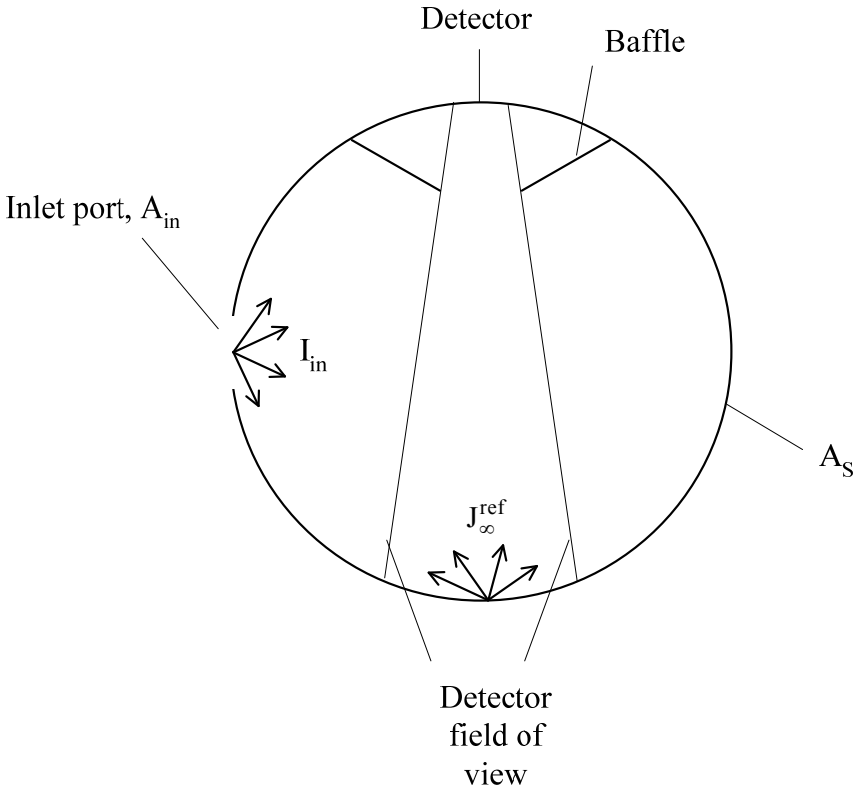

Appendix Figure A.2: Integrating Sphere showing Incident Flux and Radiosity on the Wall

APPENDIX B
UNCERTAINTY ANALYSIS

B.1 Introduction

A measurement or an experimental error is simply the difference between the measured value and the true value of a variable. By definition, uncertainty is an estimate of the experimental error. In this appendix, an uncertainty analysis pertaining to all measurements taken in this research is provided. The measurements include solar and longwave properties of flat shading materials as well as SHGC and τ_{sys} of various shading devices attached to a CDG window. First, systematic (bias) and random (precision) components of uncertainty were considered separately for each measured variable. Then by using the method of Coleman and Steele (1999), the separate propagation of the systematic and random uncertainties into the final results were estimated. Finally, the overall uncertainty was computed from the root-sum-square (RSS) combination of the systematic and random uncertainties in the intermediate results.

Since the technique used to obtain off-normal solar properties is new, particular attention is devoted to the investigation of bias errors that might be at play. Both theoretical analysis and experimentation were considered in the quantification of these possible sources of bias errors. In all cases, however, it was found that these sources of bias errors were small and were generally eliminated by calibration.

B.2 Overview of the Detailed Uncertainty Analysis

To begin, all elemental sources of bias and precision errors in each measured variable are considered separately. By definition, a bias is a fixed error that can be reduced by calibration. However, the bias that is inherent in the reference or standard used in the calibration will always be present in the output of a calibrated instrument. On the other hand, a precision error is a variable error that can be reduced by taking multiple readings.

Suppose that the final result sought in an experiment, R, depends on the measured variables, $X_1, X_2, ..., X_n$. The data reduction equation can be expressed as

$$R = R(X_1, X_2, ..., X_n) \tag{B1}$$

The goal here is to estimate the overall uncertainty in R due to the separate propagation of systematic and random uncertainties in the measured variables, X_i. The overall uncertainty in R, U_R, is given by:

$$U_R^2 = B_R^2 + P_R^2 \tag{B2}$$

where B_R and P_R are the respective systematic and random uncertainties in R.

Given the data reduction equation, it can be shown that (Coleman and Steele 1999):

$$B_R^2 = \sum_{i=1}^{n}\left(\frac{\partial R}{\partial X_i} B_{X_i}\right)^2 + 2\sum_{i=1}^{n-1}\sum_{j=i+1}^{n} \frac{\partial R}{\partial X_i}\frac{\partial R}{\partial X_j} B_{X_{ij}} \tag{B3}$$

and

$$P_R^2 = \sum_{i=1}^{n}\left(\frac{\partial R}{\partial X_i}P_{X_i}\right)^2 + 2\sum_{i=1}^{n-1}\sum_{j=i+1}^{n}\frac{\partial R}{\partial X_i}\frac{\partial R}{\partial X_j}P_{X_{ij}} \tag{B4}$$

where B_{X_i} and P_{X_i} are the respective systematic and random uncertainties in the measured variables X_i; $B_{X_{ij}}$ is the covariance estimator for the systematic uncertainties in X_i and X_j; $P_{X_{ij}}$ is the covariance estimator for the random uncertainties in X_i and X_j. The covariance estimators are typically calculated for correlated uncertainties, i.e., uncertainties that are dependent on each other as a result of measured variables sharing some identical sources of error. The values of $B_{X_{ij}}$ and $P_{X_{ij}}$ are respectively estimated using Equations B5 and B6.

$$B_{X_{ij}} = \sum_{\alpha=1}^{L}(B_{X_j})_\alpha(B_{X_j})_\alpha \tag{B5}$$

$$P_{X_{ij}} = \sum_{\alpha=1}^{L}(P_{X_j})_\alpha(P_{X_j})_\alpha \tag{B6}$$

where L is the number of identical sources of error for variables X_i and X_j.

In most instances, measurements of different variables do not share common sources of errors and each covariance estimator can be taken as zero. Under such conditions, Equations B3 and B4 reduce to Equations B7 and B8.

$$B_R^2 = \sum_{i=1}^{n} \left(\frac{\partial R}{\partial X_i} B_{X_i} \right)^2 \tag{B7}$$

and

$$P_R^2 = \sum_{i=1}^{n} \left(\frac{\partial R}{\partial X_i} P_{X_i} \right)^2 \tag{B8}$$

Also note that the ASME/ANSI Standards (Abernethy et al. 1985) recommend the use of Equations B7 and B8 as a standard approach to uncertainty calculation and disregard the expressions that include covariance estimators.

In certain instances, the uncertainty estimates are required as fractions (or percentages) of readings rather than in scientific units. Such estimates, termed relative uncertainties can readily be obtained by recasting Equations B7 and B8 in the form:

$$\left(\frac{B_R}{R} \right)^2 = \sum_{i=1}^{n} \left(\frac{X_i}{R} \frac{\partial R}{\partial X_i} \frac{B_{X_i}}{X_i} \right)^2 \tag{B9}$$

and

$$\left(\frac{P_R}{R} \right)^2 = \sum_{i=1}^{n} \left(\frac{X_i}{R} \frac{\partial R}{\partial X_i} \frac{P_{X_i}}{X_i} \right)^2 \tag{B10}$$

where $\frac{B_R}{R}$ and $\frac{P_R}{R}$ are the respective relative systematic and random uncertainties in the results while $\frac{B_{X_i}}{X_i}$ and $\frac{P_{X_i}}{X_i}$ are the respective relative systematic and random uncertainties in the measured variable.

In general, elemental systematic uncertainties in X_i can be obtained from instrument manufactures' specifications, previous experience of the experimenter and of others, analytical estimates and comparison of measurements with known values. These elemental uncertainties are then combined using RSS method to obtain the systematic uncertainty, B_{X_i}. Sometimes, overall uncertainty in the measured variable, U_{X_i}, may be reported in tables, charts, curve-fit equations and the like. The value of U_{X_i} has both random and systematic components already built into it. In such instances, the value of U_{X_i} is considered as a "fossilized" systematic uncertainty and is assigned to the value of B_{X_i}.

The random uncertainty, P_{X_i}, can be estimated from multiple readings of the variable, X_i using statistical analysis. At 95% confidence level, Coleman and Steele (1999) estimate P_{X_i} as:

$$P_{X_i} = \frac{tS_{X_i}}{\sqrt{N_i}} \tag{B11}$$

where S_{X_i} is standard deviation of N_i different readings. The value of t is obtained from t-distribution tables at 95% confidence level with $N_i - 1$ degrees of freedom. For $N_i \geq 10$, t is generally assigned a value of 2. For instances where multiple readings are not available, P_{X_i} is often taken as one-half of the least scale division for analog instruments and one-half of the least digit for digital instruments.

Alternately, the value of P_R can be determined directly from statistical analysis of N values of the results, R, giving

$$P_R = \frac{tS_R}{\sqrt{N}} \tag{B12}$$

where S_R is the standard deviation.

B.3 Determining the Uncertainty in Solar Heat Gain Coefficient

Applying uncertainty analysis, the estimation of the uncertainty in $SHGC_g$ is illustrated below.

Recall the expression for $SHGC_g$:

$$SHGC_g = \frac{A_w}{A_g} SHGC_w \tag{10.13}$$

The systematic uncertainty, B_{SHGC_g}, was calculated as:

$$B_{SHGC_g}^2 = \left(\frac{\partial(SHGC_g)}{\partial A_w} B_{A_w} \right)^2 + \left(\frac{\partial(SHGC_g)}{\partial A_g} B_{A_g} \right)^2 + \left(\frac{\partial(SHGC_g)}{\partial SHGC_w} B_{SHGC_w} \right)^2 \quad \text{(B13)}$$

which simplifies to:

$$B_{SHGC_g}^2 = \left(\frac{SHGC_w}{A_g} \cdot B_{A_w} \right)^2 + \left(\frac{SHGC_g}{A_g} \cdot B_{A_g} \right)^2 + \left(\frac{A_w}{A_g} \cdot B_{SHGC_w} \right)^2 \quad \text{(B14)}$$

The values of B_{A_w} and B_{A_g} were calculated using expressions for A_w and A_g, i.e.,

$$A_w = w_w \cdot h_w \quad \text{(B15)}$$

$$A_g = w_g \cdot h_g \quad \text{(B16)}$$

where w_w, h_w, w_g and h_g are the width of window, height of window, width of total glass area and height of total glass area, respectively.

Thus,

$$B_{A_g}^2 = \left(w_g \cdot B_{h_g} \right)^2 + \left(h_g \cdot B_{w_g} \right)^2 \quad \text{(B17)}$$

$$B_{A_w}^2 = \left(w_w \cdot B_{h_w} \right)^2 + \left(h_w \cdot B_{w_w} \right)^2 \quad \text{(B18)}$$

The value of B_{SHGC_w} was estimated from an expression for $SHGC_w$. Using Equations 10.7, 10.8 and 10.9, $SHGC_w$ was expressed as:

$$SHGC_w = \frac{Q_{abs} + Q_{mw} + Q_{al} - Q_{inp} + Q_{ht}}{A_w \cdot G_{inc}} \quad \text{(B19)}$$

Generally, the magnitudes of Q_{mw} and Q_{al} are such that they can be neglected. Hence Equation B19 simplifies to

$$SHGC_w = \frac{Q_{abs} - Q_{inp} + Q_{ht}}{A_w G_{inc}} \tag{B20}$$

Thus,

$$B_{SHGCw}^2 = \left(\frac{\partial(SHGC_w)}{\partial Q_{abs}} B_{Q_{abs}}\right)^2 + \left(\frac{\partial(SHGC_w)}{\partial Q_{inp}} B_{Q_{inp}}\right)^2 + \left(\frac{\partial(SHGC_w)}{\partial Q_{ht}} B_{Q_{ht}}\right)^2$$

$$+ \left(\frac{\partial(SHGC_w)}{\partial G_{inc}} B_{G_{inc}}\right)^2 + \left(\frac{\partial(SHGC_w)}{\partial A_w} B_{A_w}\right)^2 \tag{B21}$$

which simplifies to:

$$B_{SHGCw}^2 = \left(\frac{B_{Q_{abs}}}{A_w G_{inc}}\right)^2 + \left(\frac{B_{Q_{inp}}}{A_w G_{inc}}\right)^2 + \left(\frac{B_{Q_{ht}}}{A_w G_{inc}}\right)^2$$

$$+ \left(\frac{SHGC_w \cdot B_{G_{inc}}}{G_{inc}}\right)^2 + \left(\frac{SHGC_w \cdot B_{A_w}}{A_w}\right)^2 \tag{B22}$$

Following a similar methodology and using the expressions for Q_{abs}, Q_{ht} and Q_{inp} (Equations 10.10, 10.11 and 10.12), the values of $B_{Q_{abs}}$, $B_{Q_{ht}}$ and $B_{Q_{inp}}$ were obtained as:

$$B_{Q_{abs}}^2 = \left(\Delta T_{abs} \cdot B_{\dot{m}C_p}\right)^2 + \left(\dot{m}C_p \cdot B_{\Delta T_{abs}}\right)^2 \tag{B23}$$

$$B_{Q_{abs}}^2 = \left(U_w \cdot \Delta T_w \cdot B_{A_w}\right)^2 + \left(U_w \cdot A_w \cdot B_{\Delta T_w}\right)^2 + \left(A_w \cdot \Delta T_w \cdot B_{U_w}\right)^2 \tag{B24}$$

$$B_{Q_{inp}}^2 = \left(B_{Q_{pump}}\right)^2 + \left(B_{Q_{fan}}\right)^2 \tag{B25}$$

Since six readings were taken during the experiments and the value of $SHGC_g$ obtained as an average of these six readings, the random uncertainty, P_{SHGC_g}, at 95% confidence level was calculated as:

$$P_{SHGC_g} = \frac{tS_{SHGC_g}}{\sqrt{N}} \tag{B26}$$

Finally, the overall uncertainty, U_{SHGC_g}, was estimated using Equation B27.

$$U^2_{SHGC_g} = \left(B_{SHGC_g}\right)^2 + \left(P_{SHGC_g}\right)^2 \tag{B27}$$

B.3.1 Sample Calculation

Measurements taken for a roller blind attached to CDG window are used as an illustrative example in calculating the value of U_{SHGC_g}. Table B.1 summarises both measured and derived quantities, their nominal values and the corresponding systematic uncertainties. With the exception of w_w, h_w, w_g, h_g and U_w, all other quantities were averages of six readings taken during the experiment. The value of U_w was obtained from the current version of the ASHRAE Loads Toolkit (Barnaby et al. 2004, Pedersen et al. 2001) that incorporates the solar-thermal models (Wright et al. 2009). The systematic uncertainties listed in Table B.1. Given the systematic uncertainties of measured and derived quantities, the value of B_{SHGC_g} was calculated using Equations B13 to B25.

To calculate P_{SHGC_g}, the standard deviation, S_{SHGC_g}, was obtained from the set of six $SHGC_g$ values estimated from the measured quantities. Given $N = 6$, a t-value of 2.57 was obtained from t-distribution tables at 95% confidence level with 5 degrees of freedom. Using Equation B26, the value of P_{SHGC_g} was estimated to be 0.002. Finally, the value of U_{SHGC_g} was calculated from Equation B27 and was found to be ±0.03.

Table B.2 gives a summary of the nominal values of $SHGC_g$ and the corresponding values of U_{SHGC_g} for the CDG window as well as various shading layers attached to CDG window.

B.4 Determining the Uncertainty in System Solar Transmittance

Applying uncertainty analysis, the estimation of the uncertainty in τ_{sys} is illustrated below.

From Equation 10.14, τ_{sys} is given by

$$\tau_{sys} = \frac{G_{trans,1}}{G_{inc}} \tag{10.14}$$

The systematic uncertainty, $B_{\tau_{sys}}$, was calculated as:

$$B_{\tau_{sys}}^2 = \left(\frac{\partial \tau_{sys}}{\partial G_{trans,1}} B_{G_{trans,1}} \right)^2 + \left(\frac{\partial \tau_{sys}}{\partial G_{inc}} B_{G_{inc}} \right)^2 \tag{B28}$$

which simplifies to:

$$B_{\tau_{sys}}^2 = \left(\frac{B_{G_{trans,1}}}{G_{inc}} \right)^2 + \left(\frac{\tau_{sys}}{G_{inc}} \cdot B_{G_{inc}} \right)^2 \tag{B29}$$

Also from Equation 10.16,

$$G_{trans,1} = G_{trans,2} \left(\frac{D_2}{D_1} \right)^{1.83} \tag{10.16}$$

and the systematic uncertainty in $G_{trans,1}$ was calculated as:

$$B_{G_{trans,1}}^2 = \left(\frac{\partial G_{trans,1}}{\partial G_{trans,2}} B_{G_{trans,2}} \right)^2 + \left(\frac{\partial G_{trans,1}}{\partial D_1} B_{D_1} \right)^2 + \left(\frac{\partial G_{trans,1}}{\partial D_2} B_{D_2} \right)^2 \tag{B30}$$

which simplifies to:

$$B_{G_{trans,1}}^2 = \left(\left(\frac{D_2}{D_1} \right)^{1.83} \cdot B_{G_{trans,2}} \right)^2 + \left(1.83 \left(\frac{G_1}{D_2} \right) \cdot B_{D_2} \right)^2 + \left(1.83 \left(\frac{G_1}{D_1} \right) \cdot B_{D_1} \right)^2 \tag{B31}$$

With six readings available, the random uncertainty, $P_{\tau_{sys}}$, at 95% confidence level was calculated as:

$$P_{\tau_{sys}} = \frac{t S_{\tau_{sys}}}{\sqrt{N}} \tag{B32}$$

Finally, the overall uncertainty in $U_{\tau_{sys}}$ was estimated from

$$U_{\tau_{sys}}^2 = \left(B_{\tau_{sys}} \right)^2 + \left(P_{\tau_{sys}} \right)^2 \tag{B33}$$

B.4.1 Sample Calculation

As an illustrative example, the value of $U_{\tau_{sys}}$ was obtained using measurement taken for roller blind attached to CDG window. Nominal values of measured and derived quantities and their associated systematic uncertainties are given in Table B.3. Again, nominal values of $G_{trans,2}$ and G_{inc} were averages of six readings taken during the experiment while the values of D_1 and D_2 were taken only once. The systematic uncertainty, $B_{\tau_{sys}} = 0.01$, was estimated using Equations B29 and B31. However, the standard deviation, $S_{\tau_{sys}}$ was found to be zero and hence from Equation B32, the random uncertainty, $P_{\tau_{sys}} = 0$. Thus $U_{\tau_{sys}} = B_{\tau_{sys}} = \pm 0.01$.

A summary of $U_{\tau_{sys}}$ as well as nominal values of τ_{sys} for the CDG window as well as various shading layers attached to the CDG window is given in Table B.4.

B.5 Determining the Uncertainty in Longwave Properties

Detailed uncertainty analysis was applied in the estimation of the uncertainty in longwave properties as follows:

From Equation 7.5, the emissivity, ε, is related to the longwave transmittance, τ^{lw}, and longwave reflectance, ρ^{lw}, as

$$\varepsilon = 1 - \tau^{lw} - \rho^{lw} \tag{7.5}$$

where ρ^{lw} and τ^{lw} are given by :

$$\rho^{lw} = \frac{(\rho_{B1}/\rho_{B2})\rho_{M2} - \rho_{M1}}{(\rho_{B1}/\rho_{B2}) + \rho_{B1}(\rho_{M2} - \rho_{M1}) - 1} \tag{7.3}$$

$$\tau^{lw} = \sqrt{\frac{(\rho_{M1} - \rho^{lw})(1 - \rho^{lw}\rho_{B1})}{\rho_{B1}}} \tag{7.4}$$

Refer to Chapter 7 for the definition of the various quantities in Equations 7.3 and 7.4.

Using Equation B8, the random uncertainties in ε, ρ^{lw} and τ^{lw} were obtained from:

$$P_{\varepsilon}^2 = \left(\frac{\partial\varepsilon}{\partial\tau^{lw}} P_{\tau^{lw}}\right)^2 + \left(\frac{\partial\varepsilon}{\partial\rho^{lw}} P_{\rho^{lw}}\right)^2 \tag{B34}$$

$$P_{\rho^{lw}}^2 = \left(\frac{\partial\rho^{lw}}{\partial\rho_{B1}} P_{\rho_{B1}}\right)^2 + \left(\frac{\partial\rho^{lw}}{\partial\rho_{B2}} P_{\rho_{B2}}\right)^2 + \left(\frac{\partial\rho^{lw}}{\partial\rho_{M1}} P_{\rho_{M1}}\right)^2 + \left(\frac{\partial\rho^{lw}}{\partial\rho_{M2}} P_{\rho_{M2}}\right)^2 \tag{B35}$$

$$P_{\tau^{lw}}^2 = \left(\frac{\partial\tau^{lw}}{\partial\rho^{lw}} P_{\rho^{lw}}\right)^2 + \left(\frac{\partial\tau^{lw}}{\partial\rho_{M1}} P_{\rho_{M1}}\right)^2 + \left(\frac{\partial\tau^{lw}}{\partial\rho_{B1}} P_{\rho_{B1}}\right)^2 \tag{B36}$$

A similar set of Equations can be written for the systematic uncertainties in ε, ρ^{lw} and τ^{lw} by replacing the random uncertainty symbol, P, with the systematic uncertainty symbol, B. For each longwave property, the overall uncertainty, U, is the RSS value of P and B.

B.5.1 Sample Calculation

As an example, consider the measurement of longwave properties of the cream sheer fabric sample. Nominal values of the measured and derived quantities are listed in Table B.5. The manufacturer of the SOC 400T FTIR reflectometer has specified a reflectance repeatability

of ±0.01. This value was taken to be the random uncertainty in reflectance measurement. Thus, $P_{\rho_{B1}} = P_{\rho_{B2}} = P_{\rho_{M1}} = P_{\rho_{M2}} = 0.01$. Substituting this value of random uncertainty into Equation B35 and using MathCAD to evaluate the partial derivatives, the value of $P_{\rho^{lw}}$ was obtained. Subsequently, the value of $P_{\tau^{lw}}$ was obtained from Equation B36 again using MathCAD to evaluate the partial derivatives. Finally, the value of P_{ε} was calculated from Equations B34.

With the absence of any information on the bias of the SOC 400T FTIR reflectometer, a conservative systematic uncertainty estimate of 0.01 is suggested and a similar analysis carried out to estimate the values of $B_{\rho^{lw}}$, $B_{\tau^{lw}}$ and B_{ε} using an equations set similar to Equations B34 to B36. Finally, for each longwave property, the overall uncertainty, U, was calculated from the corresponding RSS value of P and B. Values of P , B and U so obtained from the calculations are also listed in Table B.5.

B.6 Determining the Uncertainty in Solar Properties

Uncertainty in integrating sphere measurements may be attributed to several factors and these are documented in ASTM E903-96 (1996). The uncertainty associated with the raw measurements, with or without the integrating sphere, is small. The spectrophotometer was configured as described in Chapter 3 and measurements were taken at 2 nm intervals. At each wavelength, thirty samples were taken thus the random uncertainty attached to spectral readings was well below ±0.001 at 95% confidence level. Note that the 0% and 100%

reference for transmission as well as the 0% reference for reflection are exact quantities. See Chapter 3. More significant systematic uncertainty is associated with the conversion of spectral data to solar properties. Systematic uncertainty caused by choice of solar spectrum was ignored. Since transmittance and reflectance were obtained from the ratio of sample and reference signals, correlated uncertainties in sample and reference signals tend to cancel, reducing the systematic uncertainty in transmittance and reflectance (Chakroun et al. 1993). According to ASTM E903-96 (1996), the overall uncertainty (mostly due to systematic uncertainty) associated with transmittance and reflectance measurements taken at normal incidence with an integrating sphere is typically ±0.03 at 95% confidence level.

Note that beam-total and beam-diffuse transmittance were directly measured while beam-beam transmittance is the difference between the two sets of measurements. By applying the principle of propagation of uncertainties, it can be shown that the overall uncertainty associated with beam-beam transmittance obtained with the integrating sphere is ±0.04. Details are provided in Section B.6.5. On the other hand, the overall uncertainty associated with beam-beam transmittance obtained without the integrating sphere is estimated to be ±0.02 at 95% confidence level. This estimate is considered to be conservative given the fact that majority of the systematic uncertainties in integrating sphere measurements may be attributed to the sphere design. Hence a higher uncertainty is expected for beam-beam transmittance obtained with the integrating sphere.

The technique used to achieve off-normal incidence using the integrating sphere raised questions about systematic uncertainties that might arise. However, these systematic

uncertainties were generally eliminated by calibration. Comments regarding possible sources of systematic uncertainty are included in the following subsections.

B.6.1 Using Barium Sulphate as the Reflectance Standard

The solar reflectance of barium sulphate, used as a reflectance standard in this study, was measured and found to be 2% lower than the reflectance of the PTFE reflectance standard that is customarily used with the integrating sphere. The software supplied with the spectrophotometer applies Equation 3.1 as if the PTFE is present. Therefore, a 2% correction was applied to adjust (downward) the solar reflectance measurements made when a barium sulphate reflectance was used for calibration.

B.6.2 Reduction of the Incident Beam

Preliminary investigation showed that measurements were in error by about 2% because the fixed sample holder tubes were intercepting a small portion of the incident beam. Reduction of the incident beam eliminated this error.

B.6.3 Projection of Sample Holder into the Integrating Sphere

Typical configurations for transmittance and reflectance measurements using a fixed sample holder are shown in Figure 3.8. In each case the sample holder projected into the sphere at a distance of 30 mm. Ideally, the exterior surface of the sample holder should be coated with a highly reflective coating such as PTFE or barium sulphate. Such a surface would have a very low absorptance thereby ensuring that the signal strength is not reduced. However, it was too

expensive to use PTFE coating. On the other hand, an inexpensive barium sulphate coating did not adhere well to the sample holder. A more pragmatic way of achieving a highly reflective sample holder that would not degrade the response of the sphere was to polish the exterior surface of the sample holder. However, it was not clear what an impact a polished sample holder might have on the response of the sphere.

To investigate the changes in the response of the sphere caused by the projected sample holder, a set of measurements were taken with sample holders projecting at different lengths into the sphere. Three surface finishes were considered representing the best and worst case scenarios. These were a highly polished surface with 80% reflectance, an unpolished surface with 50% reflectance and a black painted surface with 5% reflectance. Note that the reflectance of PTFE and barium sulphate are 98% and 96%, respectively. For each surface finish, a set of sample holders with projected lengths ranging from 5 to 30 mm, in 5 mm steps, were machined. Each sample holder had a 0° end angle. The following arguments are based on transmittance measurements although the same arguments pertain to reflectance measurements.

The integrating sphere was first calibrated in transmission mode. The transmittance of the sphere without any projected sample holder in place was then measured and was found to be 100% as expected. Without recalibration, a sample holder was mounted at the transmittance port with the aid of adapters and a transmittance measurement taken. This procedure was repeated for the other sample holders. Figure B.1 shows a graph of the change in response of the sphere plotted against the length of sample holder projection for the three different surface finishes considered. Note that the change in the response of the sphere in this case is

the ratio of the transmittance of the sphere with projected sample holder in place to the transmittance of the sphere without any projected sample holder. It can be seen from Figure B.1 that regardless of the surface finish, the response of the sphere decreased as the projection increased. Amongst the different surface finishes considered, the polished sample holder degraded the response of the sphere the least while the black painted sample holder degraded the sphere the most. The degradation caused by the unpolished sample holder lies between that of the polished and the black painted sample holders. At the maximum projection of 30 mm, the reduction in the response of the sphere was 3% for the polished sample holder and 4% for the black painted sample holder. Thus regardless of the surface finish, it is clear that the reduction in the response of the sphere was small.

This small reduction can further be explained by considering the amount of blockage caused by the projected sample holder in the sphere. In the worst case, the percentage of volume occupied by a 30 mm sample holder in the sphere is only 0.84% and the ratio of the surface area of the sample holder to that of the sphere is only 3.9%. Thus introducing a sample holder into the sphere creates minimal disturbance; the same kind of disturbance created by baffles that shield the detectors from direct radiation and radiation due to first reflection. Nonetheless, this systematic uncertainty that might have been caused by the presence of sample holders was eliminated by incorporating sample holders in the calibration procedure.

B.6.4 Orientation of the Sample Holder

Calibration and measurements were completed with the angled end of the sample holder facing downward, away from the detectors, as shown in Figure 3.8. This was done to be sure

that the detectors could not directly view the test sample. However, a bias error arises in the case of diffuse transmission and reflection measurements because the scattered radiation originating at the sample is not distributed uniformly over the surface of the integrating sphere and the radiation sensed by the detectors includes the first reflection of this non-uniform distribution. Using the assumption that the radiation scattered by the sample is diffuse, the following analysis is employed to ascertain the change in the response of the sphere due to this non-uniform distribution of radiation from the first reflection.

Consider a 60° sample holder having a diffusing fabric sample attached to its angled end. The sample holder is allowed to project into the sphere such that its angled end faces downward as shown in Figure B.2. Given the surface area of the sphere, A_S, the area of the inlet port, A_{in}, the diffuse flux leaving the angled end of the sample holder, I_{in}, will only illuminate a portion of the sphere with surface area, A_C. Following a similar analysis outlined in Appendix A, the flux leaving the sphere wall after the first reflection, J_1, is given by:

$$J_1 = I_{in} \frac{A_{in}}{A_C} \rho \tag{B37}$$

where ρ is the reflectance of the sphere wall. Similarly, the flux leaving the sphere wall after second reflection, J_2, is given by:

$$J_2 = \left(I_{in} \frac{A_{in}}{A_C} \rho \right) \cdot \left(\frac{A_C}{A_S} \rho \right) \tag{B38}$$

It follows that after infinite reflections, the total flux leaving at any point on the sphere, J_{∞}^{down}, is:

$$J_{\infty}^{down} = I_{in}\frac{A_{in}}{A_S}\frac{A_S}{A_C}\rho + I_{in}\frac{A_{in}}{A_S}\rho^2 + I_{in}\frac{A_{in}}{A_S}\rho^3 + ... \quad \text{(B39a)}$$

$$J_{\infty}^{down} = I_{in}\frac{A_{in}}{A_S}\rho\left(\frac{A_S}{A_C} - 1 + 1 + \rho + \rho^2 + ...\right) \quad \text{(B39b)}$$

With, $|\rho| < 1$, the sum of the geometric series is:

$$J_{\infty}^{down} = I_{in}\frac{A_{in}}{A_S}\rho\left(\frac{A_S}{A_C} - 1 + \frac{1}{1-\rho}\right) \quad \text{(B40)}$$

Recall the expression for J_{∞}^{ref}, i.e., Equation A6:

$$J_{\infty}^{ref} = I_{in}\frac{A_{in}}{A_S}\rho\left(\frac{1}{1-\rho}\right) \quad \text{(A6)}$$

Thus the change in the response of the sphere when the 60° sample holder faces downwards can be obtained by dividing Equation B40 by Equation A6, i.e.,

$$\frac{J_{\infty}^{down}}{J_{\infty}^{ref}} = \frac{I_{in}\frac{A_{in}}{A_S}\rho\left(\frac{A_S}{A_C} - 1 + \frac{1}{1-\rho}\right)}{I_{in}\frac{A_{in}}{A_S}\rho\left(\frac{1}{1-\rho}\right)} \quad \text{(B41a)}$$

which simplifies to:

$$\frac{J_{\infty}^{down}}{J_{\infty}^{ref}} = \rho\left(1 - \frac{A_S}{A_C}\right) + \frac{A_S}{A_C} \tag{B41b}$$

Substituting the value of $\rho = 0.98$ and $\frac{A_S}{A_C} = 1.885$ into Equation B41b, $\frac{J_{\infty}^{down}}{J_{\infty}^{ref}} = 1.017$.

From Equation B41b, it can be seen that the correction factor due to the change in the response of the sphere will tend to unity as the fabric sample is moved closer to the sphere wall ($A_C \to A_S$) as or as the reflectance of the sphere approaches unity ($\rho \to 1$).

If the sample holder is oriented to face upwards as shown in Figure B.3, the diffuse flux leaving the fabric sample will illuminate a portion of the sphere surface outside the detector field of view. Thus the radiosity after the first reflection, $J_1 = I_{in}\frac{A_{in}}{A_C}\rho$ will be absent from the infinite series of reflections. The radiosity, J_{∞}^{up}, in this case is given by:

$$J_{\infty}^{up} = I_{in}\frac{A_{in}}{A_S}\rho^2 + I_{in}\frac{A_{in}}{A_S}\rho^3 + ... \tag{B42a}$$

$$J_{\infty}^{up} = I_{in}\frac{A_{in}}{A_S}\rho^2\left(1 + \rho + \rho^2 .....\right) \tag{B42b}$$

$$J_{\infty}^{up} = I_{in}\frac{A_{in}}{A_S}\rho^2\left(\frac{1}{1-\rho}\right) \tag{B42c}$$

Comparing Equations B39a and B42a, it can be seen that $J_{\infty}^{down} > J_{\infty}^{up}$, since the first reflection does not contribute to the radiosity when the sample holder faces upwards. It can

be speculated that if the sample holder is positioned to face the left or the right side of the sphere, only half of the first reflection will contribute to the radiosity.

If the response of the sphere at different orientations of the sample holder is compared to the response when the sample holder faces downwards, an interesting trend is observed. Typically, the ratio between J_{∞}^{up} and J_{∞}^{down} is given by

$$\frac{J_{\infty}^{up}}{J_{\infty}^{down}} = \frac{I_{in}\frac{A_{in}}{A_S}\rho^2\left(\frac{1}{1-\rho}\right)}{I_{in}\frac{A_{in}}{A_S}\rho\left(\frac{A_S}{A_C}-1+\frac{1}{1-\rho}\right)} \tag{B43a}$$

which simplifies to:

$$\frac{J_{\infty}^{up}}{J_{\infty}^{down}} = \frac{\rho}{\frac{A_S}{A_C}(1-\rho)+\rho} \tag{B43b}$$

Again, substituting the values of $\rho = 0.98$ and $\frac{A_S}{A_C} = 1.89$ into Equation B43b, $\frac{J_{\infty}^{up}}{J_{\infty}^{down}} = 0.963$. From the above theory, it is expected that $\frac{J_{\infty}^{left}}{J_{\infty}^{down}}$ and $\frac{J_{\infty}^{right}}{J_{\infty}^{down}}$ have values between 0.963 and 1.0 where J_{∞}^{left} and J_{∞}^{right} are the responses of the sphere when the sample holder faces the left and the right side of the sphere, respectively.

To further investigate the change in the response of the sphere caused by a sample holder at various orientations, a set of measurements were obtained. The following arguments are based on reflectance measurements although the same arguments pertain to transmittance measurements. First, the integrating sphere was calibrated in the reflection mode with a pre-fabricated barium sulphate reflectance reference sample positioned normal to the incident beam. The reflectance of the barium sulphate reference was subsequently measured. Without recalibration, a set of reflectance measurements were taken on each of the reflectance references described in Section 3.4.4 facing up, down, left and right. The results are summarised in Table B.6. Note that the results in Table B.6 represent the change in the response of the sphere at different orientation relative to the case where the sample holder faces downwards. By presenting the results relative to the downward facing orientation, the sphere response due to the projected length is completely eliminated in this orientation comparison. For each reflectance reference considered, the response of the sphere is highest in the downward facing position as compared to the upward facing position. In addition, the response of the sphere for the right-facing or the left-facing sample holder lies somewhere between the up-facing and the down-facing reflectance reference. This is the expected trend based on the theory outlined above.

Note that the bias error introduced by the orientation of the sample holder in the sphere is so small (typically about 1%) and was eliminated by calibration.

B.6.5 Uncertainty in Beam-Beam Transmittance

The integrating sphere was used to measure beam-total transmittance, τ_{bt}, and beam-diffuse transmittance, τ_{bd}. Beam-beam transmittance, τ_{bb}, was subsequently obtained as the difference between τ_{bt} and τ_{bd}, i.e.,

$$\tau_{bb} = \tau_{bt} - \tau_{bd} \tag{B44}$$

Thus for τ_{bb} measurements with the integrating sphere, the principle of propagation of uncertainties was applied to Equation B44 to obtain the systematic uncertainty, $B_{\tau_{bb}}$, as:

$$B_{\tau_{bb}}^2 = \left(\frac{\partial \tau_{bb}}{\partial \tau_{bt}} B_{\tau_{bt}}\right)^2 + \left(\frac{\partial \tau_{bb}}{\partial \tau_{bd}} B_{\tau_{bd}}\right)^2 \tag{B45}$$

which simplifies to:

$$B_{\tau_{bb}}^2 = B_{\tau_{bt}}^2 + B_{\tau_{bd}}^2 \tag{B46}$$

Substituting $B_{\tau_{bt}} = B_{\tau_{bd}} = 0.03$ into Equation B46 gives $B_{\tau_{bb}} = 0.04$. Once again, the random uncertainty, $P_{\tau_{bb}}$, is negligibly small and the overall uncertainty, $U_{\tau_{bb}} = B_{\tau_{bb}} = \pm 0.04$.

However, if relative uncertainties are considered, an intriguing result is obtained. Applying Equation B9 to Equation B44, the expression for the relative systematic uncertainty, $\frac{B_{\tau_{bb}}}{\tau_{bb}}$, is given by

$$\left(\frac{B_{\tau_{bb}}}{\tau_{bb}}\right)^2 = \left(\frac{\tau_{bt}}{\tau_{bb}}\frac{B_{\tau_{bt}}}{\tau_{bt}}\right)^2 + \left(\frac{\tau_{bd}}{\tau_{bb}}\frac{B_{\tau_{bd}}}{\tau_{bd}}\right)^2 \tag{B47}$$

which simplifies to

$$\left(\frac{B_{\tau_{bb}}}{\tau_{bb}}\right)^2 = \left(\frac{B_{\tau_{bt}}}{\tau_{bb}}\right)^2 + \left(\frac{B_{\tau_{bd}}}{\tau_{bb}}\right)^2 \tag{B48}$$

Equation B48 reveals that as $\tau_{bb} \to 0$, $\frac{B_{\tau_{bb}}}{\tau_{bb}} \to \infty$; an intolerable uncertainty for practical purposes. At first glance, the forgoing result raises some concern regarding the integrating sphere method of obtaining reliable values of τ_{bb} from measurements of τ_{bt} and τ_{bd} especially for cases where $\tau_{bb} \to 0$. To address this issue, an alternate method was devised to directly measure τ_{bb} without using the integrating sphere. See Section 3.4.6. This method is much more reliable as the associated overall uncertainty was estimated to be ±0.02. Regardless, the comparison between τ_{bb} measurements made with and without the integrating sphere shows no appreciable difference. Generally, the discrepancies between the two sets of measurements did not exceed ±0.04; the stated uncertainty associated with

measurements made with the integrating sphere. The observed agreement further strengthens the credibility of the measurements made using the fixed sample holders in the integrating sphere although relative uncertainty estimate tends to show otherwise.

Appendix Table B.1: Summary of Uncertainty Estimates used in Calculating for Roller Blind attached to CDG Window

Measured quantity	Symbol	Units	Value	Systematic Uncertainty
[1]Pump power + fan power	Q_{inp}	W	34.1	1.00
[1]Temperature difference across window	ΔT_w	K	1.5	0.5
Width of window	w_w	m	1.665	0.003
Height of window	h_w	m	1.665	0.003
Width of centre glass	w_{cg}	m	1.590	0.003
Height of centre glass	h_w	m	1.590	0.003
[2]Window U-factor	U_w	W/m^2K	2.56	0.13
[1]Mass flow rate-specific heat capacity product	mC_p	W/K	95.30	0.95
[1]Temperature difference across absorber	ΔT_{abs}	K	4.2	0.2
[1]Incident solar radiation	G_{inc}	W/m^2	292.0	5.8
Derived quantity				
Area of window	A_w	m^2	2.772	0.007
Area of centre glass	A_{cg}	m^2	2.528	0.007
Heat transfer across window	Q_{ht}	W	10.65	3.59
Heat transfer across absorber	Q_{abs}	W	405.0	19.48
Solar Heat Gain Coefficient of window	$SHGC_w$	-	0.460	0.03
Solar Heat Gain Coefficient of centre glass	$SHGC_g$	-	0.504	0.03

[1]Uncertainty in these quantities include the uncertainty in the sensor and associated instumentation and the values were supplied by the NSTF staff

[2]Uncertainty was supplied by the NSTF staff

Appendix Table B.2: Summary of Uncertainty Estimates in SHGC for Various Shading Layers attached to CDG Window

Sample Description	SHGC	Uncertainty in SHGC
CDG window	0.73	±0.03
CDG window + black insect screen	0.43	±0.02
CDG window + beige pleated drape (100% fullness)	0.43	±0.02
CDG window + white venetian blind (closed)	0.40	±0.03
CDG window + white venetian blind (fully opened)	0.69	±0.03
CDG window + white venetian blind (slat angle = 30°)	0.63	±0.03
CDG window + white venetian blind (slat angle = 60°)	0.46	±0.03
CDG window + grey roller blind	0.51	±0.03
CDG window + black venetian blind (slat angle = 60°)	0.67	±0.04

Appendix Table B.3: Summary of Uncertainty Estimates used in Calculating for Roller Blind attached to CDG Window

Measured quantity	Symbol	Units	Value	Systematic Uncertainty
[1]Transmitted solar radiation at location 2	$G_{trans,2}$	W/m^2	23.8	1.2
[1]Incident solar radiation	G_{inc}	W/m^2	292.0	5.8
Distance between solar simulator and location 1	D_1	m	5.160	0.200
Distance between solar simulator and location 2	D_2	m	5.590	0.200
Derived quantity				
Transmitted solar radiation at location 1	$G_{trans,1}$	W/m^2	27.5	3.0
System transmittance	τ_{sys}	-	0.09	0.01

[1]Uncertainty in these quantities include the uncertainty in the sensor and associated instumentation and the values were supplied by the NSTF staff

Appendix Table B.4: Summary of Uncertainty Estimates for Various Shading Layers attached to CDG Window

Sample Description	τ_{sys}	Uncertainty in τ_{sys}
CDG window	0.67	±0.05
CDG window + black insect screen	0.40	±0.03
CDG window + beige pleated drape (100% fullness)	0.18	±0.01
CDG window + white venetian blind (closed)	0.03	±0.00
CDG window + white venetian blind (fully opened)	0.59	±0.04
CDG window + white venetian blind (slat angle = 30°)	0.38	±0.03
CDG window + white venetian blind (slat angle = 60°)	0.08	±0.01
CDG window + grey roller blind	0.09	±0.01
CDG window + black venetian blind (slat angle = 60°)	0.02	±0.00

Appendix Table B.5: Summary of Uncertainty Estimates in Longwave Properties

Measured quantity	Symbol	Nominal value
Reflectance of backing surface 1	ρ_{B1}	0.976
Reflectance of backing surface 2	ρ_{B2}	0.065
System reflectance with backing surface 1	ρ_{M1}	0.320
System reflectance with backing surface 2	ρ_{M2}	0.060

Derived quantity	Symbol	Nominal value	P	B	U
Longwave reflectance	ρ^{lw}	0.040	0.011	0.011	±0.016
Longwave transmittance	τ^{lw}	0.520	0.017	0.017	±0.024
Emittance	ε	0.440	0.020	0.020	±0.028

Appendix Table B.6: Orientation of Sample Holder and the Change in Response of the Sphere

	Change in response of the sphere relative to down facing orientation			
Reflectance reference	Up facing	Right facing	Left facing	Down facing
60 deg reference	0.991	0.995	0.993	1.000
45 deg reference	0.983	0.995	0.988	1.000
30 deg reference	0.985	0.997	0.991	1.000
15 deg reference	0.994	0.998	0.997	1.000

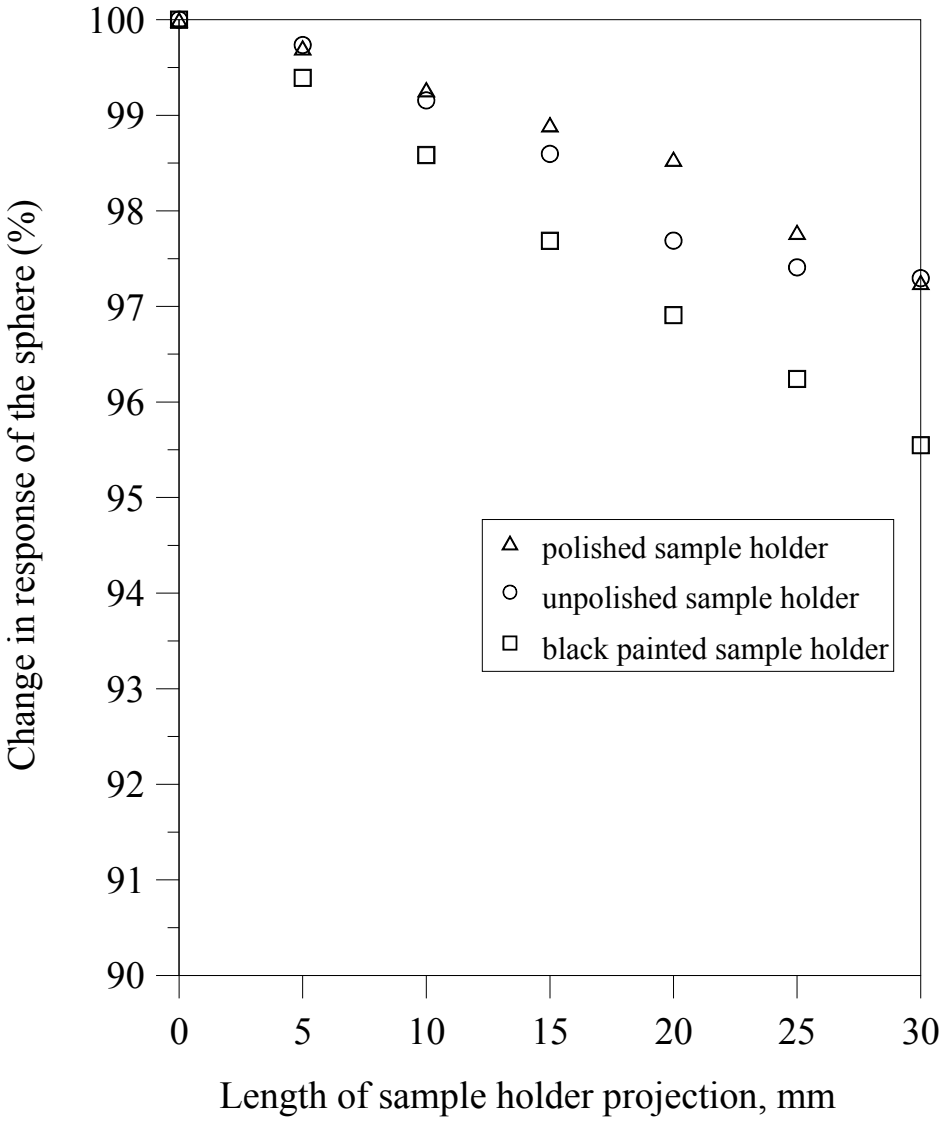

Appendix Figure B.1: Change in Response of the Sphere versus Projected Length of Sample Holder

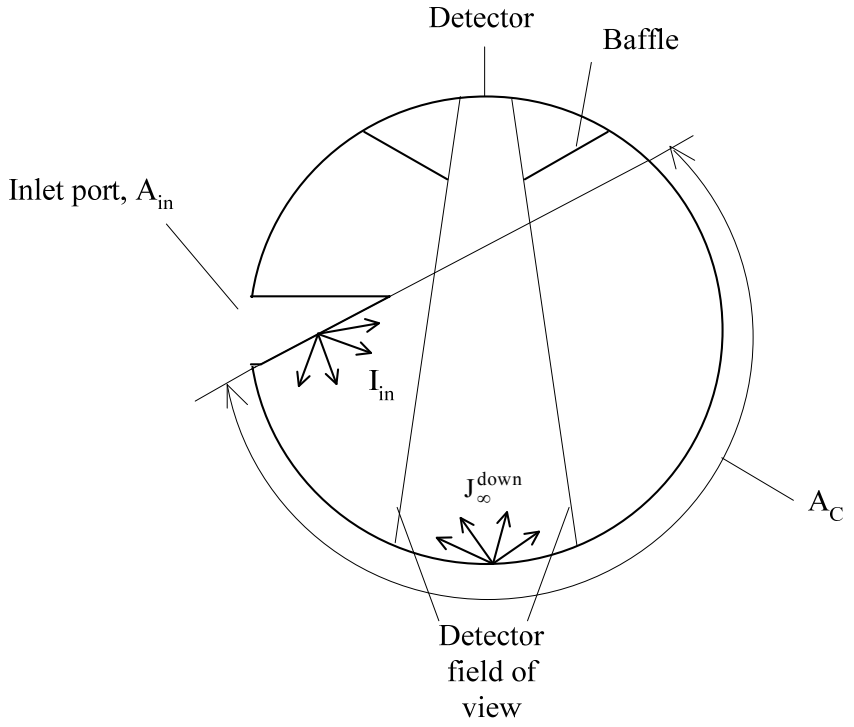

Appendix Figure B.2: Integrating Sphere with Sample Holder Facing Downwards

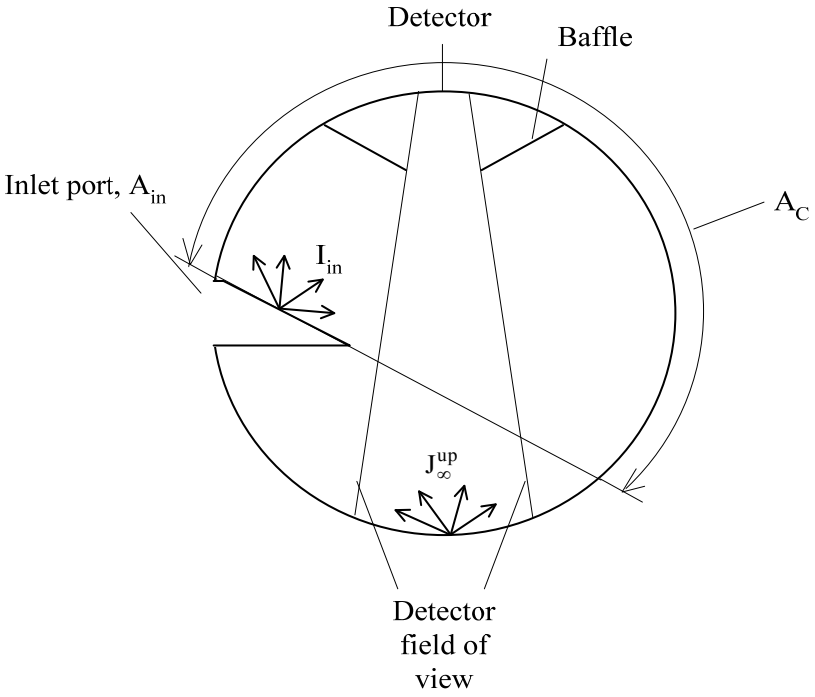

Appendix Figure B.3: Integrating Sphere with Sample Holder Facing Upwards.

REFERENCES

Chapter 1 References

ASHRAE, 2005, "Handbook of Fundamentals," American Society of Heating Refrigeration and Air Conditioning Engineers, Inc.

Breitenbach, J., Lart, S., Langle, I., and Rosenfeld, J.L.J., 2001, "Optical and Thermal Performance of Glazing with Integral Venetian Blinds," Energy and Buildings, vol. 33, pp. 433-442.

Brunger, A., Dubrous, F.M., and Harrison, S.J., 1999, "Measurement of the Solar Heat Gain Coefficient and U-value of Windows with Insect screens," ASHRAE Transactions, vol. 105, Part 2, pp. 1038-1044.

CSA A440.2-98, 1998, "Energy Performance of Windows and Other Fenestration Systems," Canadian Standards Association, Toronto, Canada.

Collins, M.R., and Harrison, S.J., 1999, "Calorimetric Measurement of the Inward-Flowing Fraction of Absorbed Solar Radiation in Venetian Blinds," ASHRAE Transactions, vol. 105, Part 1, pp. 1022-1030.

Collins, M.R., Harrison, S.J., Oosthuizen, P.H., and Naylor, D., 2002, "Sensitivity Analysis of Heat Transfer from an Irradiated Window and Horizontal Louvered Blind Assembly," ASHRAE Transactions, vol. 108, Part 1, pp. 503-511.

Collins, M.R., and Harrison, S.J., 2004a, "Calorimetric Analysis of the Solar and Thermal Performance of Windows with Interior Louvered Blinds," ASHRAE Transactions, vol. 110, Part 1, pp. 474-485.

Collins, M.R., and Harrison, S.J., 2004b, "Estimating the Solar and Thermal Gain from a Windows with an Interior Venetian Blind," ASHRAE Transactions, vol. 110, Part 1, pp. 486-500.

Collins, M.R., and Wright, J.L., 2005, "Calculating Performance Indices for Windows with a Diathermanous Layer," A draft paper submitted to ASHRAE Transactions.

EEL, 1995, "FRAMEplus toolkit: A Comprehensive Tool for Modelling Heat Transfer in Windows, Doors, Walls and Other Building Components," Enermodal Engineering Ltd., Waterloo, Ontario.

EnergyPlus, 2005, "EnergyPlus Engineering Reference – The Reference to EnergyPlus Calculations," U.S. Department of Energy, pp. 151-169.

Farber, E.A., W.A. Smith, C.W. Pennington, and J.C. Reed. 1963. Theoretical analysis of solar heat gain through insulating glass with inside shading. *ASHRAE Journal*, pp. 79.

Finlayson, E.U., Arasteh, D.K., Huizenga, C., Rubin, M.D., and Reilly, M.S., 1993, "WINDOW 4.0: Documentation of Calculation Procedures," Energy and Environment Division, Lawrence Berkeley Laboratory, Berkeley, California.

Furler, R.A. 1991. Angular dependence of optical properties of homogeneous glasses. ASHRAE Transactions, 97 (2): 1129-1133.

Garnet, J.M., 1999, "Thermal Performance of Windows with Inter-Pane Venetian Blinds," MASc. Thesis, University of Waterloo, Waterloo, Ontario.

Grasso, M., and D.R. Buchanan. 1979. Roller shade system effectiveness in space heating energy conservation. ASHRAE Transactions, 85(2520): 156-173.

Grasso, M., and Buchanan, D.R., 1982, "Window Shades in Energy Conservation," Home Economics Research Journal, vol. 11, no. 1, pp. 89-97.

Grasso, M.M., Hunn, B.D., and Rewerts, A.M., 1997, "Effect of Textile Properties in Evaluating a Directional Shading Fabric," Textile Research Journal, vol. 67, no. 4, pp. 233-247.

Harrison, S.J., and Dubrous, F., 1990, "Determination of Window Thermal Characteristics Using a Solar Simulator Based Test Method," ASHRAE Transactions, vol. 96, Part 1, pp. 912-919.

Harrison, S.J., and S.J. van Wonderen. 1998. Evaluation of solar heat gain coefficient for solar-control glazings and shading devices. ASHRAE Transactions, 104(1)

Hollands, K.G.T, Wright, J.L., and Granqvist, C.G., 2001, "Solar Energy – The State of the Art – ISES Position Papers," James and James Ltd., pp. 29-50.

Klems, J.H., 1994a, "A New Method for Predicting the Solar Heat Gain of Complex Fenestration System – 1. Overview and Derivation of the Matrix Layer Calculation," ASHRAE Transactions, vol. 100, Part 1, pp. 1065-1072.

Klems, J.H., 1994b, "A New Method for Predicting the Solar Heat Gain of Complex Fenestration System – 2. Detailed Description of the Matrix Layer Calculation," ASHRAE Transactions, vol. 100, Part 1, pp. 1073-1086.

Kotey, N.A., Collins, M.R., Wright, J.L., and T. Jiang. 2008. A Simplified Method for Calculating the Effective Solar Optical Properties of a Venetian Blind Layer for Building Energy Simulation. Accepted (May 2008) in ASME Journal of Solar Energy Engineering.

LBNL, 2008. International Glazing Database (IGDB). http://windows.lbl.gov/materials/igdb/

Mcquiston, F.C., Parker, J.D., and Spitler, J.D., 2000, "Heating, Ventilating, and Air Conditioning – Analysis and Design," John Wiley and Sons, Inc., Fifth Edition.

Ozisik, N., and L.F. Schutrum. 1959. Heat flow through glass with roller shades. ASHRAE Transactions, 65(1696): 697-716.

Parmelee, G.V., and Aubele, W.W., 1952, "The Shading of Sunlit Glass - An Analysis of the Effect of Uniformly Spaced Flat Opaque Slats," ASHVE Transactions, vol. 58, pp. 377-398.

Parmelee, G.V., Aubele, W.W., and Vild, D.J., 1953, "The Shading of Sunlit Glass - An Experimental Study of Slat-Type Sun Shades," ASHVE Transactions, vol. 59, pp. 221-240.

Pedersen, C.O., Fisher, D.E., Spitler, J.D., and Liesen, R.J., 1998, "Cooling and Heating Load Calculation Principles," ASHRAE Inc.

Petitt, R.B., 1979, "Hemispherical Transmittance Properties of Solar Glazings as a Function of Averaging Procedure and Incident Angle," Solar Energy Materials, vol. 1, pp. 125-140.

Pfrommer, P., Lomas, K.J., Seale, C., and Kupke, Chr., 1995, "The Radiation Transfer through Coated and Tinted Glazing," Solar Energy, vol. 54, no. 5, pp. 287-299.

Pfrommer, P., Lomas, K.J., and Kupke, Chr., 1996, "Solar Radiation Transport through Slat-Type Blinds: A New Model and its Application for Thermal Simulation of Buildings," Solar Energy, vol. 57, no. 2, pp. 77-91.

Rheault, S., and Bilgen, E., 1989, "Heat Transfer Analysis in an Automated Venetian Blind System," ASME Journal of Solar Energy Engineering, vol. 111, pp. 89-95.

Roos, A., 1997, "Optical Characterization of Coated Glazings at Oblique Angles of Incidence: Measurements versus Model Calculations," Journal of Non-Crystalline Solids, vol. 218, pp. 247-255.

Rosenfeld, J.L.J, Platzer, W.J., Van Dijk, H., and Maccari A., 2000, "Modelling the Optical and Thermal Properties of Complex Glazing: Overview of Recent Developments," Solar Energy, vol. 69 Supplement, nos. 1-6, pp. 1-13.

Rosenfeld, J.L.J., 2004, "WIS Database – Data Submission Procedure for Shading and Diffusing Components," Version 1.0., WinDat_N2.07.

Rubin, M., Von Rottkay, K., and Powles, R., 1998, "Window Optics," Solar Energy, vol. 62, no. 3, pp. 149-161.

Rubin, M., Von Rottkay, K., and R. Powles. 1998. Models for the angle-dependent optical properties of coated glazing. Solar Energy, 66(4): 267-276.

Rubin, M., Von Rottkay, K., and R. Powles. 1999. Window optics. Solar Energy, 62(3): 149-161.

UW, 1996, "VISION4, Glazing system thermal analysis: Users and Reference Manuals," University of Waterloo, Waterloo, Ontario.

van Dijk, H., Kenny, P., and Goulding, J. (eds), 2002, "WIS – Advanced Windows Information System – Reference Manual."

Wright, J.L., 1990, "The Measurement and Computer Simulation of Heat Transfer in Glazing Systems", PhD Thesis, University of Waterloo, Waterloo, Ontario.

Wright, J.L., de Abreu, P.F., Fraser, R.A., and Sullivan, H.F., 1994, “Heat Transfer in Glazing Edge-Seals: Calculations Regarding Various Design Options,” ASHRAE Transactions, vol. 100, Part 1, pp. 1705-1717.

Wright, J.L., 1996, “A Correlation to Quantify Convective Heat Transfer Between Vertical Window Glazings,” ASHRAE Transactions, vol. 102, Part 1, pp. 940-946.

Wright, J.L., 1998, “Calculating Center-Glass Performance Indices of Windows,” ASHRAE Transactions vol. 104, Part 1, pp. 1230-1241.

Wright, J.L., and McGowan, A., 1999, “Calculating the Solar Heat Gain of Window Frames,” ASHRAE Transactions, vol. 105, Part 2, pp. 1011-1021.

Wright, J.L., Collins, M.R., and Barnaby, C.S., 2004, “Improving Load Calculations for Fenestration with Shading Devices,” Research Proposal, ASHRAE 1311-TRP.

Wright, J.L., and Kotey N.A., 2006. Solar Absorption by Each Element in a Glazing/Shading Layer Array. ASHRAE Transactions, 112(2): 3-12.

Wright, J.L., Huang, N.Y.T., Collins, M.R., " Thermal Resistance of a Window with an Enclosed Venetian Blind: A Simplified Model," ASHRAE Transactions, Vol. 114, Pt. 1. (2008)

Wright, J.L., Collins, M.R., Barnaby, C.S., and Kotey, N.A., 2009. Improving Cooling Load Calculations for Fenestration with Shading Devices. ASHRAE 1311-RP. Final Report.

Yahoda, D.S., and Wright, J.L., 2004a, “Methods for Calculating the Effective Longwave Radiative Properties of a Venetian Blind Layer,” ASHRAE Transactions, vol. 110, Part 1, pp. 455-462.

Yahoda, D.S., and Wright, J.L., 2004b, “Heat Transfer Analysis of a Between-Panes Venetian Blind Using Effective Longwave Radiative Properties,” ASHRAE Transactions, vol. 110, Part 1, pp. 463-473.

Yahoda, D.S., and Wright, J.L., 2005, “Methods for Calculating the Effective Solar-Optical Properties of a Venetian Blind Layer,” ASHRAE Transactions, vol. 111, Part 1, pp. 572-586.

Chapter 2 References

Edwards, D.K., 1977. Solar absorption by each element in an absorber-coverglass array, Technical Note, Solar Energy, Vol. 19, pp. 401-402.

ElSherbiny, S.M., Raithby, G.D. and Hollands, K.G.T. 1982. Heat transfer by natural convection across vertical and inclined air layers, Journal of Heat Transfer, 104: 96-102.

Finlayson, E.U., Arasteh, D.K., Huizenga, C., Rubin, M.D., and Reilly, M.S. 1993. WINDOW 4.0: documentation of calculation procedures, Energy and Environment Division, Lawrence Berkeley Laboratory, Berkeley, California.

Hollands K.G.T., Wright, J.L., 1983. "Heat Loss Coefficients and Effective $\alpha\tau$ Products for Flat-Plate Collectors with Diathermanous Covers," Solar Energy 30 (3) pp. 211-216.

Hollands, K.G.T, Wright, J.L., and Granqvist, C.G., 2001, “Solar Energy – The State of the Art – ISES Position Papers,” James and James Ltd., pp. 29-50.

Huang, N.Y.T., Wright, J.L., Collins, M.R. 2006. " Thermal Resistance of a Window with an Enclosed Venetian Blind: Guarded Heater Plate Measurements," ASHRAE Transactions, Vol. 112, Pt. 2. pp. 13-21.

Klems, J. H., 1994a, A new method for predicting the solar heat gain of complex fenestration systems – 1. overview and derivation of the matrix layer calculation", ASHRAE Transactions, Vol. 100 (1), pp. 1065-1072.

Klems, J. H., 1994b, A new method for predicting the solar heat gain of complex fenestration systems – 2. detailed description of the matrix layer calculation, ASHRAE Transactions, Vol. 100 (1), pp. 1073-1086.

Klems, J. H. and Warner, J. L., 1995, Measurement of bi-directional optical properties of complex shading devices, ASHRAE Transactions, Vol. 101 (1), pp. 791-801.

Rubin, M., 1982. Calculating heat transfer through windows, Energy Research, Vol. 6, pp. 341-349.

Shewen, E., Hollands, K.G.T., Raithby, G.D. 1996. Heat Transfer by Natural Convection Across a Vertical Cavity of Large Aspect Ratio. Journal of Heat Transfer, 118: 993-995.

van Dijk, H.A.L., Goulding, J. (editors), 1996, WIS reference manual (updated draft), TNO Building and Construction Research.

Wright, J.L., 1980. "Free Convection in Inclined Air Layers Constrained by a V-Corrugated Teflon Film," M.A.Sc. thesis, The University of Waterloo, Mechanical Engineering Department.

Wright, J.L., 1995. "VISION4 Glazing System Thermal Analysis: Reference Manual," Advanced Glazing System Laboratory, University of Waterloo.

Wright, J.L. 1996. A Correlation to Quantify Convective Heat Transfer Between Vertical Window Glazings. ASHRAE Transactions, 102(1): 940-946.

Wright, J.L., and McGowan, A. Calculating solar heat gain of window frames," ASHRAE Transactions, Vol. 105, Pt. 2 (1999), pp. 1011-1021.

Wright, J.L., and N.A. Kotey. 2006. Solar absorption by each element in a glazing/shading layer array. ASHRAE Transactions, 112(2): 3-12.

Wright, J.L., 2008. Calculating Centre-Glass Performance Indices of Glazing Systems with Shading Devices. ASHRAE Transactions, 114(2).

Wright, J.L., Huang, N.Y.T., Collins, M.R., 2008. " Thermal Resistance of a Window with an Enclosed Venetian Blind: A Simplified Model," ASHRAE Transactions, Vol. 114, Pt. 1.

Wright, J.L., Collins, M.R., Barnaby, C.S., and Kotey, N.A., 2009. Improving Cooling Load Calculations for Fenestration with Shading Devices. ASHRAE 1311-RP. Final Report.

Chapter 3 References

ASHRAE. 2005. *ASHRAE Handbook-Fundamentals*. Atlanta: American Society of Heating Refrigeration and Air Conditioning Engineers, Inc.

ASTM E891-87. 1987. *Standard Tables for Terrestrial Direct Normal Solar Spectral Irradiance for Air Mass 1.5*. Philadelphia: American Society for Testing and Materials.

ASTM E903-96. 1996. *Standard Test Method for Solar Absorptance, Reflectance, and Transmittance of Materials Using Integrating Spheres*. Philadelphia: American Society for Testing and Materials.

Edwards, D.K, Gier, J.T., Nelson, K.E. and R.D. Roddick. 1961. Integrating sphere for imperfectly diffuse samples. Applied Optics, 51: 1-12.

Keyes, M.W. 1967. Analysis and rating of drapery materials used for indoor shading. ASHRAE Transactions, 73, (1): 8.4.1.

Lovell, D.J. 1984. Theory and applications of integrating sphere technology. Laser Focus/Electro-Optics. May 1984: 86-96

Pettit, R.B. 1979. Hemispherical transmittance properties of solar glazings as a function of averaging procedure and incident angle. Solar Energy Materials, 1: 125-140.

Chapter 4 References

Furler, R.A. 1991. Angular dependence of optical properties of homogeneous glasses. ASHRAE Transactions, 97 (2): 1129-1133.

Incropera, F.P. and D.P. DeWitt. 2001. *Fundamentals of Heat and Mass Transfer*. 5th Eddition. John Wiley and Sons, Inc.

Karlsson, J., and A. Roos. 2000. Modelling the angular behaviour of the total solar energy transmittance of windows. Solar Energy, 69(4): 321-329.

Keyes, M.W. 1967. Analysis and rating of drapery materials used for indoor shading. ASHRAE Transactions, 73, (1): 8.4.1.

Roos, A. 1997. Optical characterization of coated glazings at oblique angles of incidence: Measurements versus model calculations. Journal of Non-Crystalline Solids, 218: 247-255.

Chapter 5 References

Look, D.C. Jr. 1986. Characteristics of a novel awning fabric. Sun World, 10(4): 117-120.

Chapter 6 References

EnergyPlus. 2007. *EnergyPlus Engineering Reference – The Reference to EnergyPlus Calculations*, U.S. Department of Energy.

Kotey, N.A., Wright, J.L. and M.R. Collins. 2009a. Determining off-normal solar optical properties of drapery fabrics. ASHRAE Transactions, 115(2)

Kotey, N.A., Wright, J.L. and M.R. Collins.2009b. Determining off-normal solar optical properties of roller blinds. ASHRAE Transactions, 115(1).

Kotey, N.A., Wright, J.L. and M.R. Collins.2009b. Determining off-normal solar optical properties of insect screens. ASHRAE Transactions, 115(1).

McCluney, R. 2006. Personal Communication. Florida Solar Energy Centre.

Chapter 7 References

ASTM E408-71. 1971. *Standard Test Method for Total Normal Emittance of Surfaces Using Inspection-Meter Techniques*. Philadelphia: American Society for Testing and Materials.

Christie, E.A. and A.J. Hunter. 1984. Total infrared radiation property measurements of diathermanous films with a reflectometer. Solar Energy, 33(6): 613-618.

Hollands, K.G.T. 2004. *Thermal Radiation Fundamentals*. Begell House, Inc, New York.

Incropera, F.P. and D.P. DeWitt. 2001. *Fundamentals of Heat and Mass Transfer.* 5th Eddition. John Wiley and Sons, Inc.

Jaworske, D.A. and T.J. Skowronski. 2000. Portable infrared reflectometer for evaluating emittance. *Proceedings of the Space Technology and Applications International Forum, Albuquerque, New Mexico, pp. 791-796*.

Kotey, N.A., Wright, J.L. and M.R. Collins. 2009a. Determining off-normal solar optical properties of drapery fabrics. ASHRAE Transactions, 115(2)

Kotey, N.A., Wright, J.L. and M.R. Collins. 2009b. Determining off-normal solar optical properties of roller blinds. ASHRAE Transactions, 115(1).

Kotey, N.A., Wright, J.L. and M.R. Collins. 2009c. Determining off-normal solar optical properties of insect screens. ASHRAE Transactions, 115(1).

Modest, M.F. 1993. *Radiative Heat Transfer*. McGraw-Hill, Inc.

Siegel, R. and J.R. Howell. 1993. *Thermal Radiation Heat Transfer*. 3rd Edition. Taylor and Francis Inc.

Surface Optics Corporation. 2002. *SOC 400T User Guide*. San Deigo, CA.

Chapter 8 References

ASHRAE. 2005. *2005 ASHRAE Handbook—Fundamentals*. Atlanta: American Society of Heating, Refrigerating and Air-Conditioning Engineers, Inc.

Farber, E.A., W.A. Smith, C.W. Pennington, and J.C. Reed. 1963. Theoretical analysis of solar heat gain through insulating glass with inside shading. *ASHRAE Journal*, pp. 79.

Hollands, K.G.T. 2004. *Thermal Radiation Fundamentals*. New York: Begell House, Inc.

Keyes, M.W. 1967. Analysis and rating of drapery materials used for indoor shading. *ASHRAE Transactions* 73(1):8.4.1.

Kotey, N.A., J.L. Wright, and M.R. Collins. 2007. A simplified method for calculating the effective solar optical properties of a drapery. *Proceedings of the 32nd Conference of the*

Solar Energy Society of Canada Inc. (SESCI) and 2nd Conference of the Solar Building Research Network (SBRN), Calgary, Alberta, Canada, June 9–13, 2007.

Kotey, N.A., Wright, J.L. and M.R. Collins. 2008. Determining Longwave Radiative Properties of Flat Shading Materials. *In Proceedings of the SRBN-SESCI Conference. Fredericton, NB.*

Kotey, N.A., J.L. Wright, and M.R. Collins. 2009. Determining off-normal solar optical properties of drapery fabrics. *ASHRAE Transactions* 115(2).

Moore, G.L., and C.W. Pennington. 1967. Measurement and application of solar properties of drapery shading materials. *ASHRAE Transactions* 73(1):8.3.1.

Ozisik, N., and L.F. Schutrum. 1960. Solar heat gain factors for windows with drapes. *ASHRAE Transactions* 66:228.

Pennington, C.W., W.A. Smith, E.A. Farber, and J.C. Reed. 1964. Experimental analysis of solar heat gain through insulating glass with indoor shading. *ASHRAE Journal* 2:27.

Sparrow, E.M., and V.K. Johnson. 1962. Thermal radiation absorption in rectangular grooves. ASME paper 62-WA- 52.

Yellot, J.I. 1965. Drapery fabrics and their effectiveness in solar heat control. *ASHRAE Transactions* 71(1):260–72.

Chapter 9 References

Breitenbach, J., Lart, S., Langle, I., and Rosenfeld, J.L.J., 2001. "Optical and Thermal Performance of Glazing with Integral Venetian Blinds," Energy and Buildings, 33, pp. 433-442.

Jiang, T., 2005, “Transmittance Measurements of Louvered Blinds Using a Broad Area Illumination Integrating Sphere,” MASc. Thesis, University of Waterloo, Waterloo, Ontario.

Jiang, T. and Collins, M.R., 2008, “Validation of Solar/Optical Models for Louvered Shades Using a Broad Area Illumination Integrating Sphere,” ASHRAE Transactions 116 (1).

Kotey, N.A., and Wright, J.L., 2006, “Simplified Solar Optical Calculations for Windows with Venetian Blinds,” In Proceedings of the 31st Conference of the Solar Energy Society of Canada Inc. (SESCI) and 1st Conference of the Solar Building Research Network (SBRN), Montreal, Quebec, Canada, August 20-24, 2006.

Milburn D. I. and Hollands K. G. T., 1994, "Solar Transmittance Measurements Using an Integrating Sphere with Broad Area Irradiation," Solar Energy, Vol. 52, No. 6, pp. 491-301.

Parmelee, G.V., and Aubele, W.W., 1952, “The Shading of Sunlit Glass - An Analysis of the Effect of Uniformly Spaced Flat Opaque Slats,” ASHVE Transactions, 58, pp. 377-398.

Pfrommer, P., Lomas, K.J., and Kupke, Chr., 1996, “Solar Radiation Transport through Slat-Type Blinds: A New Model and its Application for Thermal Simulation of Buildings,” Solar Energy, 57(2), pp. 77-91.

Platzer W.J., 2005, “Performance Assessment for Solar Shadings – State of the Art,” Link: http://www.glassfiles.com/library/2/article978.htm.

Rosenfeld, J.L.J, Platzer, W.J., Van Dijk, H., and Maccari A., 2000, “Modelling the Optical and Thermal Properties of Complex Glazing: Overview of Recent Developments,” Solar Energy, 69 (Supplement, 1-6), pp. 1-13.

Yahoda, D.S., and Wright, J.L., 2005a, “Methods for Calculating the Effective Solar-Optical Properties of a Venetian Blind Layer,” ASHRAE Transactions, 111(1), pp. 572-586.

Yahoda, D.S., and Wright, J.L., 2005b, "Methods for Calculating the Effective Longwave Radiative Properties of a Venetian Blind Layer," ASHRAE Transactions, 110(1), pp. 455-462.

Chapter 10 References

ASHRAE. 2005. *ASHRAE Handbook-Fundamentals*. Atlanta: American Society of Heating Refrigeration and Air Conditioning Engineers, Inc.

ASTM E891-87. 1987. *Standard Tables for Terrestrial Direct Normal Solar Spectral Irradiance for Air Mass 1.5*. Philadelphia: American Society for Testing and Materials.

ASTM E903-96. 1996. *Standard Test Method for Solar Absorptance, Reflectance, and Transmittance of Materials Using Integrating Spheres*. Philadelphia: American Society for Testing and Materials.

Barnaby, C. S., J. D. Spitler, and D. Xiao. 2004. Updating the ASHRAE/ACCA residential heating and cooling load calculation procedures and data. RP-1199 final report. ASHRAE.

Brunger, A., Dubrous, F.M., and S.J. Harrison. 1999. Measurement of the solar heat gain coefficient and u-value of windows with insect screens. ASHRAE Transactions, 105(2): 1038-1044.

CANMET. 1993. The determination of fenestration solar heat gain coefficient using simulated solar irradiance. Report prepared for Natural Resources, Canada. The Solar Calorimetry Laboratory, Queen's University, Kingston, Ontario.

CSA. 1998. CSA Standard A440.2-98. Energy performance of windows and other fenestration

Harrison, S.J., and F Dubrous. 1990. Determination of Window Thermal Characteristics Using a Solar Simulator Based Test Method. ASHRAE Transactions, 96(1): 912-919.

Harrison, S.J., and S.J. van Wonderen. 1994. Determining window solar heat gain coefficient. ASHRAE Journal, 36(8): 26-32.

Harrison, S.J., and S.J. van Wonderen. 1998. Evaluation of solar heat gain coefficient for solar-control glazings and shading devices. ASHRAE Transactions, 104(1)

Kotey, N.A., Wright, J.L. and M.R. Collins. 2008. Determining Longwave radiative properties of flat shading materials. SESCI 2008, Fredericton, New Brunswick.

Kotey, N.A., Wright, J.L. and M.R. Collins. 2009a. Determining off-normal solar optical properties of drapery fabrics. ASHRAE Transactions, 115(2)

Kotey, N.A., Wright, J.L. and M.R. Collins. 2009b. Determining off-normal solar optical properties of roller blinds. ASHRAE Transactions, 115(1).

Kotey, N.A., Wright, J.L. and M.R. Collins. 2009c. Determining off-normal solar optical properties of insect screens. ASHRAE Transactions, 115(1).

Kotey, N.A., Wright, J.L. and M.R. Collins. 2009d. A detailed model to determine the effective solar optical properties of draperies. ASHRAE Transactions, 115(1).

Pedersen, C. O., R. J. Liesen, R. K. Strand, and D. E. Fisher. 2001. *Toolkit for building load calculations*. Atlanta: American Society of Heating Refrigeration and Air Conditioning Engineers, Inc.

van Wonderen, S. Experimental Determination of Fenestration Solar Heat Gain Coefficient, MASc Thesis. 1995. Queens University. Kingston. Ontario.

Wright, J.L., and A. McGowan. 1999. Calculating solar heat gain of window frames. ASHRAE Transactions, 105(2): 1011-21.

Wright, J.L., and N.A. Kotey. 2006. Solar absorption by each element in a glazing/shading layer array. ASHRAE Transactions, 112(2): 3-12.

Wright, J.L., 2008. Calculating Centre-Glass Performance Indices of Glazing Systems with Shading Devices. ASHRAE Transactions, 114(2).

Wright, J.L., Collins, M.R., Barnaby, C.S., and Kotey, N.A., 2009. Improving Cooling Load Calculations for Fenestration with Shading Devices. ASHRAE 1311-RP. Final Report.

Appendix A References

ANSI/ASHRAE 74-1988. 1988. ASHRAE Standard. Method of Measuring Solar-Optical Properties of Materials. American Society of Heating Refrigeration and Air Conditioning Engineers, Inc. Atlanta, GA.

Labsphere, 1998, A Guide to Integrating Sphere Theory and Application – Tech Guide. Labsphere Inc.

Appendix B References

Abernethy, R. B., Benedict, R. P., and Dowdell, R. B., 1985. ASME measurement uncertainty. Journal of Fluids Engineering. Vol 107. pp 161-164.

ASTM E903-96. 1996. *Standard Test Method for Solar Absorptance, Reflectance, and Transmittance of Materials Using Integrating Spheres*. Philadelphia: American Society for Testing and Materials.

Barnaby, C. S., J. D. Spitler, and D. Xiao. 2004. Updating the ASHRAE/ACCA residential heating and cooling load calculation procedures and data. RP-1199 final report. ASHRAE.

Chakroun, W., Taylor, R. P., Steele, W. G., and Coleman, H.W. 1993. Bias error reduction using ratios to baseline experiments – Heat transfer case study. Journal of Thermophysics and Heat Transfer. Vol 7. No.4. pp. 754-757.

Coleman, H. W., and Steele, W. G., 1999, *Experimentation and Uncertainty Analysis for Engineer*s, 2nd Edition, John Wiley & Sons Inc.

Pedersen, C. O., R. J. Liesen, R. K. Strand, and D. E. Fisher. 2001. *Toolkit for building load calculations*. Atlanta: American Society of Heating Refrigeration and Air Conditioning Engineers, Inc.

Wright, J.L., Collins, M.R., Barnaby, C.S., and Kotey, N.A., 2009. Improving Cooling Load Calculations for Fenestration with Shading Devices. ASHRAE 1311-RP. Final Report.